

# PROCEEDINGS

**The 13th HKBU-CSD Postgraduate Research  
Symposium**

# PG Day 2011



**Department of Computer Science  
Hong Kong Baptist University**

**March 3 & March 4, 2011**

# The 13th HKBU-CSD Postgraduate Research Symposium (PG Day) Program

March 3 <sup>rd</sup> 2011, Thursday	
Time	Sessions
09:00-09:20	<b>On-site Registration (Room T714)</b>
09:20-09:30	<b>Welcome: Prof. Jiming Liu (Head of Department of Computer Science, HKBU)</b>
09:30-12:00	<p><b>Session I (Chair: Mr. Xia Shang, T714)</b></p> <ul style="list-style-type: none"> <li>• <i>Mobile Location Detection within a WLAN Network</i> Mr. Cheng Quan Jia</li> <li>• <i>PCM Mask: Accelerating Transaction Execution with Phase Change Memory</i> Mr. Shen Gao</li> <li>• <i>Secure Proximity Monitoring in Mobile Geo-Social Services</i> Mr. Li Hong Ping</li> <li>• <i>A Signal Strength Based Location Estimation Algorithm within a Wireless Network</i> Mr. Kevin Shum</li> <li>• <i>Cooperative and Penalized EM Algorithm Based on Maximum Weighted Likelihood for Gaussian Mixture Learning</i> Ms. Hong Jia</li> </ul>
12:00-13:15	<b>Noon Break</b>
13:15-14:15	<p><b>Session II_A (Chair: Mr. Yun Peng, T714)</b></p> <ul style="list-style-type: none"> <li>• <i>Music Emotion Retrieval Based on Acoustic Features</i> Mr. Jie Deng</li> <li>• <i>The Investigation of an Exemplar-Based Hidden Markov Model for Lipreading</i> Mr. Xin Liu</li> </ul>
14:45-16:00	<p><b>Distinguished Lecture (Room LT2)</b> <b>(Chair: Prof. Jiming Liu, Head of Department of Computer Science, HKBU)</b></p> <p style="text-align: center;"><b>Machine Intelligence, F-granulation and Generalized Rough Sets: Uncertainty Analysis in Pattern Recognition and Mining</b></p> <p style="text-align: center;"><i>Prof. Sankar K. Pal</i></p> <p style="text-align: center;">FNA, FTWAS, FIAPR, Fellow IEEE Distinguished Scientist and Former Director, Indian Statistical Institute</p>
16:20-17:20	<p><b>Session II_B (Chair: Mr. Yun Peng, T714)</b></p> <ul style="list-style-type: none"> <li>• <i>Motion Capture Data Completion and Denoising by Singular Value Thresholding</i> Mr. Yongquan Lai</li> <li>• <i>Linear Dependency Modeling for Feature Fusion</i> Mr. Andy J. H. Ma</li> </ul>

# The 13th HKBU-CSD Postgraduate Research Symposium (PG Day) Program

March 4 <sup>th</sup> 2011, Friday	
Time	Sessions
09:20-10:50	<b>Session III (Chair: Ms. Hong Jia, T716)</b>
	<ul style="list-style-type: none"> <li>• <i>Texture Analysis Based on Saddle Points-based BEMD and MB-LBP</i> Mr. Pan Jianjia</li> <li>• <i>Survey of Speeding up Apriori by GPUs</i> Mr. You Li</li> <li>• <i>Scalable Data-oriented View Update Analysis</i> Mr. Yun Peng</li> </ul>
	<b>Tea Break</b>
11:00-12:30	<b>Session IV (Chair: Mr. Xia Shang, T716)</b>
	<ul style="list-style-type: none"> <li>• <i>A Survey of Bayesian Models for Network Motifs Discovery</i> Mr. Kai Liu</li> <li>• <i>An AOC-Based Approach to Solving Complex Energy Distribution Problems</i> Mr. Benyun Shi</li> <li>• <i>Toward Effective Vaccine Deployment: A Systematic Study</i> Mr. Shang Xia</li> </ul>
	<b>Noon Break</b>
14:10-15:40	<b>Session V (Chair: Mr. Jintian Deng, T716)</b>
	<ul style="list-style-type: none"> <li>• <i>Computationally Characterizing Functional Interaction of Cancer Patients in Popular Online Support Group</i> Mr. Lailei Huang</li> <li>• <i>Exploring the Wait Time Relationships Among Units in the Cardiac Care</i> Ms. Li Tao</li> <li>• <i>Multi-level Semantic Characterisation and Refinement for Web Image Search</i> Ms. Yuanxi Li</li> </ul>
	<b>Best Paper &amp; Best Presentation Awards Announcement (Room T716)</b>
17:30-18:00	<b>Sharing Session with Prof. Sankar K. Pal (Room T716)</b>
<b>Closing</b>	

# The 13th HKBU-CSD Postgraduate Research Symposium (PG Day) Program

March 3 <sup>rd</sup> 2011, Thursday	
Time	Sessions
09:00-09:20	On-site Registration (Room T714)
09:20-09:30	<b>Welcome: Prof. Jiming Liu (Head of Department of Computer Science, HKBU)</b>
09:30-12:00	<div style="background-color: cyan; padding: 2px;"><b>Session I (Chair: Mr. Xia Shang, T714)</b></div> <ul style="list-style-type: none"> <li>• <i>Mobile Location Detection within a WLAN Network</i> Mr. Cheng Quan Jia</li> <li>• <i>PCM Mask: Accelerating Transaction Execution with Phase Change Memory</i> Mr. Shen Gao</li> <li>• <i>Secure Proximity Monitoring in Mobile Geo-Social Services</i> Mr. Li Hong Ping</li> <li>• <i>A Signal Strength Based Location Estimation Algorithm within a Wireless Network</i> Mr. Kevin Shum</li> <li>• <i>Cooperative and Penalized EM Algorithm Based on Maximum Weighted Likelihood for Gaussian Mixture Learning</i> Ms. Hong Jia</li> </ul>
12:00-13:15	<b>Noon Break</b>
13:15-14:15	<div style="background-color: cyan; padding: 2px;"><b>Session II_A (Chair: Mr. Yun Peng, T714)</b></div> <ul style="list-style-type: none"> <li>• <i>Music Emotion Retrieval Based on Acoustic Features</i> Mr. Jie Deng</li> <li>• <i>The Investigation of an Exemplar-Based Hidden Markov Model for Lipreading</i> Mr. Xin Liu</li> </ul>
14:45-16:00	<p><b>Distinguished Lecture (Room LT2)</b> <b>(Chair: Prof. Jiming Liu, Head of Department of Computer Science, HKBU)</b></p> <div style="text-align: center; padding: 10px;"> <p><b>Machine Intelligence, F-granulation and Generalized Rough Sets: Uncertainty Analysis in Pattern Recognition and Mining</b></p> <p><i>Prof. Sankar K. Pal</i></p> <p>FNA, FTWAS, FIAPR, Fellow IEEE Distinguished Scientist and Former Director, Indian Statistical Institute</p> </div>
16:20-17:20	<div style="background-color: cyan; padding: 2px;"><b>Session II_B (Chair: Mr. Yun Peng, T714)</b></div> <ul style="list-style-type: none"> <li>• <i>Motion Capture Data Completion and Denoising by Singular Value Thresholding</i> Mr. Yongquan Lai</li> <li>• <i>Linear Dependency Modeling for Feature Fusion</i> Mr. Andy J. H. Ma</li> </ul>

# The 13th HKBU-CSD Postgraduate Research Symposium (PG Day) Program

March 4 <sup>th</sup> 2011, Friday	
Time	Sessions
09:20-10:50	<b>Session III (Chair: Ms. Hong Jia, T716)</b>
	<ul style="list-style-type: none"> <li>• <i>Texture Analysis Based on Saddle Points-based BEMD and MB-LBP</i> Mr. Pan Jianjia</li> <li>• <i>Survey of Speeding up Apriori by GPUs</i> Mr. You Li</li> <li>• <i>Scalable Data-oriented View Update Analysis</i> Mr. Yun Peng</li> </ul>
	<b>Tea Break</b>
11:00-12:30	<b>Session IV (Chair: Mr. Xia Shang, T716)</b>
	<ul style="list-style-type: none"> <li>• <i>A Survey of Bayesian Models for Network Motifs Discovery</i> Mr. Kai Liu</li> <li>• <i>An AOC-Based Approach to Solving Complex Energy Distribution Problems</i> Mr. Benyun Shi</li> <li>• <i>Toward Effective Vaccine Deployment: A Systematic Study</i> Mr. Shang Xia</li> </ul>
	<b>Noon Break</b>
14:10-15:40	<b>Session V (Chair: Mr. Jintian Deng, T716)</b>
	<ul style="list-style-type: none"> <li>• <i>Computationally Characterizing Functional Interaction of Cancer Patients in Popular Online Support Group</i> Mr. Lailei Huang</li> <li>• <i>Exploring the Wait Time Relationships Among Units in the Cardiac Care</i> Ms. Li Tao</li> <li>• <i>Multi-level Semantic Characterisation and Refinement for Web Image Search</i> Ms. Yuanxi Li</li> </ul>
	<b>Best Paper &amp; Best Presentation Awards Announcement (Room T716)</b>
17:30-18:00	<b>Sharing Session with Prof. Sankar K. Pal (Room T716)</b>
<b>Closing</b>	

# Mobile Location Detection within a WLAN Network

Cheng Quan Jia

## Abstract

*With the prevalence of Wi-Fi activity within a wireless network, there are growing interests in mobile surveillance and device tracking for better network services. With a good location estimation algorithm integrated into a wireless network, system administrators can closely monitor the network traffic as well as the behavior of the mobile users. By modifying the embedded software in off-the-shelf WLAN APs, our system can sniff out data packets transmitted by WLAN devices without the need to install client programs on mobile user devices. This paper proposes a wireless LAN system that can locate and track down wireless communication within the system. The proposed WLAN location system is a hybrid system that utilizes the Centre of Gravity (CG) method and switches to other methods when CG becomes ineffective. With an accuracy comparable to the fingerprinting method but without paying the high cost of training, retraining, and the maintenance of the fingerprint databases inside our WLAN system, the proposed method is well-justified for its efficiency and effectiveness in locating and mobile users' activities within a wireless network.*

## 1 Introduction

Under the Government's Digital 21 Strategy [3] to endorse the idea of a wireless city, the HKSAR government had put forward a Wi-Fi Programme (GovWiFi)[2] as an initiative to create a wireless infrastructure to facilitate mobile Internet access by citizens and businesses, in order to improve quality of living and business operations in Hong Kong. The programme also gives produces many easy targets for hacking activities among WLAN networks. In view of the heavy usage and progressively growing coverage of WLAN within indoor environment, and the relatively few research studies on efficient ways to perform WLAN positioning and tracking, there is a need to investigate the feasibility of using WLAN to locate a mobile user as well as pinpoint hacking activities in an indoor environment. In this paper, we propose a network surveillance system making use of a popular off-the-shelf wireless router by Linksys - (Model: WRT54G)[4] for detecting and locating mobile

users. We very much rely on simple assumptions or some existing intrusion detecting algorithm for detecting hackers' presence in a WLAN, but for pinpointing the hacker's location, we enhance and rewrite embedded software at the AP sensors to "listen" to "conversations" among all the sensors and wireless devices within the coverage of the WLAN network. In more technical terms, we will write software and re-program the AP and wireless Routers such that our software can collect signal strength readings when wireless devices, especially hacker devices, communicate with any of the surrounding AP sensors[5]. With these signal strength readings collected in real-time and stored in the data store at our data centre, together with the physical positions of the APs known, we can reuse some of our previous algorithms[14, 15, 12, 22, 19, 17, 16] to find out the whereabouts of the mobile devices. There are a number of ways to locate a mobile user based on Received Signal Strength Indicator (RSSI). Some of the fundamental position techniques are Location fingerprinting (LF), Propagation Loss Model (RF), Tri-lateration, Tri-angulations and Radio Maps with pattern recognition approaches [8, 18, 1, 11, 6]. Our main focus in this project is the Centre of Gravity method, for its ease of deployment and the low computation cost. The Centre of Gravity method for location estimation is adopted in our system just for demonstrating the effectiveness for network surveillance purpose[20].

## 2 Related Work

Although theoretically the same or similar location estimation algorithms for the mobile phone network can be applied to the WLAN, there is relatively few research on WLAN positioning [13, 7, 10, 9] in the literature. The difficulties are mainly attributed to the differences in penetration power, signal fading, signal attenuation, the layout of access points (regularity vs. randomness), and the more serious body effect within the WLAN as compared to the mobile phone network. Many researchers have proposed methods in providing location services using the mobile phone networks, but few projects have actually been implemented. The RADAR system [7] was one of the early WLAN-based location estimation systems. Based on the FreeBSD distribution and WaveLAN WLAN network, the RADAR system

can locate a user who carries a notebook with an accuracy of 5 meters. Y. Wang et al [13] studied on the feasibility of making use of the WLAN to locate a mobile device. They had an empirical study inside their department building and labs and reported their findings and simulation results. However, there are no systematic ways to generalize these approaches and fine tune the necessary environment parameters. Furthermore, the target environment is critical to the accuracy of WLAN positioning. Radio characteristics in an open environment are never static and there is not a single methodology that can fine tune data from time to time and adapt to the changing environment. It is only recently that they start to study on post-deployment adaptation. They try installing special hardware which monitors radio characteristics at different positions and rebuild the propagation model periodically [10, 9]. Among the commercial products that are available for WLAN positioning, Ekahau is the company that is taking a leading position in in-door positioning. Their positioning system relies on building an accurate radio map according to the layout of the access points as well as the model and specific characteristics of these access points. Nonetheless, it is a costly system; and it falls victim to environmental changes and post-deployment adaptation problems. The relationship between RSSI values and the inter-distance between a mobile device and the AP obeys the inverse square law but is also affected by interference, noise and reflection, etc. Indoor positioning technology, or the technique for locating a mobile user, is the basic technology for indoor location-aware computing. In general, there is a huge variety of location-based applications and services that rely on an accurate and stable location estimation system such as warehouse management, point-of-interest, infotainment and customer/consumer flow analysis within enclosed areas such as shopping malls and exhibition centres. Such location-based services play a crucial role in enabling e-commerce, m-commerce, and eventually bringing the society to an era of ubiquitous/pervasive computing. [21] The following sections list several RSSI-based location approaches.

## 2.1 Location Fingerprinting

Location Fingerprinting is one of the approaches which utilize signal strength for location estimation. It is divided into two phases, the off-line phase and the on-line phase. In the off-line phase, snapshots of the Received Signal Strength (RSS) vectors are collected in every location. Each snapshot of the RSS vector contains the RSS,  $S_i$ , received from the  $i^{th}$  AP sensor identified by the AP Identify Code,  $AP_i$ . The RSS vector and its corresponding location are then stored in the database. During the on-line phase, the RSS vector of the Hand-held wireless device or mobile station is measured and generalized weighted distance  $L_p$

between the measured RSS vector of the mobile station and the database entry is computed with the following formula,

$$L_p = 1/N \sum_{i=1}^N ((1/w_i |s_i - s_i^m|)^p)^{1/p} \quad (1)$$

where N is the number of the AP sensors received from the location, p and  $w_i$  are scalar factor and weighting factor of the  $i^{th}$  signal difference respectively. The weighting factor  $w_i$  is used as a bias which indicates the reliability of the database entry or the RSS measurements. The location of the mobile station is then estimated in the on-line phase by either

- Choosing the location in the database corresponding to the fingerprint with the minimum distance to the measured fingerprint of the mobile station. For example, the Manhattan distance, L1 and the Euclidean distance, L2 with  $w_i = 1$  often used for all entries.
- Estimating the location of the mobile station by averaging the M closest locations in the database with smallest  $L_p$ .

The Location Fingerprinting Approach is widely used in the indoor location estimation and has been proven for its great accuracy. However, applying the Location Fingerprinting is not practically scalable. It is because it is very difficult to collect the RSS measurement of all the locations in a large area and this large amount of measurements induces high computation and storage costs. In addition, the Location Fingerprinting is very sensitive to the surrounding environments, thus re-calibration or re-collection of data is often required. The "Least-Squares" method was adopted in our experiment as our performance measurement of fingerprint matching. "Least-Squares" tries to derive a solution that minimizes the summation of squared differences in signal strength between an AP Sensor and each of the corresponding AP Sensors, i.e.

$$\Pi = \min_{j=1}^M \left( \sum_{i=1}^n (s_i^T - s_i^t)^2 \right) \quad (2)$$

where M is the number of fingerprints registered in the database, N is the number of AP Sensor in the WLAN,  $s_i^T$  represents the  $i^{th}$  AP Sensor in the Training Data Set and  $s_{(i')^t}$  represents the Signal Strength value of the  $i^{th}$  AP Sensor in the Testing Data Set.

## 2.2 Aggregated Signal Layout

Fingerprinting is an effective location estimation method, but it is not without its problems. A Fingerprint is unique to its AP sensor network, i.e. the number of AP

sensors as well as their locations. If there is a change of AP sensor locations, or an AP sensor removed from the sensor network, we have to collect the signal (data) and to train the Fingerprints database from scratch. This drawback makes the Fingerprint method expensive to maintain for AP sensor networks that changes sensors frequently. A similar location estimation approach called Aggregated Signal Layout sets out to reduce the complexity of Fingerprinting approach. For each AP sensor in an AP sensor network, we place position markers at different distances from the AP sensor and measure the received signal strengths. The average signal strength from the position marker and the Position Marker Distance is recorded to the Signal Layout of the AP sensor. Unlike the Fingerprint method, Aggregated Signal Layout considers the Signal Layout collected by AP sensors individually. The Signal Layout of an AP sensor belongs to that AP alone, and is independent of the surrounding AP sensors. Aggregated Signal Layout performs location estimation by overlapping layers of the Signal Layouts of AP sensors in the sensor network. Consider a single AP sensor, given the received signal strength from a mobile device, the distance between the device and the AP sensor could be obtained from the sensor's Signal Layout; the inter-distance draws the possible locations of the mobile device in a circular perimeter. By aggregating the Signal Layouts of AP sensors, essentially locating the common points of the perimeters, the estimated location of the mobile device can be found. Since it is usual that the received signal strength does not conform to an AP sensor's Signal Layout, we allow some error to the distance estimation. For instance, we allow a search window of +/- 2dbm to our Aggregated Signal Layout method, such that when an AP sensor receives signal strength of -68dbm, the algorithm searches the sensor's Signal Layout for Position Marker Distances that falls between signal strengths -66 and -70dbm. This search window we call Signal Spread is used to ensure more overlaps between Signal Layouts of AP sensors.

### 2.3 Center of Gravity

The Center of Gravity (CG) is a location estimation algorithm based on Received Signal Strength (RSS). It is a location estimation algorithm focusing on areas with dense AP sensors. The location estimation formula for CG is defined as follows,

$$x = (x_1 s_1^{-b} + x_2 s_2^{-b} + x_3 s_3^{-b} + \dots + x_n s_n^{-b}) / (s_1^{-b} + s_2^{-b} + s_3^{-b} + \dots + s_n^{-b}) \quad (3)$$

$$y = (y_1 s_1^{-b} + y_2 s_2^{-b} + y_3 s_3^{-b} + \dots + y_n s_n^{-b}) / (s_1^{-b} + s_2^{-b} + s_3^{-b} + \dots + s_n^{-b}) \quad (4)$$

where (x, y) is the estimated location of the mobile user,  $(x_n, y_n)$  is the location of AP sensor n, and  $s_n$  is the RSSI from AP sensor n. The CG algorithm has proven to be very effective and can provide outstanding performance in

metropolitan area during our mobile location estimation experiments using the mobile phone network. Although CG has proved its outstanding performance in metropolitan areas, it can only estimate the mobile device inside a convex hull. The estimated position by CG algorithm is restricted within the polygonal area formed by joining the position of the outermost AP sensors even though the actual position of the mobile device is outside the area. Moreover, it seems that the performance of the CG algorithm is related to the number of AP sensors received. Thus, CG may lose its accuracy in suburban areas where the number of AP sensors received may not be as many as in metropolitan areas.

## 3 Experimental Setup

In our experiment, a programmable router - Linksys WRT54G [4], which is burned with an open-source custom-made firmware, acts as a wireless sensor to obtain information from data packets transmitted within the WLAN environment. Packet information such as Service Set Identifier (SSID), Extended Service Set Identifier (ESSID), Received Signal Strength Indicator (RSSI), Noise Level, Traffic rate and Traffic Frequency are collected by a custom-made wireless data acquisition application written for the Linksys WRT54G WLAN router. AP uses TCP socket to send the data to control server, control server analysis the data collected and estimate the location on fly and the information is stored into the database with on current timestamp for logging purpose. For better visualization and understanding of signal strength characteristics within our test bed, we will construct a software module for displaying the estimated mobile users' location as well signal-strength-based Radio Maps.

## 4 Conclusion

The experiment aims to demonstrate the feasibility of using WLAN to locate and track mobile activities in an indoor environment, by developing a location system that does not possess adaptation issues and expensive maintenance. In the future, we are going to enhance the existing signal strength based location estimation methods for indoor location estimation base on the method we have done on our previous research paper, such as a hybrid location system using two or more location estimation methods, and make use of RSSI collected from mobile terminals and/or from AP sensors (WLAN access points) for a more stable location estimation. The Center of Gravity algorithm is accurate and efficient but less so if the mobile device is outside of the convex hull or is near one of the outermost AP sensors. With our proposed system, if the first estimated location (by CG method) is outside of the convex hull, we

will switch to Fingerprinting or other location estimation algorithms. We will propose more appropriate algorithms in our progress and aim at a hybrid system that can use the best of each algorithm has to provide. In addition, for better visualization and better understanding of signal strength characteristics within our test bed, we would construct a software module for displaying information about mobile users as well as Signal Layouts for investigation in order to discover better algorithms for location and tracking mobile users within our test-bed at HKBU.

## References

- [1]
- [2] Government wi-fi programme (govwifi). <http://www.gov.hk/en/theme/wifi/program/index.htm>.
- [3] Hong kong government's digital 21 strategy. <http://www.info.gov.hk/digital21/eng/index.htm>.
- [4] Linksys wrt54g series. <http://en.wikipedia.org/wiki/Linksys>.
- [5] Open source fireware for access point. <http://www.opertwrt.org>.
- [6] P. Bahl and V. Padmanabhan. Radar: An in-building rf-based user location and tracking system. In *Proceedings of INFOCOM 2000*, volume 2, pages 775–784, March 2000.
- [7] P. Bahl and V. Padmanabhan. Radar: An in-building rf-based user location and tracking system. In *Proceedings of INFOCOM 2000*, volume 2, pages 775–784, March 2000.
- [8] K. M. Chu, K. R. Leung, J. K. Ng, and C. H. Li. A directional propagation model for locating mobile stations within a mobile phone network. *International Journal of Wireless and Mobile Computing (IJWMC): Special Issue on Applications, Services and Infrastructure for Wireless and Mobile Computing*, August 2008.
- [9] S. Ganu, A. Krishnakumar, and P. Krishnan. Infrastructure-based location estimation in wlan networks. In *Proceedings of the IEEE Wireless Communications and Networking Conference (WCNC 2004)*, volume 1, pages 465–470, March 2004.
- [10] P. Krishnan, A. Krishnakumar, W.-H. Ju, C. Mallows, and S. Ganu. A system for lease: Location estimation assisted by stationary emitters for indoor rf wireless networks. In *Proceedings of INFOCOM 2004*, volume 2, pages 1001–1011, March 2004.
- [11] Z. li Wu, C. hung Li, J. K. Ng, and K. R. Leung. Location estimation via support vector kernel regression. *IEEE Transactions on Mobile Computing*, March 2007.
- [12] J. K. Ng, J. Zhou, K. M. Chu, and K. R. Leung. A train-once approach for location estimation using the directional propagation model (dpm). *IEEE Transactions on Vehicular Technology*, July 2008.
- [13] Y. Wang, H. L. X. Jia, and G. Li. An indoor wireless positioning system based on wireless local area network infrastructure. In *Proceedings of the 6th International Symposium on Satellite Navigation Technology Including Mobile Positioning & Location Services (SatNav 2003)*, July 2003.
- [14] W. H. Wong, J. K. Ng, and W. M. Yeung. Wireless lan positioning with mobile devices in a library environment. In *Proceedings of ICDCS-MDC 2005 Workshop*, pages 633–636, June 2005.
- [15] Z. Wu, C. hung Li, and J. K. Ng. Improvements to radar location classification. In *Proceedings of the 2008 International Conference on Wireless Communications, Networking and Mobile Computing (WiCOM 2008)*, pages 633–636, 2008.
- [16] W. M. Yeung and J. K. Ng. An enhanced wireless lan positioning algorithm based on the fingerprint approach. In *Proceedings of IEEE TENCON 2006*, IEEE CS Press, pages 14–17, November 2006.
- [17] W. M. Yeung and J. K. Ng. Wireless lan positioning based on received signal strength from mobile device and access points. In *Proceedings of the 13th International Conference on Embedded and Real-Time Computing Systems and Applications (RTCSA 2007)*, pages 131–137, August 2007.
- [18] W. M. Yeung, J. K. Ng, and K. R. Leung. Large-scale location estimation over gsm networks: the gear approach. In *Proceedings of the 24th IEEE International Conference on Distributed Computing Systems Workshops (ICDCS-MDC 2004)*, pages 574–579, March 2004.
- [19] W. M. Yeung, J. Zhou, and J. K. Ng. Enhanced fingerprint-based location estimation system in wireless lan environment. In *Proceedings of the 1st International Workshop on System and Software for Wireless SoC (WSOC 2007)*, pages 273–284, December 2007.
- [20] J. Zhou. *Enhanced Signal Propagation Models and Algorithm Selector for Providing Location Estimation Services within Cellular Radio Networks*. PhD thesis.
- [21] J. Zhou, K. M. Chu, and J. K. Ng. An improved ellipse propagation model for location estimation in facilitating ubiquitous computing. In *Proceedings of the 11th International Conference on Embedded and Real-Time Computing Systems and Applications (RTCSA 2005)*, pages 463–466, August 2005.
- [22] J. Zhou, W. M. Yeung, and J. K. Ng. Enhancing indoor positioning accuracy by utilizing signals from both the mobile phone network and the wireless local area network. In *Proceedings of the IEEE 22nd International Conference on Advanced Information Networking and Applications (AINA 2008)*, pages 138–145, March 2008.

# PCM Mask: Accelerating transaction execution with Phase Change Memory

Shen Gao

Hong Kong Baptist University

sgao@comp.hkbu.edu.hk

## Abstract

*Phase change memory (PCM) is a promising memory technology with various attractive properties: it is a non-volatile and byte-addressable storage media. It has higher density than DRAM and better read latency than NAND flash memory. Thanks to its superiorities, PCM is expected to merge as a common component of the memory/storage hierarchy in near future. In this paper, we present a new system architecture named PCM Mask, which exploits advantages of PCM to accelerate transaction processing speed. Specifically, PCM Mask combines the log I/Os and dirty page I/Os together to save a large amount of I/O traffic. Meanwhile, our new commit protocol eliminates the checkpoint process and the Redo time during system recovery.*

## 1. Introduction

As current memory technology starting to encounter its physical scaling limited [1], *Phase change memory (PCM)* is being investigated as a promising alternative technology. It offers a 2-4X density than DRAM which implies a larger storage capacity for a same chip area. The less idle energy consuming [2] is another advantage of PCM since the current main memory may consume as much as 40% total energy [6]. Comparing to flash memory, the byte addressability of PCM eliminates the erase-before-write constraint. While PCM chips have already come into mass production, in near future PCM is expected to become a common part of the memory/storage system architecture [3].

Pioneer researches about PCM have investigated one important question *where should we place the PCM in front of or behind the system I/O bus?* Since the PCM's performance is more similar to the DRAM and the PCI I/O bus is designed for block-based access which disable the byte addressability of PCM, we believe PCM should belong to be exposed directly to CPU. In addition, a hybrid

system of volatile DRAM and non-volatile PCM is more favorable to support high transaction execution speed.

This paper highlights our initial research on database application of PCM and makes the following three contributions.

First, we proposed new system architecture named PCM Mask, which combines the dirty page I/Os and the logging I/Os together. The byte addressability provides us a great potential of reusing log recorders. It breaks traditional log system design principles which assume the underlying storage system is hard disk drive and log should be designed for append only. Unless there is a system crash, the system will not use the log; however, keeping log records occupies a large portion of I/O time during transaction process. PCM brings us a new way of reusing log. Specifically, its fast reading speed provides us an efficient way of retrieving log recorder, and byte alterable characteristic allows us to modify previous logs. Reusing log is a distinct feature of PCM Mask which totally breaks the traditional concept of log system.

Second, we propose a new commit protocol which assures the ACID properties of DBMSs. Since we redesign the role of log in a DBMS, the new commit protocol eliminates the checkpoint and the Redo processes which were both designed for the traditional log system.

Third, we propose a possible experiment method to prove that PCM Mask can dramatically save the system I/O cost. We also present our initial simulation ideas.

The rest of this paper is organized as follows: Section 2 introduces the Phase Change Memory technology. Section 3 presents our detail design of PCM Mask. Section 4 is an initial experiment method.

## 2. Phase Change Memory

In this section, we introduce the PCM technology and discuss different memory hierarchy layouts. Although currently there is no mature PCM product available on the market, we summarize various previous studies on PCM and introduce difference memory layouts of using PCM.

We further characterize two design principles of PCM based DBMSs which are choosing hybrid memory layout and managing page in a smaller granularity.

### 2.1. PCM technology

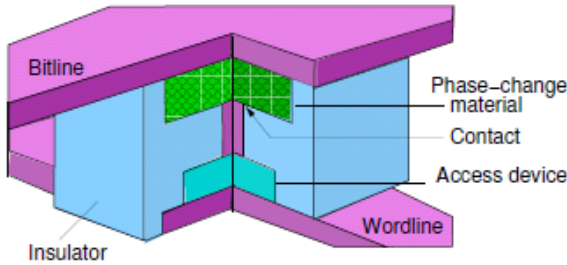


Figure 1 [3]: Phase Change Material.

As DRAM technology has touched its capacity and energy consumption limitation, researchers have investigated PCM as the next generation memory technology. PCM is based on the new storage material called chalcogenide glass which exploits large resistance contrast between amorphous and crystalline states. A typical organization of PCM cell is shown on Figure 1. The five order of magnitude difference can be used to represent binary data 1 and 0 [3]. To switch between the two states, different kind of electronic currents are applied on the material. As shown on Figure 2, to crystallize the phase change material, the “SET” current pulse is applied to heat the material for a sufficient long time period. On the other hand, “RESET” current is a sudden pulse which melts the material to largely increase its resistance. The two states retain the information even when the power is cut off. A much lower READ current is enough to sense the resistance and retrieve the information.

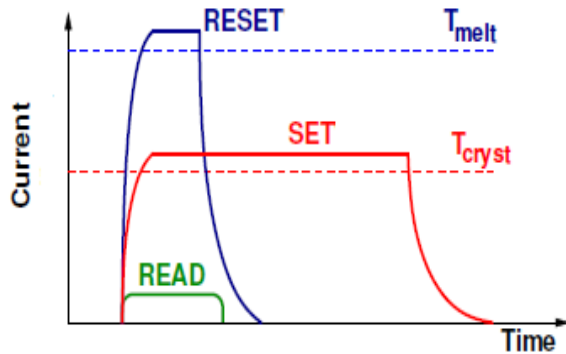


Figure 2 [3]: Currents and timings for SET, RESET, and READ operation on a PCM cell.

### 2.2. Performance comparison of memory technologies

Parameter	DRAM	NAND Flash	NOR Flash	PCM
Density	1X	4X	0.25X	2X-4X
Read Latency	60ns	25 us	300 ns	200-300 ns
Write Speed	≈1 Gbps	2.4 MB/s	0.5 MB/s	≈100 MB/s
Endurance	N/A	10 <sup>4</sup>	10 <sup>4</sup>	10 <sup>6</sup> to 10 <sup>8</sup>
Retention	Refresh	10yrs	10yrs	10 yrs

Table 1: Performance comparison of memory technologies [5]

To integrate PCM into the traditional computer architecture, we must specify its properties first. Table 1 summarizes the current researches about various performance differences among PCM, DRAM, Nor and NAND flash. We can conclude the following facts:

- Compare to Nor and NAND flash, PCM has a up to 100X faster writing speed. One possible explanation is that the byte alterability releases the PCM from the restriction of erase-before-write which is a main performance bottle neck of Nor and NAND flash. In the mean time, the reading speeds of the three technologies are very close.
- Compare to DRAM, its writing speed is only 10X slower. The reading speed is up to 5X slower. Obviously, the asymmetric factor is less significant than that compared with Nor and NAND flash memories.

### 2.3. Integration of PCM

Researchers have proposed different integration of PCM into memory/storage system as shown on Figure 2 [4].

Since PCM is a byte-alterable memory technology, it can be served as a disk cache regardless of the secondary storage devices. In this way we must put the PCM behind the system I/O bus, as shown on Figure 2 (a). However, the blocked I/O bus may disable the byte alterability of PCM, since the granularity of each I/O is in units of block.

An alternative approach of integrating PCM is a hybrid memory system of PCM and DRAM as shown on Figure 2 (b). The main memory contains the PCM and DRAM which both will be placed in front of the system I/O bus.

A third way of placing the PCM in the memory system is that the main memory contains PCM only as shown on Figure 2 (c).

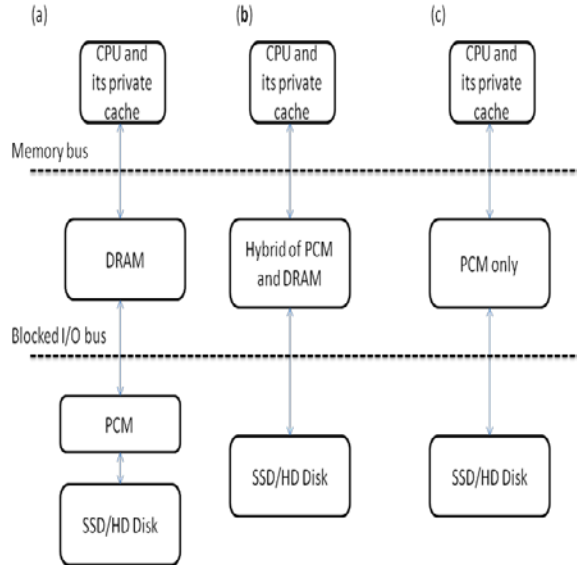


**Figure 3: Different PCM integrations**

Various previous researches already studied different possible way of integrating PCM [7] [8].

### 2.3. Design principles

Based on the performance of PCM and pervious researches about its integration, we summarized two design principles of using PCM in DBMSs. PCM Mask is a production of combining these two principles.

**Hybrid memory system.** First, we proposed a new system which managing data movement on a hybrid volatile DRAM and non-volatile PCM main memory system. Although previous studies has investigated how to reduce the write latency and energy consuming of PCM to facilitate it is used as main memory alone, it is still cannot thoroughly replace the DRAM as main memory. We propose our system based on a hybrid memory system whose architecture has been carefully designed by prior work [8]. We believe the hybrid memory has the following advantages:

- Placing PCM in front of the system I/O bus will fully utilize the byte-alterable feature. The block based I/O of system bus will hide the byte alterability of PCM.
- The performance of the PCM is much closer to the DRAM comparing to flash memory. When it is closer to the CPU, we can take more advantage of the much less access latency.
- The endurance limitation of PCM does not allow it completely replace DRAM as the main memory.

**Smaller page granularity.** We believe the page on PCM should be managed in a smaller granularity. We should divide a page into subpages level for an example:

We can divide each page in DRAM into 64 subpages. It has the following advantages:

- By dividing a page into multiple subpages, we can only update the very small dirty area of a page in PCM by the byte alterability.
- The subpage writing granularity can reduce the amount of data written to PCM which extends its endurance.

As we shown, PCM has various advantages to be the next generation memory technology. For the summary of its performance we further characterize two design principles.

### 3. PCM Mask

In this section, we present the PCM Mask which combines buffer I/Os and log I/Os together. We first present our system’s architecture, and describe the system operations of our system. We also discuss the correctness and it efficiency.

#### 3.1. System Architecture

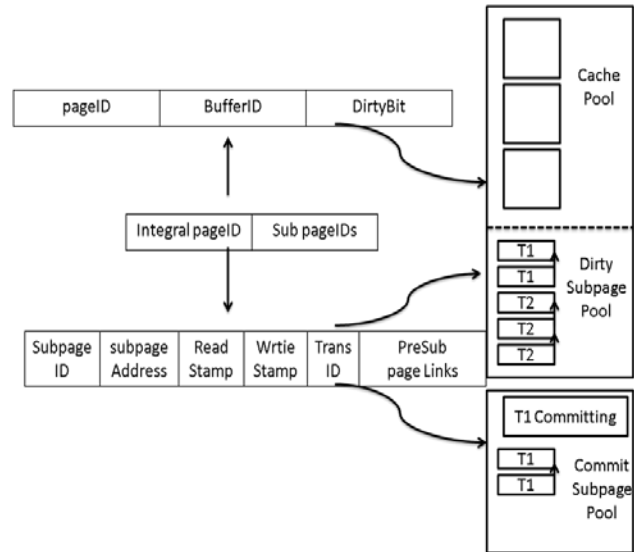


**Figure 4: System Architecture**

In the section, we present the system architecture of PCM Mast, as shown on Figure 3. In the PCM Mask, we manage page in different granularity on different types of memory.

*The volatile memory.* In the volatile memory, we manage the page in two different types, the integral page and sub-page. The integral page served as a cache function of secondary disk. It will adopt a buffer replacement policy. The sub-page area accepts a dirty subpage whenever it becomes dirty. Each dirty subpage holds some metadata, such as transaction ID, read/write

timestamp to facilitate concurrency control and a point to the previous dirty subpage of the same transaction. Please notice that since a sub-page goes to dirty subpage area once it becomes a dirty page, the integral page area can be replaced without copying back to secondary disk which contributes to a major performance improvement.

*The PCM.* The PCM stores all of dirty subpages of committed transactions. The PCM also stores the current committing transaction ID and its last dirty subpage numbers which is used during the recovery.

In the volatile memory, there also stores a transaction table. It stores all the related transaction IDs together with its last dirty subpage ID.

In the volatile main memory, there will be three tables for page management. The Cache Table (pageID, BufferID, DirtyBit) stores the page mapping of cache page IDs and its address in the volatile main memory. The DirtyBit indicates whether it has subpage in the main memory or PCM.

The second table is the Subpage table (subpageID, subpageAddress, ReadStamp, WriteStamp, TransID, PreSubpageAddress). This table retains the information about the subpages and its write and read time stamp to facilitate the multi version concurrency control. The TransID stores the transaction ID which creates this subpage and the PreSubpageAddress links to the previous subpage ID of the same transaction.

The third table is the integral page and subpage Mapping table. It accelerates the speed of combing different subpage into a whole page.

### 3.2. Transactional operations

In this section, we will discuss each transactional operation in details. PCM Mask is a fully functional system which supports all kinds of operations.

**Read.** Upon a read request, we consult the Cache Table and the Mapping table to find whether there is a whole page or parts of a page in the two memories.

As a page can be scattered in three places, the volatile cache pool, the dirty sub-page pool and the PCM. Reading can be classified into four cases.

- Case 1: Page only places in disk.  
We replace one page from the cache pool, and read in the demanded page.
- Case 2: Page places in the cache pool only.  
We find the demanded page through the Cache Table.
- Case 3: Page places in the cache pool and dirty sub-page pool.  
We find the demanded page through the Cache Table and the Subpage table.
- Case 4: Page places in the secondary storage and dirty sub-page pool.

We find the demanded page through the cache pool table and the dirty subpage pool.

**Write.** As stated, in the PCM mask there are only read I/Os between the volatile memory and the secondary storage.

Writing in the PCM Mask can be classified as three types.

- Type 1: Write dirty subpage to the dirty subpage pool. Each writing request in the volatile memory happens in the out-of-place manner. We only write the dirty part of a page in to the dirty subpage pool.
- Type 2: Write dirty subpage to the commit subpage pool. This process is the same as the commit process which we will explain shortly.
- Type 3: Writing the committed dirty subpage is a background process. The background process will flush the dirty subpages into secondary whenever the I/O is available.

**Commit.** Upon a commit request, the transaction ID and its last dirty subpage will be first write to a predefined place of PCM. Then the previous pointer of each dirty subpage will lead us to write all the dirty subpages into the PCM. The starting page of a transaction will have the point as "S" which indicates it is the first page of a transaction. Obviously, the writing of commit is also out-of-place, since we need to keep the previous version of each committing to ensure the system consistency.

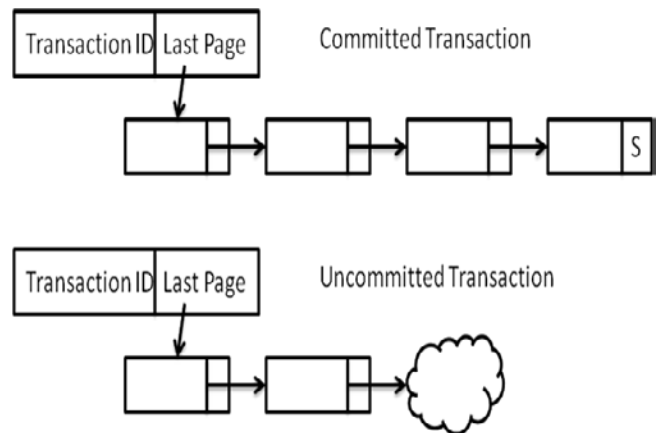


**Figure 5: Committed and Uncommitted transactions**

**Abort.** When a transaction is aborted, all its dirty subpages will be discarded as shown on Figure 4. If a transaction is aborted during committing, it should discards all of it committed pages and restore the Mapping table to its previous version.

**Recovery.** When recovery happens, all dirty subpages of the last transaction will be discarded by following the committing dirty subpage links. If we detect that we already write all dirty subpage into the PCM, we do not need to discard all dirty subpages. This is another major

performance improvement, since there is no REDO time, only undo the last transaction is enough to bring the system back the consistency status before crashed.

### 3.3. Concurrency control

We adopt the multi version concurrency control method in the PCM mask. Specifically, we give each dirty subpage a read time stamp and a write time stamp.

We give the following read and write operation in the dirty subpage pool.

- Read

If transaction T issues a read(X) operation, find the version I of X that has the highest write\_time\_stampe( $X_i$ ) of all versions of X that is also less than or equal to Trans\_time\_stamp (T); then return the values of  $X_i$ , and if the current Trans\_time\_stamp (T) is larger than read\_time\_stampe( $X_i$ ), set read\_time\_stampe( $X_i$ ) to Trans\_time\_stamp (T).

- Write

If transaction T issues a write(X) operation, and version I of X has the highest write\_time\_stamp( $X_i$ ) if all versions of X that is also less than or equal to Trans\_time\_stamp (T), and read\_time\_stampe( $X_i$ ) > Trans\_time\_stamp (T), then abort and roll back transaction T; otherwise, create a new version  $X_j$  of X.

### 3.4. Discussion

We summarize the two performance improvement as follow:

We combine the small log write I/Os and the random buffer I/Os into memory traffic to PCM and the background I/Os flushing the PCM into secondary disk which can be minimized in different ways.

The efficient commit protocol eliminates the redo time during system recovery. To recover the system into a consistent state, the only process is to discard the uncommitted transaction.

Since the checkpoint is designed for shorten the recovery time, here in the PCM Mask, each page is read by combining page from disk and PCM. So there is no need for checkpoint process.

The overhead we paid is that for each reading we may need to access more subpages to compose the most updated version of a page. However, this process is a pure memory access, whose costs are small comparing access to the disk pages.

## 4. Proposed Experiment Method

Since there is no PCM memory system on the market, we will adopt an alternative methodology to show our system's improvement. We will test our system in DRAM and count the traffic amount of the DRAM to PCM. We use a disk simulator, disksim to simulate the secondary storage.

We will test PCM Mask in three different metrics: average page access, average response time and transaction throughput.

## 5. Conclusion and Future Work

In this paper, we present the PCM Mask storage system for DBMS, to our knowledge, it is the first paper of using PCM to ensure the system consistency and improve the performance under the transaction context.

Next step, we will implement the simulator and conducted various experiments to show our system's advantages.

## 6. Acknowledgments

Many thanks to Dr. He, Bingsheng for his comments to early version of this idea. Thanks also to Mr. On, Satitung for his help on the experiments set up.

## 7. References

- [1] S. Lai. Current status of the phase change memory and its future. In *IEDM*, 2003.
- [2] E. Doller. Phase change memory and its impacts on memory hierarchy. <http://www.pdl.cmu.edu/SDI/2009/slides/Numonyx.pdf>, 2009.
- [3] S. Chen, P. Gibbons, S. Nath. Rethinking database algorithms for phase change memory. In *CIDR*, 2011.
- [4] J. Condit, E. B. Nightingale, C. Frost, E. Ipek, B. C. Lee, D. Burger, and D. Coetzee. Better I/O through byte-addressable, persistent memory. In *SOSP*, 2009.
- [5] M. Qureshi, V. Srinivasan and J. Rivers. Scalable High Performance Main Memory System Using Phase-Change Memory Technology. In *ISCA*, 2009.
- [6] C. Lefurg, K. Rajamani, F. Rawson, W. Felter, M. Kistler, and T. W. Keller. Energy management for commercial servers. *IEEE Computer*, 36(12): 39-48, Dec. 2003.
- [7] A. Caulfield, A. De, J. Coburn, T. Mollov, R. Gupta, S. Swanson. Moneta: A High-performance Storage Array Architecture for Next-generation, Non-volatile Memories. In *IEDM*, 2009.
- [7] X. Wu, J. Li, L. Zhang, E. Speight, R. Rajamony Y. Xie Hybrid Cache Architecture with Disparate Memory Technologies. In *ISCA*, 2009.

# Secure Proximity Monitoring in Mobile Geo-Social Services

Li Hong Ping  
Department of Computer Science  
Hong Kong Baptist University  
Kowloon Tong, Hong Kong  
hpli@comp.hkbu.edu.hk

## Abstract

*Recently, the importance of Location Based Services (LBS) are increasing. While we are enjoying the convenience of LBS, the LBS bring us a threat in location privacy. In some kind of applications, users may be requested to join social groups with their friends and allow exploit their approximate location in a suitable condition. Proximity Detection enable us to attain the goal. However, we are required to bear the risk of disclosure of location information, when we are using the LBS. In this paper, we propose a solution in secure proximity monitoring, in order to protect the location privacy, when they are using this kind of service. Previously, some papers contribute ideas to deal with this problem. Nevertheless, most of them assume that there is a trusted central server within their system, which is impractical in the real world. The problem under our study is to continuously monitor if any two mobile users in a social group are within a distance of  $D$ . Meanwhile, the exact location of a mobile user is not disclosed to any third party. This paper propose a computationally feasible solution in this problem, which only disclose the approximate location of the user to the authorized party. Untrusted third party (including centralized server) is not able to know the users' location.*

## 1 Introduction

As the technology advance, many mobile phones have been equipped with geo-positioning capabilities (e.g. GPS). At the same time, the rise of social networking sites to narrow the gap among people. Friend-locator services (e.g., Google Latitude), which enable user to know their friends' locations, is also becoming popular. Nevertheless, friend-locator services users usually expect certain level of privacy protection rather than completely expose their position to their friends.

The existing research work in proximity detection can

only protect users' location privacy in a certain degree. They are not enough to satisfy the requirement of requesting completely location privacy.

In this paper, we can completely protect the users' location privacy, because we do not require any trusted third party. Under the protection of secure communication, server can just receive the index value. By using those value to judge where there is any user nearby each other. Server only announces the users, when they are locating within a pre-defined distance of another user. In general, users have different location privacy requirement to other users according to different social group. Such as user Alice allow her family member to know her location when they are in the same district and allow her friend to know her location only when they are within (e.g. fifty meters) from each other.

The design of proposed solution gives three contributions at the same time. Firstly, it can preserve users' location privacy even there is no trusted third party. It outperforms many of the previous solution, which requires the existence of a centralized anonymity server. Secondly, using hash function with a set of time-varied salt gives us a better protection, because it is pretty hard for us to find the user location from the index value. We prevent unwanted party to know where we are and let the permitted party to know our approximate location. Thirdly, this solution employed grid base layered structure, which is similar to some of the previous approach. The major different between previous solution and our solution, is previous solution always quad-tree structured grid based layer and our solution use a nona-tree structured grid based layer (see Figure 1). This modification reduces the number of required layer.

Our solution not only gives a good protection in user location privacy, but also requires a low communication cost, which is directly proportional to the number of user. The paper is organized as follows. We briefly review related work in Section 2 and then give a problem definition in Section 3. System Operation is presented in Section 4. Section 5 presents the experimental results of our proposed solution. At last, we conclude our paper in Section 6.

## 2 Related Work

In this section, we review the development of the location privacy technology and show the contribution of this paper to this topic. In the literature, there are many research efforts in this topic. Most of them adopt one of the three techniques (including cloaking, dummies and encryption) when handling the user location privacy problem.

The earliest proposal for location privacy protection is spatial cloaking, which is proposed by Gruteser and Grunwald [1].

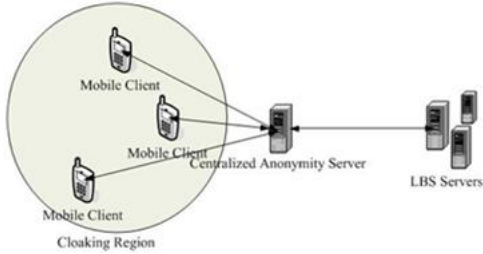


**Figure 1. General Structure of Location Cloaking**

Instead of sending a single user’s exact location to the server, spatial cloaking techniques collect  $k$  user locations and send a corresponding minimum bounding region to the server as the query parameter, see Figure 1. However the quality of service is highly depend on the density of users’ distribution. Also, it is time consuming for searching nearby users to form a cloaking region.

Later, location cloaking algorithms advanced from cloaking of snapshot locations to continuous location updates [3, 4]. The cloaking of snapshot locations is not secure enough to prevent the leakage of location privacy, if an attacker (e.g., the service provider) can collect the user’s historical cloaked regions as well as the user’s mobility pattern (e.g., users’ speed). Except the most common  $k$ -anonymity cloaking, there are other types of cloaking method, such as Hilbert curve [5] and Casper[6]. Both of Hilbert curve [5] and Casper[6] employ grid-based cell as their cloaking region, which also the idea that this paper has employed. The major advantage of grid-based cell is it requires less time for us to locate ourselves, comparing with the  $k$ -anonymity cloaking which require location of  $k$  nearest neighbor to find out our cloaking region. Also, grid-based cell can have a better resistant to path-tracking, as the locations of all cells have been predefined by the system. A. Khoshgozaran and C. Shahabi [5] guarantees the query anonymity even location information is disclosed to the adversary.

However, each client needs to maintain complex data structure and communication protocol as well as long range

communication among peers. Therefore additional computation and communication cost may be quite costly for practical use. For the Casper [6] solution, it blurs a user’s exact location information into a grid-based cloaking spatial region based on user specified privacy requirements. This framework uses a quad-tree data structure that maps the location information into grids with different levels and resolutions. Due to the limitations of the quad-tree structure, the calculated cloaking region is often larger than required, which may cause lower service quality.

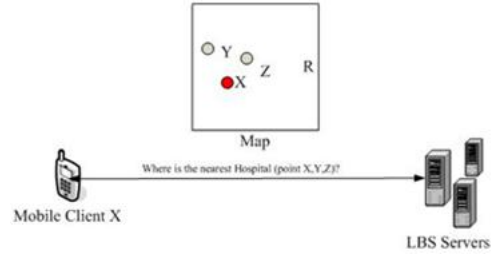


**Figure 2. Protect location privacy by using faked dummies**

On the other hand, [2] suggest that we can protect our location information by faked dummies. Just like Fig. 2 show that when client X send his location service request to the LBS server, he will also send out the  $k$  faked dummies (Y,Z,...) simultaneously, so as to diversify the risk of the discovery of his actual location. Although [2] has tried to user some movement simulation technique, we cannot prevent the threat of path tracking, because the exact location must contain in the set of dummies. Therefore, it is not difficult for us to find out the user location by using the assistance of the data mining technique.

The previous solutions only provide some protection for the location privacy. However, most of them require a trusted third party (e.g. trust anonymity server) to process the users’ location data. It is not practical for us to request for a trusted third party in the real world.

Cryptography solution in location privacy can help us to protect the location privacy, while without the existence of the trusted third party. Yao’s [7, 8] present how to exchange secret by using some comparison method. More recently, G. Ghinita and P. Kalnis [9] use

Private Information Retrieval (PIR) implementation to build up a location privacy protection framework which does not require any anonymities or collaborating trustworthy users. However, the limitation of this implementation is the cell contents have to match the query result that may cause a high storage overhead because the server required storing large amount of different content. Also, it is not easy to find the optimal size of grid partition that makes the computation and communication cost becomes huge.

Many papers have already been published for the topic of finding k-nearest neighbor (kNN).

Except the research of finding kNN, proximity detection is another important topic in location privacy application. The definition of proximity detection is the capability of a location-based service (LBS) to automatically detect when a pair of targets approaches each other closer than a pre-defined proximity distance. It is not efficient for us to do the proximity detection, if we solely use the solution of kNN. That may give us too (less/much) information when the point of interest (POI) are unevenly distributed. Ruppel [10] applies a distance-preserving coordinate transformation. By using centralized proximity detection method to detect the proximity among the transformed locations. However, Liu et al. Liu [11] show that distance preserving coordinate transformations is not safe enough, as it is easy for attacker to derive the secret mapping function. Mascetti present a solution - Hide&Crypt, presented in [12], is a privacy preserving solution which employs a filter-and-refine paradigm. Server uses the specified thresholds and computed distances to determine whether friends are in proximity. However users may need to directly communicate with their friend to check their proximity status, if they are defined as "possibly in proximity". Hide&Crypt use secure multi-party computation (SMC) protocol, which can protect the users' location privacy, but it also brings a choice between the service quality and the communication cost.

More recently, FRIENDLOCATOR [13] and VICINITYLOCATOR [14] both track users in a sparse grid while they are far away from their friends, in order to reduce the communication cost. Changing to finer grid, only when they come closer with their friend.

The limitation of the FRIENDLOCATOR is the proximity detection accuracy of it is low and uncontrollable.

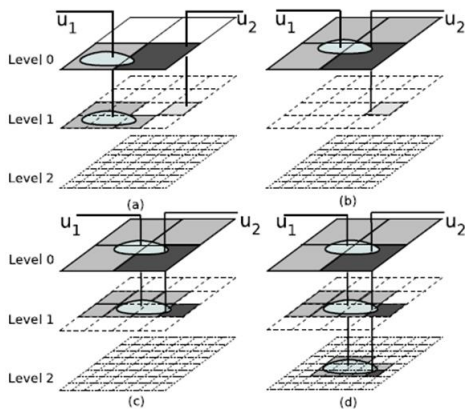


**Figure 3. Adaptive position-update policy of VICINITYLOCATOR**

For VICINITYLOCATOR [14] give a solution that allow

user to choose the "area of interest". In VICINITYLOCATOR, client requires to find all granules contained in his vicinity. It is because if we want to increase the accuracy for one level, the cost of the solution increase in an exponential manner. So VICINITYLOCATOR cannot give us a high accuracy result with a reasonable cost. Our solution can provide a high accuracy result by increasing number of grids, which require a much lower cost comparing with the VICINITYLOCATOR.

VICINITYLOCATOR employs an adaptive position-update policy (Figure. 3), which use different density layer, in order to reduce the communication cost. If there is only a few users, users can always overlap on the less dense layer, so the operation can be largely reduced. However, as the number of users increase, the performance of the policy will become worse.

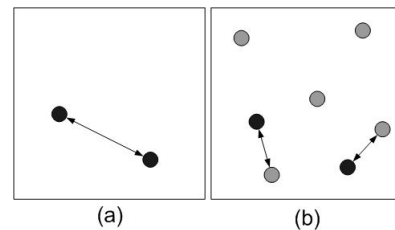


**Figure 4. Distance with the nearest neighbor**

The main reason is the cost of update is highly rely on the distance of the nearest neighbor. Figure 4(a) shows us that when there is only 2 users the average distance of the nearest neighbor should be longer than many user case, which shows in Figure 4(b). When there is more user, we are more unlikely to overlap with the nearest neighbor in a less dense layer. Therefore, that is only workable in a few users system, but fail to perform well when there is many user. Our solution purpose a 2 layer method to replace the multi-layer method purposed by many previous papers, so as to overcome the weakness of the multi-layer solution.

### 3 Research Methodology

This section describes the system model under our study. We assume users within the social group have reached a consensus on the acceptable distance of proximity detection. Our system allow users to adjust the distance threshold  $\delta$ , according to their need. After that, the users can encrypt their location and generate a set of index values by using the secret values shared within the social group. The job of the server is just used in the comparison of index value. The key idea of this framework is to preserve the location privacy by separating the information sharing into 2 parts. Traditional centralized anonymity server act as a system center, which responsible for all client requests and analysis work.

Therefore, those solutions require making an assumption, that the centralized server must be trusted. It is impractical to expect centralized server to be trusted, because the users' information is valuable. Even if centralized server is non-colluded, nobody can guarantee it will not be broken in by the attacker. Inspired by the solution of Yao's millionaire problem [7,8,15,16], our solution require users to share some standard with the other users directly and the server duty is to analyze the secret value.

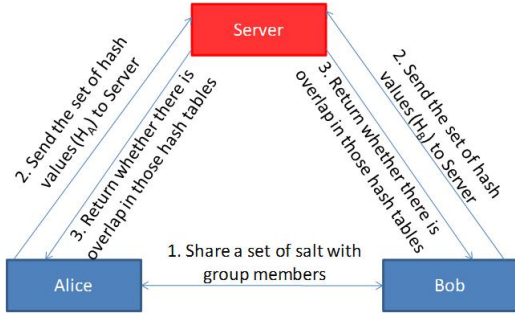


Figure 5. System Framework

Figure 5 show us the framework of our system. Firstly, one of the users in that social group shares a data processing standard with other group member. Then, all users will transform their location information to a secret value, according to the given standard. After the transformation finish, all users will send their hashed location to the server. Finally, server will check whether all user hashed location to find whether they are within the proximity distance of another user.

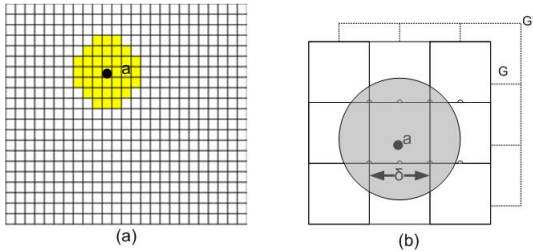


Figure 6. Static grid of VICINITYLOCATOR and Dynamic grid of Our Approach

Our solution use dynamic grids based on the distance threshold  $\delta$ . So when 2 users fall into the same cell then we can ensure that they are within a threshold distance. However, if only 1 layer is used, there will have many missing case occur (around 756(b) show us grid cell unable to cover the threshold distance region (grey region in 6(b)) of 6(b)). So we need to add a set of dynamic grid (e.g.  $G'$ ) to solve this problem. As the number of dynamic grids increase, the

probability of missing case reduce at the same time. (e.g. 5.6% when  $n = 10$ , 0.3%, when  $n = 20$ ), where  $n$  is the number of grid layer. Our system require less cost than VICINITYLOCATOR to give an accurate result. For example figure 6(a) show us in VICINITYLOCATOR if the resolution of the layer is not high enough the accuracy of the result will be low as there are many wrong report generated. If we use a higher resolution grid layer, 4 times cost required for a layer deeper. As a result, in VICINITYLOCATOR if we want a more accurate result, much higher cost (communication cost and server CPU cost) is required.

## 4 Mechanism of System Work

In this section, we give the detail explanation of our system's operation.

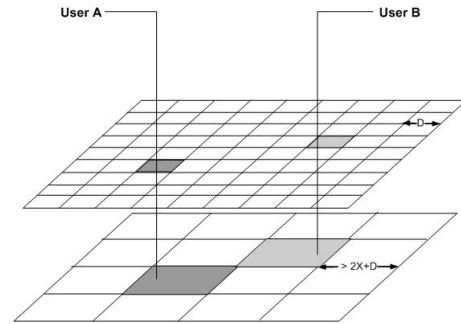


Figure 7. 2 Layer Structure

Figure 7 show us the structure of our 2 layer structure solution. The lower layer is responsible for giving an alert signal when there is possible candidate nearby, while the lower update is responsible for finding out the user who is really within our distance threshold  $\delta$ . The edge of the lower layer grid should a bit more than  $2X + \delta$ , where  $X$  is the maximum displacement of a user in a single period. The reason of this design is because we want to guarantee even there are two users, who are originally away from each other, heading each other in the maximum speed, they are still unable to overlap with each other in the upper layer in one period. That's mean users must overlap with another user in the lower layer before they overlap in the upper layer. Then the lower layer can act as a role of detecting possible candidate. However, because the aim of using the lower layer is to reduce the number of update. That's mean if the grid size of lower layer is too big, we will always overlap with other users in the lower layer. As a result, the function of the lower layer will be lost. Therefore our system will set the edge of the lower layer grid a bit larger than  $2X + \delta$ , in order to make the grid size as small as possible while maintaining the alert function of the lower layer.

## 4.1 System Initialization

This section show the initialization stage of our system.

---

### Algorithm 1 Initialization of Users

---

**Input:** Salting values  $\xi_x(g)$  and  $\xi_y(g)$  from  $U_s$

**Output:** Encrypted index values  $\{\tau < I_x(g_{00}), I_y(g_{00}) >, \dots, \tau < I_x(g_{1n}), I_y(g_{1n}) >\}$  to SP

- 1: Compute the index values  $\langle I_x(g), I_y(g) \rangle$   
 $I_x(g_{ln}) = \lfloor (u_x + \xi_x(g_{ln})) / c.len \rfloor$   
 $I_y(g_{ln}) = \lfloor (u_y + \xi_y(g_{ln})) / c.len \rfloor$
  - 2: Encrypted the index values  
 $\langle I_x(g_{ln}), I_y(g_{ln}) \rangle$  to  $\tau < I_x(g_{ln}), I_y(g_{ln}) >$
  - 3: Send the encrypted index values to SP  
 $\{\tau < I_x(g_{00}), I_y(g_{00}) >, \dots, \tau < I_x(g_{1n}), I_y(g_{1n}) >\}$
- 

First of all, one of the users in the social group generate a set of salted values  $\xi_x(g)$  and  $\xi_y(g)$  and share them to all other users within the social group without passing through the centralized server. After that, all users can compute their own index values  $\langle I_x(g_{ln}), I_y(g_{ln}) \rangle$ , where  $l$  is the level id and  $n$  is the index value id, with their own location  $\langle u_x, u_y \rangle$ , which is determined by:  $I_x(g_{ln}) = \lfloor (u_x + \xi_x(g_{ln})) / c.len \rfloor$  and  $I_y(g_{ln}) = \lfloor (u_y + \xi_y(g_{ln})) / c.len \rfloor$ . In order to protect location privacy, we define an irreversible encryption function  $\tau()$  to encrypt the index values  $\langle I_x(g_{ln}), I_y(g_{ln}) \rangle$ , after  $\tau < I_x(g_{ln}), I_y(g_{ln}) >$  are generated, we can send all of them to server and wait for the reply.

---

### Algorithm 2 Initialization of Server

---

**Input:** Encrypted index values  $\{\tau < I_x(g_{u00}), I_y(g_{u00}) >, \dots, \tau < I_x(g_{u1n}), I_y(g_{u1n}) >\}$  to SP

**Output:** Overlap level  $Overlap_n$  of user and List of positive candidate  $L_u$

- 1: Check overlap in the less dense layer
  - 2: **if** Overlap in the less dense layer **then**
  - 3:   Check overlap in the denser layer
  - 4: **end if**
  - 5: update the record  $M_{ij}$  and  $M_{ji}$  in the overlap matrix
  - 6: Find the overlap level  $Overlap_n$  from the nearest neighbor.
  - 7: Summarize a list of positive candidate  $L_u$  for each user
  - 8: Send the values  $Overlap_n$  and list of to the user.
- 

When the server finish the collection of the encrypted index values  $\tau < I_x(g_{u1n}), I_y(g_{u1n}) >$  from users, it will start to find out whether there is same encrypted index values among the users from the less dense layer  $\tau < I_x(g_{u1n}), I_y(g_{u1n}) >$  to the denser layer  $\tau < I_x(g_{u0n}), I_y(g_{u0n}) >$ . After all encrypted index values, the server can summarize the result and record the data into

the overlap matrix  $M$ . Then we can find out the overlap level  $Overlap_n$  of each user from  $M$  and summarize a list of positive candidate  $L_u$  for users. At last, send  $Overlap_n$  and  $L_u$  to users. When all users receive their  $Overlap_n$ , the system enter the update stage.

## 4.2 System Update

In the update stage, the user start to keep track with their location and determine whether it should be make an update in every period (e.g. 10 seconds).

---

### Algorithm 3 User Active Update

---

**Input:** Latest Overlap level  $Overlap_n$  and list of positive candidate  $L_u$  from server

**Output:** Some encrypted index values to SP (if required)

- 1: Use  $L_u$  to announce user who is nearby
  - 2: **if**  $Overlap_n =$  no overlap with others **then**
  - 3:   **if** no change in less dense level **then**
  - 4:     no update required
  - 5:   **else**
  - 6:     update level 1 index values
  - 7:   **end if**
  - 8: **else**
  - 9:   **if** no change in all level **then**
  - 10:     no update required
  - 11:   **else**
  - 12:     **if** no change in less dense level **then**
  - 13:       update less dense level index values
  - 14:     **else**
  - 15:       update all index values
  - 16:     **end if**
  - 17:   **end if**
  - 18: **end if**
  - 19: Send update index values to SP (if required)
- 

Firstly, the user will be announced who is nearby. Then, the users will check their latest overlap level  $Overlap_n$ , which is received from the server in the last period. If users do not overlap with other users in any level, user require to update the less dense level when change occur in that layer. If users overlap with other users, we will update the level only if change have been made. Finally, the user announce the server which information is required to update, if necessary.

After server receives response from all users, the overlap matrix will be updated. If there is update in  $Overlap_n$  or  $L_u$ , server need to all new information to users.

If users receive a new  $Overlap_n$  or  $L_u$ , the user passive update will be triggered. User update is required only if we overlap with other in a denser level and there is some modification in the upper level and do not update in the user active update process.

---

**Algorithm 4** Server Update

---

**Input:** Some encrypted index values from user

**Output:** Overlap level  $Overlap_n$  or list of positive candidate  $L_u$  of user (if required)

- 1: Receive update from client.
  - 2: Update the user overlap matrix  $M$ .
  - 3: Update  $Overlap_n$  and  $L_u$
  - 4: Check modification in  $Overlap_n$  and list of positive candidate  $L_u$
  - 5: Send  $Overlap_n$  or  $L_u$ (if required)
- 

---

**Algorithm 5** User Passive Update

---

**Input:** Latest Overlap level  $Overlap_n$  or list of positive candidate  $L_u$  from server

**Output:** Some encrypted index values to server (if required)

- 1: Use  $L_u$  to announce user who is nearby (if required)
  - 2: **if**  $Overlap_n$  = overlap in a denser level **then**
  - 3:   **if** no change in all level OR denser level has already update **then**
  - 4:     no update required
  - 5:   **else**
  - 6:     update upper(denser) level values
  - 7:   **end if**
  - 8: **end if**
  - 9: Send update index values to SP (if required)
- 

## 5 Experiment Result

In this section, we evaluate the performance of our proposed solution and validate the communication costs (in kb) and CPU cost (in ms) of original solution and 2 layers solution. Also, we have implemented a prototype of our solution, as well as VICINITYLOCATOR for comparison.

The data are generated from the same source of VICINITYLOCATOR, which [17] generate data sets based on the German city Oldenburg. The data sets cover an area of  $26915 \times 23572 \text{ units}^2$ , corresponding to  $14 \times 12:26 \text{ km}^2$ , and they contain location records for each user at each time stamp. In our experiment, we let the duration between two consecutive timestamps is 5 seconds and set different average speed to compare the system performance in various speed. For implementing a high adaptive solution, our 2 layer solution set a standard for the grid size of less dense layer to  $1200 \times 1200 \text{ units}^2$ , that mean even 2 car go ahead to each other in a speed 200 km/h, they still cannot jump from no overlap to same distance threshold within a time stamp.

In order to give a fair result, we compare 3 solutions with standard of maximum error 0.1. Therefore, we use 11 layers in VICINITYLOCATOR and 30 index values per layer in

our solution, which give similar number of errors. Most errors in our solution are providing false positive results with a relatively small amount of true negative results. For the VICINITYLOCATOR, all errors are come from providing true negative results.

Figure 8 shows us the performance of 3 solutions under different distance threshold request with a same average speed 25 units per 5 seconds. We can see that both solution of ours require much less cost than VICINITYLOCATOR, especially when the distance threshold is big. It is because when the proximity distance of VICINITYLOCATOR increase much more number of grids values are required to process. Different from VICINITYLOCATOR, our solutions use dynamic grid which is defined, according to users' requirement. Therefore no matter how big the distance threshold, only 30 index values are required. In comparing the original solution and 2 layer solution, 2 layer solution reduce number of update. Because of 2 layer solution ignore the unnecessary update, especially when the user is apart from other users. While original update require very frequent update, as it is easier to escape from one of the grids. However, the CPU cost of 2 layer solution is higher than the original solution. It is because even 2 layer solution can ignore some unnecessary index value comparisons, it still require a bit more comparison cost than original solution.

On the other hand, both of our solutions require less update when the distance threshold increase. The reason is when the distance threshold increase, user spend more time to escape from the grid of distance threshold. This effect perform stronger in the original solution because whether the users require to update is fully depend on the situation of the layer. For the 2 layer solution, we also need to consider the effect of the second layer, as it is fixed size in all case.

Figure 9 shows us the performance of 3 solutions under different speed with a same distance threshold 100 units. The communication and CPU cost of VICINITYLOCATOR are much higher than our solutions. Due to the influence of IU optimization, VICINITYLOCATOR require less communication cost, when the user move slower.

Comparing two of our solutions, 2 layer solution require less communication cost than original solution particularly when the speed is low. It is because user require more time to escape from the less dense layer than denser layer. However, higher CPU cost need for 2 layer solution, the reason is same as what we have mentioned in Figure 8.

According to the experiment result, we can conclude that our solution require less communication and CPU than VICINITYLOCATOR. We also find that 2 layer solution, perform better than original approach, especially when we require a high frequency update.

## 6 Conclusion

In this paper, we investigate the problem of secure proximity monitoring. We propose a solution, which can solve the problem in a high accuracy and finish with a reasonable cost, comparing with the previous work in the same research topic. For the future, we may extend this multi-index value concept. For example using other polygon (e.g. hexagon) or some irregular shape to form grid and investigate whether it is useful for some kind of location-based query. Also, handling a small true positive result, when our approach employ in the Euclidean distance. We may try to find out whether using a smaller and randomly rotated grid can give us a better solution.

## References

- [1] M. Gruteser and D. Grunwald, "Anonymous usage of location-based service through spatial and temporal cloaking," Proc. Of the International Conference on Mobile Systems, Applications, and Services (MobiSys'03), pp.163-168, San Francisco, USA, 2003
- [2] Hidetoshi Kido, Yutaka Yanagisawa, Tetsuji Satoh, An Anonymous Communication Technique using Dummies for Location-based Services, Pervasive Services, 2005. ICPS '05. Proceedings. International Conference
- [3] T. Xu and Y. Cai. Location Anonymity in Continuous Location-based Services. In ACM GIS'07, pages 300–307, November 2007.
- [4] Xian Pan, Jianliang Xu, Xiaofeng Meng, Protecting location privacy against location-dependent attack in mobile services, Proceeding of the 17th ACM conference on Information and knowledge management, 2007
- [5] A. Khoshgozaran and C. Shahabi. Blind Evaluation of Nearest Neighbor Queries Using Space Transformation to Preserve Location Privacy. In Proc. SSTD, 2007.
- [6] M. F. Mokbel, C. Y. Chow, and W. G. Aref. The New Casper: Query Processing for Location Services without Compromising Privacy. In Proc. of VLDB, 2006.
- [7] A.C. Yao. Protocols for secure computations. In Proceedings of the 23rd Annual IEEE Symposium on Foundations of Computer Science, 1982.
- [8] A.C. Yao How to generate and exchange secrets. In Proceedings 27th IEEE Symposium on Foundations of Computer Science.
- [9] G. Ghinita, P. Kalnis, A. Khoshgozaran, C. Shahabi, and K.-L. Tan, "Private queries in location based services: Anonymizers are not necessary," in Proc. ACM SIGMOD Int. Conf. Manage. Data, Vancouver, Canada, Jun. 2008, pp. 121-132.
- [10] P. Ruppel, G. Treu, A. Kpper, and C. Linnhoff-Popien, "Anonymous User Tracking for Location-Based Community Services," in LoCA, 2006, pp. 116-133.
- [11] K. Liu, C. Giannella, and H. Kargupta, An Attackers View of Distance Preserving Maps for Privacy Preserving Data Mining, in PKDD, 2006, pp. 297-308.
- [12] S. Mascetti, C. Bettini, D. Freni, X. S. Wang, and S. Jajodia, Privacy-aware proximity based services, in MDM, 2009, pp. 3140.
- [13] L. Łiknys, J. R. Thomsen, S. Łaltenis, M. L. Yiu, and O. Andersen, A Location Privacy Aware Friend Locator, in SSTD, 2009, pp. 405-410.
- [14] L. Łiknys, J. R. Thomsen, S. Łaltenis, M. L. Yiu, Private and Flexible Proximity Detection in Mobile Social Networks, Proceedings of the 11th International Conference on Mobile Data Management (MDM), Kansas City, Missouri, May 2010.
- [15] Artak Amirbekyan and Vladimir Estivill-Castro. Privacy-preserving k-nn for small and large data sets. In Proceedings of the ICDM Workshops, 2007.
- [16] Processing Private Queries over Private and Indexed Data
- [17] T. Brinkho. A Framework for Generating Network-Based Moving Objects. *GeoInformatica*, 6(2):153-180, 2002.

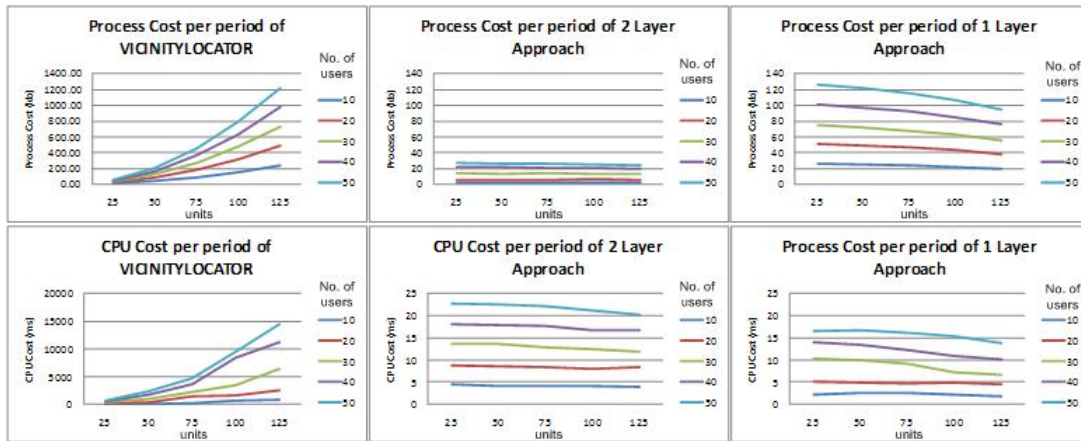


Figure 8. Comparison in different proximity distance

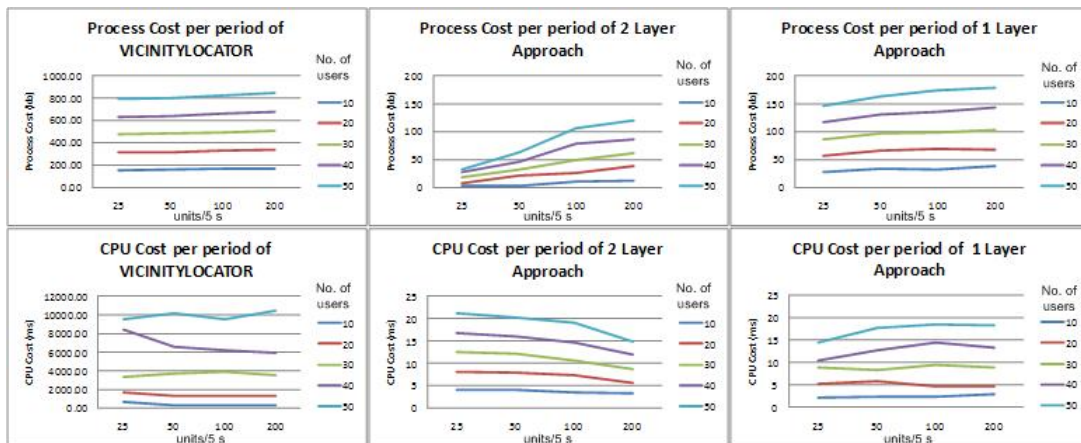


Figure 9. Comparison in different speed

# A Signal Strength based Location Estimation Algorithm within a Wireless Network

Kevin Chin Yiu Shum and Joseph Kee Yin Ng  
Department of Computer Science,  
Hong Kong Baptist University, Kowloon Tong, Hong Kong  
{ cyshum,jng }@comp.hkbu.edu.hk

## Abstract

*With the prevalence of Wi-Fi activity within a wireless network, there are growing interests in mobile surveillance and device tracking for better network services. With a good location estimation algorithm integrated into a wireless network, system administrators can closely monitor the network traffic as well as the behavior of the mobile users. By modifying the embedded software in off-the-shelf WLAN APs, our system can sniff out data packets transmitted by WLAN devices without the need to install client programs on mobile user devices. In this paper we propose the Aggregated Signal Layout location estimation algorithm. Experiment results show that once wireless activities had been detected, our signal strength based localization algorithm can estimate positions of the wireless mobile devices involved with great success rate and good accuracy. With an accuracy comparable to the fingerprinting method but without paying the high costs of training and maintenance of the fingerprint databases inside our WLAN system, the proposed Aggregated Signal Layout method is well-justified for its efficiency and effectiveness in locating and tracking mobile users' activities within a wireless network.*

## 1. Introduction

Under the Government's Digital 21 Strategy [1] to endorse the idea of a wireless city, the HKSAR government had put forward a Wi-Fi Programme (GovWiFi) [2] as an initiative to create a wireless infrastructure to facilitate mobile Internet access by citizens and businesses in order to improve quality of living and business operations in Hong Kong. The programme also raises serious concerns about hacking activities among WLAN networks. In view of the heavy usage and progressively growing coverage of WLAN within indoor environment and the relatively few research studies on effective ways to perform WLAN positioning and tracking, there is a need to investigate the feasibility of using WLAN to locate a mobile user as well as pinpoint hacking activities in an indoor environment.

The use of signal strength based fingerprinting approach for localization with a wireless network had been explored in both academic venue and in small scale commercial areas. However, the fingerprinting approach has high cost for signal strength acquisition as well as the training, retraining and maintenance of fingerprint databases. Thus, an "Aggregated Signal Layout method" is proposed in order to minimize these costs while providing similar if not better location accuracy and stability.

In this paper, we construct a mobile location estimation system using a popular off-the-shelf wireless router by Linksys – (Model: WRT54G) [3] to detect and locate mobile devices. Technically, we write the software and re-program the AP and wireless Routers such that our software can collect signal strength readings when wireless devices communicate with any of the surrounding APs. [5] With these signal strength readings collected in real-time and stored in the database at our data centre, and the physical positions of the AP Sensors being known, we can use our previous algorithms [6-12] to find out the whereabouts of mobile devices.

Not much research on the Wi-Fi positioning is implemented in real life. One of the major reasons is that indoor radio signal

propagation is very complicated and, therefore, it is difficult to obtain a steady signal reading from the same location. Signal fluctuations are caused by signal attenuation to distance, barrier, multi-path, etc. It is extremely difficult to build a signal propagation model accurate enough for location estimation and the exhaustive fingerprint approach is usually considered to be too expensive to be built and be maintained in the real-world situations.

## 2. Related work

In previous years, our research group had done quite some work on mobile phone positioning and the results are astounding [19-30]. Although theoretically the same or similar location estimation algorithms for the mobile phone network can be applied to the WLAN, there is relatively few research on WLAN positioning [31-34] in the literature. The difficulties are mainly attributed to the differences in penetration power, signal fading, signal attenuation, the layout of access points (regularity vs. randomness), and the more serious body effect within the WLAN as compared to the mobile phone network. Many researchers have proposed methods in providing location services using the mobile phone networks, but few projects have actually been implemented. The RADAR system [32] was one of the early WLAN-based location estimation systems. Based on the FreeBSD distribution and WaveLAN WLAN network, the RADAR system can locate a user who carries a notebook with an accuracy of 5 meters. Y. Wang et al [31] studied on the feasibility of making use of the WLAN to locate a mobile device. They had an empirical study inside their department building and labs and reported their findings and simulation results. However, there are no systematic ways to generalize these approaches and fine tune the necessary environment parameters. Furthermore, the target environment is critical to the accuracy of WLAN positioning. Radio characteristics in an open environment are never static and there is not a single methodology that can fine tune data from time to time and adapt to the changing environment. It is only recently that they start to study on post-deployment adaptation. They try installing special hardware which monitors radio characteristics at different positions and rebuild the propagation model periodically [33, 34]. Among the commercial products that are available for WLAN positioning, Ekahau is the company that is taking a leading position in in-door positioning. Their positioning system relies on building an accurate radio map according to the layout of the access points as well as the model and specific characteristics of these access points. Nonetheless, it is a costly system; and it falls victim to environmental changes and post-deployment adaptation problems.

## 3. Proposed System and Technologies Involved

In our experiment, a programmable router - Linksys WRT54G [3], which is burned with an open-source custom-made firmware, can act as a wireless sensor to obtain information from data packets transmitted within the WLAN environment. Packet information such as Service Set Identifier (SSID), Extended Service Set Identifier (ESSID), Received

Signal Strength Indicator (RSSI), Noise Level, Traffic rate and Traffic Frequency are collected by a custom-made wireless data acquisition application written for the Linksys WRT54G WLAN router. The data acquisition application is a cross-compiled program for the 32-bit MIPS architecture processors manufactured by Broadcom, and this embedded piece of software plays an important role in achieving our goals in locating mobile devices.

Here, we propose a surveillance system to let the network administrator to monitor and analysis the network traffic and behavior. By making use of multiple wireless routers (Linksys WRT54G) burned with our custom-made cross-compiled program. Useful information is extracted, communications among all wireless devices are sniffed and being stored into our database server at the data centre [35]. With this information, locations of the mobile users can be estimated, identified, located and tracked within our WLAN environment.

Since we have to re-program the wireless router for packet sniffing, we have done a lot of compatibility tests on different open-source wireless routers to examine its feasibility. We found out that most wireless routers are using chipsets from two major chipset manufacturers – Atheros and Broadcom; we found out that for those who had chipset from Atheros, we can make use of the public open-source system call to switch the router into monitor-mode as well as deep-monitor mode which can sniff all Wi-Fi traffic over the WLAN environment.

But for routers that adopted the chipsets from Broadcom, for instance the Linksys WRT54G, we cannot obtain the correct monitor mode to obtain the necessary information for location estimation by using the usual system calls from iwlib.lib, wl.lib, or iwlist.lib, etc. So we have to rewrite the code from the pcap library, the prism library and code from wliocli [36-38] to put the chipset into a correct monitor mode in order to extract the Wi-Fi packets one by one in order to obtain the necessary information for location estimation.

Our custom-made program for Linksys WRT54G (AP) thus turned the wireless router into a WLAN packet capture device which requires no authentication or access privileges in order to help us estimate the location of mobile devices and provide location-based services. Thus, we have made the AP to support true monitor mode, such that we can disclose and decode the 802.11 frame information.

To summarize, each AP in the WLAN is running a custom-made program to sniff data packets within the coverage of the WLAN network. Useful information is extracted from these data packets, transferred to a control server, and stored into a database together with the current timestamp for logging purpose. Later on, the data is analyzed by the control server and locations of the mobile users are estimated in real-time by our location estimation algorithm.

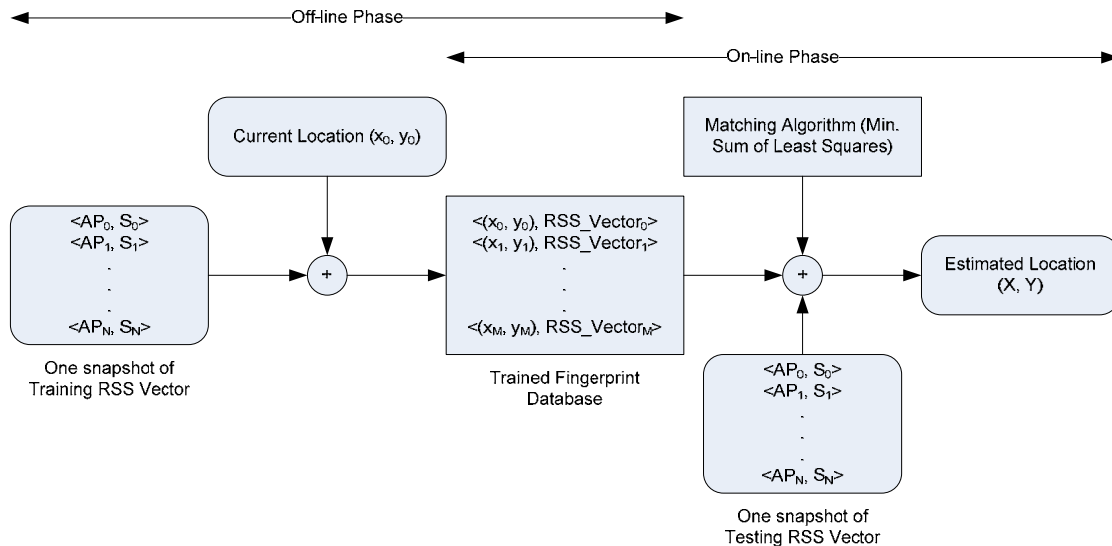


Figure 1. Location Fingerprinting Approach for Location Estimation

### 3.1 Location Estimation - The Aggregated Signal Layout approach

Fingerprinting is an effective location estimation method, but it is not without problems. A Fingerprint is unique to its AP sensor network, i.e. the number of AP sensors as well as their locations. If there is a change of AP sensor locations, or an AP sensor removed from the sensor network, we have to collect the signal (data) and to train the Fingerprints database all over again. This drawback makes the Fingerprint method expensive to maintain for AP sensor networks that changes sensors frequently.

Here we propose another location estimation approach called Aggregated Signal Layout. For each AP sensor in an AP sensor network, we place position markers at different distances from the AP sensor and measure the received signal strengths. The average signal strength from the position marker and the Position Marker Distance give the RSS vector for the AP sensor, which is recorded to the Signal Layout database. Unlike the Fingerprint method, Aggregated Signal Layout considers the Signal Layout collected by AP sensors individually. The

Signal Layout of an AP sensor belongs to that AP alone, independent of the surrounding AP sensors.

Aggregated Signal Layout performs location estimation by overlapping Signal Layouts of AP sensors in the sensor network (10 AP sensors in our experiment). Consider a single AP sensor, given the received signal strength from a mobile device, the distance between the device and the AP sensor could be obtained from the sensor's Signal Layout; the inter-distance draws the possible locations of the mobile device in a circular perimeter. By aggregating the Signal Layouts of AP sensors, essentially locating the common points of the perimeters, the estimated location of the mobile device can be found.

Since it is usual that the received signal strength does not conform to an AP sensor's Signal Layout, we allow some error to the distance estimation. For instance, we allow a search window of +/- 2dbm to our Aggregated Signal Layout method, such that when an AP sensor receives signal strength of -68dbm, the algorithm searches the sensor's Signal Layout for Position Marker Distances that falls between signal strengths -

66 and -70dbm. This search window we called it as Signal Spread is used to ensure more overlaps between layers of the Signal Layouts of AP sensors. Furthermore, we have added a parameter called Target Positions to constrain the number of estimated positions resulted from the aggregation. By controlling the Signal Spread and Target Positions one can improve the accuracy of the estimation, as demonstrated in Section 4.2.

Aggregated Signal Layout alleviates the problem of retrain the whole AP sensor network introduced by Fingerprint method. In addition, the use of Signal Spread and Target Positions enable flexibility to the algorithm.

#### 4. Experiments and Results

##### 4.1 Experiment 1 – The Fingerprint Approach with Least-Square

Figure 2 shows the layout of the AP Sensors in Experiment 1 with obscuring objects like tables, chairs, bookshelves and benches in the FSC801 lab at HKBU. During the experiment, our system detected the presence of about 55 APs or mobile stations within the coverage area and we looked into the inter-device distance and the corresponding RSSI under the influence of signal attenuation, multipath, reflection, refraction, and signal interferences. Within the WLAN, we obtained signal (data) mainly from 10 AP sensors labeled as AP31 to AP40. With their local coordinates attached (For example, 38(3.9,6.1) is a AP named AP38 and have coordinates of  $x=3.9, y=6.1$ ) hanging from the ceiling of our test bed. The other 42 APs were treated as wireless devices or mobile stations and were placed in front of the monitor of every seat. In this experiment, about 100,000 samples were taken from all AP sensors, and for each, 200 samples were taken in real-time, around 10-25 samples are used for a mobile position fingerprint.

##### Experiment 1 Result and Analysis

Table 1. The 4 Worst Positions in Experiment 1

The 4 Worst Position for Dataset 1 - Correct Position Probability		
Position	Dataset 1	Dataset 2
5	57%	87%
10	63%	85%
18	71%	94%
32	59%	93%

Table 1 shows the result for the fingerprint approach for the location estimation, and the 4 worst positions were identified. Fingerprints for dataset 1 were taken in the rush hour, with many human bodies blocking the wireless signal. We carried out an experiment again to form dataset 2 on similar physical setup with similar mobile stations but under non-working hours when there was less interference to our fingerprint measurement. We observed that the error can be as large as 43% at position 5 from dataset 1 but much better result was shown from dataset 2. The result from dataset 2 had shown that at position 5 is 87%, which is 30% better than from dataset 1. There is good indication that signal fluctuation during the fingerprint training process will lead to adverse effects in fingerprints positioning. Experiment trial 1 clearly shows that fingerprints positioning are influenced by multi-path, reflection,

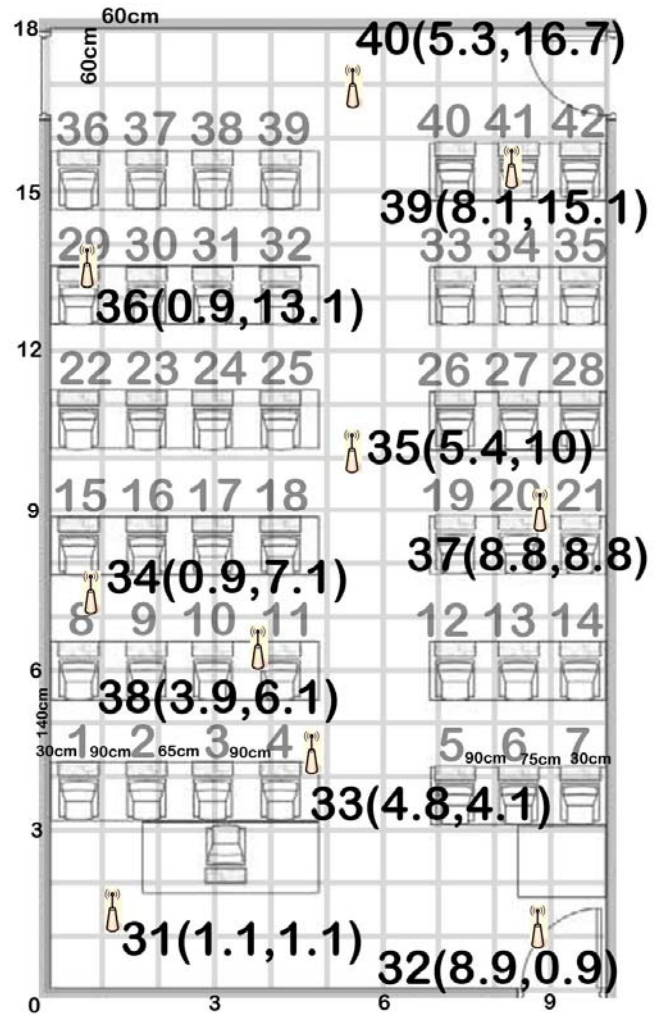


Figure 2. The Setup for Experiment 1 at a Lab in FSC801

refraction, absorption of body effect, and constructive/destructive interferences within the indoor environment.

Table 2. The Best 4 Positions Trial in Experiment 1

The Best 4 Position from Dataset 1– Correct Position Probability			
Position	Dataset 1	Position	Dataset 2
4	91%	6	99%
25	95%	7	97%
34	93%	12	97%
42	95%	39	98%

Table 2 shows the result for the fingerprint approach with the best 4 positions in our test bed. From Table 2, we observed that the error ratio can be as small as 5% at position 25 from trial 1, and 1% at position 6 from trial 2.

Table 3. Average Result on Datasets 1 and 2

Averaged Correctness on Dataset 1 and 2		
Dataset 1	Dataset 2	Average
81%	93%	87%

Table 3 shows the average result of dataset 1 and 2. The average positive probabilities for dataset 1 and dataset 2 are 81% and 93% respectively. The average result for both dataset is 87%.

Table 4. Exp. 1 dataset 1 with the nearest 5 and 9 position

The 4 Worst Positions for Dataset 1 – Correct Position Probability			
Position	Target =1	Target =5	Target =9
5	57%	91%	94%
10	63%	98%	99%
18	71%	100%	100%
32	59%	91%	100%

We adopted the “Least Square” method in matching the current signal strength snapshot with our trained fingerprint database.

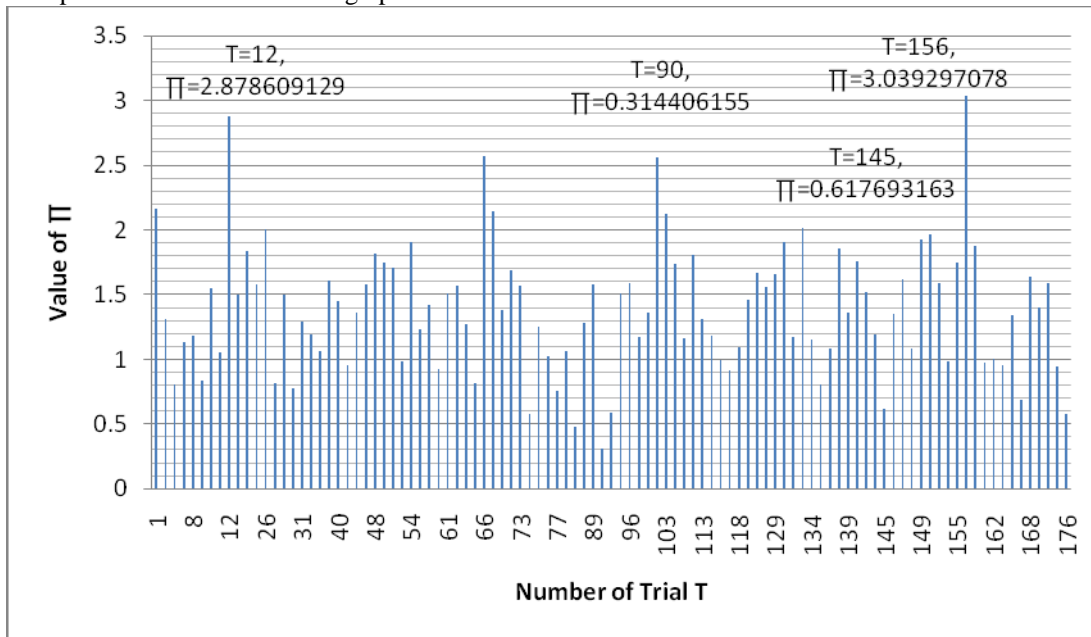


Figure 3. Positive Results in Position 5

Referring to Figure 3, Trial 90 has a minimal value of 0.3144 among 176 trials. Trial 156 has minimal value of 3.039. For better illustration, we wish all the least square value stay close to 0 for every trial. The nearer the values are to 0, the more trusted the fingerprints are.

Table 5. Ave Least Square Value at Position 5 and 6

	Position 5 in dataset 1	Position 6 in dataset 2
Average Least Square Value	1.387476891	0.960931618

Table 5 shows the result of average least square value computed for position 5 and position 6. According to Table 1 and 5, a correct position probability at position 5 in dataset 1 is 57%, the average least square value is 1.39. For Position 6 in dataset 2, a correct position probability is 99%, the average least square value is 0.96. “Least Square” algorithm (L.S) stated that the less the magnitude of squared error is, the closer the position to the fingerprints is. It can be further explained that the higher probability relates to getting the right location fingerprint for the mobile station.

Results were calculated for every position marker; and the computed results are sorted in ascending order. The result which has the smallest value is closest to the fingerprint of the estimated position. After the results are sorted, we can find out the nearest 5 and 9 possible position markers which is closest to the estimated position fingerprint, denoted as Target Position=5 and Target Position=9. According to the worst case on position 5 in Table 4, although the positive probability is only 57% for the exact position, the correct target position rate increased to 91% when Target Position=5, and the correct target position rate further improved to 94% when Target Position=9. For Position 18, we can confidently get rid of any wrong fingerprints when target position is 5 or 9. In general, when target position=9, we can almost get rid of any wrong estimation anywhere in our test bed.

## 4.2 Experiment 2 – The Aggregated Signal Layout Approach

In this experiment, the geometry co-ordinates of 42 mobile station markers are measured and stored into a database. The signals and distances between every Mobile device and AP are calculated to form a radio signal layout. We have already constructed 10 radio layouts from AP Sensor labeled from AP31 to AP40. Figure 4 shows the curve plotted from average signal strength generated by every position marker. The generated radio layout is pre-calculated and stored into our database, the aggregated signal layout is used to carry out our location algorithm, and the result is shown on Table 6.

### Experiment 2 Result and Analysis

The number of samples we used to estimate the position marker is 10, 50 and 500, respectively. In our system, we can obtain 10 useful samples from the APs within  $\Delta t = 2$  seconds in average, if they are transferring data from the mobile client to the APs. For the mobile clients that are in the idle state, we can normally accomplish the task  $\Delta t = 5$  seconds. We use the generated radio layout to estimate the position of the testing data.

In Figure 4, if the signal we received from the position marker is -68dbm, we allow some error to the position marker,

say +/- 2dbm; we call it signal spread, which is shown on Table 6. In Figure 4, the signal range is from -66dbm to -70dbm, we can find out 3 areas which are possible positions from the AP to the mobile station, which are position markers 12.1149, 12.2483, 14.4125, 14.5248 and 16.1901. Once we have the distance array, we can find out the possible position marker

from the database. As we have 10 signal sensor APs, we can find out the most accumulated possible position of the testing data. For possible position=5, all 5 position markers we obtained from the distance array carry the same weighting.



Figure 4. Signal by every position marker

Table 6. Result of Correct position estimation using Aggregated Radio Layout method.

Signal Spread (+/- dbm)	No. of Target Position	Rate of correct position marker			
		500 Samples	50 Samples	25 Samples	10 Samples
0.5	1	0.804651163	-	-	-
0.5	5	0.927906977	-	-	-
1	1	0.93255814	-	-	-
1	5	0.976744186	0.742857143	-	-
2	1	0.96744186	0.639285714	0.398809524	-
2	5	0.979069767	0.922619048	0.585119048	0.4898315
4	1	0.937209302	0.738095238	0.502702703	0.2584478
4	5	0.995348837	0.953571429	0.933928571	0.6197549
6	1	0.495348837	0.545238095	0.407738095	0.2071429
6	5	0.98372093	0.917857143	0.824404762	0.6025584

Table 7. Rate of Correct Position Marker Estimation using the Least-square fingerprint Method

Possible Positions	Rate of correct position marker estimation			
	500 Samples	50 Samples	25 Samples	10 Samples
1	0.976190	0.858333	0.694048	0.415000
5	0.996587	0.969048	0.933929	0.795714
9	1	0.986905	0.976786	0.908333

From Table 6, the sample rate is 500, which means the mobile station allows data to be collected at a stationary position for  $\Delta t > 100$ . Under a signal spread of +/- 2dbm, the rate of correct target position=1 is 96.7%, and 99.5% for the target positions=5. For signal spread=4dbm and sample rate=50, the mobile station allow data to be collected at a stationary position

for  $\Delta t > 10$ , the rate of correct target position=1 is 73.8%, and 96.4% for 5 target positions. When we use 10 samples which allow signal data to be collected for  $\Delta t > 2$ , we cannot get the correct position marker at a rate higher than 61.98%. The higher number of possible positions the location algorithm obtained, the less accurate the location estimation is.

One may also notice that while a higher number of samples increase the general accuracy of the algorithm, signal spread and target position remain the dominant factors. From Table 5, all sample sizes (except 10) with signal spread=4 and target position=5 give above 90% rates of correct position marker.

From the experiment, we can conclude that the better configuration for the experimental setup is using signal

spread=4 and target position=5 for all situations. For situations that we can obtain a lot of signal data in a short period of time, say 500 samples with  $\Delta t > 100$ , we use signal spread=2 and possible position=1 in order to capture the mobile user with great accuracy.

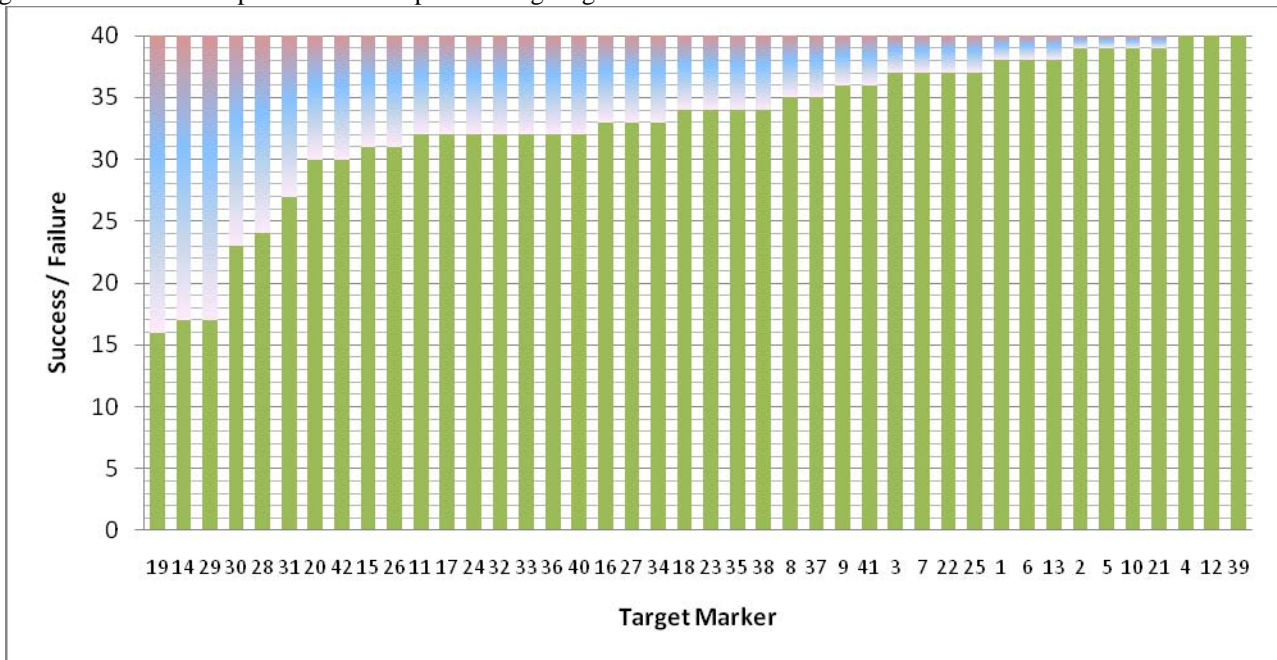


Figure 5. Rate of correct position marker estimation on Possible Positions=5, Samples=25, Signal spread=6dbm

### 4.3 Experiment 3 – Comparing Fingerprint with Aggregated Signal Layout

Table 7 shows the hit rate of position marker estimation by fingerprint technique using a similar set of data extracted from experiment 2. Each position marker has one set of fingerprint by averaging the signal received by 10 APs in the training phase. Similar experiment was carried out with different sample rates.

#### Experiment 3 Result and Analysis

Comparing Table 6 with Table 7, the rate of correct position marker using “Least-square fingerprint technique” is better than “Aggregated Signal Layout method” for all situations. In experiment 2, the accuracy much depends on the training phase. The more training time and training samples obtained in the training phase, the more accurate the fingerprint technique is. The major problem of fingerprinting is that we need a huge amount of time to train the fingerprint and we cannot find a suitable constant or variable to calibrate the fingerprint for different mobile devices. Different mobile devices have different signal transmitting characteristics; using the Aggregated Signal Layout which is a “radio map overlapping” technique, we can adjust the “signal spread” and “target position” to calibrate the location estimation algorithm.

Figure 5 shows the rate of correct position marker estimation. Each position goes through 40 estimations and the result is plotted on the graph. For position 14, only 16 out of 40 estimations locate the correct position marker. But on the other hand, position markers 4 and 12 and 39 have excellent results: they are perfectly matched. In Figure 5, position markers 19, 14, 29, 30, 28 and 31 show poorest estimation, they had less than 25% accuracy (6 out of 42), and 14.3% of the position markers display the poorest performance on “Aggregated Signal Layout method”. According to Table 7, the rate of correct position marker in average is about 69.4%, conversely,

we have 30.6% failure rate mainly distributed among 6 poorest position markers as stated above. From Table 6, the rate of correct position is 82.4%, if we get rid of the poorest position markers, the rate of correct position can be increased to 86.4% which is good enough to locate mobile devices in a lot of scenarios.

Table 8. Average Time on location estimation

	Ave. Time for estimation	
	Samples = 200	Samples = 25
Fingerprinting	91ms	45ms
Aggr. Signal Layout	253ms	40ms

Table 8 shows the time needed for location estimation with different sample size. For large sample size, Aggregated Signal Layout technique is more time consuming: more than 0.25 second is used for location estimation. The major reason is due to the overhead of mapping the possible position marker on every “signal spread”. For Sample size equal to 25, the time used by fingerprint and Aggregated Signal Layout are nearly the same, as less overhead is used on averaging the signal data and therefore less data used to pair up with fingerprint and Aggregated Signal Layout.

### 5. Packet Capture Interface on Sensor Router

On the Sensor Router, it consists of a custom-made packet capture interface for the Wi-Fi enabled router to monitor all the network traffic on the air. The Sensor Router running an embed Linux, the custom-made monitoring software which use libpcap library to capture the packets traveling over the network, the modified packet capture interface is work with a 802.11 prism\_hdr library, the decoded packets in a prism header have a monitoring mode that sticks a proprietary header on each packet with lots of information. The RSSI (receive signal strength indication) is the total power received by the radio hardware while receiving the frame, including all the signal, interference and background noise etc...

In Linux, we call the network interface like eth0, while the Wi-Fi interface is defined as something like ath0 / prism0. Once we initialize the pcap library, we need to tell which device we are sniffing on, what channel we set. The network interface picks up a packet, the Ethernet header is received then strips off and become a IP packet, the IP packet can be TCP or UDP packet which strips off and further extract into a TCP / UDP header and the payload packet, the custom-made utility is used to intercept the packet by the network interface and extract all the useful information inside the packet including RSSI as well as the sequence number of the packet `hdr80211->frag_and_seq`. The Middle Server with a custom-made server application is used to handle all the packet information, the source MAC address, the destination MAC address, the packet number, the signal strength. In our test-bed, 10 sensor APs is collecting all the packet in the air and pass the information to the middle server. The middle server acts as a relay to filter out unwanted information and store it in the data server.

The Analysis Application is written for data analysis during the data training phase and as a real-time reporting system during the online phase, the requested likelihood positions will be the final result. The whole system was build on a three layer architecture which ensure the stability of the system.

## 6. Conclusion and Future Work

On the current "Aggregated Signal Layout" technique, the entire possible position marker found from every radio map carry the same weight. In fact, it is possible to compute the maximum likelihood to every possible position marker in every signal layout, and weighting can be given to each possible position marker. The generated result can be much sophisticated than the traditional fingerprint technique and Aggregated Signal Layout technique used in this paper. We demonstrate the feasibility of using WLAN to locate mobile users and pinpointing Wi-Fi communication in an indoor environment. We had developed a custom-made cross-compiled application that can be deployed to major APs with ease. Our proposed mobile location system consists of an array of APs that constantly collect data packets within the wireless medium; the collected data, such as MAC addresses and RSSI, is then relayed and stored in a data store. We have proposed the Aggregated Signal Layout method to relieve the maintenance cost of the exhaustive Fingerprinting method. With the Government leading Hong Kong into an age of ubiquitous computing, it is imperative we develop a feasible WLAN location system that is both effective and easily deployed. Our proposed system shows that it is possible to implement a WLAN location system without the extra effort to calibrate and adapt to individual environments.

## 7. References

[1] "Hong Kong Government's Digital 21 Strategy" at <http://www.info.gov.hk/digital21/eng/index.htm>  
 [2] "Government Wi-Fi Programme (GovWiFi)" at <http://www.gov.hk/en/theme/wifi/program/index.htm>  
 [3] "Linksys WRT54G series" at <http://en.wikipedia.org/wiki/Linksys>  
 [4] T. King, S. Kopf, T. Haenselmann, C. Lubberger, and W. Effelsberg, COMPASS: A Probabilistic Indoor Positioning System Based on 802.11 and Digital Compasses, in Proc. The 1<sup>st</sup> Int. Workshop on Wireless Network Testbeds, Experimental Evaluation & Characterization (WiNTECH 06), pp. 34-40, Sep. 06.  
 [5] "Open Source Firmware for Access Point" at <http://www.opertwrt.org>  
 [6] William H. Wong, Joseph K. Ng, and Wilson M. Yeung, "Wireless LAN Positioning with Mobile Devices in a Library Environment", Proceedings of ICDCS-MDC 2005 Workshop, pp. 633-636, June 6-10, 2005.

[7] Zhili Wu, Chun-hung Li, Joseph K. Ng, "Improvements to RADAR Location Classification", in Proceedings of the 2008 International Conference on Wireless Communications, Networking and Mobile Computing (WiCOM 2008)  
 [8] Joseph K. Ng, Junyang Zhou, Kenneth M. Chu, and Karl R. Leung, "A Train-Once Approach for Location Estimation using the Directional Propagation Model (DPM)", IEEE Trans. on Vehicular Technology, 57(4), pp. 2242-2256, July 2008.  
 [9] Junyang Zhou, Wilson M. Yeung and Joseph K. Ng, "Enhancing Indoor Positioning Accuracy by utilizing signals from both the mobile phone network and the Wireless Local Area Network", in Proceedings of the IEEE 22nd International Conference on Advanced Information Networking and Applications (AINA 2008), pp 138-145, March 25-28, 2008, GinoWan, Okinawa, Japan. IEEE CS Press.  
 [10] Wilson M. Yeung, Junyang Zhou and Joseph K. Ng, "Enhanced Fingerprint-based Location Estimation System in Wireless LAN Environment", in Proc. of the 1st International Workshop on System and Software for Wireless SoC (WSOC 2007), pp 273-284, December 17-20, 2007, Taipei, Taiwan, Springer.  
 [11] Wilson M. Yeung and Joseph K. Ng, "Wireless LAN Positioning based on Received Signal Strength from Mobile device and Access Points", in Proceedings of the 13th International Conference on Embedded and Real-Time Computing Systems and Applications (RTCSA 2007), pp. 131-137, August 21-23, 2007, Daegu, Korea 2007, IEEE Computer Society Press.  
 [12] Wilson M. Yeung, and Joseph K. Ng, "An Enhanced Wireless LAN Positioning Algorithm based on the Fingerprint Approach", Proceedings of IEEE TENCON 2006, IEEE CS Press, 14-17 November 2006, Hong Kong, China.  
 [13] Kenneth M. Chu, Karl R. Leung, Joseph K. Ng, Chun Hung Li, "A Directional Propagation Model for Locating Mobile Stations within a Mobile Phone Network", International Journal of Wireless and Mobile Computing (IJWMC): Special Issue on Applications, Services and Infrastructure for Wireless and Mobile Computing, 3(1/2) pp. 12-21, August 2008, Inderscience.  
 [14] William H. Wong, Joseph K. Ng, and Karl R.P.H. Leung, "Large-Scale Location Estimation over GSM networks: the GEAR Approach", Proceedings of the 24th IEEE International Conference on Distributed Computing Systems Workshops (ICDCS-MDC 2004), pp. 574 --- 579, March 23-26, 2004.  
 [15] William H. Wong, Joseph K. Ng, and Karl R.P.H. Leung, "Large-Scale Location Estimation over GSM networks: the Gear Approach", to appear in International Journal of Wireless and Mobile Computing.  
 [16] Zhi-li Wu, Chun-hung Li, Joseph K. Ng, and Karl R.P.H. Leung, "Location Estimation via Support Vector Kernel Regression", IEEE Transactions on Mobile Computing, Vol. 6, No. 3, pp. 311-321, March 07.  
 [17] P. Bahl and V.N. Padmanabhan, "RADAR: An in-building RF-based user location and tracking system", in Proceedings of INFOCOM 2000, (2): 775-784. Available online at [citeseer.ist.psu.edu/bahl00radar.html](http://citeseer.ist.psu.edu/bahl00radar.html)  
 [18] Junyang Zhou, Enhanced Signal Propagation Models and Algorithm Selector for Providing Location Estimation Services within Cellular Radio Networks, Hong Kong Baptist University 2007  
 [19] Melyvn Wong and Joseph K. Ng, "Fleet Management System", Innovation and Technology Fund (UIM), Innovation and Technology Commission, HKSAR Government.  
 [20] Duncan Lau, Joseph Ng, Karl Leung, Lawrence Cheung, "Develop an accurate low-cost Mobile Location Estimation System (MLES) for fleet management applications using existing mobile phone infrastructure ", Innovation and Technology Fund (ITSP), Innovation and Technology Commission, HKSAR Government.  
 [21] Stephen K. Chan, Kenny K. Kan, and Joseph K. Ng, "A Dual-Channel System for Providing Location Estimation in Mobile Computing", Journal of Interconnection Networks (JOIN), Volume 4, Number 3, pp. 271 --- 290, September 2003, World Scientific Publishing Company.  
 [22] Kenny K.H. Kan, Stephen K.C. Chan, and Joseph K. Ng, "A Dual-Channel Location Estimation System for providing Location Services based on the GPS and GSM Networks", Proceedings of The 17th International Conference on Advanced Information Networking and Applications (AINA 2003), pp. 7 - 12, March 27-29, 2003, Xi'an, China.  
 [23] Joseph K. Ng, Stephen K. Chan, and Kenny K. Kan, "Location Estimation Algorithms for Providing Location Services within a Metropolitan Area based on a Mobile Phone Network", Proceedings of the 5th International Workshop on Mobility Databases and Distributed Systems (MDDS 2002), pp. 710 --- 715, Aix-en-Provence, France, September 2-6, 2002

- [24] Karl R.P.H. Leung, Joseph K. Ng, Tim K. Chan, Kenneth M. Chu, and Chung Hung Li, "Network Based Mobile Station Positioning in Metropolitan Area", Proceedings of the International Conference on Parallel and Distributed Computing (Euro-Par 2003), pp. 1017 --- 1026, Springer-Verlag, August 26-29, 2003, Klagenfurt, Austria.
- [25] Ka Ho Kan, "Location Estimation System Based on the GSM Network", M.Phil. Thesis, Hong Kong Baptist University 2004.
- [26] Kenneth M. Chu, Karl R.P.H. Leung, Joseph K. Ng, and Chun H. Li, "Locating Mobile Stations with Statistical Directional Propagation Model", Proceedings of the 18th International Conference on Advanced Information Networking and Applications (AINA 2004), pp. 230 --- 235, March 29-31, 2004, Fukuoka, Japan.
- [27] Kenneth M. Chu, Karl R. Leung, Joseph K. Ng, Chun Hung Li, "A Directional Propagation Model for Locating Mobile Stations within a Mobile Phone Network", International Journal of Wireless and Mobile Computing (IJWMC): Special Issue on Applications, Services and Infrastructure for Wireless and Mobile Computing, 3(1/2) pp. 12-21, August 2008, Inderscience.
- [28] William H. Wong, Joseph K. Ng, and Karl R.P.H. Leung, "Large-Scale Location Estimation over GSM networks: the GEAR Approach", Proceedings of the 24th IEEE International Conference on Distributed Computing Systems Workshops (ICDCS-MDC 2004), pp. 574 --- 579, March 23-26, 2004, Hachioji, Tokyo, Japan.
- [29] William H. Wong, Joseph K. Ng, and Karl R.P.H. Leung, "Large-Scale Location Estimation over GSM networks: the Gear Approach", to appear in International Journal of Wireless and Mobile Computing.
- [30] Zhi-li Wu, Chun-hung Li, Joseph K. Ng, and Karl R.P.H. Leung, "Location Estimation via Support Vector Kernel Regression", IEEE Transactions on Mobile Computing, Vol. 6, No. 3, pp. 311-321, March 2007.
- [31] Y. Wang, X. Jia, H.K. Lee, and G.Y. Li, "An indoor wireless positioning system based on wireless local area network infrastructure", Proceedings of the 6th International Symposium on Satellite Navigation Technology Including Mobile Positioning & Location Services (SatNav 2003), Melbourne, Australia, 22-25 July 2003.
- [32] P. Bahl and V.N. Padmanabhan, "RADAR: An in-building RF-based user location and tracking system", in Proceedings of INFOCOM 2000, (2): 775-784. Available online at [citeseer.ist.psu.edu/bahl00radar.html](http://citeseer.ist.psu.edu/bahl00radar.html)
- [33] P. Krishnan, A.S. Krishnakumar, W.-H. Ju, C. Mallows, and S. Ganu, "A system for LEASE: Location estimation assisted by stationary emitters for indoor RF wireless networks", in Proceedings of INFOCOM 2004, 2004.
- [34] S. Ganu, A.S. Krishnakumar, and P. Krishnan, "Infrastructure-based location estimation in WLAN networks", in Proceedings of the IEEE Wireless Communications and Networking Conference (WCNC 2004).
- [35] Wilson M. Yeung, Wireless LAN Positioning in Indoor Environment, Hong Kong Baptist University 2007
- [36] "Broadcom 802.11abg Networking Device Driver" at <https://dev.openwrt.org/browser/trunk/openwrt/package/openwrt/include/wlioctl.h?rev=375>,
- [37] "pcapsource from Kismet" at [http://www.google.com.hk/codesearch/p?hl=zh-TW#ACmMdBt9LZs/Firmware\\_Alchemy-pre5.4a.src.by.TheIndividual.tar.bz2\[g0iVX931-Yk/Firmware\\_Alchemy-pre5\\_4/src/router/kismet/pcapsource.cc&q=WLC\\_GET\\_MONITOR](http://www.google.com.hk/codesearch/p?hl=zh-TW#ACmMdBt9LZs/Firmware_Alchemy-pre5.4a.src.by.TheIndividual.tar.bz2[g0iVX931-Yk/Firmware_Alchemy-pre5_4/src/router/kismet/pcapsource.cc&q=WLC_GET_MONITOR)
- [38] "Partial driver for WAVELAN" at [http://www.google.com.hk/codesearch/p?hl=zh-TW#p-OcbD5DbwM/packages/1.2/kernel/patches/49-3rdparty/MC16\\_vt\\_ar5k-20030509.tar|xlsugco9EAs/3rdparty/vt\\_ar5k/include/vt\\_wlan.h&q=prism\\_hdr\\_t](http://www.google.com.hk/codesearch/p?hl=zh-TW#p-OcbD5DbwM/packages/1.2/kernel/patches/49-3rdparty/MC16_vt_ar5k-20030509.tar|xlsugco9EAs/3rdparty/vt_ar5k/include/vt_wlan.h&q=prism_hdr_t)

# Cooperative and Penalized EM Algorithm Based on Maximum Weighted Likelihood for Gaussian Mixture Learning

Hong Jia

Department of Computer Science, Hong Kong Baptist University  
hjia@comp.hkbu.edu.hk

## Abstract

*A general learning framework named Maximum Weighted Likelihood for density mixture model fitting has been proposed in [Cheung 2005]. It is verified that with an appropriate weight design, the component number can be automatically selected through this approach. Therefore, this paper investigates the implementation of cooperation mechanism in this learning paradigm and proposes a novel weight design, through which an algorithm named Cooperative EM (CEM) for mixture model learning with automatic model selection is presented. Moreover, in order to enhance the robustness of the previous algorithm to the initialization, we further integrate the cooperation and penalization mechanisms together and accordingly generate a Cooperative and Penalized EM (CPEM) algorithm, in which the winning component will not only cooperate with most promising rivals but also penalized some other rivals with a dynamic strength. It is found that the CPEM is insensitive to the initialization and can give a good estimate of the density mixture's parameters as well as the component number. The efficiency and accuracy of the proposed algorithms are experimentally demonstrated on both of synthetic and real data.*

## 1 Introduction

Gaussian mixture models (GMMS), which model univariate and multidimensional data with a finite mixture of Gaussian densities, is intensively used in state-of-the-art image retrieval [1], speech and handwriting recognition [2, 3, 4], gene microarray data analysis [5] and many other classification and clustering systems. Traditional method adopted to estimate the GMM parameters (i.e., priors, means and covariances) is the Expectation-Maximization (EM) algorithm [6, 7, 8], which fit the mixture models to observed data based on maximum likelihood principle. Nevertheless, as pointed out in [9], the EM algorithm is sensitive to the initializations and need to pre-assign the number of

mixture components (i.e., the number of clusters) exactly; otherwise, it will almost always lead to a poor estimate of the parameters. Unfortunately, in practice, it is hard to determine the component number in advance.

In the literature, different model selection methods have been proposed to estimate the number of mixture components. Generally, these variant methods can be roughly separated into two classes. The first kind of methods chooses the optimal number of clusters via some statistic criteria. Examples of such criteria that have been used include the Laplace-empirical criterion (LEC) [10], Schwarz's Bayesian inference criterion (BIC) [11, 12, 13], Rissanen's Minimum Description Length (MDL) [14, 15], the Minimum Message Length (MML) criterion [16, 17], Akaike's Information Criterion (AIC) [18, 19] and the Information Complexity Criterion (ICOMP) [20]. In these methods, the parameter estimation and model selection are two separated steps and the computation of is laborious because learning process needs to be repeated for different component numbers.

Alternatively, in the other kind of methods, model selection is implemented along with parameter estimation in a single paradigm. One example is the Split and Merge EM algorithms [21, 22, 23], in which uncorrect components in the density mixture are either split or merged based on some specified criteria. Then, by performing the usual EM algorithm and the split-merge operation alternately, the component number and parameters of a mixture model can be obtained synchronously. Nevertheless, the performance of these algorithms depends on the choice of split-and-merge criteria and the computations are rather heavier than the EM approach. Another example is the method based on competitive agglomeration clustering [24], in which the cost function of mixture learning is regularized by the full entropy of posterior probabilities to determine the number of components automatically. However, this algorithm has introduced a new parameter, which needs different settings under variant clustering environments; otherwise, the number of components may be underestimated.

Unlike the aforementioned methods, the approach pro-

posed by Cheung [25, 26] select the component number not based on additional criteria or operations, but by introducing a novel weight item into the likelihood cost function and generating a new learning framework namely Maximum Weighted Likelihood (MWL). It has been shown that, with an appropriate design, the MWL is able to do automatically model component section during the parameter estimate process. As in [26], with a specific weight form, a Rival Penalized EM (RPEM) algorithm for density mixture clustering has been generated. In this method, given an input data each time, the components in a density mixture will compete with each other. Then, not only the parameters of winning component are updated adapt to the input but also the parameters associated with all rivals are penalized with the strength proportional to the corresponding posterior density probabilities. Subsequently, the redundant components in the mixture will be gradually faded out and an appropriate number of densities can be automatically selected. Furthermore, a simplified version of RPEM has included the existing RPCL [27] and RPCCL [28] algorithms as its special cases with some new extensions. Additionally, a new weight design accompanied by a heuristic extended EM (X-EM) algorithm is presented in [29]. This method can also do automatic model selection by fading the redundant components from a mixture.

In this paper, we will further investigate the weight design of MWL learning framework and propose a new weight form, through which a novel algorithm named Cooperative EM (CEM) is presented. In CEM, at each time step, the winner generated from the competition of mixture components will cooperate with some other promising rivals to update to the current input together. Subsequently, the parameters of partial components will gradually converge to the same values and finally the number of components with variant parameters is exactly the component number of density mixture model fit to the given data set. Moreover, in order to enhance the robustness of the proposed algorithm to the initialization, we further modify the previous presented weight design and accordingly generate a Cooperative and Penalized EM (CPEM) algorithm, in which the winning component will not only cooperate with most promising rivals but also penalize some other rivals with a dynamic strength. It is found that the CPEM is insensitive to the initialization to a certain level and can give a good estimate of the density mixture's parameters as well as the component number. For simplicity, during our practical studies, we concentrate on Gaussian mixture model only, although both CEM and CPEM can be extended to other finite density mixture models. The outstanding performance of proposed methods is experimentally demonstrated on both synthetic and real data.

The rest of this paper is organized as follows. Section 2 will overview the MWL learning framework and a spe-

cial weight design of RPEM algorithm. Section 3 describes a novel weight design of MWL, through which the CEM algorithm is then proposed. Subsequently, in Section 4, we integrate the cooperation and penalization mechanisms into one single learning process and generate a CPEM algorithm. The performance of the proposed algorithms is experimentally demonstrated with both of synthetic and real data in Section 5. Finally, we draw a conclusion in Section 6.

## 2 Overview of MWL Learning Framework

Suppose we have  $N$  inputs,  $\mathbf{x}_1, \mathbf{x}_2, \dots, \mathbf{x}_N$ , coming from the following density mixture model:

$$p(\mathbf{x}|\Theta^*) = \sum_{j=1}^{k^*} \alpha_j^* p(\mathbf{x}|\theta_j^*) \quad (1)$$

with

$$\sum_{j=1}^{k^*} \alpha_j^* = 1, \alpha_j > 0, \forall 1 \leq j \leq k^*, \quad (2)$$

where  $\Theta^* = \{\alpha_j^*, \theta_j^*\}_{j=1}^{k^*}$  is the true parameters of the mixture model and  $k^*$  denotes the number of components. The key issue in density mixture learning is to find an estimate of  $\Theta^*$ , denoted as  $\Theta = \{\alpha_j, \theta_j\}_{j=1}^k$ , from the observations. Here  $k$  is an estimate of  $k^*$ . According to the Maximum Likelihood (ML) principle,  $\Theta$  can be obtained by maximizing the following cost function:

$$\ell(\Theta) = \int \ln p(\mathbf{x}|\Theta) dF(\mathbf{x}) = \frac{1}{N} \sum_{t=1}^N \ln p(\mathbf{x}_t|\Theta), \quad (3)$$

where  $F(\mathbf{x}) = \int_{-\infty}^{\mathbf{x}} p(u) du$  is the cumulative probability function and the second equation can be true when  $N$  is large enough [26]. Generally, once  $k$  is pre-specified, maximizing Eq. (3) can be achieved by the EM [6, 7] algorithm. However, if the value of  $k$  is assigned different from  $k^*$ , the EM algorithm will almost always give out a poor estimate of  $\Theta^*$ . Unfortunately, in practice, it is hard to determine the number of components in advance.

To circumvent this problem, a new learning framework has been proposed by Cheung [25, 26], in which a novel weight item was introduced to the conventional likelihood.

Subsequently, the cost function can be written as:

$$\begin{aligned}
Q(\Theta; \mathbf{x}_N) &= \frac{1}{N} \sum_{t=1}^N \ln p(\mathbf{x}_t | \Theta) \\
&= \frac{1}{N} \sum_{t=1}^N \sum_{j=1}^k g(j | \mathbf{x}_t, \Theta) \ln p(\mathbf{x}_t | \Theta) \\
&= \frac{1}{N} \sum_{t=1}^N \sum_{j=1}^k g(j | \mathbf{x}_t, \Theta) \ln [\alpha_j p(\mathbf{x}_t | \theta_j)] \\
&\quad - \frac{1}{N} \sum_{t=1}^N \sum_{j=1}^k g(j | \mathbf{x}_t, \Theta) \ln h(j | \mathbf{x}_t, \Theta),
\end{aligned} \tag{4}$$

where

$$h(j | \mathbf{x}_t, \Theta) = \frac{\alpha_j p(\mathbf{x}_t | \theta_j)}{p(\mathbf{x}_t | \Theta)} \tag{5}$$

denotes the probability of  $\mathbf{x}$  coming from the  $j$ -th density component and  $k$  is a preassigned constant satisfying  $k \geq k^*$ . Here  $g(j | \mathbf{x}_t, \Theta)$ s are the designable weight functions constrained by

$$\sum_{j=1}^k g(j | \mathbf{x}_t, \Theta) = 1, \text{ for any } 1 \leq t \leq N \tag{6}$$

and

$$\forall j, \quad g(j | \mathbf{x}_t, \Theta) = 0 \quad \text{if } h(j | \mathbf{x}_t, \Theta) = 0. \tag{7}$$

Since in Eq. (4), the parameter learning of each model component is adjusted by the associate weight, this equation is named the Weighted Likelihood Function. As soon as the weight is designed, the learning of  $\Theta$  can be accomplished toward maximizing Eq. (4) and this method is regarded as Maximum Weighted Likelihood (MWL) learning approach.

According to [26], an effective weight can be conducted by

$$g(j | \mathbf{x}_t, \Theta) = (1 + \xi_t) I(j | \mathbf{x}_t, \Theta) - \xi_t h(j | \mathbf{x}_t, \Theta), \tag{8}$$

where

$$I(j | \mathbf{x}_t, \Theta) = \begin{cases} 1, & \text{if } j = c = \arg \max_{1 \leq i \leq k} h(i | \mathbf{x}_t, \Theta) \\ 0, & \text{otherwise} \end{cases} \tag{9}$$

is an indicator function and  $\xi_t$  is a coefficient varying with the time step  $t$ . Specially, when  $\xi_t$  is set at a constant 1, an adaptive Rival Penalized EM (RPEM) algorithm to learn  $\Theta$  via maximizing the WL function of Eq. (4) is proposed [26]. The main steps of this new method can be summarized as follows:

**Step1:** Pre-specify the number  $k$  of components ( $k \geq k^*$ ) and initialize the parameter  $\Theta$ .

**Step2:** Given an input  $\mathbf{x}_t$  and the current parameter estimate  $\Theta^{(n)}$ , calculate  $h(j | \mathbf{x}_t, \Theta)$  and  $g(j | \mathbf{x}_t, \Theta)$  via Eq. (5) and Eq. (8), respectively, where  $j = 1, 2, \dots, k$ .

**Step3:** Given  $h(j | \mathbf{x}_t, \Theta)$ s and  $g(j | \mathbf{x}_t, \Theta)$ s, update  $\Theta$  by

$$\Theta^{(n+1)} = \Theta^{(n)} + \eta \frac{q_t(\Theta; \mathbf{x}_t)}{\Theta} \Big|_{\Theta^{(n)}}, \tag{10}$$

with

$$\begin{aligned}
q_t(\Theta; \mathbf{x}_t) &= \sum_{j=1}^k g(j | \mathbf{x}_t, \Theta) \ln [\alpha_j p(\mathbf{x}_t | \theta_j)] \\
&\quad - \sum_{j=1}^k g(j | \mathbf{x}_t, \Theta) \ln h(j | \mathbf{x}_t, \Theta),
\end{aligned} \tag{11}$$

where  $\eta$  is a pre-specified small learning rate.

The above **Step 2** and **Step 3** are iterated for each input until a stop criterion is satisfied. From the weight design we can see that, in RPEM algorithm, not only the parameters of winning component are updated to adapt to the input, but also all of the rivals are penalized with strength proportional to their posterior probabilities. Finally, the redundant components will be faded out from the density mixture and the true component number will be identified. That is, the penalization mechanism enables the RPEM algorithm to do automatically model selection.

In the following, we will consider other competition mechanisms to generate new weight design for the MWL learning framework, and correspondingly, propose a novel algorithm which features the good estimate of the density mixture's parameters as well as the component number and the robust performance against the initializations.

### 3 Cooperative EM algorithm

In Ref. [30] and [31], the cooperation mechanism has shown its feasibility in automatic model selection. Here, we will investigate the implement of this competitive mechanism in WML learning framework and present a novel mixture model learning algorithm namely Cooperative EM (CEM) Algorithm. Furthermore, during the following work, we will concentrate on Gaussian mixture models only. That is,  $p(\mathbf{x} | \theta_j)$  becomes a Gaussian density, denoted as  $G(\mathbf{x} | \mathbf{m}_j, \Sigma_j)$ , and  $\Theta = \{\alpha_j, \mathbf{m}_j, \Sigma_j\}_{j=1}^k$  ( $k \geq k^*$ ) is the estimate of the true parameter  $\Theta^*$ .

Since the weight items are constrained by Eq. (6) and Eq. (7), a reasonable design of  $g(j | \mathbf{x}_t, \Theta)$ s is as follows:

$$g(j | \mathbf{x}_t, \Theta) = \frac{f(j | \mathbf{x}_t, \Theta)}{\sum_{i=1}^k f(i | \mathbf{x}_t, \Theta)}, j = 1, 2, \dots, k, \tag{12}$$

where  $f(j|\mathbf{x}_t, \Theta)$  is a function relate to  $\mathbf{x}_t$  and  $\Theta$ , and also satisfied

$$\forall j, \quad f(j|\mathbf{x}_t, \Theta) = 0 \quad \text{if} \quad h(j|\mathbf{x}_t, \Theta) = 0. \quad (13)$$

Regulation term  $1/\sum_{i=1}^k f(i|\mathbf{x}_t, \Theta)$  is designed to make sure that  $\sum_{j=1}^k g(j|\mathbf{x}_t, \Theta) = 1$ .

In CEM method, given an input  $\mathbf{x}_t$ , the winner generated from the competition of the  $k$  components will cooperate with some other promising components and update to adapt to the current input together. A component  $j$  is regarded as a promising one if its posterior probability  $h(j|\mathbf{x}_t, \Theta)$  satisfied  $h(j|\mathbf{x}_t, \Theta) > 1/k$ . That is, the probability of  $\mathbf{x}_t$  coming from this component is larger than the average probability of all  $k$  components. As a rule of thumb, if the positions of two components are close to each other, they will be more likely in the same density region. Hence, in the cooperation mechanism, the component closer to the winner should be assigned greater cooperation strength. To this end, we assume that the center of each mixture component, i.e.  $\mathbf{m}_j$ , obeys a Gaussian distribution presented by the winner  $\mathbf{m}_c$ , denoted as  $G(\mathbf{m}_j|\mathbf{m}_c, I)$ , i.e. the Gaussian distribution with the mean  $\mathbf{m}_c$  and covariance matrix  $I$ . Then the distribution probability of each component related to the winner can be calculated by

$$p_m(j) = G(\mathbf{m}_j|\mathbf{m}_c, I), j = 1, 2, \dots, k. \quad (14)$$

This probability can be utilized to adjust the cooperation strength.

Subsequently, based on the previous definitions, the function  $f(j|\mathbf{x}_t, \Theta)$  can be designed as:

$$f(j|\mathbf{x}_t, \Theta) = \begin{cases} 1, & \text{if } j = c = \arg \max_{1 \leq i \leq k} h(i|\mathbf{x}_t, \Theta) \\ \frac{p_m(j)}{p_m(c)}, & \text{if } h(j|\mathbf{x}_t, \Theta) > \frac{1}{k}, j \neq c \\ 0, & \text{otherwise.} \end{cases} \quad (15)$$

Then, the  $g(j|\mathbf{x}_t, \Theta)$ s are determined by Eq. (12). From Eq. (15) we can see that the winner among  $k$  components will be assigned a full positive weight 1 and the weight specified to each promising component is adjusted by the distance between its center and the winner's. That is, the smaller the distance is, the greater the weight will be. Specially, when the distance is equal to 0, i.e., the centers of the cooperator and the winner are overlapped, a full positive weight will also be assigned.

Once the weights are constructed, the estimate of  $\Theta^*$  can be obtained by maximizing the cost function given by Eq. (4). Since  $\alpha_j$ s are constrained by Eq. (2), similar to [26], we can utilize the soft-max activation function to de-

note  $\alpha_j$ s as follows:

$$\alpha_j = \frac{\exp(\beta_j)}{\sum_{i=1}^k \exp(\beta_i)}, j = 1, 2, \dots, k. \quad (16)$$

Then  $\alpha_j$ s can be learned indirectly by updating the free variables  $\beta_j$ s. Moreover, during the process of CEM algorithm, if the parameters of two components have converged to the same values, we can judge that they are representing the same component of the mixture model. Therefore, they can build a learning group and compete with other components together. Notice that the proportion of this group in the whole mixture model will be the summation of its member's.

Specifically, the CEM algorithm for Gaussian mixture learning can be given as:

**Step1:** Pre-specify the number  $k$  of components ( $k \geq k^*$ ) and initialize the parameter  $\Theta$ .

**Step2:** Given an input  $\mathbf{x}_t$  each time, based on the current parameter estimate  $\Theta^{(n)}$ , calculate  $\alpha_j$ s,  $h(j|\mathbf{x}_t, \Theta)$ s and  $g(j|\mathbf{x}_t, \Theta)$ s via Eq. (16), Eq. (5) and Eq. (12), respectively, where  $p(\mathbf{x}_t|\theta_j)$  is equal to  $G(\mathbf{x}_t|m_j, \Sigma_j)$ .

**Step3:** Given  $h(j|\mathbf{x}_t, \Theta)$ s and  $g(j|\mathbf{x}_t, \Theta)$ s, update  $\Theta$  by

$$\begin{aligned} \beta_j^{(n+1)} &= \beta_j^{(n)} + \eta_\beta \frac{\partial q_t(\Theta; \mathbf{x}_t)}{\partial \beta_j} \Big|_{\Theta^{(n)}} \\ &= \beta_j^{(n)} + \eta_\beta [g(j|\mathbf{x}_t, \Theta^{(n)}) - \alpha_j^{(n)}] \end{aligned} \quad (17)$$

$$\begin{aligned} \mathbf{m}_j^{(n+1)} &= \mathbf{m}_j^{(n)} + \eta \frac{\partial q_t(\Theta; \mathbf{x}_t)}{\partial \mathbf{m}_j} \Big|_{\Theta^{(n)}} \\ &= \mathbf{m}_j^{(n)} + \eta g(j|\mathbf{x}_t, \Theta^{(n)}) \Sigma_j^{-1(n)} (\mathbf{x}_t - \mathbf{m}_j^{(n)}) \end{aligned} \quad (18)$$

$$\begin{aligned} \Sigma_j^{-1(n+1)} &= \Sigma_j^{-1(n)} + \eta \Sigma_j^{-1(n)} \frac{\partial q_t(\Theta; \mathbf{x}_t)}{\partial \Sigma_j} \Sigma_j^{-1(n)} \Big|_{\Theta^{(n)}} \\ &= [1 + \eta g(j|\mathbf{x}_t, \Theta^{(n)})] \Sigma_j^{-1(n)} \\ &\quad - \eta g(j|\mathbf{x}_t, \Theta^{(n)}) U_{t,j} \end{aligned} \quad (19)$$

with

$$U_{t,j} = \Sigma_j^{-1(n)} (\mathbf{x}_t - \mathbf{m}_j^n) (\mathbf{x}_t - \mathbf{m}_j^n)^T \Sigma_j^{-1(n)}.$$

**Step4:** Check the parameters of all mixture components. If there are two components  $p$  and  $q$  satisfied  $\|\Theta_p^{(n+1)} - \Theta_q^{(n+1)}\| < \varepsilon$  ( $\varepsilon$  is a very small value), include the two components into the same learning group  $G$  and set  $\alpha_G = \alpha_p^{n+1} + \alpha_q^{n+1}$ . Then, in the following step, when calculate the posterior probabilities of  $p$  and  $q$ ,  $\alpha_G$  will be utilized instead of  $\alpha_p$  and  $\alpha_q$ .

The above **Step 2** to **Step 4** is iterated for each input until a stop criterion is satisfied. Moreover, in **Step 3**, in order to simplify the computation, the  $\Sigma_j^{-1}$ s are updated rather than  $\Sigma_j$ s [26]. The performance of this novel CEM algorithm will be experimentally investigated in Section 5.

#### 4 Cooperative and Penalized EM Algorithm

Although the CEM algorithm can give a good estimate of the true component number as well as the density parameters, its performance is somewhat sensitive to the initialization of seed points and the overlap level of mixture model. According to [32], the combination of cooperation and penalization mechanisms can improve the robustness and convergence rate of competitive learning method. Hence, hereinafter, in order to enhance the robustness of the previous algorithm, we introduce the penalization implementation and propose a new learning approach named CPEM under the MWL framework.

In CPEM, the winning component will not always cooperate with all of the promising rivals (i.e., rivals with posterior probability larger than  $1/k$ ), but cooperate with some superiors of them and penalize the others. We utilize a threshold parameter, defined as  $T$ , to regulate the two different competitive behaviors and improve the previous weight design with:

$$f(j|\mathbf{x}_t, \Theta) = \begin{cases} 1, & \text{if } j = c = \arg \max_{1 \leq i \leq k} h(i|\mathbf{x}_t, \Theta) \\ \frac{p_m(j)}{p_m(c)}, & \text{if } h(j|\mathbf{x}_t, \Theta) \geq \frac{1}{k} \text{ and } h(j|\mathbf{x}_t, \Theta) \geq T, j \neq c \\ -h(j|\mathbf{x}_t, \Theta), & \text{if } \frac{1}{k} < h(j|\mathbf{x}_t, \Theta) < T \\ 0, & \text{otherwise.} \end{cases} \quad (20)$$

Then,  $g(j|\mathbf{x}_t, \Theta)$  can be calculated by Eq. (12). Notice that in order to let the whole algorithm have a converged process, the penalized range should be gradually reduced and converge to zero. Hence, the value of  $T$  cannot be fixed at a constant but decreases over learning epoch. Let  $S_h$  be the sorted set of the posterior probabilities of  $k$  seed points in decreasing order, then we have

$$S_h(1) = \max_{1 \leq j \leq k} h(j|\mathbf{x}_t, \Theta) \quad (21)$$

and

$$S_h(k) = \min_{1 \leq j \leq k} h(j|\mathbf{x}_t, \Theta). \quad (22)$$

Subsequently, the threshold parameter  $T$  can be defined as

$$T = S_h(q) = S_h(\min(i, k)), \quad (23)$$

where  $q = \min(i, k)$  and  $i$  stands for the current epoch number. That is the value of  $T$  is equal to the  $q$ -th largest posterior probability among  $k$  seed points. For example, in the first iterate, since  $i = 1$ ,  $T$  will be equal to  $h(c|\mathbf{x}_t, \Theta)$ , each of the promising rivals will be penalized

with a strength proportional to its posterior probability. But in the second iterate, since  $T$  becomes  $S_h(2)$ , the promising seed point with second largest posterior probability will cooperate with the winner while the others will be penalized. So, we can see that, during the learning process, the cooperation is gradually strengthened while the penalization is weakened. Once  $i$  exceeds  $k$ , the value of  $T$  will have no influence on the implement of this algorithm and the next part of CPEM will become the same with CEM method. That is, the penalization mechanism only plays a part in the early stage of CPEM. It is worth mentioning that in this algorithm the two competitive mechanisms are both performed on promising rivals. Specially, if there are no promising ones at a learning step, the winner will just update itself with no cooperators and penalization.

Based on the above descriptions, the main procedure of CPEM can be summarized as follows:

**Step1:** Pre-specify the number  $k$  of components ( $k \geq k^*$ ) and initialize the parameter  $\Theta$ .

**Step2:** According to the current iterate number, calculate the value of  $T$  via Eq. (23).

**Step3:** Fixing  $T$ , given an input  $\mathbf{x}_t$  each time, based on the current parameter estimate  $\Theta^{(n)}$ , calculate  $\alpha_j$ s,  $h(j|\mathbf{x}_t, \Theta)$ s and  $g(j|\mathbf{x}_t, \Theta)$ s via Eq. (16), Eq. (5) and Eq. (12), respectively, where  $f(j|\mathbf{x}_t, \theta)$  is calculated by Eq. (20).

**Step4:** Given  $h(j|\mathbf{x}_t, \Theta)$ s and  $g(j|\mathbf{x}_t, \Theta)$ s, update  $\Theta$  by Eq. (17), Eq. (18) and Eq. (19).

**Step5:** Check the parameters of all mixture components. If there are two components  $p$  and  $q$  satisfied  $\|\Theta_p^{(n+1)} - \Theta_q^{(n+1)}\| < \varepsilon$  ( $\varepsilon$  is a very small value), include the two components into the same learning group  $G$  and set  $\alpha_G = \alpha_p^{n+1} + \alpha_q^{n+1}$ . Then, in the following step, when calculate the posterior probabilities of  $p$  and  $q$ ,  $\alpha_G$  will be utilized instead of  $\alpha_p$  and  $\alpha_q$ .

The above **Step 2** to **Step 5** is iterated for each input until a stop criterion is satisfied.

#### 5 Experimental Results

To investigate the performance of the proposed algorithms, different experiments have been conducted on both synthetic and real data sets. The experimental results will be presented in this section.

## 5.1 Experiments on Synthetic Data

### 5.1.1 Experiment 1

In this experiment, in order to investigate the validity of the CEM and CPEM algorithms, we generated 1000 data from the following bivariate Gaussian mixture model:

$$\begin{aligned}
 p(X|\Theta^*) = & 0.3G \left[ X \mid \begin{pmatrix} 1.0 \\ 1.0 \end{pmatrix}, \begin{pmatrix} 0.1, 0.05 \\ 0.05, 0.2 \end{pmatrix} \right] \\
 & + 0.4G \left[ X \mid \begin{pmatrix} 1.0 \\ 5.0 \end{pmatrix}, \begin{pmatrix} 0.1, 0.0 \\ 0.0, 0.1 \end{pmatrix} \right] \\
 & + 0.3G \left[ X \mid \begin{pmatrix} 5.0 \\ 5.0 \end{pmatrix}, \begin{pmatrix} 0.1, -0.05 \\ -0.05, 0.1 \end{pmatrix} \right].
 \end{aligned} \tag{24}$$

We supposed that  $k$  is equal to the true number of components  $k^*$  and randomly initialized three seed points  $\mathbf{m}_1$ ,  $\mathbf{m}_2$  and  $\mathbf{m}_3$  in the input space as shown in Fig. 1. The covariance matrix  $\Sigma$  of each component was set to be an identity matrix and all  $\beta_j$ s were taken to be zero to make that the initial  $\alpha_j$ s were equal to  $1/k$ . Moreover, similar to [26], the learning rate  $\eta$  and  $\eta_\beta$  for each algorithm were set at 0.001 and 0.0001, respectively.

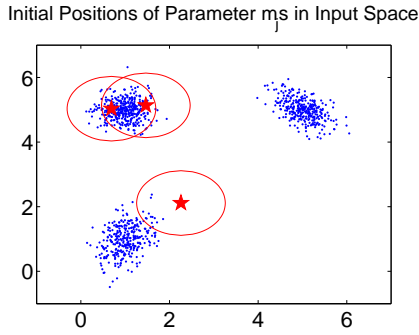


**Figure 1.** The initialization of three seed points marked by "★" in the input space of experiment 1.

After the performing of CEM algorithm, Fig. 2(a) shows the obtained positions of seed points and the shapes of the covariance matrices. A snapshot of the converged  $\alpha_j$ s is:

$$\alpha_1 = 0.3140, \quad \alpha_2 = 0.3679, \quad \alpha_3 = 0.3180. \tag{25}$$

we can see that the parameters of the mixture model has been well estimated. Moreover, the learning curves of  $\mathbf{m}_j$ s and  $\alpha_j$ s obtained by CEM are shown in Fig. 2(b) and Fig. 2(c).

Additionally, we also performed the CPEM algorithm under the same experimental environment. Fig. 3 shows that

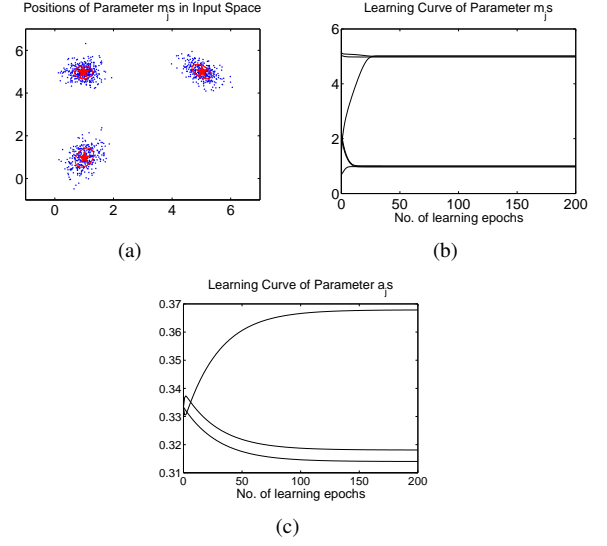


**Figure 2.** The results obtained by CEM in experiment 1: (a) the learned positions of three seed points, (b) the learning curves of  $\mathbf{m}_j$ s, and (c) the learning curves of  $\alpha_j$ s.

the three seed points have been exactly located in the corresponding cluster centers and the convergent rate of CPEM in this experiment is similar to CEM.

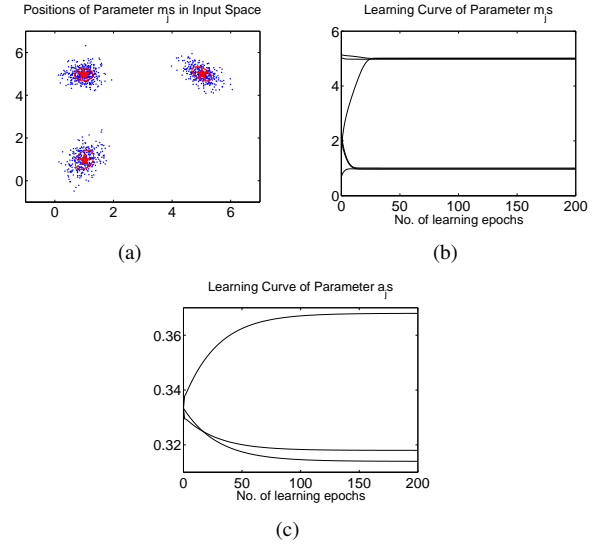


**Figure 3.** The results obtained by CPEM in experiment 1: (a) the learned positions of three seed points, (b) the learning curves of  $\mathbf{m}_j$ s, and (c) the learning curves of  $\alpha_j$ s.

### 5.1.2 Experiment 2

In the previous experiment, CEM and CPEM algorithms have demonstrated their validity when the components number  $k$  is specified equally to the true value. In the following experiment, we will further investigate their model selection ability when the true component number is unknown. With 1000 observations generated from the same density model, we randomly initialized six seed points in the input space, which is larger than the true component number. The positions of the seed points and the shapes of the initial covariance matrices have been given out in Fig. 4.

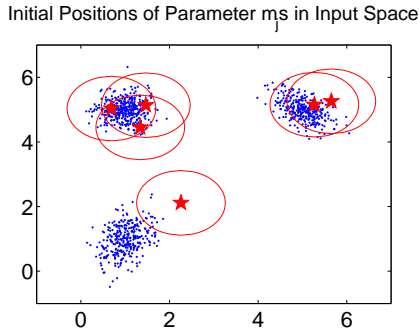


**Figure 4. The initialization of six seed points marked by "★" in the input space of experiment 2.**

The CEM and CPEM are both performed on this data, after 200 learning epochs, Fig. 5 and Fig. 6 shows the results of CEM and CPEM respectively. We can see that both of these two methods have identified the true component number and all of the six seed points have been successfully stabilized at the corresponding cluster centers. Taking the experimental results of CPEM for example, we further check the learned values of  $\alpha_j$ s. A snapshot of the converged  $\mathbf{m}_j$ s and  $\alpha_j$ s is:

$$\begin{aligned} m_1 &= \begin{pmatrix} 1.0089 \\ 0.9739 \end{pmatrix}, m_2 = \begin{pmatrix} 0.9811 \\ 4.9796 \end{pmatrix}, m_3 = \begin{pmatrix} 0.9811 \\ 4.9796 \end{pmatrix} \\ m_4 &= \begin{pmatrix} 5.0142 \\ 4.9995 \end{pmatrix}, m_5 = \begin{pmatrix} 0.9811 \\ 4.9796 \end{pmatrix}, m_6 = \begin{pmatrix} 5.0142 \\ 4.9995 \end{pmatrix} \end{aligned} \quad (26)$$

$$\begin{aligned} \alpha_1 &= 0.3126, & \alpha_2 &= 0.1239, & \alpha_3 &= 0.1239 \\ \alpha_4 &= 0.1578, & \alpha_5 &= 0.1239, & \alpha_6 &= 0.1578. \end{aligned} \quad (27)$$

It can be seen from Eq. (26) that the seed point  $\mathbf{m}_1$  has been located at the first cluster center;  $\mathbf{m}_2$ ,  $\mathbf{m}_3$  and  $\mathbf{m}_5$  have simultaneously converged to the second cluster center, while  $\mathbf{m}_4$  and  $\mathbf{m}_6$  have gathered into the third center

point. Consequently, the proportion of each cluster is the summation of the  $\alpha_j$ s accompanying with the seed points which has located at the center of this cluster. That is, according to CPEM's result, the proportions of the three components are  $\alpha_1 = 0.3126$ ,  $\alpha_2 + \alpha_3 + \alpha_5 = 0.3717$  and  $\alpha_4 + \alpha_6 = 0.3156$ , respectively. Hence, it is evident that the  $\alpha_j$ s of the true mixture model have also been well estimated. This experiment verifies that both of the CEM and CPEM algorithms can do automatical model selections by converge all the seed points to the corresponding cluster centers when  $k$  is assigned larger than  $k^*$ .

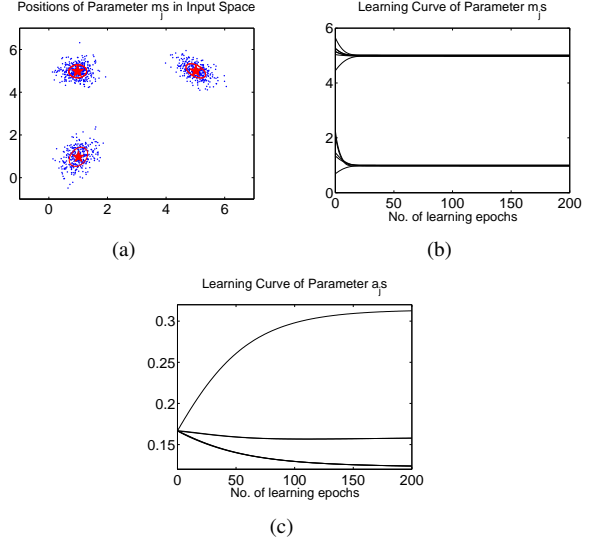


**Figure 5. The results obtained by CEM in experiment 2: (a) the learned positions of six seed points, (b) the learning curves of  $\mathbf{m}_j$ s, and (c) the learning curves of  $\alpha_j$ s.**

### 5.1.3 Experiment 3

To further analysis the characters of the proposed algorithms, we compare their performance with the RPEM [26] method, which is also generated based on the MWL learning framework and can automatically determine the cluster number by fading the redundant components out from the input region. 1000 data points were generated from a mixture of three 2-dimension Gaussian densities:

$$\begin{aligned} p(X|\Theta^*) &= 0.3G \left[ X \mid \begin{pmatrix} 1.0 \\ 1.0 \end{pmatrix}, \begin{pmatrix} 0.15, 0.05 \\ 0.05, 0.2 \end{pmatrix} \right] \\ &+ 0.4G \left[ X \mid \begin{pmatrix} 1.0 \\ 2.5 \end{pmatrix}, \begin{pmatrix} 0.15, 0.0 \\ 0.0, 0.15 \end{pmatrix} \right] \\ &+ 0.3G \left[ X \mid \begin{pmatrix} 2.5 \\ 2.5 \end{pmatrix}, \begin{pmatrix} 0.15, -0.1 \\ -0.1, 0.15 \end{pmatrix} \right]. \end{aligned} \quad (28)$$

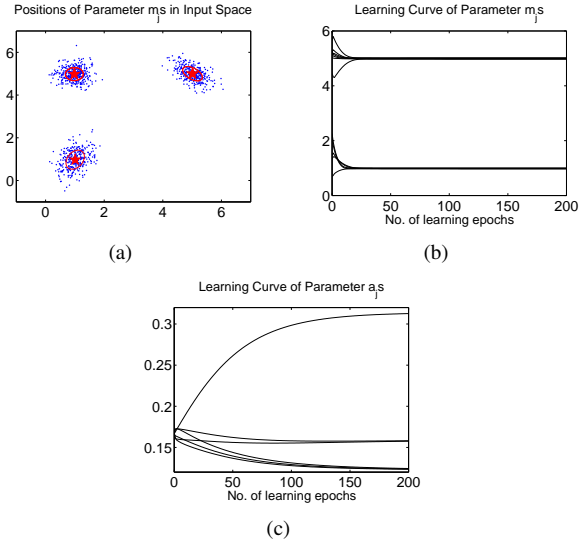


**Figure 6. The results obtained by CPEM in experiment 2: (a) the learned positions of six seed points, (b) the learning curves of  $m_j$ s, and (c) the learning curves of  $\alpha_j$ s.**

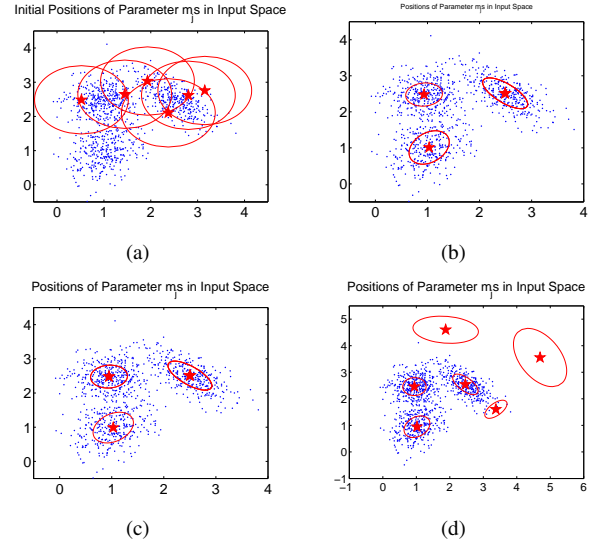


**Figure 7. The positions of six seed points marked by "★" in the input space in experiment 3: (a) the initial positions, (b) the positions learned by CEM, (c) the positions obtained by CPEM, and (d) the positions learned by RPEM.**

From Fig. 7(a) it can be observed that the data points generated from this mixture model are moderately overlapped. For each algorithm, the learning rate  $\eta$  and  $\eta_\beta$  were set at 0.001 and 0.0001, respectively. As shown in Fig. 7(a), six seed points with unitary covariance matrix were randomly localized in the input space. The CEM and CPEM algorithms had converged during 300 learning epochs while the RPEM method had cost 400 epochs. The learned positions of the seed points obtained by the three different approaches has been shown in Fig. 7. We can see that all of them have identified the true component number successfully and the parameters of the mixture model are also well estimated. Comparing the learning curves of  $m_j$ s showed in Fig. 8, we can find that CPEM has the best convergence rate among the three algorithms. Moreover, Fig. 9 has given out the learning curves of  $\alpha_j$ s obtained by variant methods, in which CPEM has also revealed its good performance.

Additionally, it is worth mentioning that although the RPEM can automatically select the true cluster number by driving the superfluous seed points away from the input space and converging the corresponding  $\alpha_j$ s close to zero, the discarded  $\alpha_j$ s can not reach zero exactly. Hence, the proportion of each component obtained by this method will always have a deviation from the true one. But this problem is not faced by the proposed algorithms.

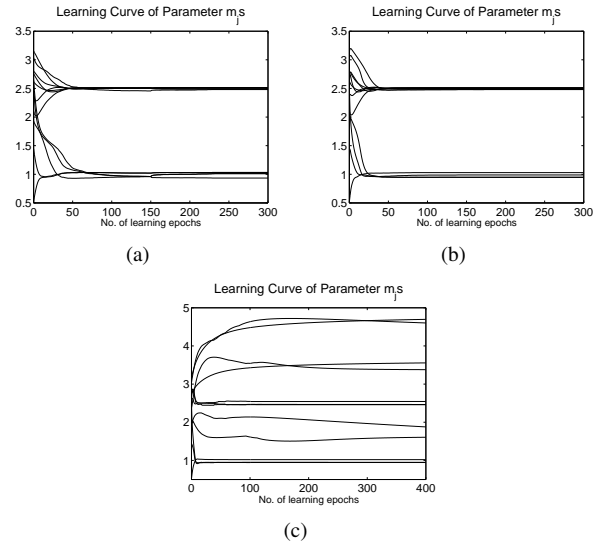


**Figure 8. The learning curves of  $m_j$ s obtained by (a) CEM, (b) CPEM, and (c) RPEM in experiment 3.**

#### 5.1.4 Experiment 4

In this experiment, we further investigate the performance robustness of CPEM to the initializations. Different from

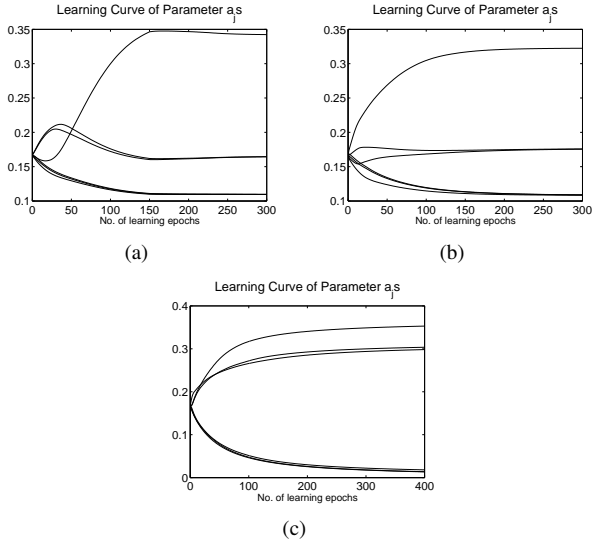


**Figure 9. The learning curves of  $\alpha_j$ s obtained by (a) CEM, (b) CPEM, and (c) RPEM in experiment 3.**

the previous experiments, we generated 1200 data points from a mixture of four bivariate Gaussian densities:

$$p(X|\Theta) = 0.3G[X|\mathbf{m}_1, \Sigma_1] + 0.2G[X|\mathbf{m}_2, \Sigma_2] + 0.2G[X|\mathbf{m}_3, \Sigma_3] + 0.3G[X|\mathbf{m}_4, \Sigma_4], \quad (29)$$

with

$$\begin{aligned} \mathbf{m}_1 &= (1.0, 1.0)^T & \mathbf{m}_2 &= (1.0, 2.5)^T \\ \mathbf{m}_3 &= (2.5, 1.0)^T & \mathbf{m}_4 &= (2.5, 2.5)^T \end{aligned}$$

and

$$\begin{aligned} \Sigma_1 &= \begin{pmatrix} 0.20, 0.05 \\ 0.05, 0.20 \end{pmatrix} & \Sigma_2 &= \begin{pmatrix} 0.15, 0.00 \\ 0.00, 0.15 \end{pmatrix} \\ \Sigma_3 &= \begin{pmatrix} 0.2, -0.05 \\ -0.05, 0.2 \end{pmatrix} & \Sigma_4 &= \begin{pmatrix} 0.15, 0.00 \\ 0.00, 0.15 \end{pmatrix} \end{aligned}$$

It can be observed from Fig. 10(a) that the four clusters are seriously overlapped and with variant proportions and shapes. In order to verify that CPEM is insensitive to the initial positions of seed points, we forcibly located seven highly centralized seed points which were gathered in the territory of one density component as shown in Fig. 10(a). After 400 learning epochs, the positions of density centers and the learning curves of  $\mathbf{m}_j$ s and  $\alpha_j$ s are shown in Fig. 10. The satisfactory results indicate the good performance of CPEM in this experiment. We can see that the initial positions of seed points have little influence on CPEM's efficiency.

Furthermore, we investigated the learning capability of CPEM when the number of seed points  $k$  was preassigned

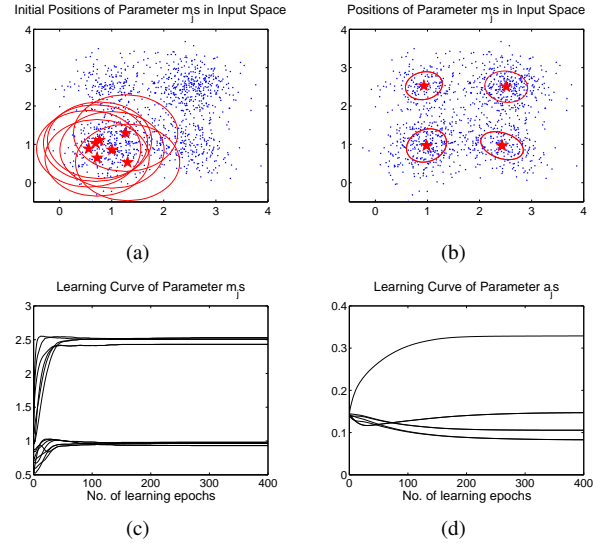


**Figure 10. (a) shows the initial positions of seven gathered seed points marked by "★" in the input space, (b) shows the center positions learned by CPEM, (c) shows the learning curves of  $\mathbf{m}_j$ s, and (d) shows the learning curves of  $\alpha_j$ s.**

much larger than the true component number. As shown in Fig. 11(a), we arbitrarily initialized 15 seed points in the input space. After 500 learning epochs, the experimental results obtained by CPEM are given out in Fig. 11(b) to Fig. 11(d). It can be observed that true component number as well as the density parameters have been accurately estimated. Hence, combining with the previous experiment, we can come to the conclusion that the CPEM method has a robust performance against the initialization of seed points.

## 5.2 Real Data Set Analysis

In this experiment, in order to investigate the practical effectiveness of the proposed algorithms, we utilized them to analyze the well known Iris data set, which can be achieved from the UCI Machine Learning Repository. This data set contains 150 instances coming from three different types of iris plants and each instance has 4 attributes. Supposing that the class label as well as the true number of clusters were unknown, we utilized the CEM and CPEM algorithms to do cluster analysis and compared their performance with the existing RPEM method. 10 seed points were randomly initialized in the input space and the experimental results, including the average cluster numbers and accuracy rate, obtained by different methods over 10 trials are summarized in Table 1. Notice that the success rate stands for the per-

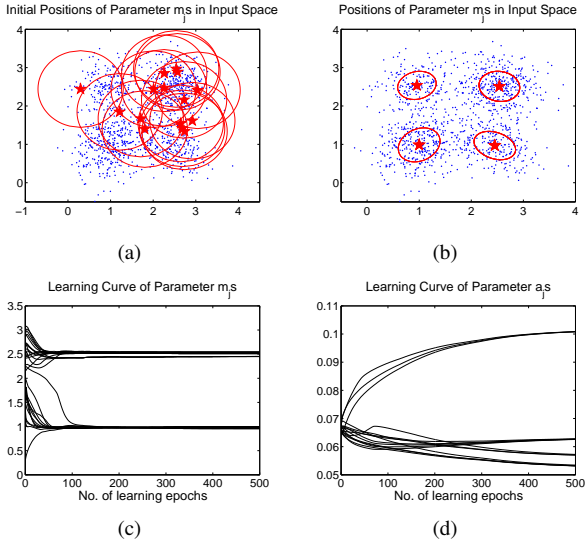


**Figure 11. (a) shows the initial positions of 15 seed points marked by "★" in the input space, (b) shows the center positions learned by CPEM, (c) shows the learning curves of  $m_j s$ , and (d) shows the learning curves of  $\alpha_j s$ .**

cent of identifying the true cluster number  $k^*$  over all trials and the accuracy is calculated only when  $k^*$  is achieved.

**Table 1. Experimental results of variant algorithms on Iris data set**

Methods	Cluster Numbers (mean±std)	Success Rate	Average of Accuracy
CEM	4.1000±1.5239	40%	0.8967
CPEM	3.3000±0.8233	60%	0.9147
RPEM	3.4000±0.5164	60%	0.8811

From this table, it can be observed that the performance of CPEM and RPEM is much more robust to different initializations because they have a higher success rate as well as a lower standard deviation. This result demonstrates the advantage of penalization mechanism. Moreover, although the component-number-detection abilities of CPEM and RPEM are similar to each other, the CPEM has a better clustering accuracy. It is indicated that the combination of cooperation and penalization mechanisms can give a better estimate of the density mixture's parameters.

### 5.3 Color Image Segmentation

The image segmentation capabilities of CEM and CPEM were investigated in this experiment in comparison with RPEM algorithm on two different color images. The segmentation was implemented in HSV color space. For each algorithm, we randomly initialized 20 seed points in the input space. Once the clustering process converged, we transform the result back into RGB color space and show the images in Fig. 12 and Fig. 13, respectively.

In the first experiment, segmentation was performed on the Dolphin image. After the cluster learning, 7 seed points were retained in the input space by RPEM while CEM and CPEM converged all seed points to 8 and 6 different cluster centers respectively. The obtained images are shown in Fig. 12(b) to Fig. 12(d). We can see that the image obtained by CPEM is much more legible and the profile of the dolphin is complete and accurate. Moreover, only in this image, the status and area of the splash are recognizable.

In the other experiment, Wolf image was utilized. This image contains a small object and the background is consist of snowfield and forest. After the clustering process, 6 cluster centers were learned by both CPEM and RPEM algorithms while 10 cluster centers were achieved by CEM. From Fig. 13(b) to Fig. 13(d), we can see that the snowfield and forest in the image obtained by CPEM are much more homogenous than the others. Additionally, it can be observed that in Fig. 13(d), the color of the wolf become the same with the forest, so the object nearly disappears into the background. But the profile of the wolf as well as its shadow is well preserved by CPEM in Fig. 13(c).

## 6 Conclusion

In this paper, we have investigated the implementation of competition and cooperation mechanisms under MWL learning framework and proposed a novel CEM algorithm for density mixture model learning through a specific weight design. The cooperation mechanism in CEM algorithm enables the winner generated from the competition of mixture components to cooperate with some other promising rivals to update to the current input together. Subsequently, the parameters of partial components are gradually converged to the same values and finally the number of components with variant parameters is exactly the component number of density mixture model fit to the given data set. Hence, CEM can do automatic model selection as long as the component number is preassigned larger than or equal to the true one. Moreover, in order to enhance the robustness of the proposed algorithm to the initialization, we further modified the previous presented weight design and accordingly generated a CPEM algorithm, in which the winning component not only cooperated with most promis-

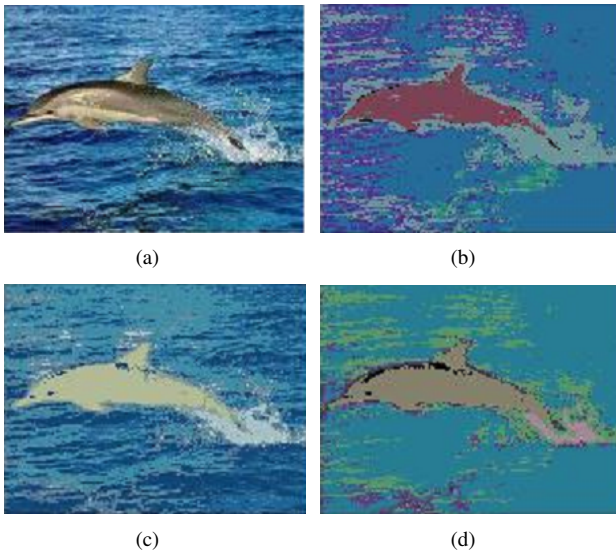


**Figure 12. (a) shows the "Dolphin" image, while (b), (c) and (d) show the segmented image obtained by CEM, CPEM and RPEM, respectively.**

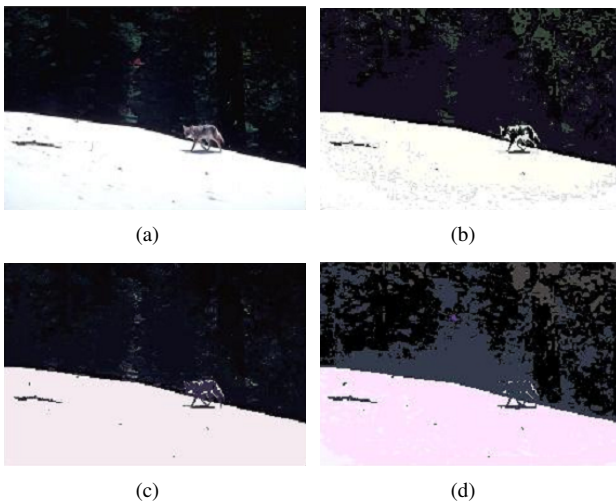


**Figure 13. (a) shows the "Wolf" image, while (b), (c) and (d) show the segmented image obtained by CEM, CPEM and RPEM, respectively.**

ing rivals but also penalized some other rivals with a dynamic strength. It has been found that the CPEM is insensitive to the initialization to a certain level and can give a good estimate of the density mixture's parameters as well as the component number. Numerical studies on synthetic and real data have shown the outstanding performance of

the proposed approaches.

## References

- [1] H. Permuter, J. Francos, and I. H. Jermyn, "Gaussian mixture models of texture and colour for image database retrieval," in *Proc. IEEE Int'l Conf. Acoustics, Speech, and Signal Processing*, vol. 3, 2003, pp. 569–572.
- [2] D. A. Reynolds and R. C. Rose, "Robust text-independent speaker identification using Gaussian mixture speaker models," *IEEE Trans. Speech and Audio Processing*, vol. 3, no. 1, pp. 72–83, 1995.
- [3] F. Jelinek, *Statistical Methods for Speech Recognition*. Cambridge: MA: MIT Press, 1998.
- [4] D. N. K. S. Nathan, J. R. Bellegarda, and E. Bellegarda, "On-line handwriting recognition using continuous parameter hidden markov model," in *Proc. IEEE Int'l Conf. Acoustics, Speech, and Signal Processing*, vol. 5, 1993, pp. 121–124.
- [5] A. M. A. E. R. K. Y. Yeung, C. Fraley and W. L. Ruzzo, "Model-based clustering and data transformations for gene expression data," *Bioinformatics*, vol. 17, pp. 977–987, 2001.
- [6] A. Dempster, N. Laird, and D. Rubin, "Maximum likelihood estimation from incomplete data via the EM algorithm," *J. Royal Statistical Soc. B*, vol. 39, pp. 1–38, 1977.
- [7] G. McLachlan and T. Krishnan, *The EM Algorithm and Extensions*. New York: John Wiley & Sons, 1997.
- [8] G. McLachlan and D. Peel, *Finite Mixture Models*. New York: John Wiley & Sons, 2000.
- [9] M. A. F. Figueiredo and A. K. Jain, "Unsupervised learning of finite mixture models," *IEEE Trans. Pattern Analysis and Machine Intelligence*, vol. 24, no. 3, pp. 381–396, 2002.
- [10] S. Roberts, D. Husmeier, I. Rezek, and W. Penny, "Bayesian approaches to Gaussian mixture modelling," *IEEE Trans. Pattern Analysis and Machine Intelligence*, vol. 20, no. 11, pp. 1133–1143, Nov. 1998.
- [11] J. Campbell, C. Fraley, F. Murtagh, and A. Raftery, "Linear flaw detection in woven textiles using model-based clustering," *Pattern Recognition Letters*, vol. 18, pp. 1539–1548, 1997.

- [12] A. Dasgupta and A. Raftery, "Detecting features in spatial point patterns with cluster via model-based clustering," *J. American Statistical Association*, vol. 93, pp. 294–302, 1998.
- [13] C. Fraley and A. Raftery, "How many clusters? which clustering method? answers via model-based cluster analysis," Department of Statistics, University of Washington, Seattle, WA, Technical Report 329, 1998.
- [14] J. Rissanen, "Modeling by shortest data description," *Automatica*, vol. 14, no. 5, pp. 465–471, Sep. 1978.
- [15] S. Marsland, C. J. Twining, and C. J. Taylor, "A minimum description length objective function for groupwise non-rigid image registration," *Image and Vision Computing*, vol. 26, no. 3, pp. 333–346, Mar. 2008.
- [16] C. S. Wallace and D. L. Dowe, "Minimum message length and kolmogorov complexity," *Computer J.*, vol. 42, no. 4, pp. 270–283, 1999.
- [17] N. Bouguila and D. Ziou, "Unsupervised selection of a finite dirichlet mixture model: An MML-based approach," *IEEE Trans. Knowledge and Data Eng.*, vol. 18, no. 8, pp. 993–1009, Aug. 2006.
- [18] H. Akaike, "A new look at the statistical model identification," *IEEE Trans. Automatic Control*, vol. AC-19, no. 6, pp. 716–723, Dec. 1974.
- [19] T. Bengtsson and J. E. Cavanaugh, "An improved akaike information criterion for state-space model selection," *Computational Statistics & Data Analysis*, vol. 50, no. 10, pp. 2635–2654, Jun. 2006.
- [20] H. Bozdogan, "Choosing the number of component clusters in the mixture model using a new informational complexity criterion of the inverse-fisher information matrix," in *Information and Classification*, O. Opitz, B. Lausen, and R. Klar, Eds. Springer Verlag, 1993, pp. 40–54.
- [21] N. Ueda, R. Nakano, Z. Ghahramani, and G. E. Hinton, "SMEM algorithm for mixture models," *Neural Computation*, vol. 12, pp. 2109–2128, 2000.
- [22] B. Zhang, C. Zhang, and X. Yi, "Competitive EM algorithm for finite mixture models," *Pattern Recognition*, vol. 37, pp. 131–144, 2004.
- [23] Y. Li and L. Li, "A novel split and merge EM algorithm for gaussian mixture model," in *Proc. Fifth Int'l Conf. Natural Computation*, 2009, pp. 479–483.
- [24] Z. W. Lu, Y. X. Peng, and H. Ip, "Gaussian mixture learning via robust competitive agglomeration," *Pattern Recognition Letter*, vol. 31, no. 7, pp. 539–547, 2010.
- [25] Y. M. Cheung, "A rival penalized EM algorithm towards maximizing weighted likelihood for density mixture clustering with automatic model selection," in *Proc. Int'l Conf. Pattern Recognition*, vol. 4, 2004, pp. 633–636.
- [26] Y. M. Cheung, "Maximum weighted likelihood via rival penalized EM for density mixture clustering with automatic model selection," *IEEE Trans. Knowledge and Data Eng.*, vol. 17, no. 6, pp. 750–761, 2005.
- [27] L. Xu, A. Krzyzak, and E. Oja, "Rival penalized competitive learning for clustering analysis, RBF net, and curve detection," *IEEE Trans. Neural Networks*, vol. 4, no. 4, pp. 636–648, Jul. 1993.
- [28] Y. M. Cheung, "Rival penalization controlled competitive learning for data clustering with unknown cluster number," in *Proc. 9th Int'l Conf. Neural Information Processing*, Nov. 2002, pp. 18–22.
- [29] Z. Y. Zhang and Y. M. Cheung, "On weight design of maximum weighted likelihood and an extended EM algorithm," *IEEE Trans. Knowledge and Data Eng.*, vol. 18, no. 10, 2006.
- [30] Y. M. Cheung, "A competitive and cooperative learning approach to robust data clustering," in *Proc. IASTED Int'l Conf. Neural Networks and Computational Intelligence*, 2004, pp. 131–136.
- [31] T. Li, W. J. Pei, S. P. Wang, and Y. Cheung, "Cooperation controlled competitive learning approach for data clustering," in *Proc. Int'l Conf. Computational Intelligence and Security (CIS'08)*, 2008, pp. 24–29.
- [32] Y. M. Cheung and H. Jia, "A cooperative and penalized competitive learning approach to Gaussian mixture clustering," in *Proc. 20th Int'l Conf. Artificial Neural Networks*, vol. 3, 2010, pp. 435–440.

# Music Emotion Retrieval Based on Acoustic Features

DENG Jie, Department of Computer Science  
Hong Kong Baptist University, Hong Kong  
jdeng@comp.hkbu.edu.hk

## Abstract

*Music emotion expresses inherent and high-level state of mind and spiritual quality. In this paper, a hierarchical framework is proposed, which consists of two layers: external layer that represents preliminary and superficial emotions and inherent layer that represents psychic and resonant emotions. According to these two layers, Resonance-Arousal-Valence (RAV) emotion model has been constructed. Five feature sets, including intensity, timbre, rhythm, pitch and tonality, and harmony, are extracted to represent music emotions in RAV model. In order to effectively represent emotions with extracted features, suitable weighting schemes are utilized to balance the difference of features. As each music clip may have rather complex emotions, supervised multiclass label model will be adopted to annotate emotions with emotion multinomial. Preliminary experiment results indicate that the proposed emotion model and retrieval approach are satisfied.*

**Index Terms:** Music emotion, music emotion retrieval, resonance, arousal, valence

## 1 INTRODUCTION

Music is an art form and language that encompasses mind, body, feeling, emotion, culture and other aspects of human beings. In this sense, music plays a vital role in people's daily life, not only relieving stress, but also cultivating sentiment. Since fast development of the Internet and digital devices, there are enormous amount of digital music services. Currently most of music retrieval approaches are based on the traditional metadata information such as the music title artist, genre, and album. Improved content-based approaches relying on melody, rhythm, timbre, harmony also strengthen the music retrieval. However, according to the study of musicology and psychology, emotion is the core component of music that expresses the inherent and high level spiritual quality and state of mind. It is a natural way in an attempt to describe feelings or emotions when people listen to music. Music emotion retrieval satisfies the

higher music inherent needs which have significant commercial and research promise.

As emotion is the complex psychological and physiological human subjective and experience, even though for the same music, different listeners may gain drastically different emotions. There are commonly two ways to indicate emotions expressed and induced by music [1]: categorical psychometrics and scalar/dimensional psychometrics. Categorical approach utilizes some emotional descriptors or adjectives to express music emotion. Scalar or dimensional approach measures emotions by scalar values or multidimensional matrices. Valence and Arousal are the two-dimensional representation mostly adopted in emotion. In this paper, an expanded three-dimensional emotion cube will be highly modeled to express music emotion. Resonance is defined as the third dimension that represents the influence or further spirit factor related valence and arousal. The abstract value of resonance is from self-destructive to self-constructive. Thus there are eight areas in the emotion cube forming eight emotion clusters. However, how to effectively reflecting the relationships between Resonance and Valence-Arousal is still a major problem.

In this paper, a hierarchical framework will be utilized to model music emotion. According to the Resonance-Valence-Arousal (RAV) model, music emotions are able to express in continuous format in the emotion cube. In order to represent music emotion intrinsically and naturally, music informative such as biography and context will be ignored. This paper mainly focuses on the acoustic features in classical music: intensity, timbre, rhythm, pitch and tonality. These five feature sets will be extracted to express the particular emotions of selected music. Thus, each given music emotion in RAV model will be computed by the above feature sets. As every music clip may contains one or multiple emotion descriptors or words, supervised multiclass label model and K-Nearest Neighbour approach will be adopted to annotate music emotions with predefined labels. Thus, each music in the database is represented by emotion multinomial and labels. Therefore, this paper proposes a query-by-emotion-text system for retrieval music by ranking them according to compute the distance from

the query emotion multinomial to the previously computed music emotion multinomial in database.

The paper is structured as follows. A brief review of related work is provided in Section II. Section III presents continuous music emotion RAV model. Section IV gives the five feature sets extracted for representing music emotions, including intensity, timbre, rhythm, pitch and tonality, and harmony. Section V deals with music emotion annotation based on RAV values, and music emotion retrieval will be addressed in detail. Experiments and performance evaluations will be conducted in Section VI. Section VII is the conclusions.

## 2 RELATE WORK

The key factor in music emotional retrieval is to measure and represent emotions induced by music. The most common way to describe emotions is to use adjectives such as pleased, peaceful, and sad. However, the amount of these adjectives related to emotion is enormous. Tim Pohle et al. [1] evaluated frequently used audio features for emotion categories (soft / neutral / aggressive) and mood classification (happy / neutral / sad). Music Information Retrieval

**Table 1. MIREX MOOD CATEGORY**

Clusters	Mood Adjectives
Cluster1	passionate, rousing, confident,boisterous, rowdy
Cluster2	rollicking, cheerful, fun, sweet, amiable
Cluster3	literate, poignant, wistful, bittersweet, autumnal
Cluster4	humorous, silly, campy, quirky, whimsical, witty
Cluster5	aggressive, fiery,tense, intense, volatile,visceral

Evaluation eXchange (MIREX) has already classified music mood into five categories by clustering mood labels for popular music, shown in Table 1. The disadvantage of above approach is that emotions are only discrete.

Thayer utilizes two-dimensional Valence-Arousal (VA) space model, dividing emotions into four quadrants. Thus, the emotion in the plane is regarded as a continuous variable. However, the major problem is how to effectively compute valence and arousal values of the given music. Youngmoo E. Kim et al. [8] has already given a state of the art review of music emotion recognition. LuLei et al. [7] has proposed a hierarchical framework to automatically detect music emotions based on the four clusters derived by VA emotion model. Yi-HsuanYang et al. [2, 3, 4] have presented music emotion classification approaches, where categorical and scalar emotion models and regression approach on continuous valence and arousal values were adopted to classify music emotions. Tuomas Eerola et al. [9] compared

two common paradigms of music emotion representation above mentioned, and proposed multidimensional and multivariate regression model to predict music emotions and moods.

Feature extraction from the audio music is another key factor to effectively formulate music emotion. Nicola Orio in [11] has already introduced basic music elements and concepts such as Pitch, Intensity, Timbre, Tempo, Tonality, Rhythm, Melody and Harmony, which are able to represent the music contents. LuLei et al. [7] extracted intensity related to 'arousal', timbre and rhythm which are related to 'valence' to build emotion model. Intensity is computed by audio energy, and Mel-frequency cepstral coefficients (MFCC) is utilized to represent timbre. Average correlation peak and the ratio between the average peak and valley strength are extracted to represent rhythm. Youngmoo E. Kim et al. [8] also summarized acoustic features such as RMS energy, spectral shape and contrast, zero-crossing rate, rhythm strength and regularity influencing emotions.

Though less paper addressed music emotion retrieval in the past few years, there are still other related approaches available. Douglas Turnbull et al. [12, 13, 14] presents supervised multiclass labeling model to semantically annotate music and retrieve music by rank-order music through calculating Kullback-Leibler (KL) divergence. According to the previous works, this paper will utilize effective and efficient approaches to construct a query-by-emotion-text music emotion retrieval system.

## 3 MUSIC EMOTION MODEL

As mentioned above, one major impediment to music emotion retrieval is how to effectively build emotion model. On the basis of musicology and music psychology, this paper proposes a hierarchical emotion framework, which consists of two layers: external layer that represents preliminary and superficial emotions and inherent layer that represents psychic and resonant emotions. According to these two layers, Resonance-Arousal-Valence (RAV) emotion model has been constructed. Valence ranging from low to high and arousal ranging from negative to positive reflect external layer. Resonance with range from self-destructive to self-constructive describes internal layer. Therefore, this RAV emotion model can be regarded as music emotion cube that consists of eight subspaces which represent continuous emotions. The three-dimensional RAV model is illustrated in Figure 1.

After above music emotion model constructed, music emotion denotes  $E = \langle cluster_i, rav_i \rangle$ , where  $cluster_i$  represent in the  $i$ -th area of the cube, and  $rav = \langle resonance, arousal, valence \rangle$ . Suppose arousal  $\alpha$ , valence  $\nu$  are independent variables, resonance  $\gamma$  has a relationship with  $\alpha$  and  $\nu$ , and unknown factors denoted as  $\beta$ , thus  $\gamma$  represents by

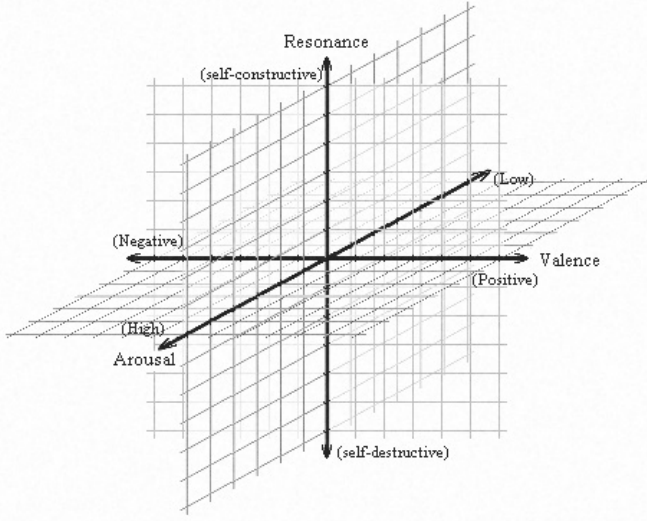


Figure 1. Three-dimensional RAV model

$\gamma \approx f(\alpha, \nu, \beta)$ . Given a set  $C = \{c_1, c_2, \dots, c_i\}$  to describe these eight cubes, thus music emotion will be represent as  $E = \langle c_i, (f_i(\alpha, \nu, \beta), \alpha_i, \nu_i) \rangle$ . In order to simplify computation, each valence and arousal value is confined with  $[-1, 1]$ . Thus, Figure 2 shows distribution of RAV values

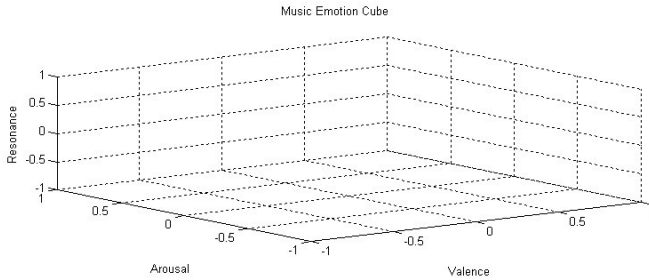


Figure 2. Distribution of RAV values

in the music emotion cube. In this cube, how to calculate  $\gamma$  is a key procedure. Multivariate linear regression will be utilized to estimate  $\gamma$  in the following equations.

$$\gamma = b_0 + b_1 * \alpha + b_2 * \nu + b_3 * \beta + \epsilon, \epsilon \sim N(0, \epsilon^2) \quad (1)$$

where  $b_0, b_1, b_2, b_3$ , and  $\epsilon$  are unknown independent parameters, and  $-1 < \alpha, \nu < 1$ . Least square method is utilized to estimate above parameters.

$$Q = \sum_{i=1}^n (\gamma_i - b_0 - b_1 * \alpha_i - b_2 * \nu_i - b_3 * \beta_i)^2 \quad (2)$$

Then, calculate the partial derivatives with respect to these four parameters, after that these four partial derivatives are

assigned to zero as follows.

$$\frac{\partial Q}{\partial b_i} = 0, \text{ where } i = 0, 1, 2, 3 \quad (3)$$

According to the above equations, estimated parameters  $b_0, b_1, b_2, b_3$  gained are used to construct predicted regression function.

## 4 FEATURE EXTRACTION

As mentioned above, feature extraction is the key issue to effectively emotion retrieval. Different attributes such as timbre, intensity, rhythm, harmony and different acoustic features such as spectrum and tempo represent different emotional expressions. This paper extracts features of intensity, timbre, rhythm, pith, tonality, and harmony to express emotions in RAV model.

### 4.1 Intensity Features

Intensity represents loudness or volume of a sound, which is correlated to arousal such as high intensity arousing excited or joyful feelings or emotions, while low intensity arousing neutral or depress emotions. The acoustic feature often utilized to describe intensity is energy. The average energy of the given music clip can be computed by the following equation.

$$rms = \sqrt{(x_1^2 + x_2^2 + \dots + x_n^2)/n} \quad (4)$$

Low energy and high energy are also used to express percentage of frames contrasted to average energy. Thus, three factors contributing to arousal are root mean square energy, low energy and high energy.

### 4.2 Timbre Features

Timbre is a key and comprehensive factor to express different emotions. A special timbre inspires valence response from the listener. The acoustic features often utilized to represent timbre are MFCC, spectral shape and contrast. Figure 3 shows the process of computation of audio mu-

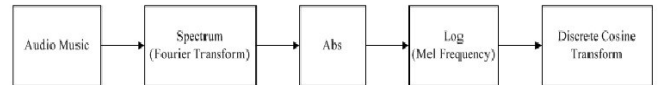


Figure 3. MFCC computation process

sic MFCCs. Spectral shape features contains brightness, rolloff and roughness, effectively representing valence extent. Brightness is often measured by spectral centroid, and

rolloff is the frequency that 85% distribution concentrated is less than. Spectral contrast focuses on peak, valley, and zero-cross, which reflect valence change. Thus, this paper utilizes seven factors to represent timbre: MFCCs, brightness, rolloff, roughness, spectral peak and valley, and zero-cross.

### 4.3 Rhythm Features

Rhythm reflects different duration over steady background of the beat, which often related to rhythm strength, regularity, and tempo. A particular rhythm inspires valence response from the listener. The acoustic features utilized to represent rhythm are onset, fluctuation, event density, and tempo, which consist of four factors contributing to rhythm in this paper.

### 4.4 Pitch and Tonality Features

Pitch represents fundamental frequency of a sound. High or low pitch represents different emotional expression such as active or inactive. Tonality reflects hierarchical pitch relationship between center key. They all inspire emotion response from listeners. Thus, in RAV model, pitch and tonality are regarded as the sub-factors of arousal. This paper utilizes four factors such as pitch, key, key strength, and mode to express pitch and tonality features.

### 4.5 Harmony Features

Harmony refers to simultaneously perform tones or chords that represent mixture sounds such as muddy, sharp, and smooth. Harmony is based on consonance, compared with RAV model, harmony is corresponding to resonance. This paper employs two factors such as fusion and roughness to represent music harmony.

### 4.6 Feature Representation

After above introduced features extracted from the audio music, music emotion will be represented by combining above five feature sets. According to RAV model, intensity, pitch and tonality features are correlated to arousal; Timbre and rhythm are related to valence; Resonance has a relationship with harmony, and depends on valence and arousal. Thus, in RAV model, there are seven-dimension arousal values, eleven-dimension valence values, and two-dimension resonance values. In order to simplify computation, any numeric features have been normalized to the range [-1, 1].

## 5 Music Emotion Retrieval

This paper utilizes query-by-emotion-text to retrieval music, thus music in the database have to be annotated with

emotion words firstly. Considering each music emotion may containing multiple emotion adjectives such as comfortable, happy, supervised multiclass labeling model will be adopted in music emotion annotation. After that music emotion retrieval are able to implement conveniently.

### 5.1 Music Emotion Annotation

Music annotation can be regarded as a multi-class or multi-label problem in which each emotion descriptor or words  $\omega \in \nu$  represents a class and the goal is to label each music with a subset of emotion words predefined. This paper adopts K-Nearest Neighbor (KNN) approach to annotate music emotions. Given a music training set  $M = \{m_1, m_2, \dots, m_i\}$ , these examples are described by RAV emotion model. Each training example is labeled with one or multiple emotion labels predefined. Thus, music emotion annotation is to label an unknown emotion of music  $q$  with these emotion labels. In the training sample, music with the same emotion labels will be selected as  $k$  nearest neighbors. The expectation of music emotion  $x_i$  with the same labels will be computed by these  $k$  nearest neighbors in RAV model.

$$x_i = \frac{1}{k} \sum_{i=1}^k (\gamma_i, \alpha_i, \nu_i) \quad (5)$$

Suppose one music clip with multiple emotion labels, there is no priority among these labels, a discounting factor  $\varrho$  is utilized to adjust expectation of music emotions.

$$x_i = \frac{1}{m} \sum_{i=1}^m (\gamma_q, \alpha_q, \nu_q) + \varrho * \frac{1}{n} \sum_{i=1}^n (\gamma_p, \alpha_p, \nu_p) \quad (6)$$

where  $m + n = k$ , for each  $x_i \in M$ , the distance between  $x_i$  and  $q$  is calculated as follows:

$$d(q, x_i) = \|(\gamma_q, \alpha_q, \nu_q) - (\gamma_{x_i}, \alpha_{x_i}, \nu_{x_i})\| \quad (7)$$

Emotion multinomial is defined by standard deviation between  $q$  and  $x_i$  in RAV model as follows.

$$var(q) = \sqrt{\frac{1}{k} \sum_{i=1}^k (rav_q - rav_i)^2} \quad (8)$$

According to the emotion distance  $d(q, x_i)$  and emotion deviation  $var(q)$ , a threshold  $\delta$  is set to decide the emotion labels given to the novel music. Thus, supervised multiclass labeling based on KNN is able to effectively annotate music with multiple emotion words.

### 5.2 Emotion Retrieval

After music emotion annotation completed, it is very natural and convenient to retrieve music based on their emotions. In order to efficiently retrieve music, hash table data

structure is built to index music based on their emotions. Search keys are emotion labels such as comfortable, happy.

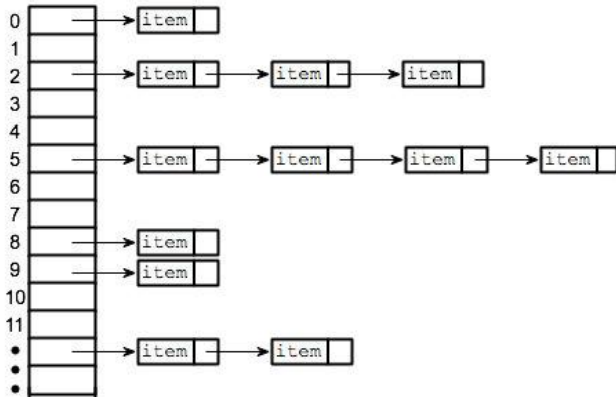


Figure 4. Hash Table Indexing

In the same search key, there may be many music stored in the gradually increasing order of emotion multinomials computed in Figure 4.

This paper uses query-by-emotion-text to construct music emotion retrieval. When user enter a query string, a query multinomial is build  $\omega = \{\psi_1, \psi_2, \dots, \psi_n\}$ , suppose  $\psi_i$  is in the emotion label collections. More weights will be give words that appear earlier in the query sting, thus accurate query results will be returned in a reasonable way.

## 6 EXPERIMENTS

There are 150 classical music clips in the dataset, whose style contains concerto, sonata, symphony, and string quartet. These digital music clips in a uniform format, with sampling rate 22,050Hz, 16 bits, and mono channel. There are 24 predefined music emotions labels in three-dimension RAV models, and each cube contains 3 labels. These emotion labels are collected from music informative contexts, biographies, and descriptions, which are able to represent music emotions. MIRtoolbox and PsySound are useful tolls to extract acoustic features from audio music. After computation and normalization, these emotions of music clips are able to express in RAV model. Figure 5 shows the distribution of music emotion in cube 1, where all the extracted features values transformed in to RAV model and normalized between -1 and 1.

In music annotation process, k parameter is assigned to five. Thus table 2 shows the annotation precision, and retrieval precision and recall for one, two, and three music emotion labels. According to the observation, if more accurate feature values extracted form the audio, more accurate annotation and retrieval results will be gained.

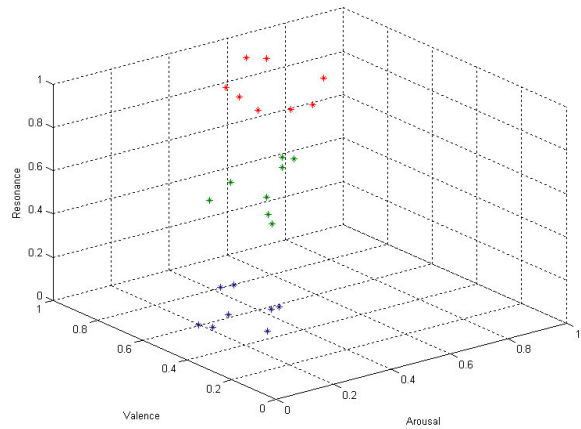


Figure 5. Emotion Distribution in Cube 1

Table 2. Annotation & retrieval results

Label Length	A - Precision	R - Precision	R - Recall
One label	0.6875	0.667	0.545
Two labels	0.5714	0.625	0.533
Three labels	0.5667	0.529	0.45

## 7 CONCLUSION

This paper proposes a hierarchical music emotion framework, which consists of two layers: external layer that represents preliminary and superficial emotions and inherent layer that represents psychic and resonant emotions. Based on these two layer, a reasonable music emotion model Resonance-Arousal-Valence (RAV) model is constructed. The advantage of this model is that it represents emotions in a three-dimensional and continuous space. Music will be placed in the RAV space based on the extracted feature sets: intensity, timbre, rhythm, pitch and tonality, and harmony. Supervised multiclass labeling based on KNN method is adopted to effectively annotate music with multiple emtion labels. Emotion multinomial and hash table are used to retrieve music based on query-by-emotion-text. The preliminary experiment results show satisfied performance.

## References

[1] T. Pohle, E. Pampalk, and G. Widmer: Evaluation of Frequently Used Audio Features for. Classification of Music into Perceptual Categories. CBMI 2005

[2] Yi-Hsuan Yang, Chia Chu Liu, Homer H. Chen: Music

emotion classification: a fuzzy approach. *ACM Multimedia* 2006:81-84

- [3] Yi-Hsuan Yang, Yu-Ching Lin, Ya-Fan Su, Homer H. Chen: Music Emotion Classification: A Regression Approach. *ICME* 2007:208-211
- [4] Yi-Hsuan Yang, Yu-Ching Lin, Heng Tze Cheng, I-Bin Liao, Yeh-Chin Ho, Homer H. Chen: Toward Multimodal Music Emotion Classification. *PCM* 2008:70-79
- [5] Konstantinos Trohidis, Grigorios Tsoumakos, George Kalliris, Ioannis P. Vlahavas: Multi-Label Classification of Music into Emotions. *ISMIR* 2008:325-330
- [6] Xiaoyu Sun, Yongchuan Tang: Automatic Music Emotion Classification Using a New Classification Algorithm. *ISCID* 2009:540-542
- [7] Lie Lu, Dan Liu, HongJiang Zhang: Automatic mood detection and tracking of music audio signals. *IEEE Transactions on Audio, Speech & Language Processing (TASLP)* 14(1):5-18 (2006)
- [8] Youngmoo E. Kim and Erik M. Schmidt and Raymond Migneco and Brandon G. Morton and Patrick Richardson and Jeffrey Scott and Jacquelin A. Speck and Douglas Turnbull: Music Emotion Recognition: A State of Art Review. *ISMIR* 2010
- [9] Tuomas Eerola, Olivier Lartillot, Petri Toiviainen, "Prediction of Multidimensional Emotional Ratings in Music From Audio Using Multivariate Regression Models", *International Conference on Music Information Retrieval*, Kobe, 2009
- [10] Emotional responses to music: The need to consider underlying mechanisms. *Behavioral and Brain Sciences*, 31, pp 559-575
- [11] Nicola Orio: Music Retrieval: A Tutorial and Review. In: *Foundations and Trends in Information Retrieval*, Volume 1 Issue 1, 2006
- [12] Douglas Turnbull, Luke Barrington, D. Torres, Gert R. G. Lanckriet: Semantic Annotation and Retrieval of Music and Sound Effects. *IEEE Transactions on Audio, Speech & Language Processing (TASLP)* 16(2):467-476 (2008)
- [13] Douglas Turnbull, Luke Barrington, David A. Torres, Gert R. G. Lanckriet: Towards musical query-by-semantic-description using the CAL500 data set. *SIGIR* 2007:439-446
- [14] Douglas Turnbull, Luke Barrington, Gert R. G. Lanckriet: Modeling music and words using a multi-class naive Bayes approach. *ISMIR* 2006:254-259

# THE INVESTIGATION OF AN EXEMPLAR-BASED HIDDEN MARKOV MODEL FOR LIPREADING

*Yiu-ming Cheung and Xin Liu*

Department of Computer Science, Hong Kong Baptist University, Hong Kong SAR, China  
{ymc, xliu}@comp.hkbu.edu.hk

## ABSTRACT

In this paper, we investigate an exemplar-based hidden markov model that represents the lip motion activity using visual cues for lipreading. Both the geometric shape parameters and contour-constraint spatial histogram in each image frame are chosen as the feature vector. Then, a set of exemplars associated with the HMM is learned jointly to serve as a typical representation of a speech utterance. Based on these exemplars, the high-dimensional image features are transformed to the lower dimensional ones, namely Frame to Exemplar Distance (FED) vector. Subsequently, a continuous HMM is trained using such FED vector sequences for learning and recognition. Experiments show the promising results of the proposed method.

**Index Terms**— Exemplar, HMM, lip motion, lipreading, FED vector.

## 1. INTRODUCTION

Automatic recognition of speech by using the visual information of the lip motion activities, namely lipreading or visual speech recognition, has received considerable attention in the community because of its wide applications in audio-visual speech recognition, human-computer interfaces, the command-control applications [1] and so forth. In general, lipreading can not only help the hearing impaired people understand the speech contents, but also has been demonstrated to improve the speech recognition rate especially in the presence of acoustic noise [2].

In the last decade, a few techniques such as neural Networks (NN) [3], fuzzy logic and hidden Markov model (HMM) [4, 5] have been developed for lipreading recognition problem. As the lip motion activities contain strong temporal correlation between the adjacent observed frames. Hence, among these methods, HMM has been the most popular approach because its underlying state structure can successfully model the temporal variations in lipreading signals. Usually, to model these signals, a left-right HMM is employed because the underlying state sequence associated with the model has the property of adapting to the states transferring to the next or staying at the same as the time increases. In special, before

performing the recognition task, the parameters of the HMM need to be sufficiently learned.

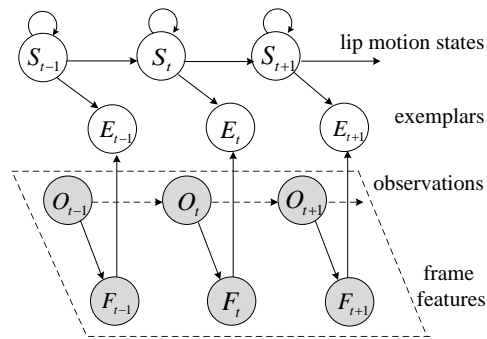


**Fig. 1.** An exemplar-based HMM framework.

The successful utilization of HMM to achieve lipreading lies in a closer investigation of the physical process of the corresponding lip motion activity. Usually, the lip movements of a speech activity can be modeled as a transition across several hidden states. However, almost all the existing HMM-based methods do not give a clear representation of these states, where each state can be exemplified by an exemplar like in [6]. The advantage of using an exemplar to model the state is that it represents what the observed output would be at its associated state. The temporal correlation between the adjacent states can be model by the HMM, which gives an appropriate way to describe such a dynamic process. Meanwhile, The utilization of an HMM will update each state's exemplar to better represent the observed data. Hence, these exemplars can be associated with the states of the HMM where the switch from one exemplar to another one can be represented by transition probabilities between states. This type of methods have been successfully applied to human identification [6], gesture recognition [7], action recognition [8] and so forth. In a nutshell, the exemplars associated with the HMM can jointly serve as a typical representation of a lip motion activity of a speech utterance as well. Consequently, it can generate a group of low dimensional distance vectors between the test frames and these exemplars, namely Frame to Exemplar Distance (FED) vector. With these FED vectors, we can train a continuous HMM incorporated the pre-learned

transition probabilities for recognition.

In this paper, we investigate an exemplar-based HMM framework inspired by the works of Amit Kale et.al [6] for lipreading as shown in Fig. 1. Both the geometric shape parameters and contour-constraint spatial histogram are chosen as the feature vector to represent each frame. We model the states corresponding to every lip motion activity in terms of exemplars, and the dynamical aspect described by transition between these states using the transition matrix. Then, we can obtain a group of FED vectors and compute the likelihood for learning and recognition. The experiments show the promising results of the proposed approach.

## 2. THE EXEMPLAR-BASED HMM FRAMEWORK

In this section, we only consider the speaker-dependent case. Let the video databases consist of frame sequences of  $S$  speech elements. The HMM model for the  $s^{th}$  speech is modeled by  $\lambda_s = (A_s, B_s, \pi_s)$  with  $N$  number of hidden states. The model  $\lambda_s$  is built from the observation sequence  $\mathcal{O}_s = \{O_1^s, O_2^s, \dots, O_{T_s}^s\}$  with its corresponding feature vector denoted as  $\mathcal{F}_s = \{F_1^s, F_2^s, \dots, F_{T_s}^s\}$ , where  $T_s$  is the total number of frames in a sequence of the  $s^{th}$  speech element,  $A_s$  is the transition matrix, and  $\pi_s$  is the initial distribution. The parameter  $B_s$  represents the probability distribution of a feature vector conditioned on the state index, i.e., the set of  $\{P_1^s(\cdot), P_2^s(\cdot), \dots, P_N^s(\cdot)\}$ . The probability distribution is defined in terms of a set of exemplars, where the  $j^{th}$  exemplar is a typical representation of the  $j^{th}$  state. The exemplars for the  $s^{th}$  speech are denoted as  $\mathcal{E}_s = \{E_1^s, E_2^s, \dots, E_N^s\}$ . The superscript corresponding to the index of the speech element is dropped for simplicity. The motivation behind using an exemplar-based model is that the recognition can be based on the FED vector measured between the observed frame feature and the exemplars. The distance metric is crucial in this framework.  $P_j^s(F_t)$  is defined as a function of  $D(F_t, E_j^s)$  representing the distance of the observed feature vector  $F_t$  from the  $j^{th}$  exemplar of the  $s^{th}$  speech element:

$$P_j^s(F_t) = \frac{\alpha}{\sqrt{\pi}} \cdot e^{-\alpha \cdot D(F_t, E_j^s)}. \quad (1)$$

During the training phase, the model is built for all the speech elements, indexed by  $s = 1, 2, \dots, S$ . An initial estimate of  $\mathcal{E}_s$  and  $\lambda_s$  is formed from  $\mathcal{O}_s$ , and these estimates are refined iteratively. It is noteworthy that  $B$  is completely defined by  $\mathcal{E}$ , in which  $\alpha$  is fixed beforehand. We can iteratively estimate  $A$  and  $\pi$  by using the Baum-Welch algorithm [9] and keeping  $\mathcal{E}$  fixed. The algorithm to re-estimate  $\mathcal{E}$  is determined based on the distance metric. During the testing phase, given speech model  $\lambda = \{\lambda_1, \lambda_2, \dots, \lambda_S\}$  and the testing speech sequence of length  $L$ , i.e.,  $\mathcal{F} = \{f_1, f_2, \dots, f_L\}$ , we can obtain its traversing path of  $\mathcal{Q} = \{q_1, q_2, \dots, q_L\}$ , where  $q_t$  is the state index at time  $t$ . It can thus obtain the most likely serial ID of the speech element as follows:

$$ID = \arg \max_{1 \leq s \leq S, \mathcal{Q}} P[\mathcal{Q} | \mathcal{F}, \lambda_s]. \quad (2)$$

## 3. THE PROPOSED APPROACH TO LIPREADING

### 3.1. Feature Extraction

It is well known that the visual cues of lip movement contain the important speech relevant information. To perform lipreading, we need to obtain the appropriate visual speech features from the recorded image sequences. In the last decade, various sets of visual features have been proposed for representing each image frame, which can be roughly classified into two categories: contour-based features and area-based ones. In the contour-based feature, i.e., geometric shape parameters such as mouth area, perimeter, height and width derived from binary mouth image, can be chosen as the visual features [10]. In the area-based case, image transforms of the region of interest (ROI) such as PCA, DWT and DCT have also been utilized for visual feature extraction [5]. Often, the contour-based and area-based features jointly together give a more significant visual features [4].

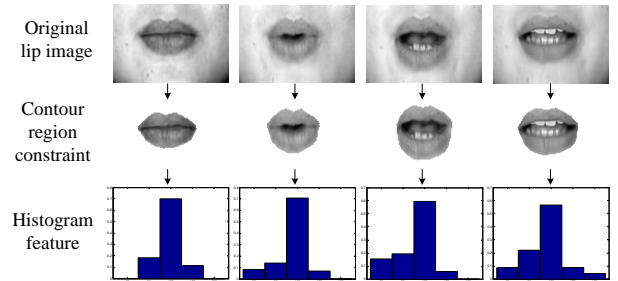


**Fig. 2.** The contour-constrained spatial histogram (CCSH) feature of lip sequence.

In this paper, we firstly extract the lip contour with a 16-point lip model constraint [11], and then compute geometric shape parameters, i.e.,  $\{L_1, L_2, L_3, L_4, L_5, L_6, L_7, L_8\}$  and mouth area  $\Delta A$  to model the contour-based feature denoted as  $V_{CF}$ . The temporal variations of the geometric shape parameters can be utilized to describe the lip motion activities. Meanwhile, to reduce the computational complexity that caused by image transforms and avoid variations that outside the lip region, we utilize an effective area-based spatial feature, namely contour-constrained spatial histogram (CCSH) feature denoted as  $V_{AF}$ , which is simple but very effective to represent the area feature among the lip movements. After extracting the lip contour of each frame, it is easy to obtain a contour-constrained mouth region and compute the spatial histogram with  $b$  bins in grey level case. We select the gray-scale image distribution with centers specified by  $\{B_1, B_2, \dots, B_b\}$ . The first bin includes the data between the minimum grey value and  $\frac{1}{2} \cdot (B_1 + B_2)$  while the last bin includes

the data between the  $\frac{1}{2} \cdot (B_{b-1} + B_b)$  and the maximum grey value. As the teeth, tongue and black hole are always appeared in oral cavity during the speech. Such a feature can better reflect the variations of intensity distribution during the lip movements as shown in Fig. 2. For the experiments, the geometric shape parameters are normalized with respect to the corresponding values of the first lip frame in sequence. The CSSH feature is normalized against its entire mouth area enclosed by the lip contour at each frame as shown in Fig. 3.

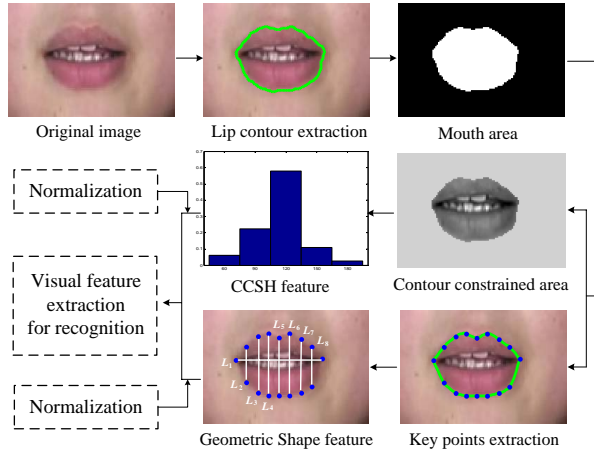


Fig. 3. Visual feature extraction.

### 3.2. Initialize the Exemplar and HMM parameters

In order to obtain a good estimate of the exemplars and the transition matrix to represent lip motion activity, we firstly need to obtain an initial estimate of both the exemplars and transition matrix from the observation speech sequence, and then we can consecutively refine the estimates. According to the above-mentioned framework, the initial estimate for the exemplars, i.e.,  $\mathcal{E} = \{E_1^0, E_2^0, \dots, E_N^0\}$  has the Markov property that the only transitions between them are from the  $j^{th}$  state to either itself ( $j^{th}$ ) or the next state ( $j \bmod N + 1$ ) incrementally. Usually, the initial probabilities  $\pi_j$  are set to be equal to  $1/N$ . A corresponding initial estimate of the transition matrix  $A^0$  can be set as follows:

$$A_{j,k}^0 = \begin{cases} 0.5, & k = j \text{ or } j \bmod N + 1 \\ 0, & \text{otherwise.} \end{cases} \quad (3)$$

During the repetition of the speech collection in training set, it can be considered as the sense that the lip movements transit between its associated exemplars. Intuitively, each utterance can be regarded as a ‘‘cycle’’, and it is possible to model this cycle by several distinctive hidden states. Therefore, in order to get a good initial estimate of  $E_j$  belonging to the  $j^{th}$  state from the observed feature vectors, we can partition each cycle into  $N$  temporally adjacent parts of approximately equal size. The  $j^{th}$  state can be visualized to be generated from the  $j^{th}$

parts of all the cycles. For instance, the training sequence is given by  $\mathcal{V} = \{V_1, V_2, \dots, V_T\}$ , and it can be divided into  $K$  cycles. The  $k^{th}$  cycle is denoted by the frames in terms of the set  $\mathcal{V}_k = \{V_{S_k+1}, V_{S_k+2}, \dots, V_{S_k+L_k}\}$ , where  $S_k$  and  $L_k$  are the index of the first frame and length of the  $k^{th}$  cycle, respectively. Therefore, the exemplar attributed to the  $j^{th}$  state consists of the frames with the indices  $S_k + (j-1) \cdot \frac{L_k}{N} + 1, \dots, S_k + j \cdot \frac{L_k}{N}$ . Therefore, the initial exemplar for each state can be computed by averaging the feature vectors of all the training cycles as shown in Fig. 4.

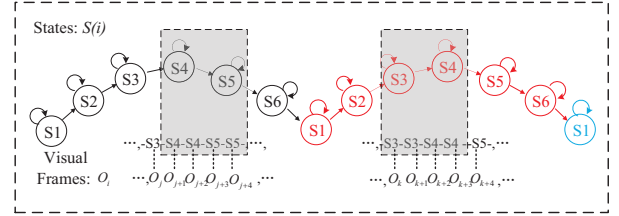


Fig. 4. The estimate of the initialized states during the repetition of the speech utterance.

### 3.3. Learn the Exemplar and HMM parameters

The iterative refining of the pre-initialized parameters is performed in the two steps. In the first step, the feature vectors are clustered iteratively according to the most likely state they originated through a Viterbi evaluation [9] using the current values of the exemplars and the transition matrix. Subsequently, the exemplars for representing the hidden states are re-estimated from these clusters. Using the current values of the exemplars  $\mathcal{E}^{(i)}$  and the transition matrix  $A^{(i)}$ , the Viterbi decoding algorithm [9] is performed on the training sequence  $\mathcal{V}$  to obtain the most probable path  $Q = \{q_1^{(i)}, q_2^{(i)}, \dots, q_T^{(i)}\}$ , where  $q_t^{(i)}$  is the state at the time  $t$ . Hence, the set of observation indices with its corresponding observations generated from state  $j$  is given by  $T_j^{(i)} = \{t : q_t^{(i)} = j\}$ . Subsequently, we have a new set of frames for re-estimating each state, and select the exemplars so as to maximize the probability as follows:

$$E_j^{(i+1)} = \arg_E \max \prod_{t \in T_j^{(i)}} P(V_t | E). \quad (4)$$

The actual method for maximizing the probability in Eq. 4 depends on minimizing a distance function like in Eq. 1, the following equation is thus obtained:

$$E_j^{(i+1)} = \arg_E \min \sum_{t \in T_j^{(i)}} D(V_t, E). \quad (5)$$

As introduced in feature extraction section, two different feature vectors are jointly employed to model the visual lip movement information. We thus model the probability in terms of FED vector between the frame feature vector  $F_t$  and exemplar  $E_j^s$  of the  $s$  speech element using a non-uniform

weighted distance measure  $\mathcal{D}_t^j[F_t, E_j^s]$ , which serves as a lower dimensional representation of the frame at time  $t$ , i.e.,

$$\mathcal{D}_t^j[F_t, E_j^s] = \sum_{p \in V_{CF}} (f_p^t - e_p^s)^2 + \frac{1}{\delta} \cdot \sum_{q \in V_{AF}} \frac{(f_q^t - e_q^s)^2}{f_q^t + e_q^s} \quad (6)$$

The parameter  $\delta$  is manually chosen so that the  $\chi^2$  distance of the spatial histograms and squared Euclidean distance of the geometric feature are of approximately the same magnitude. The parameter  $\delta$  is fixed across all categories. Therefore, the update of the  $j^{\text{th}}$  element of the exemplar estimated from the observed frame sequence is given as follows:

$$E_j^{(i+1)}(j) = \frac{1}{|T_j^{(i)}|} \sum_{t \in T_j^{(i)}} V_t(j) \quad (7)$$

In the second step, if  $\mathcal{E}^{(i+1)}$  and  $A^{(i)}$  are computed beforehand,  $A^{(i+1)}$  can be calculated using the Baum-Welch algorithm [9]. Therefore, we can successively refine the estimates of the HMM parameters along this line through a training process, which usually takes only a few iterations to obtain an appropriate estimate [6].

### 3.4. Recognition Phase

In the recognition phase, the test lip sequences of each speech element are performed using the same image processing operations as the training sequence to extract the visual features in each frame. The likelihood between the test feature vectors and pre-learned exemplars can thus be modeled in terms of the FED vector using the distance metric. With these vectors for each test speech sequence, we can obtain the most probable ID as formulated in Eq. 2 through the exemplar-based HMM framework for recognition.

## 4. EXPERIMENTAL RESULTS

To evaluate the performance of the proposed lipreading algorithm, a database consisting of 10 isolated English digits (0 to 9) uttered by eleven different individuals (6 males and 5 females) has been established. All speakers were asked to repeat each digit twenty times under the uniform lighting condition. Each utterance was recorded at the same rate and contained 30 color lip frames per second. Eight utterances in each digital were selected as a training set while the remaining twelve utterances for testing. We learned the exemplars and HMM parameters through the training set. According to the experiments tested on the database, by a rule of thumb, the bins [60, 90, 120, 150, 180] were selected appropriately. The parameter  $N$  and  $\delta$  were set at 6 and 0.2, respectively.

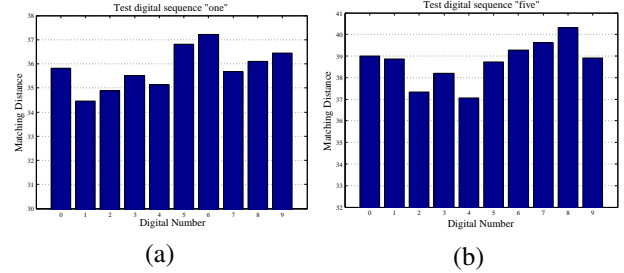


**Fig. 5.** Successful lipreading examples. (a) Test sequence “one”. (b) Test sequence “five”.

**Table 1.** The recognition accuracy.

Digital	Accuracy rate		Digital	Accuracy rate	
	rank 1	rank 3		rank 1	rank 3
0	75.8%	87.1%	5	90.9%	97.7%
1	92.4%	100%	6	76.5%	83.3%
2	81.8%	88.6%	7	86.4%	94.7%
3	90.2%	95.5%	8	82.6%	91.7%
4	85.6%	93.2%	9	78.8%	89.4%

Two successful recognition examples obtained using the proposed approach are shown in Fig.5. It can be clearly seen that the test sequences of the digit “one” and “five” have correctly matched the corresponding numbers, which have the minimum matching distance among all digital numbers. Table 1 list the details of the recognition accuracy of the each digit in the experiments. It can be found that the accuracy rates of digit “one”, “three” and “five” are all over 90% when selecting Rank 1 for reference. Furthermore, all the test sequences of the digit “one” have been successfully recognized when selecting Rank 3, and the accuracy rates of another digits, i.e., “four”, “seven” and “eight”, are all higher than 90%. Therefore, this type of method can greatly minimize the ranges for further lipreading recognition problems.

## 5. CONCLUSION

This paper investigates an exemplar-based HMM for lipreading. Both the geometric shape parameters and spatial histogram have been chosen to represent the visual feature vector of every image frame in lip sequence. The exemplars associated with the HMM jointly serve as a typical representation of the lip motion activity that can lead to satisfactory recognition rates. Experiments have shown the promising results. It is worth noting that we just integrate two discriminative features for application in this framework, which brings the great expectation that the multiple discriminative features can also be embedded into this framework as well for better recognition results.

## References

- [1] I. Matthews, T. F. Cootes, J. A. Bangham, S. Cox, and R. Harvey, "Extraction of visual features for lipreading," *IEEE Transactions on Pattern Analysis and Machine Intelligence*, vol. 24, no. 2, pp. 198–213, 2002.
- [2] X. Zhang, R. M. Mersereau, M. Clements, and C. C. Broun, "Visual speech feature extraction for improved speech recognition," in *Proc. IEEE International Conference on Acoustics, Speech, and Signal Processing*, 2002, vol. 2, pp. 1993–1996.
- [3] A. Rogozan and P. Deleglise, "Visible speech modelling and hybrid hidden markov models/neural networks based learning for lipreading," in *Proc. IEEE International Joint Symposia on Intelligence and Systems*, 1998, pp. 336–342.
- [4] H. E. Cetingul, Y. Yemez, Erzin Engin, and A. M. Tekalp, "Discriminative analysis of lip motion features for speaker identification and speech-reading," *IEEE Transactions on Image Processing*, vol. 15, no. 10, pp. 2879–2891, 2006.
- [5] G. Potamianos, H. P. Graf, and E. Cosatto, "An image transform approach for hmm based automatic lipreading," in *Proc. International Conference on Image Processing*, 1998, pp. 173–177 vol.3.
- [6] A. Kale, A. Sundaresan, A. N. Rajagopalan, N. P. Cuntoor, A. K. Roy-Chowdhury, V. Kruger, and R. Chellappa, "Identification of humans using gait," *IEEE Transactions on Image Processing*, vol. 13, no. 9, pp. 1163–1173, 2004.
- [7] A. Elgammal, V. Shet, Y. Yacoob, and L. S. Davis, "Learning dynamics for exemplar-based gesture recognition," in *Proc. IEEE International Conference on Computer Vision and Pattern Recognition*, 2003, vol. 1, pp. I–571–I–578 vol.1.
- [8] D. Weinland, E. Boyer, and R. Ronfard, "Action recognition from arbitrary views using 3d exemplars," in *Proc. International Conference on Computer Vision*, 2007, pp. 1–7.
- [9] L. R. Rabiner, "A tutorial on hidden markov models and selected applications in speech recognition," *Proc. IEEE*, vol. 77, no. 2, pp. 257–286, 1989.
- [10] M. N. Kaynak, Zhi Qi, A. D. Cheok, K. Sengupta, Jian Zhang, and Chung Ko Chi, "Analysis of lip geometric features for audio-visual speech recognition," *IEEE Transactions on Systems, Man, and Cybernetics Part A: Systems and Humans*, vol. 34, no. 4, pp. 564–570, 2004.
- [11] S.L. Wang, W.H. Lau, and S.H. Leung, "Automatic lip contour extraction from color images," *Pattern Recognition*, vol. 37, no. 12, pp. 2375–2387, 2004.

# On Exploiting Low-Rank Structure of Human Motion for Computer Animation

Lai Yongquan

## Abstract

*Human motion is of high articulation and correlation. When a human motion sequence is represented by a matrix, it will be approximately low-rank. In this paper, we try to exploit this low-rank structure of human motion for computer animation. We first justify that human motion sequences of different styles commonly have a low-rank structure. Based on this justification and recently developed low-rank matrix completion theory, we show that incomplete human motion can be effectively reconstructed. We also demonstrate that a noise-corrupted motion can be nicely recovered. The contribution of this paper is twofold: 1) we conjecture and justify that human motion is of low-rank, and 2) We propose to exploit this structure to deal with human motion for computer animation and provide two toy experiments showing the effectiveness of exploiting this structure.*

## 1 Introduction

A well-known truth about human motion is that it is articulated: the entire motion is described by the movement of joints which are connected by inflexible bones. The movement of one joint is correlated with that of another. If we record the trajectories of all joints and represent them as a motion matrix, then obviously this correlation is completely contained in the matrix. The problem is how to extract and model the correlation from the matrix. When the correlation is linear, the best property to be used will be the rank, which by definition measures the linear dependence of the rows (or columns) of a matrix. The higher the correlation is, the lower the rank will be. In cases when the correlation is non-linear, it is still tempting to approximate it by a linear one. Specifically, we are tempted to use a low-rank motion to (linearly) approximate the original motion. Hopefully, the approximation error is small, and in such case we say that the original motion has a approximately low-rank structure. For compactness reason, we ignore the word *approximately* from the phrase *approximately low-rank structure* in rest of this paper, and simply refer to it as *low-rank structure* even we know that the motion matrix is close to but not precisely

low-rank. In this paper, we conjecture that human motion of many (if not all) styles has a similar low-rank structure. We will soon justify this conjecture and propose to exploit this low-rank structure for applications in computer animation.

The rest of this paper is organized as follows. We introduce related work as well as notation and experimental setting in the final part of this section. In section 2, we discuss the low-rank structure of human motion. We then provide two toy applications of this property in section 3. In section 4, we conclude our work and discuss future work.

**Related work** Previous work concerning linear correlation of human motion is mostly based on Principle Component Analysis [12]. Non-linear correlation has also been considered and modeled by latent variable models [7, 14] and other non-linear dimension reduction methods [9].

Research on low-rank matrix completion theory and algorithms has become booming since a recent introduction of (non-smooth but convex) nuclear norm approximation to solve the originally NP-hard problem [6]. It can be shown that under some conditions, incomplete low-rank matrix can be recovered exactly using such approximation [5]. Many algorithms have been and are being developed, trying to solve the matrix completion problem as fast and as accurate as possible, see [4, 11] for examples.

Applications related to low-rank matrix completion can be found in realm of computer vision and image processing, see [8] for example. However, previous work on applying low-rank matrix completion theory to general motion modeling is very limited, and probably can only be found in [3, 13]. For human motion modeling, to our knowledge, there is no previous work on application of low-rank theory.

**Notation and experimental setting** We use  $\mathbf{y}_1, \dots, \mathbf{y}_n \in \mathbf{R}^m$  to denote a sequence of length- $n$  human motion, where each frame is an  $m$ -dimensional vector. We assume that  $n > m$ . A motion sequence is denoted by a matrix  $\mathbf{Y} = [\mathbf{y}_1, \dots, \mathbf{y}_n]$ . CMU mocap database [1] is used for analysis and experiments. Human skeleton model is described by the acclaim asf file. It consists of 31 joints including the root joint. The degrees of freedom (DOF) for each joint vary from 1 to 3. There are totally 62 DOF's for a skeleton. The motion data are stored in the acclaim amc file, which contains the recorded data for the DOF's. Our experiments are based on Matlab. A mocap toolbox [2] is used

for decoding asf/amc files and for displaying motion. Each motion sequence is represented by a  $m \times n$  matrix, where  $m = 31 \times 3 = 93$ . Although other motion sequences work equally well, for consistence, the motion used for all experiments except the first one (which involves multiple motion sequences) is a walking motion of trial 1, subject 7 from CMU mocap database.

## 2 Low-rank structure of human motion

In this section, we show that the human motion indeed has a low-rank structure. Notice that if an  $m \times n$  matrix is of rank  $r$ , it should have  $r$  positive singular values and  $\min\{m, n\}$  zero singular values. To check whether a motion  $\mathbf{Y}$  has a low-rank structure, we can find the spectrum of  $\mathbf{Y}^T \mathbf{Y}$  (or equivalently the singular values of  $\mathbf{Y}$ ), and observe how fast the spectrum decays.

We collect a large set of 112 motion sequences, each from one of the 112 subjects in CMU mocap database. The subjects cover various motion styles, including walking, jumping, running, complex dancing, etc. For each motion, its spectrum (denoted by  $\mathbf{s} \in \mathbf{R}^m$ ) is first calculated. The spectrum is further normalized such that  $\|\mathbf{s}\|_1 = 1$ . Finally the normalized spectrum of all 112 motion sequences is showed in figure 1. We can see that the spectrum of each motion concentrates in the bottom-left area and indeed decays very rapidly, implying that different styles of motion has a similar low-rank structure.

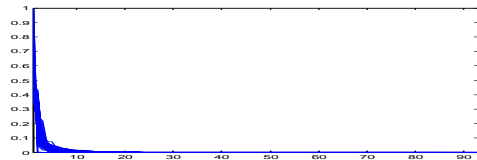


Figure 1. Normalized spectrum of various motion sequences

Another interpretation for such matrices which have fast-vanishing spectrum is that they consist of two components, namely, signal and noise. The signal component is precisely low-rank, while the additive noise component corrupts the signal and results in an *appropriately* low-rank observation. This interpretation is interesting, as we can see from figure 2 (accompany video clip 2-3), in which the motion is decomposed into a low-rank motion and a noise component. The decomposition process is: given a motion  $\mathbf{Y}$ , its singular value decomposition(SVD) is found and denoted by  $\mathbf{Y} = \mathbf{U}\Sigma\mathbf{V}^T$ ; the signal component is determined as  $\mathbf{S} = \mathbf{U}_{1:r}\Sigma_{1:r}\mathbf{V}_{1:r}^T$ , i.e., the  $r$  largest singular values are retained; the noise component is then given by  $\mathbf{Y} - \mathbf{S}$ . For the example shown in figure 2, we set  $r = 5$ (very low com-

pare to  $m$ ), and the resulting motion(top, green) still looks close to the original motion(top, blue), whereas the noise component (bottom, red) is small and looks random.

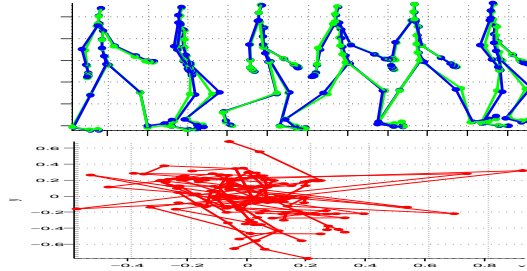


Figure 2. Decomposition of a motion into low-rank and noise components

Based on the above two experiments, we claim that with a high probability, human motion has a low-rank structure. Otherwise we could not have observed so many low-rank motion sequences of difference styles but not any high-rank ones.

One of the underlying reasons for this low-rank structure of human motion is that, with some approximation, the position of a joint could be determined linearly, given the positions of other joints directly related to it. For example, if we can observe the positions of thorax and upper-neck, the position of lower-neck(located in-between) can be estimated as the linear combination(with constant coefficients) of the two observed joints with small error, because the independent movement of lower-neck should be small, otherwise this movement will be weird for a normal walking sequence. Situations for other joints should follow this argument similarly, except that they may not necessarily be so extreme.

One might suspect that the low-rank structure comes from the periodicity property of human motion, other than the structure of human model. We argue that although it is true that periodicity can contribute to the low-rank structure of motion, it does not determine it. On one hand, even for complex and non-periodical motion like dancing, the spectrum still decays very fast; on the other hand, though depending on the sampling rate and motion speed, a period of motion usually spans more frames than dimension  $m$  of human model. Take the walking sequence for example, its first period spans from around frame 20 to 150, which is larger than  $m = 93$ . What's more, when  $n \geq m$ (as we assume), increasing the motion length  $n$  will decrease the rank unless the newly-added column is precisely in the column space of that motion matrix, which is a condition difficult to satisfy.

### 3 Applications

In this section, we provide two toy examples showing that the low-rank structure can be exploited for applications in computer animation.

**Reconstructing missing joints** We first consider the situation when some entries of the motion  $\mathbf{Y}$  are missing. Given only such an incomplete motion, and with no physical information(e.g. joint limit, bone length) or training set available, how can we recover the unknown entries? As we know from section 2 that human motion has low-rank structure, we can make use of low-rank matrix completion theory to estimate the missing entries.

For mathematical convenience, a design matrix  $\mathbf{P}$  is used to denote the missing entries of  $\mathbf{Y}$  where  $P_{ij} = 0$  indicates  $Y_{ij}$  is missing. The reconstructed motion is given by the solution to the following optimization problem with variable  $\mathbf{X}$ :

$$\begin{aligned} & \text{minimize} && \text{rank}(\mathbf{X}) \\ & \text{subject to} && \mathbf{P} \cdot \mathbf{X} = \mathbf{P} \cdot \mathbf{Y} \end{aligned}$$

Where the operator  $\cdot$  denotes the matrix dot product. This problem is generally NP-hard due to the rank objective, and is usually approximated using nuclear norm of  $\mathbf{X}$  in place of the rank objective. Despite that there are many off-the-shelf algorithms to solve the matrix completion problem, we adopt a recent one, namely, Singular Value Thresholding(SVT) [4], which can be interpreted as a subgradient algorithm for minimizing the weighted nuclear norm of  $\mathbf{X}$ . Figure 3 (accompany video clip 4-5) shows a recovery of 50% randomly selected missing joints(marked in red) from an incomplete motion(blue) with mean square error of 0.0253. The recovered motion(green) has a rank of 16.

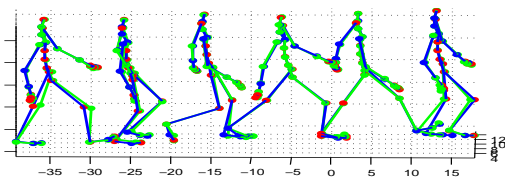


Figure 3. Recovering an incomplete motion

We can see that the even though up to 50 percent of motion data are missing, we can still recover the motion very well, and the resulting motion is low-rank. Potential applications related to this toy example can range from mocap data processing, motion editing to interactive motion synthesis. For instance, in one application, the animator sketches the positions of some joints, the computer then automatically completes the rest joints. This will greatly help reduce tedious and burdensome labor work. In another application, a novice animator modifies (nearly randomly) an

originally smooth motion. Fortunately, the computer discovers that the low-rank structure is destroyed. Then it automatically modifies the motion again to trade off between the low-rank constraint (so that the motion is not invalid) and the intention of the novice animator. In this case, the assumption is that for a motion to be good(in the sense of physically valid and well-coordinated), it must first satisfy the low-rank constraint. This assumption is reliable based on our discussion in section 2.

**Recovering corrupted motion data** Here we provide another toy example showing how to exploit the low-rank property for recovering human motion corrupted by noise. Given a motion  $\mathbf{Y}$ , we generate a zero-mean Gaussian noise  $\mathbf{G}$  with standard deviation denoted by  $\sigma$ . We then obtain the corrupted motion by  $\tilde{\mathbf{Y}} = \mathbf{Y} + \mathbf{G}$ . Based on  $\tilde{\mathbf{Y}}$  and a rough guess of standard deviation denoted by  $\hat{\sigma}$ , we estimate the original motion by solving the following optimization problem with variable  $\mathbf{X}$ :

$$\begin{aligned} & \text{minimize} && \text{rank}(\mathbf{X}) \\ & \text{subject to} && \text{Avec}(\mathbf{X}) \leq \mathbf{b} \end{aligned} \quad (1)$$

Where  $A \in \mathbf{R}^{k \times mn}$ ,  $\mathbf{b} \in \mathbf{R}^k$  are problem data.  $\text{vec} : \mathbf{R}^{m \times n} \rightarrow \mathbf{R}^{mn}$  is an operator that reshapes a matrix into a vector. (1) defines a linear inequality that imposes constraint on every entry of  $\mathbf{X}$ . For this experiment, we set  $\sigma = 0.5$ ,  $\hat{\sigma} = 2$ . The constraint for each entry  $(i, j)$  is  $-\hat{\sigma} + \tilde{Y}_{ij} < \mathbf{X}_{ij} < \tilde{Y}_{ij} + \hat{\sigma}$ . These constraints are encapsulated in (1). This problem is solved by SVT with minor modifications to ensure convergence. Figure 4 (accompany video clip 6-11) shows the corrupted motion(top) and the recovered motion(bottom, green) plotted with the original motion(bottom, blue). We can see that the corrupted motion is visually unbearable, while the recovered motion has a very good structure, except that it contains global vibrations. These vibrations can be eliminated using usual signal filtering techniques. We also provide a comparison with the result of directly using average filtering (which is inherently effective to deal with i.i.d. zero-mean Gaussian noise) in the accompany video. The compare is not shown here due to space limitation. From the video, we can see that the recovery using this approach is much better than moving average filtering.

Inspired from this toy example, we can seek for real applications in computer animation(similar to the first toy example) and in computer vision(e.g., human motion estimation and tracking).

### 4 Conclusion

This paper present our recent work on dealing with human motion capture data. We showed that human motion is approximately low-rank due to the intrinsic structure of

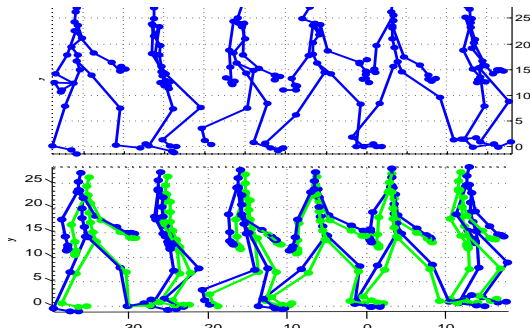


**Figure 4. Recovering a noise-corrupted motion**

human model itself. We also provided two preliminary examples which prove the effectiveness of exploiting the low-rank structure of human motion for computer animation. Notice that there is no physical information or auxiliary training set involved in the two examples. We believe that if we can incorporate physical model or training set into the optimization problem, much better results in the two experiments can be obtained. For instance, if we know the bone length, we can constrain the position of a missing joint to obtain a better estimate. This can be done by, for instance, forming a convex inequality constraint extracted from physical model to replace the constraint in (1). We leave this extension to future work.

One limitation of using this low-rank property might be the complexity issue. Although nuclear norm approximation relaxes the NP-hard problem to a convex optimization problem, the complexity is still relatively high. For toy example 1, it takes about 10 seconds to estimate 50 percent of missing entries for the motion of length 316 on a modern PC. One reason for that is, although what we have shown is a toy problem, it is still very challenging. Another reason might be that SVT is a first order algorithm that innately has a slow convergent rate. We could have used a second order algorithm such as interior point method [10], but for the purpose of this paper, SVT is sufficient. Anyway, we believe this limitation can be tackled either by the fast advancing optimization theory, or by other adjustment and assistance in real applications.

Another limitation is inherited from low-rank matrix completion theory, which tells us that when a whole row or column is missing, it is impossible to recover the incomplete matrix. This is not difficult to understand: to recover a low rank matrix, one solution will be to fill the missing row(or column) with all zeros. Without any addition information(e.g. axillary data or training set), it is very difficult not to arrive at this trivial and useless solution. Even with such information in hand, how to make use of it is another problem. Our future research will mainly focus on solving

this problem by using addition information and applying it to more sophisticated applications in computer animation .

## References

- [1] Cmu graphics lab motion capture database. <http://mocap.cs.cmu.edu/>.
- [2] Mocap toolbox for matlab.
- [3] A. Bartoli, V. Gay-Bellile, U. Castellani, J. Peyras, S. Olsen, and P. Sayd. Coarse-to-fine low-rank structure-from-motion. In *Computer Vision and Pattern Recognition, 2008. CVPR 2008. IEEE Conference on*, pages 1–8. IEEE, 2008.
- [4] J. Cai, E. Candès, and Z. Shen. A Singular Value Thresholding Algorithm for Matrix Completion. *Siam Journal of Optimization*, 20(4):1956–1982, 2010.
- [5] E. Candès and B. Recht. Exact matrix completion via convex optimization. *Foundations of Computational Mathematics*, 9(6):717–772, 2009.
- [6] M. Fazel. *Matrix rank minimization with applications*. PhD thesis, PhD thesis, Stanford University, 2002.
- [7] K. Grochow, S. Martin, A. Hertzmann, and Z. Popović. Style-based inverse kinematics. *ACM Transactions on Graphics (TOG)*, 23(3):531, 2004.
- [8] H. Ji, C. Liu, Z. Shen, and Y. Xu. Robust video denoising using low rank matrix completion. In *Computer Vision and Pattern Recognition (CVPR), 2010 IEEE Conference on*, pages 1791–1798. IEEE, 2010.
- [9] C. Lee and A. Elgammal. Human motion synthesis by motion manifold learning and motion primitive segmentation. *Lecture Notes in Computer Science*, 4069:464–473, 2006.
- [10] Z. Liu and L. Vandenberghe. Interior-point method for nuclear norm approximation with application to system identification. *SIAM Journal on Matrix Analysis and Applications*, 31(3):1235–1256, 2009.
- [11] R. Meka, P. Jain, and I. Dhillon. Matrix completion from power-law distributed samples. In Y. Bengio, D. Schuurmans, J. Lafferty, C. K. I. Williams, and A. Culotta, editors, *Advances in Neural Information Processing Systems 22*, pages 1258–1266. 2009.
- [12] A. Safonova, J. Hodgins, and N. Pollard. Synthesizing physically realistic human motion in low-dimensional, behavior-specific spaces. In *ACM SIGGRAPH 2004 Papers*, page 521. ACM, 2004.
- [13] L. Torresani, D. Yang, E. Alexander, and C. Bregler. Tracking and modeling non-rigid objects with rank constraints. In *Computer Vision and Pattern Recognition, 2001. CVPR 2001. Proceedings of the 2001 IEEE Computer Society Conference on*, volume 1. IEEE, 2001.
- [14] J. Wang, D. Fleet, and A. Hertzmann. Gaussian process dynamical models for human motion. *IEEE transactions on pattern analysis and machine intelligence*, 30(2):283–298, 2008.

# Texture analysis based on saddle points-based BEMD and MB-LBP

Jianjia Pan

Department of Computer Science, Hong Kong Baptist University

*jjpan@comp.hkbu.edu.hk*

## Abstract

*In this paper, a renovate texture analysis method is proposed. BEMD is a locally adaptive method and suitable for the analysis of nonlinear or nonstationary signals. The texture image can be decomposed to several BIMFs (intrinsic mode functions) by BEMD, which present new characters of the images. In this paper, firstly, we proposed a saddle points based BEMD to improve the original BMED, and then the new BEMD method is used to decompose the image to components (BIMFs). After then, the Multiscale Block Local Binary Patterns (MB-LBP) method is used to detect the feature from the BIMFs. Experiments shown the OI is reduced by the saddle points based BEMD, and the texture image recognition rate based on our method is better than the LBPV, MB-LBP, and RIFT.*

## 1. Introduction

Texture analysis is widely recognized as a difficult and challenging computer-vision problem. It provides many applications such as in remote sensing image and medical image diagnosis, document analysis, and target detection, etc.

Many methods have been used in texture analysis, among which, signal-processing methods try to characterize textures through filter responses directly. Gabor functions and wavelets transforms have been used in texture analysis. These multi-scale techniques intended to transform image into a representation in which both the spatial and frequency information is presented.

Recently, Empirical mode decomposition (EMD), developed by Huang [1], has been used for the texture analysis and face recognition [2]. EMD is a data driven processing algorithm which applies no predetermined filter. The EMD is based on the local characteristic scale of the data, which is able to perfectly analyze the nonlinear and nonstationary signals. The EMD has been used to analyze the two-dimensional signals, for example, the images, which are known as bidimensional EMD (BEMD). BEMD has present some better quality than Fourier, wavelet and other decomposition algorithms in extracting intrinsic components of textures because of its data driven property [2, 4]. It is different from the wavelet-based multiscale analysis that characterizes the scale of a signal event using pre-specified basis functions.

One research topic in BEMD is the extrema points detection method [7,8,9], which supply the supporting

points for the following interpolation. If the extrema detection loses some important supporting points, the BIMFs' orthogonality will be increase. In this paper we proposed to add the saddle points [19] as the supporting points for the interpolation, and give the definition of saddle points. Combined with the neighbor local maxima and minima points[18], three type points are treated in the same way. Experiments shown the OI is reduced by the saddle points added BEMD.

Based on the BEMD, we use the Multiscale Block Local Binary Patterns (MB-LBP) as the texture descriptor to detect the characteristic of texture images. The BEMD decomposed the original image to a new multi-scale components, in these new components, the Multiscale Block LBP can be better work than in the original images. Experiments shown the texture image recognition rate based on our method is better than the LBPV, MB-LBP, and RIFT.

## 2. Review of BEMD

EMD is first proposed by Huang et al. [1] for the processing of non-stationary functions. The tool decomposes signals into components called Intrinsic Mode Functions (IMFs) satisfying the following two conditions:

(a).The numbers of extrema and zero-crossings must either equal or differ at most by one;

(b).At any point, the mean value of the envelope defined by the local maxima and the envelope by the local minima is zero.

Huang [1] have also proposed an algorithm called 'sifting' to extract IMFs from the original signal  $f(t)$  as follows:

$$f(t) = \sum_{i=1}^N I_i(t) + r_N(t) \quad (1)$$

Where  $I_i(t)$ ,  $i=1,\dots,N$  are IMFs and  $r_N(t)$  is the residue.

The bidimensional EMD (BEMD) process is conceptually the same as the one dimension EMD, except that the curve fitting of the maxima and minima envelope now becomes a surface fitting exercise and the identification of the local extrema is performed in space to take into account for the connectivity of the points.

The main process of the BEMD can be described as:

(a).Locate the maximum and minimum points in the image  $I(k)$ ;

(b). Interpolation the surface between the all maxima (resp. minima) to build the envelope  $Xmax(k)$  and  $Xmin(k)$ ;

(c). Compute the mean envelope function  
 $Xm(k) = (Xmax(k) + Xmin(k))/2$ ; (2)

(d). Update the  $I(k) = I(k-1) - Xm(k)$ ;

(e). Check the stopping criterion

$$SD = \frac{1}{N} \sum_{k=0}^K \frac{(I_{i,j-1}(k) - I_{i,j}(k))^2}{I_{i,j-1}^2(k)} \quad (3)$$

if SD is larger than a threshold  $\epsilon$ , repeat the steps (a)-(e) with  $I(k)$  as the input, other wise,  $I(k)$  is an IMF  $d(k)$ ;

(f). Update the residual  $I(k) = I(k-1) - d(k)$ ;

(g). Input the  $I(k)$  to steps(a)-(e) until it can not be decomposed, and the last residual  $I(k) = r(n)$ .

After the BEMD, the decomposition of the image can be written as following form:

$$I(n) = \sum_{k=1}^K d_k(n) + r(n) \quad (4)$$

The  $d(k)$  is the IMFs (intrinsic mode functions) of the images, and  $r(n)$  is the residual function.

### 3. A new BEMD based on saddle points

With the intension of some difficult in implement BEMD, we have used some methods to improve the BEMD [18]. The local extrema are detected based on its neighbor and the extended parts are rebuilt based on self-similarity. The detail of the self-similar boundary processing and Delaunay triangulation surface interpolation method can be found in our previous work [18]. In this paper we proposed to add the saddle points as the supporting points for the interpolation.

The first step for BEMD is to detect the local extrema points. In one dimensional EMD, the extrema points are local maxima and minima points. In BEMD, except the local maxima or minima points, there will be some new conditions, one points may be a maxima point in one dimensional but a minima point in other dimensional. The saddle points are simultaneously a local maximum and local minimum point evaluated in different directions, and they also give important supporting features about the local variation of the original function [19].

*Definition 1:* a two dimensional function or a three dimensional curve  $u(x,y)$ , in the points  $(x_0, y_0)$  can be Taylor expansion :

$$u(x,y) = u(x_0, y_0) + \left(\frac{\partial u}{\partial x}\right)\Delta x + \left(\frac{\partial u}{\partial y}\right)\Delta y + \frac{1}{2} \left[ \frac{\partial^2 u}{\partial x^2} (\Delta x)^2 + 2 \frac{\partial^2 u}{\partial x \partial y} \Delta x \Delta y + \frac{\partial^2 u}{\partial y^2} (\Delta y)^2 \right] + \dots \quad (5)$$

Where

$$\Delta x = x - x_0, \Delta y = y - y_0,$$

If  $\left. \frac{\partial u}{\partial x} \right|_0 = 0, \left. \frac{\partial u}{\partial y} \right|_0 = 0$ , we have

$$u(x,y) - u(x_0, y_0) =$$

$$\frac{1}{2} \left\{ u_{xx} (\Delta x + \frac{u_{xy}}{u_{xx}} \Delta y)^2 + (\Delta y)^2 (u_{yy} - \frac{u_{xy}^2}{u_{xx}}) \right\} + \dots \quad (6)$$

the extrema point is *saddle point*, if  $u_{xy}^2 > u_{xx} u_{yy}$ .

In the normal BEMD methods [1,4], the mathematical morphology method is used to local the maxima and minima points, but we find the extrema points will be reduced fast. It means that, after two or three surface interpolations, the image will be too smooth to detect any significative extrema points. Neighbor location method [7] is used to detect the extrema in our method.

*Definition 2:*  $f[i,j]$  is a maximum (or. minimum) if it is larger (or. lower) than the value of  $f$  at the nearest neighbors of  $[i,j]$ .

Let  $X$  be an  $M \times N$  2D matrix represented by

$$X = \begin{bmatrix} x_{11} & x_{12} & \dots & x_{1N} \\ x_{21} & x_{22} & \dots & x_{2N} \\ \vdots & \vdots & \dots & \vdots \\ x_{M1} & x_{M2} & \dots & x_{MN} \end{bmatrix} \quad (7)$$

$x_{mn}$  is the element of  $X$  located in the  $m$ th row and  $n$ th column.

Let the window size for local extrema determination be  $(2w+1) \times (2w+1)$ , Then,

$$x_{mn} = \begin{cases} \text{Local Maximum} & \text{if } x_{mn} > x_{ij} \\ \text{Local Minimum} & \text{if } x_{mn} < x_{ij} \end{cases} \quad (8)$$

Where

$$x_{ij} = \{x \mid (m-w) : i : (m+w), (n-w) : j : (n+w)\} \\ i \neq m, j \neq n$$

From the experimental, we find  $3 \times 3$  window results in an optimum extrema map for a given image. The larger windows are also used in some conditions to reduce the computation, but as the mathematical morphology method, the extrema points will be reduced fast. As the experimental result shown in Part 5, the saddle points-add BEMD can reduce the OI of each BIMFs.

## 4. MB-LBP based on BEMD

### 4.1 Local Binary Patterns (LBP)

The LBP operator was originally developed for texture description. The operator assigns a label to every pixel of an image by thresholding the  $3 \times 3$ -neighborhood of each pixel with the center pixel value and considering the result as a binary number. Then the histogram of the

labels can be used as a texture descriptor. Figure 1 shows an example of the LBP operator[16].

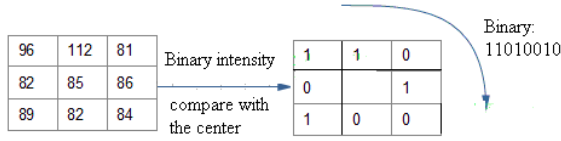


Figure 1 The LBP operator

The form of the resulting 8-bit LBP code can be defined as follows:

$$LBP(x_c, y_c) = \sum_{n=0}^7 s(i_n - i_c) 2^n \quad (9)$$

where  $i_c$  corresponds to the gray value of the center pixel  $(x_c, y_c)$ , into the gray values of the 8 neighborhood pixels, and function  $s(x)$  is dedined as:

$$s(x) = \begin{cases} 1 & \text{if } x \geq 0 \\ 0 & \text{if } x < 0 \end{cases} \quad (10)$$

From the above processing, the LBP present that it will be not affected by any monotonic gray-scale transformation which preserves the pixel intensity order in a local neighborhood. Each bit of the LBP code has the same significance level and that two successive bit values may have a totally different meaning.

To deal with textures at different scales, the LBP operator was later extended to use neighborhoods for different sizes [12]. The local neighborhood is extended to as a set of sampling points evenly spaced on a circle centered at the pixel to be labeled allows any radius and number of sampling points[14]. If a sampling point is not in the center of a pixel, it will be rebuilt by bilinear interpolation. The notation (P;R) is defined as the pixel neighborhoods which means P sampling points on a circle of radius of R. Figure 2 shows an example of circular neighborhoods.

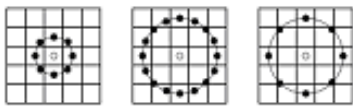


Figure2 The circular (8,1) (16,2) (8,2) neighborhoods

#### 4.2 MB-LBP based on BEMD

In this paper, the texture image is firstly decomposed by BEMD into several sub-images BIMFs, and then, the MB-LBP is used to extract those BIMFs.

BEMD is based on the local characteristic scale of the data, which is able to perfectly analyze the nonlinear and nonstationary signals. The details in the global and local information of the different script are extracted.

Because of the invariance of the LBP features, the LBP can be suit for the considerable gray-scale variations in

images and no normalization of input images is needed. LBP is a nonparametric method, which means that no prior knowledge about the distributions of images is needed.

We use the following notation for the texture features: Firstly, the original image  $I$  is decomposed to its BIMFs  $d_k$ :

$$I(n) = \sum_{k=1}^K d_k(n) + r(n) \quad (11)$$

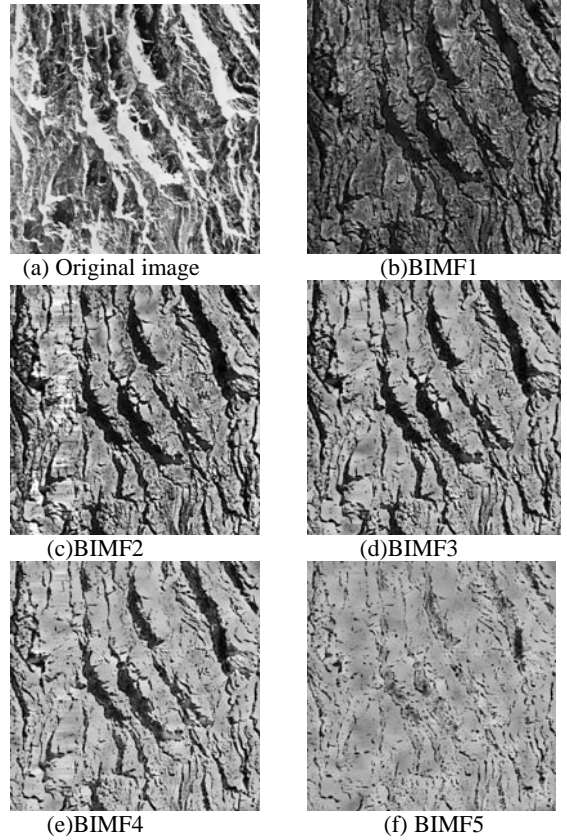


Figure 3 BIMFs of the texture image

Secondly, as we can find from the texture images' BIMFs (Fig 3), the first and the second BIMFs remain the mainly details of the original images, and the last BIMFs represent the information in a large scale, the characteristic points in those BIMFs are keep away from each other. Use the same size of LBP to detect the LBP code will be ineffective. In [12], the LBP operator was extended to use neighborhoods for different sizes. However, this extension is not enough for BIMFs because it is also based on points. To make the LBP feature more robust, Multiscale Block Local Binary Patterns (MB-LBP) is proposed [17]. The comparison operator between single pixels in LBP is replaced with comparison between average gray-values of subregions. Each sub-region is a square block containing neighboring pixels. The whole filter is composed of 9 blocks. And the value of pixel is replaced by the average of the block pixels.

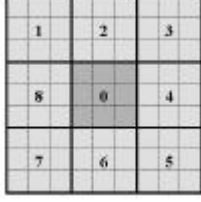


Figure 4 The 9×9 MB-LBP operator. In each sub-region, average sum of image intensity is computed. These average sums are then thresholded by that of the center block.

In our experiment, the 1st and 2nd BIMF is detected by the 3×3 LBP, the 3rd and 4<sup>th</sup> BIMF is detected by 9×9 MB-LBP, and the 5<sup>th</sup> BIMF is detected by 15×15 MB-LBP. Thirdly, as the Ref[17] points that the MB-LBP codes' statistical is different from the original LBP. The uniform pattern of MB-LBP is changed.

Denote  $f_s(x, y)$  as an MB-LBP feature of scale  $s$  at location  $(x, y)$  computed from images. Then histogram of the MB-LBP feature  $f_s(\cdot, \cdot)$  over a certain image  $I(x, y)$  can be defined as:

$$H_s(l) = 1_{\{f_s(x,y)=l\}}, \quad l = 0, \dots, L-1 \quad (12)$$

where  $1_{(S)}$  is the indicator of the set  $S$ , and  $l$  is the label of the MB-LBP code.

To reflect the uniform appearance of MB-LBP, the statistically effective MB-LBP (SEMB-LBP) set of scale  $s$  is defined as follows[17]:

$$SEMB-LBP_s = \{l | \text{Rank}[H_s(l)] < N\} \quad (13)$$

where  $\text{Rank}[H_s(l)]$  is the index of  $H_s(l)$  after descending sorting, and  $N$  is the number of uniform patterns.

Lastly, features are detected from the MB-LBP:

The different Multiscale Block LBP  $EMLBP_{i,s}^u(P,R)$  for BIMF <sub>$i$</sub>  are combined with weighting rules:

$$WEMLBP = \sum_{i=1}^n w_i * EMLBP_{i,s}^u(P, R) \quad (14)$$

Where  $EMLBP_{i,s}^u(P,R)$  indicate the MB-LBP corresponding to the BIMF <sub>$i$</sub> , and  $w_i$  is computed based on the each BIMFs' energy.

$$w_i = \frac{En_{imfi}}{\sum_{i=1}^N En_{imfi}} \quad (15)$$

$$En_{imfi} = \sum_{i=0}^{255} f_i p(f_i) \quad (16)$$

## 5. Experimental results

### 5.1 The new BEMD decomposition result

In this section, we present the experimental results of the image to decompose by using saddle points based BEMD. Image can be regarded as nonlinear signal in two-dimensional. The BEMD can decompose the signals

adaptively so it is suitable for analyzing the image. The proposed BEMD create a filter bank when applied to the texture images.

The orthogonality index (OI), has been proposed for IMFs in [1], the extended formula for two dimensional is defined as follows:

$$OI = \sum_{x=1}^M \sum_{y=1}^N \left( \frac{\sum_{i=1}^{K+1} \sum_{j=1}^{K+1} C_i(x, y) C_j(x, y)}{\sum C^2(x, y)} \right) \quad (17)$$

A low value of the OI indicated a good decomposition in terms of local orthogonality among the IMFs [4, 7]. The texture image's OI by our proposed method and some other methods are shown in the Table 1.

Methods	OI	Consuming time (s)
Nunes[8]	0.0034	73.64
Linderhed [9]	0.0031	65.81
Our pervious method[18]	0.0025	46.37
Our new method	0.0021	51.26

Table 1. Compared result of Orthogonality index (OI) and the consuming time

As the Table 1 shown, our new method can reduce the OI compare with [8], [9] and our pervious approach [18], which improves the BEMD method. The consuming time is higher than our pervious method but still lower than [8] and [9].

### 5.2 BEMD combined with MB-LBP feature for texture image recognition

The Brodatz database is a widely used for texture recognition. It consists of 111 images. Following the same processing in previous approaches [15, 20], each class image is partitioned into nine non-overlapping fragments, for a total of 999 images. Each image is on the gray level of 0-255. As Lazebnik and many authors point [15], the wide variety of Brodatz textures, combined with a certain degree of subjectivity in assigned texture classes makes the Brodatz database a particularly challenging and interesting platform for performance analysis.

The classifier is based on the correlation nearest-neighbor classifier. The proposed feature is compared with MB-LBP[17], LBPV [13], RIFT[15].

Classification Accuracy				
MB-LBP	LBPV (8,1)	LBPV (8,2)	RIFT	WEMLBP
0.7568	0.8258	0.7883	0.7628	0.8468

Table 2 Classification accuracy of proposed WEMLBP in the Brodatz database, compared with MB-LBP, LBPV, RIFT

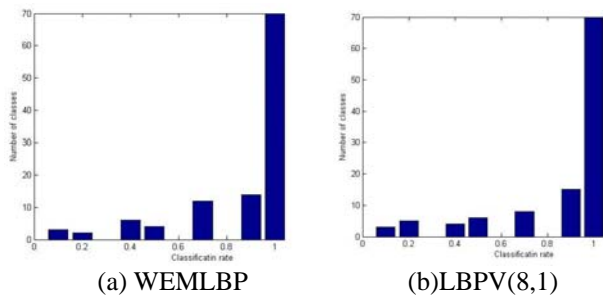


Figure 5 Histogram of classification rates (WEMLBP and LBPV(8,1)) for all 111 classes.

Table 2 show recognition results for outputs of WEMLBP using the new BEMD and MB-LBP. The original MB-LBP[17], LBPV [13] and RIFT[15] methods are used in the same database. By comparing the classification rate, we can see that the proposed WEMLBP method gives better performance than MB-LBP, LBPV and RIFT method. BEMD decomposed the texture image into BIMFs, and the Multiscale Block processing is suit for BIMFs' multiscale decomposition. The experimental results shown that the Multiscale Block LBP can be better work in the BIMFs than in the original images.

At the same time, from the Table 2, we can find WEMLBP and LBPV(8,1) produce very similar results. Figure 5 give us a more detailed means of performance analysis. It shown a histogram of classification rates for all 111 classes obtained by putting three images from each class into the training set. Comparing those histograms, the WEMLBP can achieve more classes in higher classification rate and fewer classes in low classification rate.

## 6. Conclusion

Texture analysis is widely recognized as a difficult and challenging computer-vision problem. In this paper, a new global-local feature is proposed for texture analysis. Firstly, a new BEMD method based on saddle points is proposed, which can reduce the OI of BIMFs. And then the new BEMD decompose the image to different BIMFs, which present different scale information of the original image. After, the MB-LBP method is used to detect the local information of BIMFs. Experiments shown the texture image recognition rate based on our method is better than the LBPV, MB-LBP, and RIFT.

In the following work, we will improve the features to be adaptive to more databases and use this feature for texture segmentation.

## References

- [1] N. E. Huang, Z. Shen, S. R. Long, M. C. Wu, et. "The empirical mode decomposition and the Hilbert spectrum for nonlinear and non-stationary time series analysis". Proceedings of Royal Society. Lond, (A) vol.454, pp:903-1005.1998
- [2] J.C.Nunes, Y. Bouaoune, E. Delechelle, O.Niang, Ph. Bunel. "Image analysis by bidimensional empirical mode decomposition". Image and Vision Computing Vol.21(12) , pp:1019-1026, November 2003
- [3] C.Damerval, S.M Meignen, and V.Perrier. "A fast algorithm for bidimensional EMD", IEEE signal processing letters, vol.12,no.10, pp 701-704, 2005
- [4] N.E.Huang, M.L.C.Wu, S.R.Long, "A confidence limit for the EMD and Hilerbet spectral analysis", Proceeding of the royal society A, vol 459., pp 2317-345, 2003
- [5]P. Flandrin, G. Rilling and P. Goncalves. "Empirical mode decompositionas a filter bank". IEEE Signal Processing Letters, vol.11(2),pp:112-114, 2004.
- [6]Bhagavatula,R., MariosSavvides, and M. "Acoustics. Analyzing Facial Images using Empirical Mode Decomposition for Illumination Artifact Removal and Improved Face Recognition." IEEE International Conference on Speech and Signal Processing, 2007. Vol. 1, pp. 505-508. April 2007
- [7] Sharif M. A. Bhuiyan, Reza R. Adhami, and Jesmin F. Khan. "Fast and Adaptive Bidimensional Empirical Mode Decomposition Using Order-Statistics Filter Based Envelope Estimation". EURASIP Journal on Advances in Signal Processing, vol. 2008, Article ID 728356, 18 pages, 2008.
- [8] Nunes J. C., Guyot S., and Deechelle E. "Texture analysis based on local analysis of the Bidimensional Empirical Mode Decomposition". Machine Vision and Applications vol.16(3), pp. 177-188, 2005.
- [9] Linderhed, A., "Variable sampling of the empirical mode decomposition of two-dimensional signals," International Journal of Wavelets, Multiresolution and Information Processing., vol.3, 435-452, 2005
- [10] Damerval, C., S. Meignen, and V. Perrier, "A fast algorithm for bidimensional EMD", IEEE Signal Processing Letter, vol.12(10), 701-704, October, 2005.
- [11] Zhao Na, "A Periodic Extension Approach for HHT Empirical Mode Decomposition", Computer Simulation, vol.25(12) 2008
- [12] T. Ojala, M. Pietikäinen, and T. T. Mäenpää, "Multiresolution gray-scale and rotation invariant texture classification with Local Binary Pattern," PAMI, vol. 24, no. 7, pp. 971-987, 2002.
- [13] Zhenhua Guo, Lei Zhang, David Zhang "Rotation invariant texture classification using LBP variance(LBPV) with global matching" Pattern Recognition, 706-719 vol 43. 2010
- [14] Guoying Zhao and Matti Pietikainen, "Dynamic Texture Recognition Using Local Binary Patterns with an

Application to Facial Expressions", PAMI, vol. 29, no. 6, pp. 915-928, 2007

[15] Svetlana Lazebnik, Cordelia Schmid, Jean Ponce, "A Sparse Texture Representation Using Local Affine Regions" PAMI, August 2005 (vol. 27 no. 8) pp. 1265-1278

[16] Timo Ahonen, Abdenour Hadid, and Matti Pietikainen, "Face recognition with local binary patterns", Lecture Notes in Computer Science, ECCV, pp.469-481, 2004.

[17] Shengcai Liao, Xiangxin Zhu, Zhen Lei, Lun Zhang and Stan Z. Li, "Learning Multi-scale Block Local Binary Patterns for Face Recognition", ICB-2007, Seoul, Korea, August 2007,

pp.828-837.

[18] JianJia Pan; Dan Zhang; YuanYan Tang; 'A fractal-based BEMD method for image texture analysis', SMC2010, Istanbul, Turkey, Oct. 2010 pp. 3817 - 3820

[19] Y. XU, B. LIU, J. LIU, S. RIEMENSCHNEIDER. "Two-dimensional empirical mode decomposition by finite elements", Proceedings of Royal Society. (2006) 462, pp.3081-3096

[20] K. Xu, B. Georgescu, D. Comaniciu and P. Meer, "Performance Analysis in Content-based Retrieval with Textures", *Proc. ICPR*, 2000.

# Survey of speeding up Apriori by GPUs

Li you, Chu Xiaowen

*Department of Computer Science*

*Hong Kong Baptist University*

*RRS720, HKBU, Kowloon Tong, Hong Kong*

*{youli, chxw}@comp.hkbu.edu.hk*

## Abstract

Association rule mining (ARM) plays a critical role in a wide variety of applications; but it is now facing the computational challenge due to the continuously increasing data volume. Parallel computing is one of the most promising solutions to overcoming the computational challenge. In this paper, we target at parallelizing Apriori, which is one of the most popular clustering algorithms, by using the widely available Graphics Processing Units (GPUs). We analyze the existing GPU based Apriori and propose a new strategy to most the most use of GPUs.

## 1. Introduction

Association rule mining (ARM) is one of the core data mining problems that attract tremendous attention and find a lot of real applications. On the other hand, ARM is computationally intensive, and therefore a plenty of parallel and distributed ARM algorithms have been developed to handle large databases [1]. Most of the parallel association algorithms are based on Apriori method [2], which is an iterative algorithm that uses bottom-up search and enumerates all frequent itemsets. In Count Distribution (CD) algorithm, each processor has a partial database, and executes the serial Apriori algorithm on the locally stored transactions [3]. Data Distribution (DD) algorithm generates disjoint candidate sets on each processor in order to utilize the whole system memory. However, it suffers from high communication overhead [3]. In [4], Intelligent Data Distribution (IDD)

algorithm is proposed to parallelize the process of building hash tree. The Hybrid Distribution algorithm further combines the advantages of CD and IDD [4]. Another sequential ARM algorithm, DHP [5], has also been parallelized by partitioning the database [6].

Recently, as a general-purpose and high performance parallel hardware, Graphics Processing Units (GPUs) develop continuously and provide another promising platform for parallelizing Apriori. GPUs are dedicated hardware for manipulating computer graphics. Due to the huge computing demand for real-time and high-definition 3D graphics, GPUs have evolved into highly parallel many-core processors. The advances of computing power and memory bandwidth in GPUs have driven the development of general-purpose computing on GPUs (GPGPU).

In this paper, we propose a strategy for paralleling Apriori algorithm on GPUs by using a general-purpose parallel programming model, namely Compute Unified Device Architecture (CUDA) [7, 8]. CUDA has been used for speeding up a large number of applications [9, 10, 11, 12]. Some association rule mining algorithms have been implemented on the GPUs, including Apriori. The main existing GPU-based Apriori is algorithm GPUMiner [13]. These existing works have shown the promising high performance advantage of GPUs. However, the above GPU-based algorithms have not yet fully exploited the computing power of GPUs.

The rest of this paper is organized as follows. Section II introduces the GPU architecture and existing GPU-based Apriori algorithms. Section

III presents the ARM and Apriori, and our research plan of parallel Apriori algorithm on GPUs.

## 2 Related work

In this section, we first briefly introduce the GPU architecture, and then review the existing GPU-based Apriori algorithms.

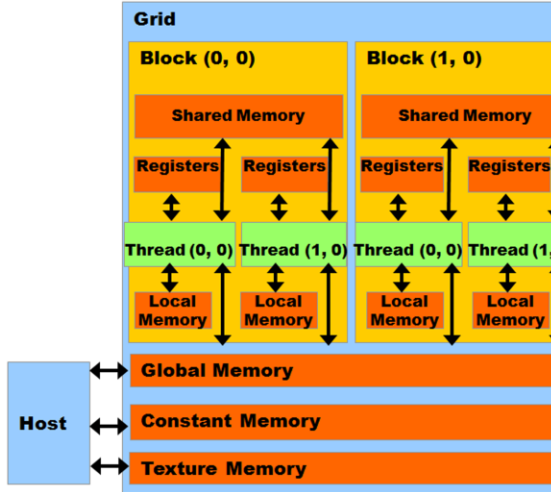


Figure 1. Hardware architecture of the GPU

### A. The GPU architecture

We take NVIDIA GTX280 as an example to show a typical GPU architecture. GTX 280 has 30 Streaming Multiprocessors (SMs), and each SM has 8 Scalar Processors (SPs), resulting in a total of 240 processor cores. The SMs have a Single-Instruction Multiple-Thread (SIMT) architecture: at any given clock cycle, each SP executes the same instruction, but operates on different data. Each SM has four different types of on-chip memory, namely registers, shared memory, constant cache, and texture cache, as shown in Fig.1. Constant cache and texture cache are both read-only memories shared by all SPs. Off-chip memories such as local memory and global memory have relatively long access latency, usually 400 to 600 clock cycles [8]. The properties of the different types of memory have

been summarized in [8, 10]. In general, the scarce registers and shared memory should be carefully utilized to amortize the global memory latency cost.

In CUDA model, GPU is regarded as a coprocessor which is capable of executing a great number of threads in parallel. A single source program includes host codes running on CPU and also kernel codes running on GPU. Compute-intensive and data-parallel tasks have to be implemented as kernel codes so as to be executed on GPU. GPU threads are organized into thread blocks, and each block of threads are executed concurrently on one SM. Threads in a thread block can share data through the shared memory and can perform barrier synchronization. But there is no native synchronization mechanism for different thread blocks except by terminating the kernel. Another important concept in CUDA is warp, which is formed by 32 parallel threads and is the scheduling unit of each SM. When a warp stalls, the SM can schedule another warp to execute. A warp executes one instruction at a time, so full efficiency can only be achieved when all 32 threads in the warp have the same execution path. There are two consequences: first, if the threads in a warp have different execution paths due to conditional branch, the warp will serially execute each branch which increases the total time of instructions executed for this warp; second, if the number of threads in a block is not a multiple of warp size, the remaining instruction cycles will be wasted. Besides, when accessing the memory, half-warp executes as a group, which has 16 threads. If the half-warp threads access the coalesced data, the data access operation will perform within one instruction cycle. Otherwise, the access operation will occupy up to 16 instruction cycles.

### B. The GPUMiner

The GPUMiner designs a method on GPU which adopts the bit-map data structure, and

achieves as speedup of six to twelve compared with CPU version. The main problem of GPUMiner is the poor utilization of memory in GPU, since GPUMiner accesses most of the data (input data point) from global memory directly. Besides, the bitmap approach is elegant in expressing the problem, but not a good method for high performance, since bitmap takes more space when the scale of the dataset is large and requires more shared memory.

### 3 Research plan of parallel Apriori on GPUs

ARM tries to find the set of all subsets of items that frequently occur in a large set of records or transactions, and to extract rules on how a subset of items influences the presence of another subset. Let  $I$  be a set of items and  $T$  a set of transactions, where each transaction is associated with a unique identifier and contains an itemset (a subset of  $I$ ). An itemset with  $k$  items is called a  $k$ -itemset. The support of an itemset  $R$ , denoted by  $S(R)$ , is defined as the number (or frequency in percent) of transactions in which  $R$  occurs as a subset. An itemset is frequent if its support is more than a predefined threshold. ARM has two steps: (1) frequent itemset mining (FIM); (2) rule discovery. A lot of algorithms have been proposed to solve the FIM problem, such as Apriori [1] and FPGrowth [14]. Currently it is not obvious which algorithm is best suited to be parallelized on GPUs, and we shall explore both algorithms in this paper. A general approach is to partition the database into equal-sized chunks, and each thread works on a chunk. The main challenge is that the data structure (i.e., hash tree or trie for Apriori, FP-tree for FPGrowth) needs to be updated by all the threads, and hence the data structure should be carefully designed to minimize writing conflicts. Another issue we shall address is rule discovery, which has a linear complexity to the number of frequent itemsets. Hence, it is

valuable to parallelize rule discovery when there is a huge number of frequent itemsets.

In the following, we intend to conduct following works:

Firstly, implement the Apriori and FPGrowth on CPU with multi-threads, analyze the time consuming to find the hot point in the whole work flow;

Secondly, design a GPU method by dividing the data and dispatching to each thread, then analyze the time consuming in each processing step and the communication time on each type of memory;

Base on the above results, we intend to adopt the suitable data structure and design a new method to minimize the reading latency and make the most use of the GPU's computing power.

### Reference

- [1] M. J. Zaki. Parallel and Distributed Association Mining: A Survey. *IEEE Concurrency*, 1999, 14-25.
- [2] R. Agrawal, and R. Srikant. Fast Algorithms for Mining Association Rules. In *Proceedings of the 20th VLDB Conference*, 1994, 487-499.
- [3] R. Agrawal and J. Shafer. Parallel Mining of Association Rules. *IEEE Trans. On Knowledge and Data Engg*, Vol. 8, 1996.
- [4] E. H. Han, G. Karypis, and V. Kumar. Scalable Parallel Data Mining for Association Rules. In *Proceedings of ACM SIGMOD Conf. Management of Data*, 1997.
- [5] J. S. Park, M. Chen, and P. S. Yu. An Effective Hash Based Algorithm for Mining Association Rules. In *Proceedings of SIGMOD Intl. Conf. Management of Data*, 1995.
- [6] J. S. Park, M. Chen, and P. S. Yu. Efficient Parallel Data Mining for Association Rules. In *Proceedings of ACM Intl. Conf. Information and Knowledge Management*, 1995.
- [7] NVIDIA CUDA:  
<http://developer.nvidia.com/object/cuda.html>.

- [8] NVIDIA CUDA Compute Unified Device Architecture: Programming Guide, Version 2.0, June 2008.
- [9] S. A. Manavski, "CUDA compatible GPU as an efficient hardware accelerator for AES cryptography," In Proceedings of IEEE International Conference on Signal Processing and Communication, Nov. 2007.
- [10] S. Ryou, C. I. Rodrigues, S. S. Bagsorkhi, S. S. Stone, D. B. Kirk, and W. Hwu, "Optimization Principles and Application Performance Evaluation of a Multithreaded GPU Using CUDA," in Proceedings of the 13th ACM SIGPLAN Symposium on Principles and practice of parallel programming Salt Lake City, UT, USA: ACM, 2008.
- [11] X.-W. Chu, K. Zhao, and M. Wang, "Practical Random Linear Network Coding on GPUs", in Proceedings of IFIP Networking'09, Archen, Germany, May 2009.
- [12] X.-W. Chu, K. Zhao, and M. Wang, "Massively Parallel Network Coding on GPUs," IEEE IPCCC'08, Austin, Texas, USA, Dec 2008.
- [13] W. Fang, K. K. Lau, M. Lu, X. Xiao, C. K. Lam, P. Y. Yang, B. He, Q. Luo, P. V. Sande, and K. Yang, "Parallel Data Mining on Graphics Processors," Technical Report HKUSTCS08, 2008.
- [14] J. Han, J. Pei, and Y. Yin. Mining Frequent Patterns without Candidate Generation. In Proceedings of SIGMOD, 2000.

# A Survey of Bayesian Models for Network Motifs Discovery

Kai Liu

## Abstract

*This paper gives a survey of methods for network motifs discovery based on Bayesian models in biological networks and social networks. Network motifs are interaction patterns recur in many different parts of a network at frequencies much higher than those found in randomized networks. Firstly, Sequence motifs (recurring patterns in sequence) discovery methods in DNA sequence are discussed, these methods use Bayesian methods and some other related statistical methods to model the Position Weight Matrix (PWM). Similar to sequence motifs, network motifs also have some properties like correlation between motifs and uncertainties within a motif. These properties motivate us to use statistical methods to study them. This survey has compared the efficiency of the Bayesian models and other strategies like Maximum Likelihood (ML), Expectation Maximization (EM) and Gibbs Sampling, aims to build a more efficiency and effective network motifs discovery model based on Bayesian method, considering as many network motifs properties as possible.*

## 1 Introduction

Networks studies are abundant in many scientific fields. For example, biological networks, Social Networks, World Wide Web, Citation Networks, electronic circuits, etc. These different types of network contain a set of similar basic building blocks [17]. These basic building blocks, are often called “network motifs” [20], which are defined as patterns of interactions that recur in many different parts of a network at frequencies much higher than those found in randomized networks. Nowadays, discovering the network motifs is promising in the research on networks. Many studies [17, 16, 20, 15, 14, 1] use experimental approaches to discover network motifs in World Wide Web, the electronic circuits, the transcriptional regulatory networks, and the neural network. These experimental approaches are almost enumeration methods, in order to uncover the motifs, we must scan all of the networks. Further more, these approaches do not consider many networks’ uncertainties (incomplete and incorrect observations, systematic error,

noises etc.). For these reasons, network motifs detection can be formulated as a standard missing-value inference and parameter estimation problem using Bayesian model.

In the article, we focus on network motifs discovery in the biological network and social network using Bayesian models.

Gene transcription regulatory network is an typical biological network. The identification of motif structure in DNA sequence is an important task we should understand when we analysis the biological network. Gene transcription is regulated by interactions between protein regulators called Transcription Factors (TFs) and their target binding sites in DNA, often referred as to Transcription Factor Binding Sites (TFBSs). A motif is a repetitive sequence pattern recognized by a TF to mediate such interaction [27]. Because the motifs occur several times in the same genome, the regulatory elements of gene transcription can be discovered by searching for overrepresented motifs across regulatory regions.

The most widely used probabilistic model is the position weight matrix (PWM), which contains column-wise probabilities of each nucleic acid to occur. The PWM assumes independence between positions, so the log-likelihood of the motif follows a product multinomial distribution [11]. However, the positions are not completely independent, but have some extent correlations. Many extensions to the basic PWM have concerned the positional dependencies within a motif, the most direct way of incorporating these dependencies is to extend the independent PWM to include pairs of correlated columns of the matrix [28], under the restriction that no two pairs of correlated columns can share a column in common.

Another extension approach of PWM is using a mixture model in which the prior distribution is described by a mixture of Dirichlet distribution [7]. Tang et al. [7] divide these biological knowledge into three partly overlapping categories: motif, background and alignments (position of sites). He built a Bayesian based motif discovery framework, which described the prior information of the motif as a mixture of Dirichlet distribution, and used a Markov generalization of the mixture of Dirichlet multinomial (MoDM) to model the background. Besides, Xing et al. [26, 24, 25] employ Hidden Markov Dirichlet- Multinomial (HMDM),

which can model site-clustering, these clusters of binding sites cooperate TFs.

On the other hand, motif detection can be formulated as a standard missing-value inference and parameter estimation problem Using Bayesian or maximum likelihood methods. MEME [2] uses the EM algorithm to maximum a posteriori. Lawrence et al. [12] proposed to use stochastic search based upon Gibbs sampling. This method has been extended by adding several features. For example, MotifSampler [22], Gibbs Recursive Sampler [23] and BioProspector [13] extended the Gibbs Sampler with higher order background model. PhyloGibbs [21] uses phylogenetic information directly as a part of Gibbs sampling. In addition, nucleosome positioning preferences [18, 19], DNA duplex stability [6] or cis-regulatory modules [29] can be incorporated as prior information to improve the performance of the Gibbs Sampling.

We have discussed the sequence motif discovery problem in gene transcription. However, in biological networks, there are thousands of genes interacting with each other at any given time to accomplish complicated biological tasks, not just one DNA sequence. Sometimes, the interactions are more important than genes themselves, for example, the complexity of an organism [3]. Therefore, discovery the motifs in biological networks becomes one of the central tasks in studying biological networks. “Network motifs” in biological networks are suggested to be the basic cellular information-processing units in these networks [8]. “Network motifs” have been found in a wide variety of biological networks and technological networks, ranging from the regulatory network of E.coli to the neural network of C.elegans, from World Wide Web to electronic circuits [17, 16]. In the early studies, they use exhaustive enumeration methods to count all the subgraphs with a given number of nodes in the networks [17, 16, 20]. But the numbers of subgraphs and algorithm runtime will increase dramatically when the sizes of subgraph became large. Kashtan et al. [10] proposed a probabilistic algorithm termed “sampling method for subgraph counting”. This algorithm samples subgraphs to estimate their relative frequency, not enumerate subgraphs exhaustively. The runtime of the algorithm does not depend on the network size, so this method can discovery the large size network motifs. However, these works didn’t consider the stochastic nature of biological interactions in these networks and experimental uncertainties. Researchers [8, 9, 4, 5] have proposed to model biological networks as “stochastic networks” and to model network motifs as “stochastic network motifs” [8, 9]. Stochastic network motifs discovery can be thought of finding mutually similar but not necessarily identical interaction patterns (subgraphs) from a background random ensemble [9], which is very similar to the sequence motif identification, regarded as retrieving the probabilistic patterns (sub-

graphs) from a background sequence. So, the problem of identifying the stochastic network motifs can be treated as Bayesian inference problem. Jiang et al. [9, 8] have proposed Bayesian model, Gibbs sampling, Expectation Maximization (EM) strategies, to estimate the stochastic network motifs. Jiang et al. [8] use the subgraph sampling method as proposed by Kashtan [10] to address the problem of large subgraph size, which can not be solved in [9] using enumeration methods.

## 2 Modeling

### 2.1 Bayesian Approach for Sequence Motif discovery

#### 2.1.1 Notations

We denote a regulatory DNA sequence by a character string  $y = (y_1, \dots, T)$ .

Motif type  $k$ , with width  $w_k$ , is characterized by Position Weight Matrix (PWM)  $\Theta_k = (\theta_{k1}, \dots, \theta_{kw_k})$ ,

We assume that motif widths  $w_k (k = 1, \dots, K)$  are known and the locations of the motif sites are unknown, denoted by an array of missing indicator variables  $\mathbf{A} = (A_{ijk})$

#### 2.1.2 Bayesian models

Product-Multinomial model

mixture of Dirichlet Multinomial model

Hidden Markov Dirichlet Multinomial model

#### 2.1.3 Estimate the Parameters

EM, Variational EM, Gibbs Sampling, MCMC

### 2.2 Bayesian Approaches for Network Motifs Discovery

#### 2.2.1 Notations

Without considering uncertainties, a biological interaction network, often referred to as a graph with a collection of nodes and edges between the nodes. Two types of edges, one type is directed edges, like regulatory interactions between the proteins (transcription factors) and the genes in transcription regulation networks; the other one type is undirected edges, like physical interactions between the proteins in protein-protein interaction networks. A graph  $G$  with  $N$  nodes is described using an adjacency matrix  $\mathbf{A} = (a_{ij})_{N \times N}$ , where  $a_{ij} = 1$  if there is a directed edge pointing from node  $i$  to node  $j$  in a transcriptional regulatory network or an undirected edge connecting these two nodes in a protein-protein interaction network, and  $a_{ij} = 0$ , otherwise.

### 2.2.2 Bayesian models

Bayesian model, EM, Gibbs Sampling,

## 3 Research Plan

### 3.1 Focus

### 3.2 Research Issue

Considering the correlation between motifs.

- build a efficiency and effective bayesian model.
- Considering the correlation between motifs.
- apply the bayesian model to different types of networks.
- apply the bayesian model to large scale networks extended abstract.

## References

- [1] U. Alon. Network motifs: theory and experimental approaches. *Nature Reviews Genetics*, 8(6):450–461, 2007.
- [2] T. Bailey and C. Elkan. Fitting a mixture model by expectation maximization to discover motifs in biopolymers. In *Proceedings/... International Conference on Intelligent Systems for Molecular Biology*, volume 2, page 28.
- [3] J. Berg. Bayesian analysis of biological networks: clusters, motifs, cross-species correlations. *Statistical and Evolutionary Analysis of Biological Networks*, page 65, 2009.
- [4] J. Berg and L. Michael. Local graph alignment and motif search in biological networks. *Proceedings of the National Academy of Sciences of the United States of America*, 101(41):14689, 2004.
- [5] J. Berg and L. Michael. Cross-species analysis of biological networks by Bayesian alignment. *Proceedings of the National Academy of Sciences*, 103(29):10967, 2006.
- [6] R. Gordân and A. Hartemink. Using DNA duplex stability information for transcription factor binding site discovery. In *Pacific Symposium on Biocomputing 2008: Kohala Coast, Hawaii, USA, 4-8 January 2008*, page 453.
- [7] M. hung Eric Tang, A. Krogh, and O. Winther. Bayesmd: Flexible biological modeling for motif discovery. *Journal of Computational Biology*, 15(10):1347–1363, 2008.
- [8] R. Jiang, T. Chen, and F. Sun. Bayesian Models and Gibbs Sampling Strategies for Local Graph Alignment and Motif Identification in Stochastic Biological Networks. *Communications in Information & Systems*, 9(4):347–370, 2009.
- [9] R. Jiang, Z. Tu, T. Chen, and F. Sun. Network motif identification in stochastic networks. *Proceedings of the National Academy of Sciences*, 103(25):9404, 2006.
- [10] N. Kashtan, S. Itzkovitz, R. Milo, and U. Alon. Efficient sampling algorithm for estimating subgraph concentrations and detecting network motifs. *Bioinformatics*, 20(11):1746, 2004.
- [11] P. M. Kim-Anh Do and M. Vannucci. *Bayesian Inference for Gene Expression and Proteomics*. Cambridge University Press, 2006.
- [12] C. Lawrence, S. Altschul, M. Boguski, J. Liu, A. Neuwald, and J. Wootton. Detecting subtle sequence signals: a Gibbs sampling strategy for multiple alignment. *Science*, 262(5131):208–214, 1993.
- [13] X. Liu, D. L. Brutlag, and J. S. Liu. Bioprospector: Discovering conserved dna motifs in upstream regulatory regions of co-expressed genes. In *Pac. Symp. Biocomput.*, pages 127–138, 2001.
- [14] S. Mangan, S. Itzkovitz, A. Zaslaver, and U. Alon. The incoherent feed-forward loop accelerates the response-time of the gal system of Escherichia coli. *Journal of molecular biology*, 356(5):1073–1081, 2006.
- [15] S. Mangan, A. Zaslaver, and U. Alon. The coherent feedforward loop serves as a sign-sensitive delay element in transcription networks. *Journal of molecular biology*, 334(2):197–204, 2003.
- [16] R. Milo, S. Itzkovitz, N. Kashtan, R. Levitt, S. Shen-Orr, I. Ayzenshtat, M. Sheffer, and U. Alon. Superfamilies of evolved and designed networks. *Science*, 303(5663):1538, 2004.
- [17] R. Milo, S. Shen-Orr, S. Itzkovitz, N. Kashtan, D. Chklovskii, and U. Alon. Network motifs: simple building blocks of complex networks. *Science*, 298(5594):824–827, 2002.
- [18] L. Narlikar, R. Gordân, and A. Hartemink. A nucleosome-guided map of transcription factor binding sites in yeast. *PLoS Comput. Biol.*, 3(11):E215, 2007.
- [19] L. Narlikar, R. Gordân, and A. Hartemink. Nucleosome occupancy information improves de novo motif discovery. In *Research in Computational Molecular Biology*, pages 107–121. Springer, 2007.
- [20] S. Shen-Orr, R. Milo, S. Mangan, and U. Alon. Network motifs in the transcriptional regulation network of Escherichia coli. *Nature genetics*, 31(1):64–68, 2002.
- [21] R. Siddharthan, E. Siggia, and E. Van Nimwegen. PhyloGibbs: a Gibbs sampling motif finder that incorporates phylogeny. *PLoS Comput Biol.*, 1(7):e67, 2005.
- [22] G. Thijs, K. Marchal, M. Lescot, S. Rombauts, B. De Moor, P. Rouze, and Y. Moreau. A gibbs sampling method to detect overrepresented motifs in the upstream regions of coexpressed genes. *Journal of Computational Biology*, 9(2):447–464, 2002.
- [23] W. Thompson, E. Rouchka, and C. Lawrence. Gibbs Recursive Sampler: finding transcription factor binding sites. *Nucleic acids research*, 31(13):3580.
- [24] E. Xing and R. Karp. Motifprototyper: a profile bayesian model for motif family. In *Proc. Natl. Acad. Sci.*, volume 101, pages 10523–10528.
- [25] E. Xing, W. Wu, M. I. Jordan, and R. M. Karp. Logos: a modular bayesian model for de novo motif detection. *Computational Biology*, 2, 2004.
- [26] E. P. Xing, J. I. Jordan, R. M. Karp, and S. Russell. A hierarchical bayesian markovian model for motifs in biopolymer sequences. *NIPS*, 2002.
- [27] Q. Zhou and M. Gupta. Chapter 8 regulatory motif discovery: from decoding to meta-analysis.

- [28] Q. Zhou and J. S. Liu. Modeling within-motif dependence for transcription factor binding site predictions. *Bioinformatics*, 20(6):909–916, 2004.
- [29] Q. Zhou and W. H. Wong. Cismodule: De novo discovery of cis-regulatory modules by hierarchical mixture modeling. In *Proceedings of the National Academy of Sciences of the United States of America*, volume 101, pages 12114–12119.

# An AOC-Based Approach to Solving Complex Energy Distribution Problems

Benyun Shi

## Abstract

*Energy distribution problems are complex, which may involve many issues such as distribution efficiency, robustness, and reliability. In this paper, we focus mainly on studying the energy distribution efficiency, i.e., minimizing distribution costs. We adopt an AOC-based approach in order to (i) understand the relationships between the interactions and behaviors of suppliers and consumers at a microscopic level and the distribution efficiency at a macroscopic level, and (ii) provide feasible distribution solutions in open and dynamic environments. Two nature-inspired behavioral rules, i.e., interaction and decision-making rules, are proposed that regulate entities to (i) have incentives to share information with each other, and (ii) trade with lower distribution costs. Simulation results for both static and dynamic distribution environments have shown that even with partial information, our approach can perform as well as a centralized algorithm by means of tuning a control parameter (i.e., memory size), and that it is scalable to solve large-scale distribution problems. Since our AOC-based approach is aimed at modeling and studying the characteristics of energy distribution by focusing on the self-organization of autonomous entities, it may also be extended to study other important distribution issues in the future.*

## 1 Introduction

As our daily life depends more and more heavily on various energy resources, the imbalance between energy supply and demand becomes extremely serious. The general problem of energy distribution may involve many issues either endogenously or exogenously, such as human activities, national security, environmental issues. All these issues make the energy distribution very complex in terms of energy distribution efficiency [16, 17], system vulnerability [1] and reliability [14]. The complexity of the real-world energy distribution may be in part reflected in the following aspects:

- The distribution environment is open, where energy suppliers and consumers may enter or leave the environment at any time;

- The energy supply and demand may dynamically change either endogenously or exogenously (e.g., disturbed by abnormal weather, wars);
- Energy suppliers and consumers may make decisions based on their own considerations (e.g., price, reliable relationships, etc.);
- Energy suppliers and consumers are self-interested, i.e., they make decisions based on their own benefits or utility.

With respect to these aspects, it is necessary to understand the underlying mechanisms of energy distribution problems, i.e., the relationships between the interactions and behaviors of energy suppliers and consumers at a microscopic level and the distribution properties (e.g., distribution efficiency and robustness) at a macroscopic level. By doing so, it may be helpful in practice to study the impact of human activities on energy distribution from a macroscopic point of view.

In this paper, we focus on the issue of energy distribution efficiency, i.e., how to minimize the energy distribution costs at a macroscopic level. Many studies [18, 3, 16, 17, 13] have focused on energy distribution under physical constraints of existing distribution networks (e.g., pipeline network, power grid). Most of them have adopted centralized optimization algorithms to find the optimal energy flows that minimize the distribution costs. However, centralized algorithms require complete distribution information, they are impractical for dynamic and large-scale energy distribution problems. Recently, some decentralized algorithms such as agent-based algorithms [9, 6, 5, 8] have been proposed to solve distributed constraint satisfaction problems. However, at the moment, most of them focus on strategy design with the purpose of solving specific engineering problems. They are still limited in methodology and applications in order to practically characterize the relationships between the local interactions and the global properties of an open, unpredictable energy distribution system from the point of view of a complex system [20, 2].

We present an AOC-based approach to modeling and studying the characteristics of the energy distribution problems. AOC, which stands for Autonomy-Oriented Comput-

ing [11, 12, 10], is a self-organized computing paradigm, which focuses on the local interactions and behaviors of energy suppliers and consumers. According to AOC, autonomous entities (representing energy suppliers or consumers) can spontaneously interact with each other as well as their local environments based on certain behavioral rules, such as the interaction and decision-making rules in this paper. By doing so, the global objectives can be collectively achieved through entities' self-organization. The goal of our AOC-based approach is twofold: (i) to understand the relationships between the self-organization of energy suppliers and consumers at a microscopic level and the distribution efficiency at a macroscopic level, and (ii) to provide feasible solutions for efficient energy distribution. By carrying out simulations for both static and dynamic distribution environments, we can obtain the following observations:

- Based on the interaction rules defined in Section 4.3, there is a unique Nash equilibrium in which each pair of entities agrees to interact with each other;
- Even with incomplete information and simple behaviors, our AOC-based approach can perform as well as a centralized algorithm by means of tuning the control parameter, i.e., entities' memory size;
- Our AOC-based approach is computationally scalable, which is one of the most important characteristics for solving large-scale distribution problems;
- The performance of our AOC-based approach can be well explained with respect to entities' local interaction rules and decision-making rules even in open and dynamic environments.

Starting from modeling the interactions and behaviors of autonomous entities at a local level, the AOC-based approach may help us gain an insight into more complex distribution issues in the future.

## 2 Problem Statement

In this section, we present an energy distribution problem, which focuses on the issue of energy distribution efficiency. For the reason that most energy suppliers and consumers are located in different geographic regions, the energy distribution efficiency will be measured by the energy distribution costs of all energy flows among suppliers and consumers.

Consider a set of  $n$  energy suppliers and consumers. Each supplier/consumer  $i$  has a volume of energy  $I_i(t)$  to be distributed/consumed at time  $t$ , where  $I_i(t) > 0$  represents the volume supply, and  $I_i(t) < 0$  represents the volume of demand. Suppose that at any time  $t$ , the total supply

from energy suppliers equals to the total demand from energy consumers, i.e.,  $\sum_{i=1}^n I_i(t) = 0$ . The primary goals of the energy distribution problem are twofold: (i) to balance the energy supply and demand at any time (i.e., to distribute all energy resources from suppliers to consumers), and (ii) to minimize the total energy distribution costs. We abstract distribution costs among energy suppliers and consumers to be a predefined costs matrix  $CM_{n \times n} = \{c_{ij} | 1 \leq i, j \leq n\}$ , where  $c_{ij}$  represents the per unit distribution costs from  $i$  to  $j$  directly. In this paper, we assume  $CM_{n \times n}$  is symmetric, which means that  $c_{ij} = c_{ji}$ , for  $1 \leq i, j \leq n$ . However, triangle inequality may not be correct, i.e.,  $c_{ij} + c_{jk}$  may not definitely greater than or equal to  $c_{ik}$ . In this case, all energy suppliers and consumers together with the per unit energy distribution costs among them form an energy distribution network.

**Definition 1** (Energy Distribution Network). *The costs matrix  $CM_{n \times n}$  forms a fully-connected energy distribution network, where each node represents an energy supplier or a consumer, and each link is associated with the per unit energy distribution costs.*

During energy distribution, energy flows from one node to another on the distribution network. After all resources have been distributed, the energy flows can be represented by an undirected network  $G = \langle V, L, Q \rangle$ , where the node set  $V = \{v_i | 1 \leq i \leq n\}$  denotes the set of  $n$  suppliers/consumers, the link set  $L = \{l_{ij} | 1 \leq i, j \leq n\}$  represents all existing energy flows (if there are energy flows from  $v_i$  to  $v_j$ , then  $l_{ij} = 1$ ; otherwise,  $l_{ij} = 0$ ), and the quantity set  $Q = \{q_{ij} | 1 \leq i, j \leq n\}$  represents the volume of energy flows on each link  $l_{ij}$ . In the following, we provide two measurements, i.e., the global costs and per unit costs, to measure the distribution efficiency.

**Definition 2** (Global Costs). *The global costs of an energy flow network measure the total distribution costs for distributing all energy supply to corresponding consumers. In this case, the total costs of all energy flows can be calculated by*

$$TC = \sum_{l_{ij} \in L} q_{ij} \cdot c_{ij} \cdot l_{ij} \quad (1)$$

**Definition 3** (Per Unit Costs). *The per unit costs of an energy flow network measure the average distribution costs of energy that have been distributed from energy suppliers to corresponding consumers.*

In this paper, we present an AOC-based approach (see Section 4) for the energy distribution problem to study the self-organization of energy suppliers and consumers at a microscopic level and the distribution efficiency at a macroscopic level. The specific research questions that we are interested in are as follows:

- *Distribution rate*: Can the AOC-based approach balance the energy supply and demand through local interactions among suppliers and consumers?
- *Distribution costs*: How about the distribution efficiency (i.e., per unit costs) of the AOC-based approach as compared with a centralized algorithm?
- *Computational Efficiency*: How long does the AOC-based approach need to finish the distribution comparing with a centralized algorithm? What is the key factor that determines the computational time?
- *Scalability*: When the number of entities increases, can the performance of the AOC-based approach remain efficient (i.e., higher distribution rate and lower distribution costs)?

### 3 A Centralized Algorithm for Static Energy Distribution

In order to evaluate the performance of the AOC-based algorithms (see Section 4.4), it would be necessary to compare it with that of other algorithms in order to address the above-mentioned questions. In this section, we present a centralized algorithm, where an authoritative “third party” is assumed to have complete information of the distribution network and be powerful to manage all distribution flows. For static energy distribution, this algorithm will be advantageous to provide better solutions with respect to distribution costs. Thus, we will use it as our benchmark for the evaluation purpose.

An energy distribution problem is said to be *static* if the number of suppliers and consumers as well as the total supply/demand does not change. To solve the static energy distribution problem, there are two important issues we should consider: (i) how to determine appropriate pairs of energy supplier and consumer to distribution energy between them, and (ii) how to determine the quantity of energy resources that should be distributed between each pair of supplier and demander. The details of the centralized algorithm are shown in Algorithm 1. There are two major steps in the algorithm. First, the path (i.e.,  $Path_{ij}(\cdot)$ ) with the lowest distribution costs between each pair of nodes  $(v_i, v_j)$  on the distribution network will be calculated using Floyd algorithm (see Steps 4-11). By doing so, energy can always be distributed along the path with the lowest distribution costs. Second, the distribution order and the distribution quantity of each pair of nodes will be determined (see Steps 12-25). Energy will be distributed between pairs of nodes in an increasing order of distribution costs, i.e., the distribution pair with lower distribution costs will have higher priority to distribute.

```

Input:  $CM_{n \times n}$ ; Supply/demand of each
supplier/consumer  $I_i$ ;
1 Initialize  $Path_{ij}(\cdot)$  for each pair  $(v_i, v_j)$ ;
2 Initialize  $DMatrix(i, j) = CM(i, j)$  for each pair
 $(v_i, v_j)$ ;
3 // record the lowest distribution costs between  $v_i$  and  $v_j$ 
4 foreach  $k = 1:n$  do
5   foreach pair  $(v_i, v_j)$  do
6     if  $DMatrix(i, k) + DMatrix(k, j) <$ 
 $DMatrix(i, j)$  then
7        $DMatrix(i, j) =$ 
 $DMatrix(i, k) + DMatrix(k, j)$ ;
8       Update  $Path_{ij}(\cdot)$ ;
9     end
10  end
11 end
12  $newMatrix =$ 
 $DMatrix([SupplierList], [ConsumerList])$ ;
13  $minCost = \min(\min(newMatrix))$ ;
14 while  $minCost \neq Inf$  do
15    $[v_i, v_j] = find(newMatrix == minCost)$ ;
16   Distribute energy from  $v_i$  to  $v_j$ ;
17   if  $I_i == 0$  then
18     //The supply/demand of  $v_i$  is distributed;
19      $newMatrix(i, :) = Inf$ ;
20   end
21   if  $I_j == 0$  then
22     //The supply/demand of  $v_j$  is distributed;
23      $newMatrix(:, j) = Inf$ ;
24   end
25 end

```

**Algorithm 1:** The heuristic centralized algorithm for static energy distribution. In the algorithm, Steps 4-11 are to calculate the path with the lowest distribution costs for each distribution pair; Steps 12-25 are to distribute energy from suppliers to consumers in an increasing order of distribution costs.

With complete information of the distribution network, Algorithm 1 controls the distribution flows in a centralized manner. Hence, it can provide wonderful solution for the static energy distribution. However, there are several limitations to use the centralized algorithm in practice. First, real-world energy distribution usually happens in an open and dynamic environment, which means that suppliers or consumers may enter or leave at any time and the supply/demand of suppliers/consumers may dynamically change over time. In this case, the assumption about the existence of an authoritative “third party” is unrealistic. Second, the computational complexity of the centralized algorithm (e.g., Algorithm 1 has the computational complexity of  $O(n^3)$ ) makes it unsuitable for solving large-scale energy distribution problems. Finally and most importantly, in reality, energy is distributed between suppliers and consumers through bilateral or multilateral trading. This means that the energy distribution is, by nature, a decentralized problem. In the next section, we present an AOC-based approach, which is a self-organized computing paradigm for

solving computational problems as well as modeling complex systems [10], to study energy distribution problems in terms of distribution efficiency.

## 4 An AOC-based Approach for Distribution Efficiency

The AOC-based approach studies the energy distribution from a bottom-up viewpoint, where energy suppliers and consumers behave and make decisions based on their own interests. According to AOC, each supplier or consumer can be represented by an autonomous entity. Entities spontaneously interact with each other as well as their local environments, based on certain *behavioral rules*.

### 4.1 Entities Profiles

Suppose we have  $n$  entities  $E = \{e_i | 1 \leq i \leq n\}$ , each of which represents either an energy supplier or a consumer. There are two major components for each entity  $e_i$ , i.e., the *Memory* and the interaction component (*IC*). The  $e_i$ .*Memory* records: (i)  $e_i$ 's potential trading partners, (ii) the quantity of resources each partner has, and (iii) the distribution path from  $e_i$  to each partner.  $e_i$  makes trading decisions based on quantity and costs information in  $e_i$ .*Memory* (see Section 4.3 for details). Meanwhile, as the environment evolves,  $e_i$  can also dynamically update its *Memory* through interacting with other entities in its interaction component. The interaction components of  $e_i$ ,  $e_i$ .*IC*, records: (i) a set of entities that  $e_i$  can interact with, (ii) the distribution path from  $e_i$  to each of them, and (iii) the quantity of resources each entity has. The detailed interaction component and interaction rule will be introduced in Section 4.2.

In practice, restricted by many factors such as negotiation power, the capability to collect information, few suppliers/demanders may have complete information of the energy distribution network. Therefore, we assume that each entity only has partial information about the distribution network. With respect to our AOC-based approach, for the reason that each entity can only trade with entities in its *Memory* and interact with entities in its *IC*, we can restrict entities' trading capability (respectively, interaction capability) through its *Memory* size, or *M.size* (respectively, *IC* size, or *IC.size*). The information stored in each entity's *Memory* will be dynamically updated through interacting with other entities in its *IC*. In the next, we will introduce in detail entities' interaction rules.

### 4.2 Interaction Component and Interaction Rules

Entities interact with each other through their interaction components. Initially, an entity  $e_i$  will only memorize the

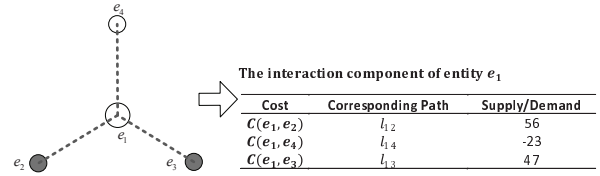


**Figure 1:** An illustration of entity  $e_1$ 's interaction component structure (left) and contents (right). The distribution costs is sorted in an increasing order in the first column. The corresponding paths to other nodes in its memory are recorded in the second column. The supply/demand status of each entity is memorized in the third column. The empty circles represent consumers, the filled circles represent suppliers.

direct distribution paths to other entities in  $e_i$ .*IC*. Fig. 1 illustrates an example of an entity's initial interaction component. As illustrated, entity  $e_1$  only knows the direct distribution paths (i.e.,  $l_{12}$ ,  $l_{13}$ , and  $l_{14}$ ) from itself to  $e_2$ ,  $e_3$ , and  $e_4$ . According to our AOC-based approach, if an entity  $e_j$  agrees to interact with  $e_i$ ,  $e_i$  can then update its interaction component based on information in  $e_j$ .*IC* following the two interaction rules:

- Based on the information shared by  $e_j$ ,  $e_i$  will calculate the distribution costs from  $e_i$  to each entity (e.g.,  $e_k$ ) in  $e_j$ .*IC* by passing through  $e_j$ , i.e., the sum of distribution costs from  $e_i$  to  $e_j$  in  $e_i$ .*IC* and that from  $e_j$  to  $e_k$  in  $e_j$ .*IC*;
- Entity  $e_i$  will update its *IC* by memorizing the top *IC.size* number of entities and corresponding paths that have lower distribution costs. During updating, any new path from  $e_i$  to entity  $e_k \in e_j$ .*IC* must pass through entity  $e_j$ , and only the path with the lowest distribution costs from  $e_i$  to  $e_k$  will be memorized by  $e_i$ .

The detailed interaction procedure for an entity  $e_i$  is shown in Algorithm 2. There are two kinds of update behaviors: link updating and node updating. Link updating happens when  $e_i$  finds a new path with lower distribution costs to an entity that has already been in its *IC*. Fig. 2(a) shows an example of link updating from  $e_1$  to  $e_3$ . Comparing with Fig. 1, a new link  $l_{23}$  is added into  $e_1$ .*IC* while an old link  $l_{13}$  is deleted from  $e_1$ .*IC*. Node updating happens when  $e_i$  finds a new entity which has not been recorded in its *IC*. Fig. 2(b) shows an example of node updating of  $e_1$ .*IC*. Comparing with entity  $e_3$  in Fig. 1,  $e_1$  has a lower distribution costs to  $e_5$  through interacting with  $e_4$ . Hence,  $e_5$  and the path  $l_{14} \rightarrow l_{45}$  will be recorded, while  $e_3$  and associated link  $l_{23}$  will be deleted from  $e_1$ .*IC*. Step 3 in Algorithm 2 together with the interaction rule 2 makes sure that the size of  $e_i$ 's interaction component does not change during updating.

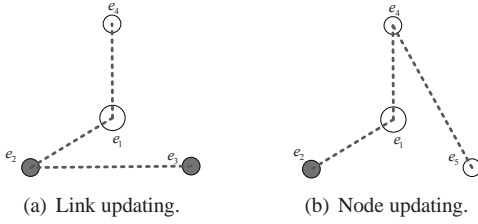


**Figure 2:** An illustration of both link updating and node updating for  $e_1$ 's interaction component. (a) Link updating of  $e_1.IC$ . Comparing with Fig. 1, the path  $l_{13}$  from  $e_1$  to  $e_3$  is updated by the path  $l_{12} \rightarrow l_{23}$ . (b) Node updating of  $e_1.IC$ . Comparing with Fig. 1, a new node  $e_5$  is added into  $e_1$ 's interaction component to replace  $e_3$ . Correspondingly, a new link  $l_{45}$  is added to replace the link  $l_{13}$ . Both link updating and node updating do not change the size of  $e_1.IC$ .

Based on the interaction rules, each entity updates its  $IC$  using entities and paths with lower distribution costs. If all entities would like to interact with each other, there will be a nonlinear aggregation of information about distribution costs among entities. This kind of positive mechanism, which is one of the most important features for autonomy-oriented computing [10], will significantly improve the distribution efficiency. In Section 4.5, we will show that all entities have incentives to interact with each other under the above-mentioned interaction rules.

### 4.3 Decision-making Rules

Each entity updates its  $Memory$  based on information in its  $IC$ . In this paper, because we only consider the energy distribution efficiency (i.e., minimizing energy distribution costs), we assume that each entity will update its  $Memory$  based only on the distribution costs, i.e., only those entities with lower distribution costs will be memorized. After updating the  $Memory$ , an entity will make decisions about (i) how to send trading requests to trading partners in its  $Memory$ , and (ii) how to determine its trading behavior when it receives multiple requests from other entities. In this section, we introduce two kinds of decision-making rules:

- **Rule A:** At each round, each entity  $e_i$  will send only one trading request to the trading partner with the lowest distribution costs in its  $Memory$ ; at the same time, when an entity receives multiple trading requests from other entities, it will only choose the request with the lowest distribution costs to trade with.
- **Rule B:** At each round, each entity  $e_i$  will send trading request to each trading partners in its  $Memory$ ; at the same time, when an entity receives multiple trading requests from other entities, it will trade with them

```

1  foreach  $e_j \in e_i.IC$  do
2    // sort entities in terms of their distribution costs to  $e_i$ ;
3     $S_j \leftarrow \text{sort}(e_j.IC, 'ascend')$ ;
4    foreach  $e_k \in S_j$  do
5      // find the entity with maximal distribution costs
        to  $e_i$  in  $e_i.IC$ ;
6       $e_{max} \leftarrow \arg \max\{disCost(e_i, :)\}$ ;
7      if  $disCost(e_i, e_{max}) >$ 
         $disCost(e_i, e_j) + disCost(e_j, e_k)$  then
8        Remove  $e_{max}$  and the link associate with
         $e_{max}$  from  $e_i.IC$ ;
9        Add  $e_k$  into  $e_i.IC$ ;
10       Update  $path(e_i, e_k)$  using  $path(e_i, e_j)$ 
        and  $path(e_j, e_k)$ ;
11     end
12   end
13 end

```

**Algorithm 2:** The procedure of entity  $e_i$  interacting with each  $e_j \in e_i.IC$ . Steps 7-11 show that  $e_i$  will update its  $IC$  if  $e_k \in e_j.IC$  has a smaller distribution costs to  $e_i$ , where  $disCost(e_i, e_j)$  represents the distribution costs between  $e_i$  and  $e_j$  based on the path from  $e_i$  to  $e_j$  (i.e.,  $path(e_i, e_j)$ ) in  $e_i.IC$ .

one by one in ascending order in terms of distribution costs.

It is obvious that Rule A is suitable for the situation that entities have enough time to distribute their energy resources, where minimizing the distribution costs is the first priority for entities; while Rule B is for the case that there is no enough time for entities (i.e., “urgent entities”) to find trading partners with the minimal distribution costs, where maximizing distribution rate becomes the first priority.

*Remark.* In practice, there may be many decision-making rules for energy suppliers and consumers to trade with each other. However, in this paper, our goal is not to exhaust all possible decision-making rules but to study how to regulate entities' local interactions so that global distribution efficiency can be reached under certain decision-making rules, where all entities prefer to low distribution costs.

### 4.4 Behavior-based Algorithms

Corresponding to the decision-making rules A and B, we present two behavior-based algorithms (i.e., Algorithms A and B, respectively) in this section. There are two types of behaviors for the behavior-based algorithms, i.e., the updating behaviors and the trading behaviors. The updating behaviors help an entity to find paths to other entities with lower distribution costs in open and dynamic environments so that it can dynamically update its  $Memory$ . The updating behavior of each entity  $e_i$  consists of the following three behaviors:

```

1 // The updating behaviors for all entities in a random order;
2 foreach  $e_i \in E$  do
3   Interact with each  $e_j \in e_i.IC$  one by one based on
   Algorithm 2;
4   Self-exploration;
5   Update  $e_i.Memory$ ;
6   Send trading requests to all  $e_k \in e_i.Memory$ ;
7 end
8 // The trading behaviors for all entities in a random order;
9 foreach  $e_k \in E$  do
10  Receive trading request from other entities;
11  Trade based on decision-making rules in Section 4.3;
12 end

```

**Algorithm 3:** The dynamics of our behavior-based algorithms at each round. Steps 2-7 show the updating behaviors of all entities in a random order, while Steps 9-12 show the trading behaviors of all entities in a random order.

- *Interaction:*  $e_i$  interacts with entities in  $e_i.IC$  one by one based on the interaction rules in Section 4.2;
- *Self-exploration:*  $e_i$  randomly select an *available* trading partner (with non-zero supply/demand), which is not in its *Memory*, to update its *Memory*;
- *Updating Memory:* The available energy of each partner in  $e_i.Memory$  is first updated. Then, if all partners in  $e_i.Memory$  is available,  $e_i$  updates the entity with maximal distribution costs. Otherwise,  $e_i$  will update the entity with both zero supply/demand and maximal distribution costs.

The trading behaviors of Algorithms A and B adopts decision-making rules A and B, respectively, in Section 4.3. At the start of the algorithms, each entity's *Memory* is initialized by randomly selected trading partners. The details of the following rounds are shown in Algorithm 3. In this paper, we present our algorithms in a sequential manner, i.e., entities behave one by one. However, our algorithms can easily be adopted in an asynchronous manner, where entities can interact and trade whenever they want to.

#### 4.5 A Game-Theoretic Analysis

As analyzed in Section 4.2, entities' incentives to interact with each other is particularly crucial for our AOC-based approach. In this section, we design a "cooperate-defect" game for each pair of entities to study their interaction incentives. We show that two entities will be in a Nash equilibrium if they both adopt "cooperate" (i.e., interact) strategy under the following two assumptions: (i) when an entity trades with a partner, the lower the distribution costs are, the higher payoff the entity will get; and (ii) when an entity plays as a middleman for two other entities, the entity will get a positive payoff.

		Player $e_j$	
		C	D
Player $e_i$	C	$f_c + f_d, f_c + f_d$	$f_c, f_d$
	D	$f_d, f_c$	0, 0

**Figure 3:** A  $2 \times 2$  payoff matrix between two entities  $e_i$  and  $e_j$ , which specifies the interaction between them with two different strategies, i.e., cooperate and defect.

Consider a game between two entities  $e_i$  and  $e_j$ . During the interaction, one entity may either "defect" or "cooperate" with the other. If  $e_i$  cooperates with  $e_j$ ,  $e_i$  will share information in its  $IC_i$  to  $e_j$  based on the interaction rule so that  $e_j$  can update its interaction component  $IC_j$  and *Memory*. Otherwise, if  $e_i$  defects with  $e_j$ ,  $e_i$  will not share any information with  $e_j$ . Based on the above-mentioned two assumptions, there are two kinds of payoffs for each entity. Firstly, when  $e_j$  cooperates, no matter  $e_i$  cooperates or not,  $e_i$  may receive a payoff  $f_d$  ( $f_d \geq 0$ ) in terms of distribution costs. This is because  $e_i$  may possibly find trading partners (e.g.,  $e_k \in IC_j$ ) with lower distribution costs by interacting with  $e_j$ . Secondly, when  $e_i$  cooperates, no matter  $e_j$  cooperates or not,  $e_i$  may receive a payoff  $f_c$  ( $f_c \geq 0$ ) in terms of virtual benefits as a middleman. This is because when  $e_j$  update its *Memory* using  $e_k \in IC_i$ , based on the interaction rule (i.e., Step 10 in Algorithm 2),  $e_i$  will always play as a middleman between  $e_j$  and  $e_k$ . Note that  $f_d$  and  $f_c$  may dynamically change and be determined by several issues, such as the possibility of finding better trading partners, the quantity of costs a new partner can saved.

A  $2 \times 2$  payoff matrix between two entities  $e_i$  and  $e_j$  is shown in Fig. 3, which specifies the interaction between them with two different strategies, i.e., cooperate and defect. The first term (respectively, second term) of each cell in the matrix shows the payoff of  $e_i$  (respectively,  $e_j$ ) corresponding to  $e_j$ 's (respectively,  $e_i$ 's) strategy. It can be found that if both entities cooperate with each other, each will receive payoff  $f_c + f_d$ . Since  $f_c \geq 0$  and  $f_d \geq 0$  under the above two assumptions, we conclude that both entities are in a unique Nash equilibrium if they decide to cooperate with each other.

#### 4.6 Discussion

There are several differences between the behavior-based algorithms based on our AOC-based approach and existing optimization algorithms (e.g., [19, 9]) based on traditional decentralized approach. First, most existing decentralized algorithms design agents' operations based on the nature and requirements of specific engineering problems, while our behavior-based algorithms aim at modeling and studying the characteristics of the problems, focusing

on the self-organization of autonomous entities. For example, the authors in [19] studied the optimization problem of controlling network congestion, where the global congestion was translated into congestion price for each route. To achieve the global objective, each agent was restricted to adopt a predefined control strategy to determine its transmission rate based on corresponding route prices. In this paper, entities may have multiple human-inspired decision-making strategies (see Section 4.3). We aim at investigating what kinds of entities' behavior are crucial for achieving distribution efficiency. Second, from the point of view of problem solving, most existing decentralized algorithms have focused on designing deliberate strategies for agents to interact with other agents or the environment, while our behavior-based algorithms focus on local mechanism design (e.g., the interaction rules for nonlinear information aggregation as in this paper) to motivate/regulate entities' local behaviors so that the global objective can be collectively achieved through entities' self-organization. Third, since the interactions and behaviors of entities in our AOC-based approach are modeled after certain human behaviors, in addition to solving the engineering problems, they may also be extended to model more complex human behaviors so as to study more complex distribution problems, for example, to study the impact of human activities on energy distribution from a macroscopic point of view.

## 5 Simulations and Observations

The main goal of our AOC-based approach is not restricted to solving specific energy distribution problems. It is also aimed at studying what kinds of local mechanisms that motivate/regulate interactions and behaviors of energy suppliers and consumers are crucial for distribution efficiency. Unfortunately, real-world data about suppliers/consumers' behaviors with respect to distribution costs would be extremely difficult to collect. In this section, we carry out simulations to (i) evaluate the performance of our behavior-based algorithms by comparing with the centralized algorithm proposed in Section 3, (ii) study the impacts of entities' memory size, (iii) compare the performance of the two behavior-based algorithms with different decision-making rules, and (iv) observe the performance of our AOC-based approach in an open and dynamic environment.

### 5.1 Settings

In this section, we introduce the experimental settings for both static and dynamic energy distribution environments. With respect to the two parameters, i.e.,  $IC.size$  and  $M.size$ , in our AOC-based approach, we have performed several simulations to examine the effects of  $IC.size$ . The results show that it only slightly influences the performance

of the two behavior-based algorithms proposed in Section 4.4. This is because entities' interaction components play a role to update their memories, which only indirectly influence the energy distribution. Therefore, for all evaluations in this paper, we set  $IC.size$  to be a constant value, i.e.,  $IC.size = 10$ . We focus mainly on uncovering the impacts of  $M.size$  for our AOC-based approach.

#### 5.1.1 Static Distribution Environments

There are three inputs for simulating the static distribution environments: the number of entities  $n$ , the per unit distribution costs matrix  $CM_{n \times n}$ , and the supply/demand of each entity.

- *Number of entities:* In reality, the energy distribution problems may have different scales, for example, the distribution network may have scale about 100 (i.e., the number of transmission transformer) at a city level, but about 1000 at a country level [17]. Hence, it is necessary to evaluate the performance of our AOC-based approach in different scales. In this section, we do simulations for the distribution problems with  $n$  ranging from 100 to 1000.
- *Per unit distribution costs matrix:* The values in the per unit distribution cost matrix are randomly generated from region  $[10, 1000]$  to reflect the high cost heterogeneity between each pair of suppliers/demanders.
- *Supply/Demand:* The supply/demand of each entity is randomly generated from region  $[-100, 100]$ . We assume that the global supply and demand are balanced, i.e., the total supply equals to the total demand.

Because we focus on the relative comparison of the behavior-based algorithms, the absolute values of the per unit distribution costs and entities' supply/demand will not affect our observation.

#### 5.1.2 Open and Dynamic Environments

To simulate the open and dynamic energy distribution environments, we adopt the crude oil production pattern reported in [21]. Wood et al. adopt two functional forms to match the production pattern, the first of which extends production from history along a constant percentage growth path ( $\approx 2\%$ ) until the production peak is reached, the second of which declines production post-peak at a constant reserves to production ( $R/P$ ) ratio ( $R/P = 10$ ). However, the objective of our simulation is not to estimate the peak year of the world's crude oil production but to simulate an open and dynamic environment to evaluate the performance of our AOC-based strategies. The detailed settings for the simulation inputs are shown in Table 1. The dynamic supply

Variables	Descriptions	Values
$T$	The time duration of the simulation	300
$n$	Maximum number of suppliers and consumers	1000
$GrowthRate$	Pre-peak production growth rate	0.02
$R/P$	Post-peak reserves to production ratio	10
$s(i)$	Initial supply of suppliers $i$	[0, 100]
$PeakYear(i)$	Peak year of supplier $i$	[100, 250]

**Table 1:** The inputs for open and dynamic energy distribution.

of each supplier is determined by three parameters: (i) the initial supply, (ii) the rate of pre-peak production growth, and (iii) the post-peak reserves to production ratio. To simulate the open environment, in our simulations, suppliers enter or leave the environment based on their quantity of supply. If a supplier’s supply exceeds 50 before its peak year is reached, the supplier will be allowed to enter into the environment. Meanwhile, if a supplier’s supply is less than 50 after its peak year, the supplier will be forced to leave the environment. Similar to the static energy distribution, the total energy demand at each time is assumed to be balanced with the total energy supply. Hence, in our settings, each consumer’s demand is dynamically adjusted with a constant rate according to the change of total energy supply. Note that it does not mean that the consumers know the total energy supply in our algorithms.

There are totally 300 rounds in our simulation. Each entity operates updating and trading behaviors only once a round. After trading with each other, the remainder of energy of current round will not accumulate to the next round. However, entities’  $IC$ s and memories will be updated. In this case, we adopt Algorithm B for our simulation in open and dynamic environments.

## 5.2 Measurements

We adopt three global measurements to evaluate the performance of our AOC-based approach in both static and dynamic environments. The details are described as follows:

- *Per Unit Costs:* As defined in Section 2, the per unit costs measure the average distribution costs of all energy that has been distributed;
- *Distribution Rate:* The distribution rate measures the percentage of all energy that has been distributed;
- *CPU Time:* We use CPU time to compare the computational efficiency of different algorithms.

## 5.3 Simulation Results for Static Energy Distribution

The simulation objectives for energy distribution in static environments are to (i) evaluate the performance of our

behavior-based algorithms by comparing with the centralized algorithm, (ii) evaluate the performance of the AOC-based approach with different decision-making rules, and (iii) evaluate the effects of the control parameter (i.e., memory size) to the performance of our AOC-based approach. Our simulations are carried out for different size of distribution networks ranging from 100 to 1000. For each network size, the measurements are averaged by 100 runs of simulations.

### 5.3.1 Distribution Rate

The distribution rate is measured by the percentage of energy supply that has been distributed to consumers. For static energy distribution, our two behavior-based algorithms can reach 100% energy distribution rate. The reasons are as follows: Based on entities’ updating behaviors in Section 4.4, entities’ self-exploration can guarantee to find new trading partners at each round. In this case, each entity will interact with all other entities within  $n$  rounds. According to the trading behaviors, when each pair of entities trades with each other, at least one of them will be satisfied. Therefore, all supply will be distributed within  $n$  rounds, because the supply/demand of each entity remains unchanged in a static distribution environment.

### 5.3.2 Distribution Efficiency

The distribution efficiency is measured by per unit costs of the final energy flows. Fig. 4 shows the comparison of Algorithms A and B with the centralized algorithm in terms of per unit costs. The left figure (respectively, the right figure) shows the results of Algorithm A (respectively, Algorithm B) with different memory sizes for different distribution network sizes, where the memory size is proportional to the network size. It can be observed that as the memory size increases to 100%, both Algorithms A and B can produce results close to those from the centralized solution. We can also observe from Fig. 4 that memory size is an important control parameter for the performance of our behavior-based algorithms. As the memory size increases, the performance of our behavior-based algorithms become better and better. This is because comparing with entities with smaller memory size, it is more likely for an entity

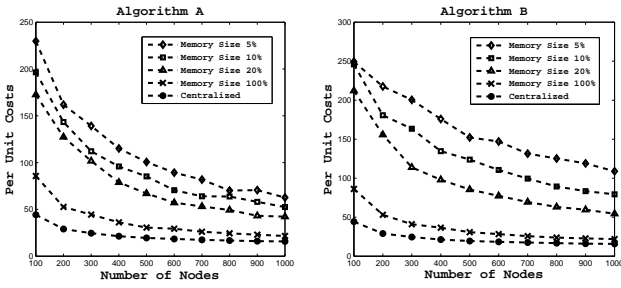


**Figure 4:** Comparing Algorithms A and B with the centralized algorithm in terms of per unit costs. The left figure (respectively, the right figure) shows the results of Algorithm A (respectively, Algorithm B) with different memory sizes for different numbers of distribution nodes. Each values of per unit costs is averaged over 100 runs of simulations. The memory size is calculated by the number of nodes times the corresponding percentage value.

with larger memory size to find distribution paths to trading partners with lower distribution costs.

We also compare the performance of Algorithms A and B in Fig. 5. The left figure in Fig. 5 shows the comparison of Algorithms A and B with the same memory size (i.e., 10%) but different sizes of distribution networks, while the right figure shows the comparison of Algorithms A and B for the same size of distribution network but different memory sizes. It can be observed that Algorithm A performs better than Algorithm B in both two cases. (Simulations for other memory size and network size have also been done, and the same observations can be found.) This is because entities with Algorithm A will have long time to update its memory through self-exploring and interacting with other entities, while entities with Algorithm B will quickly accept requests from other entities, which makes them have short time to update the distribution paths.

Another observation about our AOC-based approach is the computational scalability. We can observe from Fig. 4 that the per unit costs of the final distribution of Algorithms A and B approaches to the centralized solution as the number of nodes increases from 100 to 1000. This is because in our algorithms, entities update *Memory* by self-exploration and mutual interaction, the larger the network size is, the longer time entities can interact with each other, hence, the more effective and efficient the algorithms will be. Computational scalability is one of the most important characteristics for our AOC-based approach to tackle large-scale energy distribution problems, where the centralized approach cannot perform well.

### 5.3.3 Computational Time

As analyzed in Section 3, the computational complexity of the centralized algorithm is  $O(n^3)$ , where  $n$  is the size of

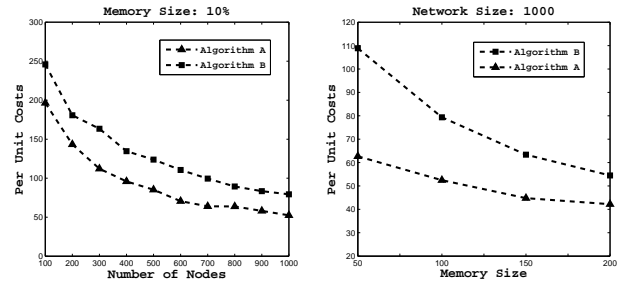


**Figure 5:** Comparing Algorithms A and B in terms of per unit costs. The left figure shows the comparison of Algorithms A and B with the same memory size but different number of distribution nodes. The right figure shows the comparison of Algorithms A and B with different memory sizes for the case that the number of distribution nodes is 1000. Each values of per unit costs is averaged over 100 runs of simulations.

the distribution networks. Though the behavior-based algorithms in this paper can easily be realized by parallel computation, in our simulations, we adopt sequential computation (i.e., entities behave one by one during the distribution) to compare computational time with the centralized algorithm. The sequential computational complexity of the behavior-based algorithms are  $O(n \cdot (IC.size)^2)$ . Fig. 6 shows the CPU time comparison of Algorithms A and B with the centralized algorithm. The left figure shows that (i) Algorithm A is much faster than the centralized algorithm, and (ii) Algorithm A with larger memory size run slightly slower than that with smaller memory size. The right figure shows the comparison of Algorithms A and B with the same memory size 10% (Simulations for different memory size have also been done, and the same observation can be found.) The results show that Algorithm B is faster than Algorithm A. This is because the decision-making rule B will make Algorithm B finish distributing energy resources within a smaller number of rounds.

### 5.3.4 Decision-making Rules

As described in Section 4.3, “urgent entities” would like to adopt decision-making rule B for the case that there is not enough time to find trading partners. We do simulations to validate the performance of entities with different decision-making rules by randomly setting 10% entities to be “urgent entities”, and compare the average per unit costs of the “urgent entities” with the case that they are not urgent. The left figure in Fig. 7 shows the average per unit costs comparison of the 10% selected entities for algorithms with and without “urgent entities”. The right figure in Fig. 7 shows the average per unit costs comparison of all entities for algorithms with and without “urgent entities”. The results show that entities adopting decision-making rule B will increase their

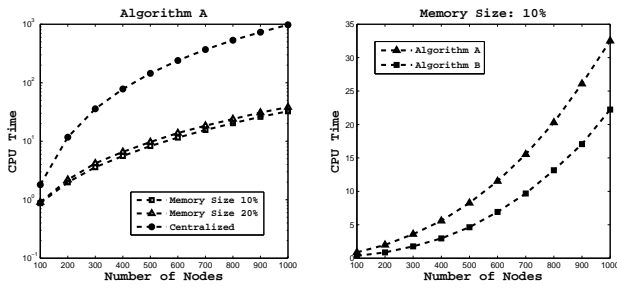


**Figure 6:** Comparing Algorithms A and B with the centralized algorithm in terms of CPU time. The left figure shows the comparison of Algorithm A with memory size 10% and 20% and the centralized algorithm. The logarithmic scale of CPU time shows Algorithm A is much faster than the centralized algorithm. The results also show that Algorithm A with larger memory size runs slightly slower than with smaller memory size. The right figure shows the CPU time comparison between Algorithms A and B with the same memory size but different network size. The results show that Algorithm B is faster than Algorithm A. This is because entities with the decision-making rule B will finish distributing energy resources within small number of rounds.

per unit distribution costs, and further increase the per unit costs of all entities. This is because “urgent entities” will always send requests to all trading partners in their memories or accept all trading requests from other entities, which make them have no enough time to find distribution paths with lower distribution costs.

#### 5.4 Simulation Results for Open and Dynamic Energy Distribution

Since it is impractical to adopt centralized algorithms for open and dynamic energy distribution, in this section, we focus mainly on simulating the performance of our AOC-based approach with different memory sizes in an open and dynamic energy distribution environment. We can observe from Fig. 8 that the evolution of per unit costs of Algorithm B with memory sizes 50, 100, and 150, respectively. We can observe that there are three phases: (i) at the beginning, the curves show that algorithm with larger memory size reaches lower per unit costs than that with smaller memory size, and the per unit costs for each curve decreases over time; (ii) after the number of suppliers reaches its peak value, the per unit distribution costs slightly increase; and (iii) after the total energy supply reaches the peak value, the algorithm with a smaller memory size will have not only lower the per unit costs but also lower the distribution rate (shown in Fig. 10). The reason is that at the beginning, when more and more suppliers enter into the environment, entities can perform better and better through interacting with each other and updating their memories. However, when suppliers begin to leave the environment at time 118, more and more

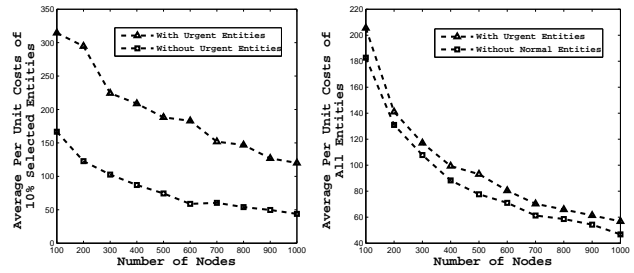


**Figure 7:** The performance of algorithm with “urgent entities”, where the 10% “urgent entities” are randomly selected from  $n$  number of entities. The left figure shows the average per unit costs comparison of the 10% selected entities for algorithms with and without “urgent entities”. The right figure shows the average per unit costs comparison of all entities for algorithms with and without “urgent entities”. The results show that “urgent entities” with decision-making rule B will increase their own per unit distribution costs, and further increase the per unit costs of all entities.

suppliers in consumers’ *Memory* become unavailable. In this case, consumers may have to trade with suppliers with larger distribution costs, thereby, slightly increase the per unit distribution costs. Finally, after the total supply reaches its peak value at time 217 and the number of suppliers becomes smaller, there will be much more consumers than suppliers in the environment. Based on the dynamic procedure in Algorithm 3, entities will behave in a random order. Hence, the possibility that the suppliers are forced to trade with consumers with high distribution costs becomes very high. In this case, the distribution costs increase unexpectedly. One possible solution is to design a local behavior to regulate entities’ trading behaviors (e.g., entities are only forced to trade with partners who have already been in its memory). For space limitation, we will not describe it in detail. The reason that the algorithm with smaller memory size (e.g., 50) performs better than that with larger memory size is that it has smaller distribution rate (see Fig. 10). This means that only a small portion of resources is distributed along paths with small distribution costs, which decrease the average per unit distribution costs. In summary, our simulation results have shown that the performance of our behavior-based algorithms can well be explained by entities’ local behaviors as well as the global distribution environment. The simulation results have indicated that for open and dynamic energy distribution, the local interactions and behaviors of autonomous entities should be adaptive for different distribution environments.

For the computational time, Fig. 9 shows that algorithm with a larger memory size have higher computational time than that with a smaller memory size. Another observation is that the computational time of our algorithms is positively correlated with the total number of entities in the environ-

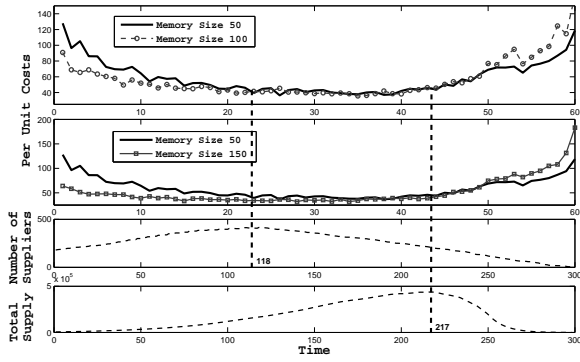


**Figure 8:** The evolution of per unit costs of Algorithm B with memory size 50, 100, and 150. We can observe that: (i) at the beginning, the algorithm with larger memory size reaches lower per unit costs than that with smaller memory size; (ii) after the number of suppliers reaches its peak value, the per unit distribution costs slightly increase; and (iii) after the total supply reaches peak value, the algorithm with smaller memory size will have not only lower per unit costs but also lower distribution rate (shown in Fig. 10).

ment.

## 6 Conclusion and Future Work

In this paper, we have presented an AOC-based approach to studying the energy distribution problems, focusing on the self-organization of energy suppliers and consumers. For the reason that the practical energy distribution problems are involved in an open and dynamically evolving environment, traditional centralized optimization algorithms have their limitations in providing feasible solutions. Meanwhile, recent decentralized approaches are also quite limited in methodology and applications to practically characterize the underlying mechanisms behind the distribution systems. The goal of the AOC-based approach is not restricted to solving specific energy distribution problems. It is aimed at investigating the relationships between the local interactions and behaviors of energy suppliers and consumers and the global efficiency of energy distribution.

According to AOC, autonomous entities, each of which represents either an energy supplier or a consumer with incomplete information, can spontaneously interact with each other and make decisions based on their behavioral rules. With respect to energy distribution efficiency, we have proposed two kinds of behavioral rules, i.e., entities' interaction rules and decision-making rules. The interaction rules motivate entities to have incentives to interact with each other so that costs information can be nonlinearly aggregated among entities. This kind of positive mechanism, which is one of the most important features of AOC, will significantly improve global distribution efficiency. Two decision-making

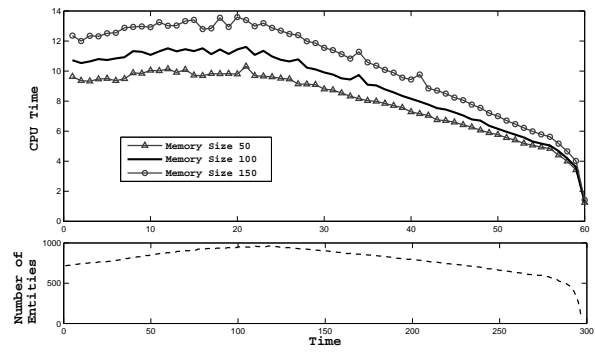


**Figure 9:** The evolution of computational time of Algorithm B with memory size 50, 100, and 150. We can observe that the computational time for algorithm with larger memory size are larger than that with smaller memory size. Also, the computational time is positively correlated with the total number of entities.

rules, where all entities are assumed to favor low distribution costs, have been proposed to simulate two real-world trading scenarios. Simulation results for both static and dynamic energy distribution have shown that, our AOC-based approach can perform as well as a centralized algorithm by tuning a control factor (i.e., memory size). Furthermore, the AOC-based approach also exhibits an important property, i.e., computational scalability, which is crucial for solving large-scale energy distribution problems.

In addition to the distribution efficiency, the energy distribution problems may also exhibit other global properties, such as robustness, vulnerability, and reliability. From the point of view of problem solving, a robust and adaptive energy distribution system plays important roles in distribution efficiency and fault tolerance (e.g., transportation dysfunction for abnormal weather). The AOC-based approach together with appropriate systematic measurements may help us answer the following challenging questions of a complex energy distribution system in the future:

- What kinds of energy distribution systems are robust (respectively, stable, reliable) in an open, dynamic energy distribution environment?
- What kinds of local behaviors and mechanisms are crucial for the robustness (respectively, vulnerability, and reliability) of an energy distribution system?
- What kind of global patterns can be formed through entities' interactions in an efficient, robust, as well as reliable energy distribution system?

Although the AOC-based approach in this paper focuses only on the issue of energy distribution efficiency, it can be extended to answer the above-mentioned questions by modeling after relevant human behaviors. By doing so, our

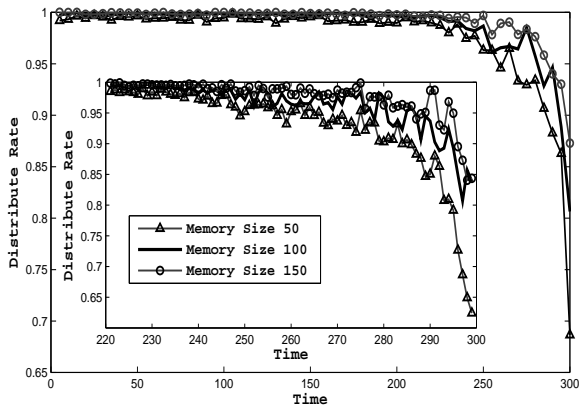


**Figure 10:** The evolution of distribution rate of Algorithm B with memory size 50, 100, and 150. It can be observed that the algorithm with small memory size will have lower distribution rate. The inset shows the evolution of distribution rate from round 220 to 300 rounds.

approach may help us gain an insight into more complex energy distribution problems (i.e., involving distribution efficiency, robustness, and reliability) from the viewpoint of human activities, so that more effective energy policies can be made in practice. This will be pursued in our future studies.

## References

- [1] R. Albert, I. Albert, and G. L. Nakarado. Structural vulnerability of the north american power grid. *Physical Review E*, 69(2):025103, 2004.
- [2] P. Ball. *Critical Mass: How One Thing Leads to Another*. Farrar, Straus and Giroux, 1st edition, 2004.
- [3] M. Barthélemy and A. Flammini. Optimal traffic networks. *Journal of Statistical Mechanics: Theory and Experiment*, 7:L07002, 2006.
- [4] British Petroleum. BP statistical review of world energy 2009. Technical report, British Petroleum, London, UK, 2009.
- [5] P. S. Dutta, N. R. Jennings, and L. Moreau. Adaptive distributed resource allocation and diagnostics using cooperative information-sharing strategies. In *Proceedings of the Fifth International Joint Conference on Autonomous Agents and Multiagent Systems*, pages 826–833, 2006.
- [6] T. Hadžić, A. Wasowski, and H. R. Andersen. Techniques for efficient interactive configuration of distribution networks. In *Proceedings of the Twentieth International Joint Conference on Artificial Intelligence*, pages 100–105, 2007.
- [7] IEA. International energy outlook 2009. Technical report, International Energy Agency, 2009.
- [8] M. Jacyno, S. Bullock, M. Luck, and T. Payne. Understanding decentralised control of resource allocation in a minimal multi-agent system. In *Proceedings of the Sixth International Joint Conference on Autonomous Agents and Multiagent Systems*, pages 1–3, 2007.
- [9] A. Kumar, B. Faltings, and A. Petcu. Distributed constraint optimization with structured resource constraints. In *Proceedings of the Eighth International Conference on Autonomous Agents and Multiagent Systems*, pages 923–930, 2009.
- [10] J. Liu. Autonomy-oriented computing: The nature and implications of a paradigm for self-organized computing. In *Proceeding of the Fourth International Conference on Natural Computation, and the Fifth International Conference on Fuzzy Systems and Knowledge Discovery*, pages 3–11, 2008.
- [11] J. Liu, X. Jin, and K. C. Tsui. *Autonomy Oriented Computing-From Problem Solving to Complex Systems Modeling*. Kluwer Academic Publishers, 2005.
- [12] J. Liu and K. C. Tsui. Toward nature inspired computing. *Communications of the ACM*, 49(10):59–64, 2006.
- [13] K. T. Midthun, M. Bjorndal, and A. Tomagard. Modeling optimal economic dispatch and system effects in natural gas networks. *The Energy Journal*, 30(4):155–180, 2009.
- [14] National Energy Board. A compendium of electric reliability frameworks across canada. Technical report, The National Energy Board, Canada, 2004.
- [15] Oil and Gas Journal. Worldwide look at reserves and production. *Oil and Gas Journal*, 106(48):23–24, 2008.
- [16] A. Quelhas, E. Gil, J. D. McCalley, and S. M. Ryan. A multiperiod generalized network flow model of the U.S. integrated energy system: Part I - Model description. *IEEE Transaction on Power Systems*, 22(2):829–836, 2007.
- [17] A. Quelhas and J. D. McCalley. A multiperiod generalized network flow model of the U.S. integrated energy system: Part II - Simulation results. *IEEE Transaction on Power Systems*, 22(2):837–844, 2007.
- [18] F. Schweppe, M. Caramanis, R. Tabors, and R. Bohn. *Spot Pricing of Electricity*. Kluwer Academic Publishers, 1988.
- [19] S. Shakkottai and R. Srikant. Network optimization and control. *Foundations and Trends in Networking*, 2(3):271–379, 2007.
- [20] D. Sornette. *Critical Phenomena in Natural Sciences*. Springer-Verlag, 2nd edition, 2003.
- [21] J. H. Wood, G. R. Long, and D. F. Morehouse. Long-term world oil supply scenarios. Technical report, U.S. Energy Information Administration, 2004.

# Toward Effective Vaccine Deployment: A Systematic Study\*

Shang XIA  
Department of Computer Science  
Hong Kong Baptist University

## Abstract

*Vaccination is a commonly-used epidemic control strategy based on direct antiviral immunization and indirect reduction of virus transmissibility. There exist three factors related to the efficacy of vaccine deployment; they are: (1) vaccine coverage, (2) releasing time, and (3) deployment methods. Yet, the exact impacts of these factors still remain to be systematically studied. In our work, we examine the effectiveness of vaccination-based epidemic control in adjusting the composition of susceptible and infectious individuals (referred to as composite structure) in a host population. We develop a modified compartmental infection model for characterizing virus spreading dynamics in several age-specific host populations (one host population for each age group). We consider vaccine deployment schedules that correspond to different settings of the three deployment factors. Based on our simulation-based experiments, we evaluate the impacts of deployment factors on virus spreading dynamics as well as their implications for an effective vaccination strategy.*

## 1 Introduction

Fast spreading of infectious viruses can cause worldwide epidemic outbreaks, e.g., 2009 H1N1 influenza epidemic [28]. Until 1 August 2010, more than 214 countries had reported laboratory confirmed cases of H1N1 infection, including over 18449 deaths [29]. In order to control epidemic outbreaks, vaccination has been considered as one of the useful strategies, in that it provides both direct protection for those vaccinated through antiviral immunization and indirect protection for those unvaccinated by reducing infection transmissibility. As have been discussed in our previous work [15], the effectiveness of vaccination is related to three deployment factors: (1) vaccine coverage (the total number of vaccine doses available), (2) releasing time

(the starting date of vaccine deployment), and (3) deployment methods (the distributions of vaccine doses to age-specific host populations). However, the exact impacts of these factors on virus spreading dynamics as well as epidemic control remain to be further examined. The knowledge gained from such a study would provide us with new insights into the practice of optimal vaccine deployment. This is especially important given the facts that before an epidemic outbreak, there sometimes exists only very limited knowledge about a newly-emerged virus and that vaccine doses may not be sufficiently prepared in advance (e.g., due to inadequate capabilities of vaccine manufacturing, storage, and transportation). As a result, an optimal deployment of available vaccine doses to various age-specific host populations would be therefore desirable. The problem of evaluating the impacts of vaccine deployment is not only interesting but also challenging. As we know, the virus spreading dynamics would further depend on individuals' unique demographical and social characteristics.

The effects of vaccination may be viewed as changes in the composition of a host population (called composite structure), i.e., increasing virus immunized individuals and decreasing susceptible ones. The changed host population structure will thus have a significant influence on the virus spreading dynamics, by having a reduced transmission rate. In order to achieve effective vaccination-based epidemic control, it would be necessary for us to gain a good understanding of the impacts of vaccine deployment factors on the dynamics of virus infection and transmission.

Past studies have approached this issue from various angles, while offering different perspectives [13][9][8]. For example, the population-based epidemic studies, known as the 'mean-field' or 'compartmental' epidemic models, i.e., SIS, SIR and SEIR models [2][8][9][3], assume that virus infection and transmission is a homo-mixing process. In these models, virus infection is described by a system of deterministic equations, where virus transmission is represented by a reproduction number  $R_0$  (i.e., the number of secondary infections caused by a single infectious case in a completely susceptible population [2][9]). The virus spreading dynamics is then characterized by changes in the

---

\*A preliminary version of this paper was presented at the 1st ACM International Health Informatics Symposium (IHI'10), November 11-12, 2010, Arlington, VA, USA.

infected population. Studies on vaccine deployment based on these models have focused mainly on the quantity of vaccine doses needed to achieve a threshold reproduction number,  $R_0 < 1$ , with the natural decay of epidemic spread. These studies represented epidemic spread and vaccine deployment as dynamic processes using the population-level descriptions of infected and vaccinated populations. However, most of them do not take into consideration population heterogeneities.

To address the issue of population heterogeneities, individual-based studies adopt network structures to further describe the process of virus spreading through contact activities. In an epidemic network, nodes depict host individuals and links represent contact relationships. The virus spread is then modeled as the propagation of infections on a contact network [16][25][11]. Vaccination in such an epidemic network is treated as the immunization of the key nodes that play crucial roles in virus spreading, such as the nodes of hubs or bridges [12][14]. However, in practice, vaccinated individuals may be neither part of a homogenized population, nor a group of important individuals. Vaccine deployment should target groups of individuals based on their influences on the virus spreading dynamics, e.g., hospital staff due to their high risk of infection exposure and school students for their frequent contact activities [6][5].

In a host population with several heterogeneous sub-populations (called heterogeneous host populations), the problem of vaccine deployment has also been viewed as that of optimal resource allocation [19][20][18]. By performing constrained optimization, one may arrive at a conclusion on how vaccine doses should be deployed to the heterogeneous host populations. Medlock [19] and Milne [22] suggested that a vaccine deployment strategy based on individuals' transmissibility would have a greater impact on reducing overall infections. The benefits of preferentially vaccinating school-aged children have been discussed in view of their disproportionately high probability of influenza transmission [24][17][4]. As for vaccine deployment with respect to different stages of epidemic spreading, Medlock [20] proposed a solution by addressing the infection dynamics with vaccine releasing date as an initial condition for the optimization of vaccine deployment. Following this approach, Matraj [18] showed that it would be better to protect the high-transmission groups before the peak of an epidemic, and to protect the most vulnerable groups afterward would be optimal. This would suggest that vaccination in different stages will need different deployment strategies.

Given the situations they are concerned with, the above-mentioned studies have dealt with the problem of finding optimal vaccine deployment strategies in heterogeneous host populations. In doing so, the conditions under which an optimal deployment strategy is derived are treated as being

static. In reality, however, the landscape of a host population will dynamically change with respect to the dynamics of epidemic spreading. In this paper, we evaluate the effectiveness of vaccine deployment in epidemic control. We investigate the impacts of three vaccine deployment factors on the epidemic spreading dynamics. We develop a compartmental infection model, in which we take into consideration population heterogeneities in infection vulnerability and contact patterns. By simulating the dynamics of virus infection and transmission, we obtain some valuable insights into the relative impacts of vaccine deployment factors on epidemic control.

The remainder of this paper is organized as follows: Section 2 states the problem to be tackled in this paper. Section 3 details vaccination-based epidemic control. Section 4 presents an age-specific epidemic infection model. Section 5 describes simulation-based experiments and results. Section 6 concludes the paper and highlights the major contributions of this work.

## 2 Problem Statement

In order to find an effective epidemic control strategy based on vaccination, it would be desirable to investigate the impacts of vaccine deployment factors on epidemic spreading dynamics. In our study, we view vaccination as a process of adjusting the host population structure by providing antiviral immunity to a certain group of host individuals. The adjusted population structure in turn influences the virus transmission process, and hence controls epidemic spreading. Here, we especially interest in three deployment factors: (1) vaccine coverage (the total number of vaccine doses available), (2) vaccine releasing time (the starting date of vaccine deployment), and (3) vaccine deployment method (the distribution of vaccine doses to different host populations).

In order to evaluate the above-mentioned deployment factors, it is essential for us to develop a means of modeling and simulating the dynamics of epidemic spreading under various vaccine deployment conditions. Toward this end, we propose and apply an age-specific computational infection model for characterizing virus spreading dynamics. With this proposed model, we perform several simulation-based experiments under different vaccine deployment schedules, which correspond to different settings of vaccine deployment factors, i.e., vaccine coverage, releasing time, and deployment methods. Then, we evaluate the effectiveness of vaccine deployment by measuring epidemic spreading dynamics as reflected in the total number of infections, the emergence of infection outbreaks, and the dates and severity of infection peaks. By analyzing simulation results, we evaluate the relative and combined influences of those deployment factors on the efficacy of vac-

cine deployment, in terms of these measurements, in virus spreading dynamics.

In what follows, we, first of all, provide a detailed description of vaccination-based epidemic control. Then, we discuss the process of virus infection and transmission in several age-specific host populations, and investigate how the vaccine deployment conditions can influence the epidemic spreading dynamics.

### 3 Vaccination-Based Epidemic Control

Vaccination is regarded as one of the most important intervention means for controlling epidemic spreading. The effect of vaccination can be represented as changes in the composition of a host population (i.e., composite structure) in terms of susceptible, infectious, and vaccinated individuals. Thus, the problem of finding an effective vaccination strategy can be viewed as that of whether or not the adjusted host population's composite structure can exert positive impacts on the control of epidemic spreading. Section 3.1 analyzes the mechanism of vaccine deployment in epidemic control. Section 3.2 discusses three factors related to vaccine deployment.

#### 3.1 Virus Spreading Dynamics

Epidemic spreading includes two sub-processes: (1) virus infection and (2) virus transmission. Virus infection means susceptible host individuals may be infected when they are engaged in infectious exposures. There exist many factors that can influence the process of virus infection, e.g. individuals' natural immunity and infection history or other associated physical conditions, which can be generalized as individuals' infection vulnerability. Virus transmission characterizes the infectious exposures based on infectious contact activities between susceptible and infected individuals. Here, infectious contacts would have different meanings for different types of infectious viruses, e.g., intimate relationships for sexual transmitted HIV/AIDS, and homomixing contacts for air-born influenza. Two factors are related to virus transmission: patterns of contact activities and dynamics of virus infection. The former depicts the features of contact relationships, such as the structure and frequency of contact activities among host populations. The latter describes the composite structure of a host population in the current epidemic spreading process. Thus, during the process of virus infection and transmission, epidemic spreading dynamics will be affected by: (1) individuals' infection vulnerability, (2) contact relationships, and (3) a host population's composite structure.

In this study, we investigate virus infection and transmission among several heterogeneous host populations. In

doing so, we characterize epidemic spreading based on the following aspects:

- **Population Infection Rate**

We use infection rate,  $\beta$ , to depict the infection vulnerability in each host population.  $\beta$  is defined as the probability of successful infection for susceptible individuals engaged in infectious exposures. In our study, we assume infection rate equals to the virus attack rate of a certain host population. It represents for the heterogeneity of population pathological feature in epidemic spreading process.

- **Population Contact Patterns**

We represent the structure and frequency patterns of contact activities between different host populations with a contact matrix  $C$ . For the matrix element  $c_{i,j}$ , If  $c_{i,j} \neq 0$ , there is a contact relationship between the host populations of  $i$  and  $j$ . The value of  $c_{i,j}$  represents the frequency of contact activities. Thus matrix  $C$  is a representation of the heterogeneity in population contact relationships.

- **A Host Population's Composite Structure**

During epidemic spreading process, each host population is composed by susceptible, infectious, vaccinated or recovered individuals. A host population's composite structure describes the relative percentage of susceptible and infectious individuals in that population. The rate of infectious contacts is defined as the probability of a mutual contact to be an infectious one, which is proportional to the percentage of infectious individuals in contact populations. Thus, the composite structure can influence the virus transmission base on its impacts of infectious contact rate.

- **Infection Risk**

Infection risk  $\lambda$  is used to characterize the dynamics of epidemic spreading among heterogeneous host populations.  $\lambda_i$  is defined as the probability of susceptible individuals in host population  $i$  to be infected on current situation of epidemic spreading. Infection risk is a comprehensive investigation of virus spreading dynamics by estimating both the infection vulnerability in virus infection and the rate of infectious contacts in virus transmission.

As has been discussed, epidemic spreading dynamics will be affected by the above-mentioned three aspects. As an effective epidemic control strategy, vaccination will control the virus spreading dynamics by reducing the virus

transmission rate by adjusting a host population's composite structure. In the following section, we describe the working mechanism of vaccine deployment and its related deployment factors.

### 3.2 Vaccine Deployment

The effects of vaccination on epidemic control involve two aspects: (1) directly providing antiviral immunities for vaccinated population, and (2) indirectly protecting susceptible population by reducing infection transmissibility. The deployment of vaccine doses will change a host population's composite structure by increasing the immunized population and decreasing the susceptible population, which lead to a reduced rate of infectious contacts. Therefore, the deployment of vaccine doses will control epidemic spreading by reducing the risk of virus infection as a whole.

In this study, we focus only on the epidemic spread in a single circulation. Our concern is about the impacts of an adjusted host population's composite structure on epidemic spreading dynamics. Our discussion in the following sections will be based on the assumption of effective vaccination, that is, we ignore the vaccine efficacy and time delays between vaccine injection and antiviral protection. Thus, the mentioned vaccine deployment implies the population transitions from the state of susceptible to vaccinated, which is a population-level description of an adjusted host population's composite structure.

The problem of understanding the effectiveness of vaccination can be reduced to that of examining whether or not an adjusted host population's composite structure can control epidemic spreading dynamics. To address this problem, the following three factors in the adjustment of a host population's composite structure will be considered: (1) the size of population to be adjusted, (2) population adjustment in different situations of infection dynamics, and (3) population adjustment in different host populations. These three factors in composite structure adjustments are related to the three deployment factors in vaccination process: (1) vaccine coverage, (2) vaccine releasing time, and (3) vaccine deployment method.

- **Vaccine Coverage** ( $Q_{vaccine}$ )

Vaccine coverage refers to the population that can be covered in vaccination. It determines the directly vaccinated population and the adjustment of the composite structure in a host population.

- **Vaccine Releasing Time** ( $T_{vaccine}$ )

Vaccine releasing time refers to the date when vaccine doses will be deployed. The study of vaccination in different times is aimed at estimating the efficacy of an adjusted host population's composite structure in

the different stages of epidemic spreading.

- **Vaccine Deployment Method** ( $D_{vaccine}$ )

A vaccine deployment method is concerned with the distribution of vaccine doses to different host populations. As has been discussed, host populations may have different infection vulnerabilities and different contact patterns. Different strategies for adjusting a host population's composite structure may impose a distant influence on epidemic spreading dynamics.

We have analyzed the mechanism of vaccination and the related factors in vaccine deployment. In the following sections, we provide a modified compartmental model for characterizing epidemic spreading dynamics and investigate the above-mentioned impacts of vaccine deployment on epidemic control by adjusting a host population's composite structure.

## 4 Epidemic Modeling

Vaccine deployment can have bearings on the dynamics of epidemic spreading, in that it can reduce the rate of virus transmission by adjusting the composite structure of a host population. In order to model the changes of the composite structure, in Section 4.1, we describe a modified compartmental model that considers age-specific host populations with the heterogeneities of infection vulnerability and contact patterns. In Section 4.2, we describe the epidemic spreading dynamics in terms of the compartmental infection and contact-based virus transmission. In Section 4.3, we evaluate the reproduction number  $R_0$  in our proposed model.

### 4.1 Population Infection Vulnerability and Contact Structure

In our proposed model, the entire host population is divided into five age groups,  $A_1(5-14)$ ,  $A_2(15-24)$ ,  $A_3(25-44)$ ,  $A_4(45-64)$ ,  $A_5(65+)$ , which are regarded as five different host populations. Here, we do not include the population between the ages of 0 to 4 for the consideration that they do not have independent social contact activities. The size of population in each age group is based on the demographical statistics of 2006 Hong Kong Population By-census [1].

Based on the population age structure, we address two population heterogeneities in virus infection and transmission respectively: (1) generic infection vulnerability and (2) contact frequency patterns among age groups. The generic infection vulnerability is characterized by infection rate  $\beta$  that the probability of successful infection when susceptible individuals exposed to infectious contacts. We adopt Wu's

work [30] on the estimation of attack rates of H1N1 influenza for parameterizations of the infection rates. For the contact relationships, we use the contact frequency matrix  $C$ , that  $C = \{c_{i,j} | i, j \in (1, N)\}$ , to characterize the heterogeneity of contact activities within or between age groups. The element  $c_{i,j}$  means the average number of contacts for an individual in age group  $A_i$  with individuals in group  $A_j$ . In our present work, for the sake of demonstration, we parameterize the contact matrix with a survey-based study of age-specific contact patterns that observe the contact frequency between age groups by recording the participants' daily contact activities [23]. The contact matrix is presented in Table 1.

**Table 1. Contact Matrix  $C = \{c_{i,j} | i, j \in (1, N)\}$ . A survey based study of human daily contact activities.**

	$A_1$	$A_2$	$A_3$	$A_4$	$A_5$
$A_1$	8.27	1.395	4.165	1.51	0.715
$A_2$	1.395	5.65	2.385	1.83	0.895
$A_3$	4.165	2.385	6.55	3.425	1.383
$A_4$	1.51	1.83	3.425	4.2	2.055
$A_5$	0.715	0.895	1.383	2.055	2.66

## 4.2 Compartmental Infection Dynamics

In each age group, the individuals will be divided into five compartments to represent their infection states. They are: susceptible (**S**), exposed (**E**), infectious (**I**), recovered (**R**) and vaccinated (**V**). We name our model as the SEIR-V infection model. Thus individual virus infection can be represented as state transitions between these infection compartments. The infection dynamics in each age group can be characterized by the percentage of individuals in different infection compartments, that is  $(S_i(t), E_i(t), I_i(t), R_i(t), V_i(t))$ .

For each age group,  $S_i(t), E_i(t), I_i(t), R_i(t), V_i(t)$  ( $i \in (1, \dots, N)$ ) represent the composite structure of a host population. Thus we can use a set of deterministic equations to characterize the epidemic spreading among population age groups. The dynamics of virus compartmental infection are defined as follows:

$$\begin{cases} dS_i/dt = (-\lambda_i) \cdot [S_i - \Delta V_{acc}] + (-\Delta V_{acc}) \\ dE_i/dt = (-\gamma) \cdot E_i + \lambda_i \cdot [S_i - \Delta V_{acc}] \\ dI_i/dt = (-\tau) \cdot I_i + \gamma \cdot E_i \\ dR_i/dt = \tau \cdot I_i \\ dV_i/dt = \Delta V_{acc} \end{cases} \quad (1)$$

$\lambda_i$  is the infection risk for susceptible individuals in group  $A_i$ .  $\lambda_i$  is composed by two parts: (1) risk of infec-

tious contacts and (2) generic infection vulnerability, infection rate  $\beta_i$ . Thus  $\lambda_i$  is defined as:

$$\lambda_i = \frac{1}{N} \cdot \left( \sum_{j=1}^N c_{ij} \cdot \frac{I_j}{P_j} \right) \cdot \frac{S_i}{P_i} \cdot \beta_i \quad (2)$$

The incubation rate  $\gamma$  that we use here is computed based on a generic incubation period for a homogenous population. We parameterize  $\gamma$  with the result of Miller's cross-sectional serological survey on H1N1 immunization and incubation for different age groups [21].  $\tau$  describes the recovery period from the infectious phase to the recovery phase.

## 4.3 Reproduction Number

The basic reproduction number,  $R_0$ , refers to the number of new infection cases caused by a typical infectious individual in a completely susceptible population as defined by Diekmann [10] and Driessche [26]. It is an important indicator for characterizing the impact of virus infection and transmission within a host population. During the virus spreading in Hong Kong, the basic reproduction number  $R_0$  was around 1.4-1.5 at the start of the epidemic [7]. Thus, based on the next-generation matrix technique [26], we can calibrate our SEIR-V model with the actual reproduction number of an epidemics outbreak, in which recovery rate  $\tau$  is the free variable to adjust the parameterizations of our model. The set of parameters in our model are listed in Table 2.

With this framework of epidemic modeling, we can investigate the virus spreading dynamics in each age group. In the next section, we design simulation experiments for vaccine deployment. Based on the simulation results we estimate the impacts of vaccine deployment on epidemic spreading dynamics.

## 5 Simulation and Results

In this section, we describe some simulation-based experiments to examine the impacts of vaccine deployment on epidemic spreading dynamics. In Section 5.1, we first validate our model by simulating the spreading dynamics in 2009 Hong Kong H1N1 epidemic. In Section 5.2, we investigate the variations of infection dynamics in different host populations in terms of infection risks. In Section 5.3, we discuss the relative impacts of the three vaccination deployment factors on virus spreading process and their implications for epidemic control.

**Table 2. Population age structure**

Age Groups	Population $P_i$	Infection Rate $\beta_i$	Incubation Rate $\gamma$	Recovery Rate $\tau$
$A_1$ (5-14)	0.94 m	0.0434	0.25	0.334
$A_2$ (15-24)	0.91 m	0.0158	0.25	0.334
$A_3$ (25-44)	2.30 m	0.118	0.25	0.334
$A_4$ (45-64)	1.86 m	0.046	0.25	0.334
$A_5$ (65+)	0.85 m	0.046	0.25	0.334

### 5.1 2009 Hong Kong H1N1 Swine-flu Epidemic

We collected the data on laboratory confirmed infection cases reported by Center for Health Protection (CHP) of Hong Kong during 2009 Hong Kong H1N1 epidemic. In this study, we study the efficacy of vaccination deployment on epidemic control. However, in practice, the epidemic interventions are not only confined on vaccination but also include many non-pathological strategies, such as social distancing strategies. In Hong Kong H1N1 epidemic, the administrative decision on infection isolation was issued immediately after the appearance of first infection in May 1, 2009. Furthermore, school closure was suggested by public health department in May 8. Since middle of July, many secondary schools were suspended for the appearance of infection cases. Therefore, the actual infection dynamics curve is a reflection of epidemic control by both pathological and non-pathological intervention strategies.

With the model parameter fittings of Hong Kong H1N1 epidemic, we simulate the epidemic spreading dynamics without vaccination in terms of the size of the virus attacked population. In order to reasonably validate the proposed epidemic model, we adopt the data of accumulated infection cases between May 10, 2009 and July 6, 2009 to compare with that of the simulation results. During that time, we believe that the social distancing interventions have only limited effects on the epidemic spreading dynamics. The results of our simulations, as shown in Figure 1, are consistent with the observed epidemic dynamics in Hong Kong. Thus, the proposed SEIR-V model can address a reasonable simulation of H1N1 spreading dynamic, which provide us a consolidated framework for the discussion of vaccination deployment factors.

### 5.2 Virus Spreading Dynamics without Vaccination

For the process of epidemic spreading, the infection curve is a standard bell shape. There is no substantial spreading before day 50. The exponential infection phase of epidemic spreading starts around on day 60. The peak of an infection outbreak is around day 90. Then, the total number of infections decreases and the epidemic decays.

As we have mentioned in previous section, the infection risk,  $\lambda_i$ , in each age group is determined by vulnerability of virus infection and probability of infectious contacts. Figure 2 shows the dynamics of infection risks for each age group during the entire process of virus spreading. In the earlier days of virus spreading, individuals with direct contacts with the initial infected individuals will suffer a higher infection risk. As shown in Figure 2b, during the first ten days, age group  $A_2$  (point line) is the infection initial points, thus its infection risk is the highest. Once the infections widely spread into all age groups, it is changed as the age groups with higher infection rates will face with a higher infection risk. In our simulations, the normalized infection risks are decreased among these age groups,  $A_2$ ,  $A_4$ (dash-dot line),  $A_5$ (plus line), while the infection risk for age group  $A_1$  increased sharply. This can be explained by the following points:

1.  $A_1$  has an intensive contact frequency  $\tau$  with infection initial population group  $A_2$ , which lead a fast transmission of virus to susceptible individuals in  $A_1$ .
2. Individuals in  $A_1$  have strongest assortive mixing contacts, that is the strong diagonal elements in contact frequency matrix as shown in Table 1. That means virus infections would spread fast within population group  $A_1$  which leads to a higher probability of infectious contacts within age host populations.
3. The infection rate in  $A_1$  is of the large value. That means, when exposed in infectious contacts, susceptible individuals would be more vulnerable to virus attack. This also leads to a higher risk of infection in  $A_1$ .

During the stage of an infection outbreak, that all age groups are infection attacked, the age groups with higher contact frequency would suffer higher infection risk. In our simulation, age groups  $A_2$  and  $A_3$  show the relative highest infection risks. This is because during the stage of an epidemic outbreak the infections are rampant in all population age groups. Thus the higher contact frequency

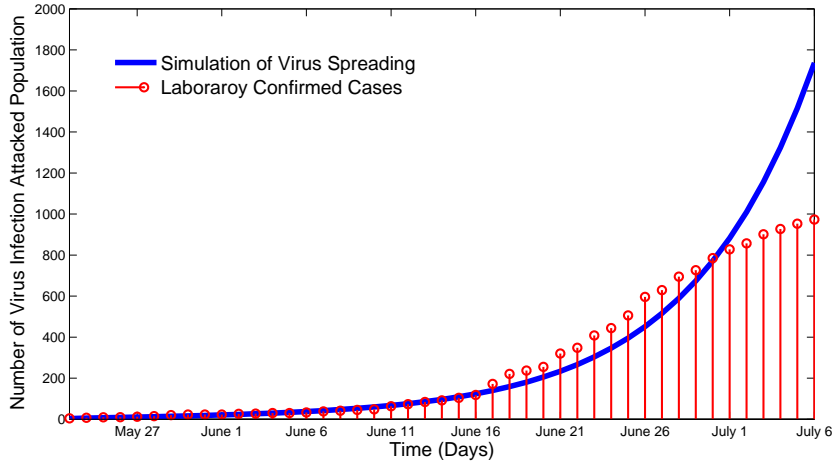


**Figure 1. Comparison of infection dynamics of accumulated infected population between simulation results and laboratory confirmed cases of Hong Kong 2009 H1N1 epidemic during the first 60 days of epidemic.**

means the higher probability of infectious contacts. Those results are consistent with the vaccination deployments that in the earlier day vaccine should be released to individuals with closer contact relationships with infection cases to suppress infection transmission. During the infection dispersing stage, vaccine doses should be released to the most vulnerable individuals to protect them from intensive infection outbreaks. And in the stage of an epidemic outbreak, individuals with high contact frequency should limit their exterior contact activities in order to lower their exposure of infectious contacts [20][18][27]. Thus we suggest infection risk is an important criterion for vaccination deployment.

### 5.3 Infection Dynamics with Vaccine Deployment

In this section, we design some experiments of vaccination strategies with different settings of vaccine deployment. Based on the simulation results, we investigate the impacts of three vaccine deployment factors on virus spreading dynamics.

#### 5.3.1 Vaccine Deployment Settings

In our simulations, vaccine coverage ( $Q_{vaccine}$ ) is set with three levels, as shown in Table 3: (1) small quantity,  $Q_S = 0.3million$  (5% of total population), (2) middle quantity,  $Q_M = 0.6million$  (10%), and (3) large quantity,  $Q_L = 1.2million$  (20%). Vaccine releasing time ( $T_{vaccine}$ ) has three scenarios, as shown in Table 4, (1) pre-spread,  $T_1 = 0$  day, (2) infection dispersing,  $T_2 = 50$  day, and (3) an infection outbreak,  $T_3 = 100$  day. The vaccine

doses are deployed following three deployment methods ( $D_{vaccine}$ ), shown in Table 5: (1) vaccination by transmissibility,  $D_{trans}$ , where the number of vaccine doses deployed to an age group should be proportional to the frequency of contact activities of that age group,  $\sum_{j=1}^N c_{i,j}$ , (2) vaccination by vulnerability,  $D_{vulner}$ , where a vaccination priority is assigned by following a population's infection vulnerability, that is, infection rate  $\beta_i$ , and (3) vaccination by infection risk,  $D_{risk}$ , which means the number of vaccine doses deployed is proportional to the infection risk  $\lambda_i$  in each age group. Then we can investigate the virus spreading dynamics with vaccine deployment in different coverage, releasing time and deployment methods.

**Table 3. Vaccine Coverage**

	Doses	Population
$Q_S$	0.3 million	5%
$Q_M$	0.6 million	10%
$Q_L$	1.2 million	20%

**Table 4. Vaccine Releasing Time**

	Releasing Time	Stage
$T_1$	0 day	Pre-spread
$T_2$	50 day	Infection dispersing
$T_3$	100 day	Infection outbreak

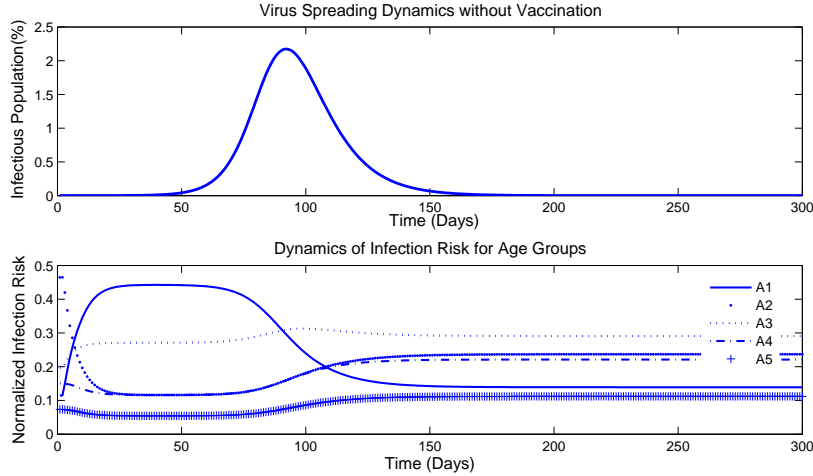


**Figure 2. Virus spreading dynamics without vaccination and the dynamics of infection risk in each host population.**

**Table 5. Deployment Methods**

	Methods	Priority
$D_{trans}$	Transmissibility	$\sum c_{i,j}$
$D_{vulner}$	Vulnerability	$\beta_i$
$D_{risk}$	Infection Risk	$\lambda_i$

### 5.3.2 Virus Spreading Dynamics with Vaccination

In this section, we investigate the impacts of the three vaccine deployment factors on epidemic spreading dynamics by simulating virus infection and transmission with different settings of vaccine deployment.

- **Impact of Vaccine Coverage**

The vaccine coverage ( $Q_{vaccine}$ ) means the total size of vaccinated population, that is, the size of population will be engaged in the adjustment of a host population's composite structure by vaccine deployment. In this section, three batches of vaccine doses will be deployed:  $Q_S = 0.3m$  (5%),  $Q_M = 0.6m$  (10%),  $Q_H = 1.2m$  (20%). Vaccine releasing starts at 50 days since the beginning of infection spread,  $T_{vaccine} = 50day$ , and vaccine deployment to each age group is based on infection risk,  $D_{vaccine} = D_{risk}$ . Then the results of simulations are shown in Figure 3.

As compared with the infection dynamics without vaccination (solid curve), the vaccine deployment can effectively suppress epidemic outbreaks. The coverage of vaccine doses can influence the severity of peak infection. The simulation results show that the size of

the infected population with 10% vaccination coverage (diamond curve) in the peak of an infection outbreak is only half of that with 5% vaccine coverage (triangle curve). Furthermore, for a host population with 20% vaccination coverage (star curve), the dynamics of virus spread may enter a decay stage even before an infection outbreak, which can reduce the size of the virus attacked population significantly. Thus the quantity of available vaccine doses can control the severity of an infection outbreak. If the vaccination coverage is wide enough, a potential outbreak can be eliminated.

- **Impact of Vaccine Releasing Time**

Vaccine releasing time ( $T_{vaccine}$ ) is the date of vaccine doses to be ready for deployment, is of critical importance in the control of virus spread for the infection dynamics in host populations are dynamically changed. In this section, we simulate epidemic spread dynamics with three starting dates of vaccine deployment: (1)  $T_1 = 0$  day, vaccine doses are prepared before virus infection, (2)  $T_2 = 50$  day, virus disperses among the host populations but an outbreak has appeared, and (3)  $T_3 = 100$  day, virus infection outbreaks have occurred. Vaccine coverage is  $Q_{vaccine} = 0.3m$  (5%) and the deployment method is based on infection risk,  $D_{vaccine} = D_{risk}$ . The results of simulations are shown in Figure 4.

In the epidemic spread dynamics without vaccination (solid curve), day 100 is around the peak of an infection outbreak. The simulation results show that

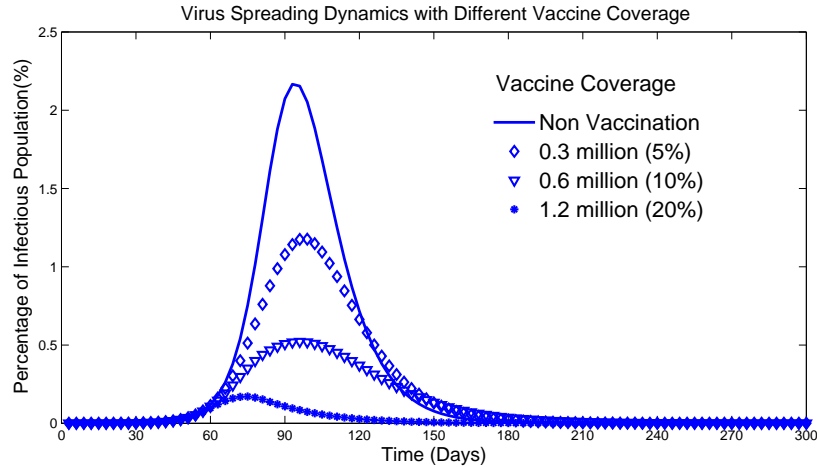


**Figure 3. Virus spreading dynamics with respect to three different settings of vaccine coverage.**

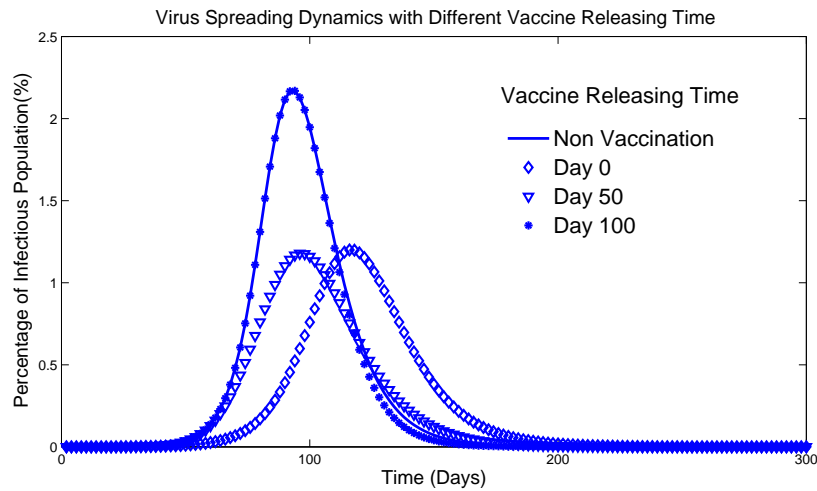


**Figure 4. Virus spreading dynamics with respect to three different settings of vaccine releasing time.**

vaccine deployment during an infection outbreak,  $T_3 = 100$  day (star curve), is ineffective for epidemic control. Therefore, once in the situation of virus mass infection and an epidemic outbreak, vaccination is no longer a commonly-used means for epidemic control. Whereas, in the stage of a prior infection outbreak, the vaccine releasing time plays an important role in epidemic control by delaying infection outbreaks. Simulation results show that the outbreak of infection with vaccination began on day 0 (diamond curve) is delayed around 30 days as compared with that of vaccination began on day 50 (triangle curve). Therefore, an earlier vaccine deployment can delay an infection outbreak during the epidemic spreading process.

#### • Impact of Vaccine Deployment Methods

Given a limited number of vaccine doses, the vaccine doses deployed to different population groups should be differentiated based on their situations in epidemic spreading dynamics. In our simulation, we assume the deployment of vaccine doses to each age group is proportional to the estimation of its normalized vaccination priority. In this section we investigate three measurements of vaccination priority for each age group: (1) vaccination by transmissibility,  $D_{trans}$ , (2) vaccination by infection vulnerability,  $D_{vulner}$ , and (3) vaccination by infection risk,  $D_{risk}$ . Vaccine coverage is

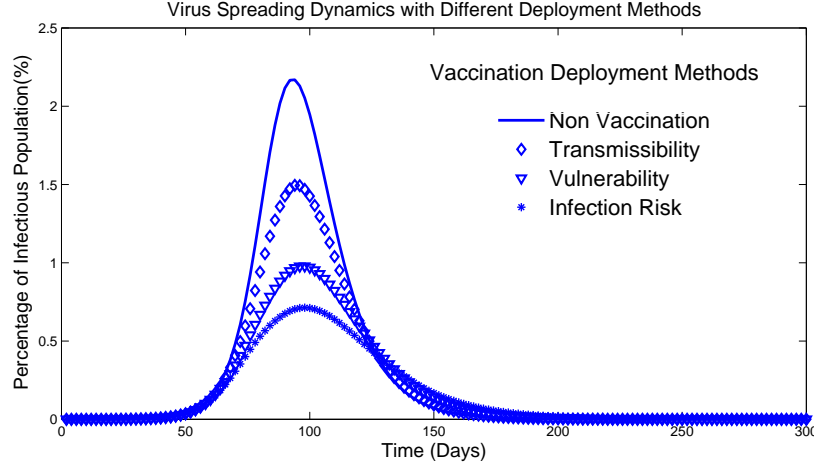


**Figure 5. Virus spreading dynamics with respect to three different vaccine deployment methods.**

$Q_{vaccine} = 0.3m$  (5%) and vaccine releasing time is  $T_2 = 50$  day. The results of simulations are shown in Figure 5.

The deployment of vaccine doses can effectively attenuate the severity of infection dynamics. An optimal deployment of vaccine doses to different population groups can further mitigate the infection outbreaks. The simulation results show that the total size of infected population in the peak of an infection outbreak is sequentially reduced with the vaccine deployment methods of  $D_{trans}$  (diamond curve),  $D_{vulner}$  (triangle curve) and  $D_{risk}$  (star curve). This result shows that the vaccination by infection risk can be more effective in controlling virus spread. This can be explained as the measurement of infection risk is a dynamical indicator that is adjusted by the infection dynamics in each age group. Whereas the other two methods, vaccination by transmissibility and by vulnerability, are static measurements that fail to include variations of infection dynamics in each age group. We propose that an optimal vaccine deployment would be a dynamical process that is correlated infection dynamics in each host population. In our model, we use the infection risk as the vaccine deployment criterion. The infection risk describes the probability of infection for susceptible population in each age group, which is a combination of contact frequency, infection vulnerability and current infection dynamics. Our simulation results show that  $D_{risk}$  as a dynamical/adaptive strategy can self-adjust vaccination priority of host populations to the current situations of epidemic spreading dynamics. The efficacy of  $D_{risk}$  is better than static, transmissibility or vulnerability based vaccination deployment methods.

In summary, vaccine coverage can influence an infection outbreak in that wider vaccination coverage can lower the severity of an infection outbreak and accelerate the phase transition from an infection outbreak to infection decay. Vaccine releasing time plays a role in the time of an infection outbreak that an earlier vaccine deployment can postpone the appearance of an infection outbreak. Finally, an optimal vaccine deployment to different population groups can effectively suppress the size of the infected population during an infection outbreak. We suggest that infection risk may be viewed as a suitable indicator for dynamically estimating the vaccination priority of each age group.

## 6 Conclusion

In practice, vaccine deployment will be constrained by many factors, such as vaccine coverage, releasing time, distribution priorities, and so on. Thus, it is necessary for us to understand the relative impacts of these deployment constraints on the efficacy of vaccine deployment. Based on our simulation results, we have found that the vaccine coverage, that is the size of the vaccinated population, is important for controlling an infection outbreak. The results of our study suggest that a wider vaccination coverage can suppress the peak of an infection outbreak or even eliminate it by accelerating the arrival of the natural decay stage during the process of epidemic spreading.

Vaccine releasing time is another important deployment factor related to the time of an infection outbreak. Our simulation results show that an earlier deployment of vaccine doses can delay an infection outbreak. Furthermore, the days before infection proliferation would be the best

time to vaccinate a susceptible population in order to stop a forth-coming infection outbreak. If vaccine doses are released immediately following infection dispersion, vaccination can decrease the severity of an outbreak. However, if vaccine is available during the phase of an infection outbreak, the control of epidemic spreading through vaccination will no longer be effective.

Given a certain number of vaccine doses and fixed releasing time, an optimal vaccination deployment method would be the next important factor that affects the efficacy of vaccine deployment. Previous work has suggested that a highly vulnerable population should be prioritized, or the population with a high contact frequency should be vaccinated first. Our study agrees with these vaccine deployment criteria. However, we further suggest that the priority of vaccine deployment should be set dynamically/adaptively in different infection phases. To characterize this dynamical process, in our model, we trace the infection risk for each age group. We propose that the infection risk considering both infection vulnerability and infectious contact rate would be an effective criterion for vaccination priority. During the infection spreading process, the composite structure in a host population changes, so do the infection contact rates and infection risk in each host population. Based on the dynamically-evolved infection risk, we have proposed a vaccine deployment method that can dynamically/adaptively modify vaccination priorities. Our simulation results show that our proposed vaccination deployment method is better than vaccination by transmissibility or by vulnerability.

In our current work, we are concerned only with vaccination as an epidemic control strategy that adjusts a host population's composite structure in each host population. Several interesting issues have not been considered in this paper, such as the efficacy of vaccine and time delay for vaccine deployment. These factors can affect the effectiveness of vaccination-based epidemic control. Besides vaccine, the host individuals' acceptance of vaccination can also play an important role in the actual implementation of vaccine deployment. Such issues are worth further studies in the future.

Finally, it should be noted that our simulations can be sensitive to the population structure, such as the percentage of each age group and their contact patterns. Also, related uncertainty in the virus (e.g., H1N1) infection parameters, if any, will require caution.

## References

[1] Statistical tables of the 2006 hong kong population by-census. <http://www.byccensus2006.gov.hk/en/data/data3/index.htm>.

[2] R. M. Anderson and R. M. May. *Infectious Diseases of Humans: Dynamics and Control*. Oxford University Press, 1992.

[3] A. Barrat and M. Barthelemy. *Dynamical Processes on Complex Networks*. Cambridge University Press, 2008.

[4] S. Cauchemez, A.-J. Valleron, P.-Y. Boelle, A. Flahault, and N. M. Ferguson. Estimating the impact of school closure on influenza transmission from sentinel data. *Nature*, 452:750–754, 2008.

[5] Center for Health Protection. Prevention of Human Swine Influenza. [http://www.chp.gov.hk/en/view\\_content/16615.html](http://www.chp.gov.hk/en/view_content/16615.html).

[6] Centers for Disease Control and Prevention. 2009 H1N1 Vaccination Recommendations. <http://www.cdc.gov/h1n1flu/vaccination/acip.htm>.

[7] B. J. Cowling, M. S. Lau, L. M. Ho, S. K. Chuang, T. Tsang, S. H. Liu, P. Y. Leung, S. V. Lo, and E. H. Lau. The effective reproduction number of pandemic influenza: Prospective estimation. *Epidemiology*, 21(6):842–846, November 2010.

[8] D. J. Daley and J. M. Gani. *Epidemic Modelling: An Introduction*. Cambridge University Press, 2000.

[9] O. Diekmann and J. A. P. Heesterbeek. *Mathematical Epidemiology of Infectious Diseases: Model Building, Analysis and Interpretation*. Wiley, 2000.

[10] O. Diekmann, J. A. P. Heesterbeek, and J. A. J. Metz. On the definition and the computation of the basic reproduction ratio  $r_0$  in models for infectious diseases in heterogeneous populations. *Journal of Mathematical Biology*, 28:365–382, 1990.

[11] S. Eubank, H. Guclu, V. S. A. Kumar, M. V. Marathe, A. Srinivasan, Z. Toroczkai, and N. Wang. Modelling disease outbreaks in realistic urban social networks. *Nature*, 429:180–184, May 2004.

[12] C. Gao, J. Liu, and N. Zhong. Network immunization with distributed autonomy-oriented entities. *IEEE Transactions on Parallel and Distributed Systems*, 2010.

[13] N. C. Grassly and C. Fraser. Mathematical models of infectious disease transmission. *Nature Reviews Microbiology*, 6(6):477–487, Jun 2008.

[14] J. Liu, C. Gao, and N. Zhong. Autonomy-oriented search in dynamic community networks: A case study in decentralized network immunization. *Fundamenta Informaticae*, 99:207–226, 2010.

[15] J. Liu and S. Xia. Effective epidemic control via strategic vaccine deployment: A systematic approach. *Proceeding Health Informatics Symposium (IHI'10)*, pages 91–99, November 2010.

[16] A. L. Lloyd and R. M. May. How viruses spread among computers and people. *Science*, 292(5520):1316–1317, 2001.

[17] L. Manzoli, F. Schioppa, A. Boccia, and P. Villari. The efficacy of influenza vaccine for healthy children: A meta-analysis evaluating potential sources of variation in efficacy estimates including study quality. *The Pediatric Infectious Disease Journal*, 26(2):97–106, February 2007.

[18] L. Matrajt and I. M. Longini. Optimizing vaccine allocation at different points in time during an epidemic. *PLoS One*, 5(11):e13767, 2010.

- [19] J. Medlock and A. P. Galvani. Optimizing influenza vaccine distribution. *Science*, 325(5948):1705–1708, September 2009.
- [20] J. Medlock, L. A. Meyers, and A. Galvani. Optimizing allocation for a delayed influenza vaccination campaign. *PLoS Currents Influenza*, 1(RRN1134), 2009.
- [21] E. Miller, K. Hoschler, P. Hardelid, E. Stanford, N. Andrews, and M. Zambon. Incidence of 2009 pandemic influenza a h1n1 infection in england: A cross-sectional serological study. *The Lancet*, 375(9720):1100–1108, March 2010.
- [22] G. J. Milne, J. K. Kelso, H. A. Kelly, S. T. Huband, and J. McVernon. A small community model for the transmission of infectious diseases: Comparison of school closure as an intervention in individual-based models of an influenza pandemic. *PLoS One*, 3(12):e4005, 2008.
- [23] J. Mossong, N. Hens, M. Jit, P. Beutels, K. Auranen, R. Mikolajczyk, M. Massari, S. Salmaso, G. S. Tomba, J. Wallinga, J. Heijne, M. Sadkowska-Todys, M. Rosinska, and W. J. Edmunds. Social contacts and mixing patterns relevant to the spread of infectious diseases. *PLoS Medicine*, 5(3):e74, March 2008.
- [24] E. Negri, C. Colombo, L. Giordano, N. Groth, G. Apolone, and C. L. Vecchia. The efficacy of influenza vaccine for healthy children: a meta-analysis evaluating potential sources of variation in efficacy estimates including study quality. *Vaccine*, 23:2851–2861, 2005.
- [25] M. E. J. Newman. The spread of epidemic disease on networks. *Physical Review*, 66(1), 2002.
- [26] V. D. D. P. and W. James. Reproduction numbers and sub-threshold endemic equilibria for compartmental models of disease transmission. *Mathematical Biosciences*, 180(1-2):29–48, 2002.
- [27] A. R. Tuite, A. L. Greer, M. Whelan, A.-L. Winter, B. Lee, P. Yan, J. Wu, S. Moghadas, D. Buckeridge, B. Pourbohloul, and D. N. Fisman. Estimated epidemiologic parameters and morbidity associated with pandemic h1n1 influenza. *Canadian Medical Association Journal (CMAJ)*, 182(2):131–136, 2010.
- [28] WHO. World Now at The Start of 2009 Influenza Pandemic. <http://www.who.int/mediacentre/news/statements/2009>, June 2009. accessed October 11, 2010.
- [29] WHO. Weekly Update: Pandemic (H1N1) 2009 - update 112. [http://www.who.int/csr/don/2010\\_08\\_06/en/index.html](http://www.who.int/csr/don/2010_08_06/en/index.html), August 2010. accessed October 11, 2010.
- [30] J. T. Wu, E. S. K. Ma, C. K. Lee, D. K. W. Chu, P.-L. Ho, A. L. Shen, A. Ho, I. F. N. Hung, S. Riley, L. M. Ho, C. K. Lin, T. Tsang, S.-V. Lo, Y.-L. Lau, G. M. Leung, B. J. Cowling, and J. S. M. Peiris. The infection attack rate and severity of 2009 pandemic influenza(h1n1) in hong kong. *Clinical Infectious Diseases, IDSA*, 51(10):1184–1191, 2010.

# Exploring the Wait Time Relationships Among Units in the Cardiac Care

Li Tao

Department of Computer Science, Hong Kong Baptist University  
ltao@comp.hkbu.edu.hk

## Abstract

*Discovering and controlling some important factors are effective to shorten long wait time for cardiac surgery. However, prior studies pay attention to the impact of the characteristics (e.g., demand, capacity) on wait time from an isolated unit perspective. Seldom of them consider the cross unit influences. Our object is to evaluate the extent to which the preceding units' characteristics (i.e., demand, capacity, throughput, wait time) account for the wait time of cardiac surgery. Prior to it, we evaluate the relationships of these characteristics within a unit for helping identify the causal paths. Based on the Partial Least Squares-based Structural Equation Modeling approach and the cardiac care data published by Ontario, Canada, our testing results suggest that: (i) Within a single unit, the relationships of the four characteristics may change from unit to unit. The extent and the attributes (i.e., positive impact or negative impact) of the impacts may be varied depending on the unit's properties. (ii) Across units, the characteristics of preceding units have direct and indirect impacts on the wait time of subsequent units.*

## 1 Introduction

The impact of highly fluctuating *demand* (patient inflow) and available service *capacity* on the *performance* of a health care system deserves long standing attention [37][28]. As a key characteristic of a health care system, *demand* is often represented by the number of visits to services [22][49] or the expenditures on services [23][43]. There are many factors affecting the demand of a health care system, including increasing number of patients due to aging and growing population [19], the growing incidence of diseases such as diabetes [35], the development of diagnostic and treatment technology [19], patient status such as the seriousness of the illness [44], the position of the patient on a waiting list [33], the geographic distance to the services [53], patient personal profile (e.g., demographics [13], so-

cioeconomic condition [46][58]), and unpredictable patient behaviors like balking, reneging, jockeying, and repeating [38][20].

Another important characteristic of a health care system is *capacity*, which denotes the resources (e.g., financial, human, physical) available to meet the demand [7][11]. *Capacity* is usually judged by the quantity and quality of resources at hand [19][64] or the working time available [47]. Commonly interested factors affecting the capacity include human resources such as skilled doctors and assistants (e.g., nurses, anesthetists) [64], physical resources such as beds and equipments [19], management strategies such as resources utilization and allocation [14], resource planning and scheduling [14][39].

The third important characteristic of a health care system is the *performance*. Two common indicators of *performance* are *throughput* and *wait time* [38][5][1]. *Throughput* is typically quantified by counting the number of patients who have received a needed health care service in a given time period [50]. It is thus a way to observe the utilization of resource. Different from *throughput*, *wait time* is the amount of time a patient has to wait for receiving a needed health care service [5][4]. Wait time is a particular concern in health care, especially for such key services as catheterization and cardiac surgery. Long wait time is not only an impediment to quality care but also a risk factor for patients [2][21]. There are various measurements for wait time, including (i) median wait time (i.e., the point at which half of the patients have received their treatment and the other half are still waiting), (ii) 90th percentile wait time (i.e., the point at which 90 percent of the patients have received their treatment and the other 10 percent are still waiting), and (iii) queue length (i.e., the total number of patients in the waiting list) [5][4]. *Wait time* is often different depending on patient urgency categories. In a government dominated health care system (e.g., Hong Kong, or Canada), patients who wait in the key units are assigned an urgency rating score according to the presenting symptoms [34] [12][45]. Wait time strategies are adopted based on different urgency categories [5]. The higher urgent score a patient has, the shorter time s/he

will wait.

Prior research has investigated the relationships among *demand*, *capacity*, *throughput*, and *wait time* empirically for a long time. It has revealed that *demand* has a significant impact on *capacity* [10], *throughput*, and *wait time* in various units (e.g., congested recovery room, emergency department) [64] [52] [32] [8]. *Capacity* has also been found to exert a significant negative influence on *throughput* and *wait time* [64][52][32][8][60]. Although some researchers argue that *capacity* has a positive impact on *demand* (higher capacity attracting more patients coming to hospitals, especially the non-urgent patients) [54][55], such argument has not been supported with plenty empirical evidence [26]. In addition, although prior research suggests that the improvement of throughput often accompanies the reduction of wait time [15], the impact of *throughput* on *wait time* has not been empirically investigated.

Health care units and services have generally evolved in silos focusing on satisfying their own customers [41]. Accordingly, extant research has focused on the relationships among the characteristics within a specific unit. However, we argue that it is inadequate to examine the within-unit relationships in isolation [41][18], because, in the real world, all the units in a health care system are networked via patient flow. For example, based on the cardiac treatment guidelines [57][6], units involved in the cardiac care are sequentially connected according to patient visits (Figure 1). Two units with a directed link denote they are temporally related, i.e., patients usually visit the unit the arrow points toward (i.e., subsequent unit) after visiting the unit the arrow points away from (i.e., preceding unit). There usually exists a “funnel and filter” effect (i.e. preceding units determine the absolute numbers and speed of throughput for patients proceeding into the subsequent units) between two temporally related units [3]. In the context of the catheterization unit (CU) and the cardiac surgery unit (SU), a “diagnostic-therapeutic” cascade effect (more catheterization diagnostic tests performed are also likely to have more cardiac surgeries) may also exist [42][63][62]. Thus, investigating the impact of the cross-unit relationships, in addition to within-unit relationships, may reveal more important insights for wait time management [18].

In sum, the impact factors for a health care unit’s performance (i.e., *wait time*, and *throughput*) have been studied from the demand-side and capacity-side perspectives (shown in Figure 2). The relationships among *demand*, *capacity*, *throughput*, and *wait time* have been investigated within a unit. However, little attention has been paid to the relationships among the characteristics in a cross-unit context, a gap this study aims to fill. In this study, we explore whether and how the characteristics of one unit exert an influence on the characteristics (*wait time* in particular) of other temporally related units (Figure 2 shows the overall

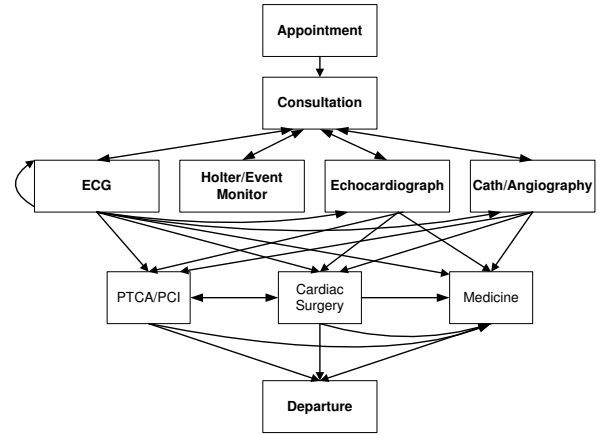


**Figure 1: The unit framework of cardiac care drawn from the cardiac treatment guidelines [57][6].** (ECG: Electrocardiogram; PTCA: Percutaneous transluminal coronary angioplasty; PCI: Percutaneous coronary intervention.)

research framework). We choose the CU and the SU as our research context, because (i) they both provide key services [5][4], (ii) they are temporally connected [56], and (iii) published data about the two units are available<sup>1</sup>. We propose a two-layer wait time model (see detailed discussion in the next section) to investigate the CU’s characteristics on the wait time of SU, with each layer representing a unit. Both within-unit and cross-unit relationships are represented in the model.

We employ the Structural Equation Modeling (SEM) [17] [31] to explore the underlying relationships among the characteristics of two units (i.e., CU and SU). Compared to traditional statistic techniques (e.g., regression, ANOVA), the SEM (i) has the ability to construct latent variables (abstract concepts cannot be measured directly) [29], and (ii) permits exploring and confirming complex (e.g., hierarchical or non-hierarchical, recursive or non-recursive) variable relationships concurrently, in addition to traditional pairwise variable relationships [29][30]. As a result, the SEM enables us to identify the complete causal paths of the cross-unit relationships among latent variables (i.e., *demand*, *capacity*, *throughput*, and *wait time* in this study), which are not supported by any traditional statistic method individually.

The data for this study is obtained from the Cardiac Care Network of Ontario<sup>1</sup> and the Ontario Physician Human Resources Data Centre<sup>2</sup>. We choose such data because it has been collected and released by the Ontario government regularly for more than ten years. It provides comprehensive information on health care services in Ontario for carrying

<sup>1</sup><http://www.ccn.on.ca/>

<sup>2</sup><https://www.ophrdc.org/Home.aspx>

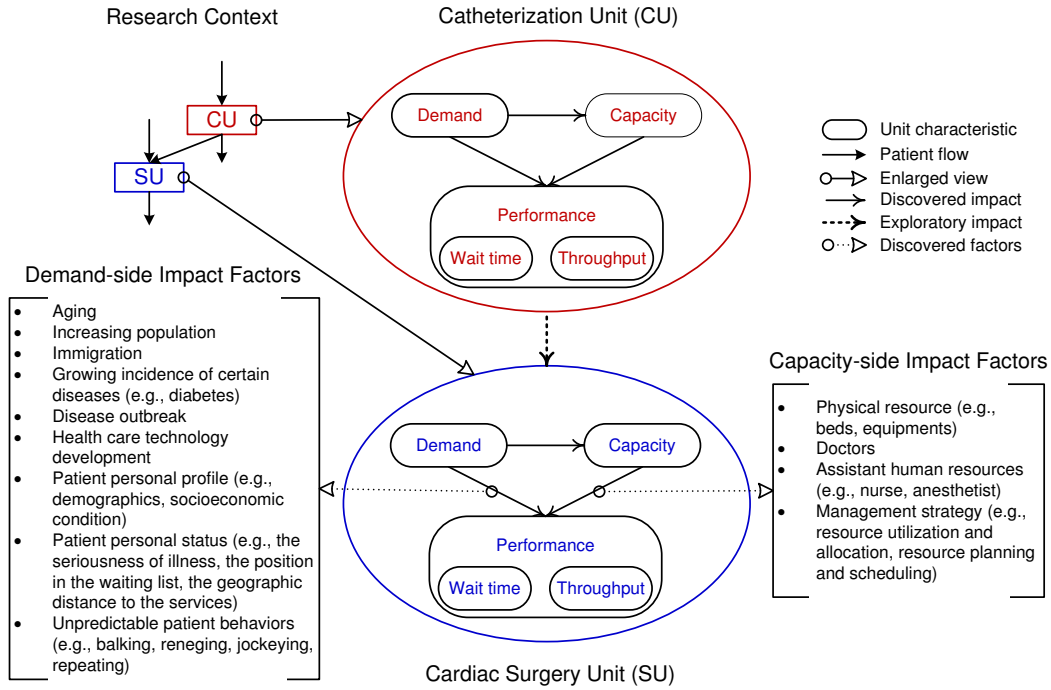


**Figure 2: The research framework with the summarization of the impact factors for throughput and wait time.**

out our research.

It has been recognized that matching fluctuating demand for health care systems with available capacity is important for bettering the outcomes (e.g., morbidity and mortality rate, or wait time) [36]. Thus, there has been extensive research examining the relationships among *demand*, *capacity*, *throughput*, and *wait time*, especially within a single unit.

## 2 HYPOTHESES AND RESEARCH MODEL

Prior research has shown that *demand* has a positive impact on *throughput* and *wait time*. For example, Asaro et al. [8] found in the context of an emergency department that increasing the arrivals (i.e., demand) increased the throughput and the wait time. Harindra et al. [64] showed that clinical demand was an important factor for the access inequalities (i.e., wait time) of catheterization in Canada. Schoenmeyr et al. [52] revealed a sensitive relationship between the caseload (i.e., demand) and the wait time in a congested recovery room. Harewood et al. [32] found that annual wait time for routine endoscopic procedures lengthened dramatically because of a significant increase in annual procedure demand on endoscopy services. Therefore, we hypothesize that *demand* has a positive impact on *throughput*

(**Hypothesis 1, H1**) and *wait time* (**Hypothesis 2, H2**).

In analyzing the current research on the relationship between *demand* and *capacity*, Baker [10] noted that the desire to meet patient demands was a dominant driving force for capacity changing. Buerhaus [16] pointed out that demand increasing for aging population may result in expanding nursing workforce (human resources) to avoid threatening the health care quality. Justman et al. [40] indicated that HIV scale-up needed to develop laboratory systems and infrastructures (i.e., physical resources). Several researchers have argued that *capacity* has a positive impact on *demand* [54]. For instance, Smethurst and Williams [54] noted that for each specific disease, there were many more patients who did not visit the doctors than those who did visit (i.e., “latent” patients). To meet these potential overwhelming demand, the supplier may increase the capacity. Changes in the capacity may trigger changes in demand because more patients are then attracted to the service providers. However, this argument has not been evidently tested [26]. Therefore, in this study, we hypothesize that *demand* has a positive impact on *capacity* (**Hypothesis 3, H3**), and *capacity* does not have an effect on *demand*.

Regarding the impact of *capacity* on *throughput* and *wait time*, prior research has indicated that *capacity* is important to ensure better performance (e.g., *throughput*, *wait time*) of a health care system. For instance, Harindra et al. [64]

found that supplier capacity was an important factor determining access inequalities (i.e., wait time) of catheterization in Canada. Schoenmeyr et al. [52] showed that the physical capacity of supplier (e.g., beds) had a significant impact on the wait time in a congested recovery room. Trzeciak and Rivers [60] also found that inpatient capacity (e.g., beds) had an effect on the throughput in an emergency department. Harewood et al. [32] further showed that modifications in routine clinical practice (i.e., service capacity) could significantly affect procedure’s wait time.

A few studies have revealed that improving the capacity management may help improve the *throughput* and the *wait time* of a health care unit. Mukherjee [59] found that improving the management of physicians (e.g., staffing mix) improved patient throughput. Others showed that improving the capacity management (such as employing intelligent patient scheduling) shortened the wait time efficiently [51][48]. Therefore, in this study, we hypothesize that *capacity* has a positive impact on *throughput* (**Hypothesis 4, H4**) and *wait time* (**Hypothesis 5, H5**) within a unit.

Little prior research has investigated the relationship between *throughput* and *wait time*. Brenner et al. suggested that the improvement of throughput often accompanied the reduction of wait time [15]. An intuitive explanation is that given a stable demand (i.e., determined number of arrivals) in a unit, if resources (physical or human resources) in this unit can be more efficiently used, the patients may be treated quicker. So that the wait time of each patient may be shortened. Therefore, in this study, we hypothesize that *throughput* has a positive impact on *wait time* (**Hypothesis 6, H6**) within a unit.

Prior research has examined the relationships of characteristics among several units within a hospital. Reported by Alter et al. [3], the catheterization has a “funnel and filter” effect on the cardiac surgery. That means the demand and capacity of CU determine the absolute numbers and speed of throughput for patients proceeding into the SU. Similarly, researches have found that the CU and the SU have a “diagnostic and therapeutic” cascade effect [42]. This implies that more catheterization diagnostic tests performed in CU may trigger more patients to undergo cardiac surgeries. Some studies have examined the interrelationships among several units within a hospital for bed allocation [24]. Results showed that inappropriate patient placement was a function of the capacities of all the units. However, such research does not explain clearly how and to what extent the capacity of one unit might influence the wait time of another. In addition, to the best of our knowledge, no prior research has studied whether and to what extent the wait time of one unit influences the wait time of a temporally related unit. In this study, we explore such a wait time relationship between the CU and the SU and hypothesize that (i) the *demand* of CU has a positive impact on the *de-*

*mand* of SU (**Hypothesis 7, H7**), (ii) the *capacity* of CU has a positive impact on the *demand* of SU (**Hypothesis 8, H8**), and (iii) the *wait time* of CU has a positive impact on the *wait time* of SU (**Hypothesis 9, H9**).

Based on the literature review, we postulate a two-layer wait time model (Figure 3) to represent the hypothesized within-unit and cross-unit wait time relationships. In this model, the relationships of four characteristics within the CU and the SU are illustrated in Layer 1 and Layer 2. Cross-unit wait time relationships are represented via the effects between the two layers.

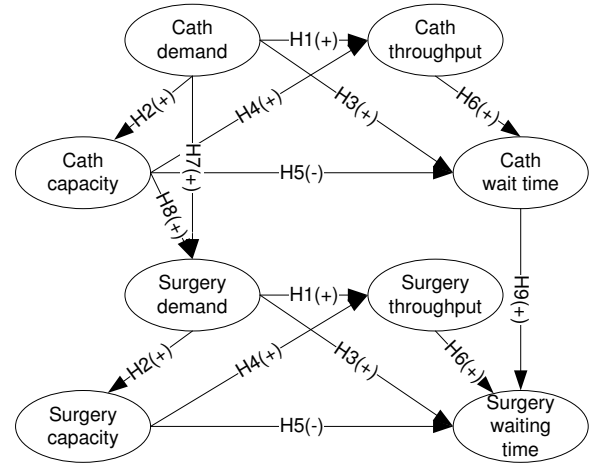


**Figure 3: An illustration of a two-layer wait time model.** (Cath: the abbreviation of catheterization; Surgery: the shorter form of cardiac surgery; H1-H9: the research hypotheses; +/-: a positive or a negative relationship between the variables towards the arrow.)

### 3 METHODS

#### 3.1 Cardiac Care Statistic Data

The data used in this study mainly comes from two data sources in Ontario, Canada. The first one is the Cardiac Care Network (CCN), a network of 18 member hospitals providing cardiac services in Ontario. Since 2004, CCN reports the wait time facts quarterly for selected cardiac procedures (i.e., catheterization, cardiac surgery, and percutaneous coronary intervention) in member hospitals across Ontario. The reported data includes the number of completed cases in a month, the average number of patients waited at the end of a month, the monthly average median wait time, and the monthly average 90th percentile wait time for selected cardiac procedures. In this study, we are particularly interested in the units of catheterization and cardiac surgery, because a regional priority rating score system has been established for these two units (but not other

$$Arrival_{i,j} = Throughput_{i,j} + QueueLength_{i,j} - QueueLength_{i-1,j} \quad (1)$$

units) in Ontario [12][45]. CCN thus provides more detailed statistics for CU and SU than for other units.

We propose an equation (Equation 1) to calculate the monthly average number of arrivals from the existing statistic data, so that the *demands* of CU and SU can be estimated successfully.

where,  $Arrival_{i,j}$  is the monthly average number of arrivals in quarter  $i$  of unit  $j$ ,  $Throughput_{i,j}$  is the monthly average number of patients who have received treatment in quarter  $i$  of unit  $j$ , and  $QueueLength_{i,j}$  is the average number of patients waiting at the end of a month in quarter  $i$  of unit  $j$ .

The second data source is the Ontario Physician Human Resources Data Center (OPHRDC)<sup>2</sup>, a definitive source for information on physician usage in Ontario. It provides data about physicians in Ontario by specialties (e.g., cardiac surgery, diagnostic radiology) annually. In this study, the capacities of SU is exactly measured by the number of physicians specialized in cardiac surgery. The *capacity* of CU is approximately measured by the number of physicians operating diagnostic radiology, because catheterization is one of the tests utilizing radiology, and information about the physicians operating catheterization is unavailable. However, since the OPHRDC data is organized by Local Health Integration Networks (LHINs)<sup>3</sup>, not by hospitals, it needs to be processed so as to align with the CCN data. From the CCN data<sup>1</sup>, we can observe direct correspondences between the LHINs and CCN Member Hospitals, except the LHINs of Toronto Central (TC) and North East (NE), which have more than one CCN hospital. To facilitate data analysis, the two LHINs' data should be decomposed to generate data for related hospitals.

The main idea behind data decomposition is to utilize hospitals' physician ratio (calculated from the number of specific physicians in a hospital to the total number of the specific physicians in the corresponding LHIN in year of 2010) in TC and NE to compute the number of physicians for relevant hospitals from 2005 to 2008. The physician ratios for CU and SU in each hospital in TC and NE can be obtained from the website of The College of Physicians and Surgeons of Ontario (CPSO)<sup>4</sup>, the governing body for medical doctors in Ontario. Then, after observing the OPHRDC data, we found that in TC and NE, the change in CU ranges from 0 to 9 physicians per LHIN year to year (the total average number of catheterization physicians per hospital in the two LHINs is 60); and the change in SU ranges from 0 to 1 physician per LHIN year to year (the total average number

of cardiac surgery physicians per hospital in the two LHINs is 7). Therefore, we can assume that the physician ratios in TC and NE are relatively stable, i.e., the physician ratios are the same in each year since 2005. So that the number of specific physicians in each hospital can be calculated successfully by the specific physician ratio of each hospital multiplied by the number of the specific physicians in the corresponding LHIN each year.

By integrating and processing the two sets of data as discussed above, we obtain comprehensive information about the 11 hospitals that provide catheterization and cardiac surgery. Table 1 outlines the characteristics of the two units and their measurements with the data summary. Specifically, we focus on the data from April 2005 to March 2008 (three fiscal years in total), because the year of 2004 is the end of the first six-year cardiac expansion plan [19] and the start of the second ten-year cardiac improvement plan [5][65]. In total, there are 132 data points for CU and SU (one hospital one quarter is regarded as a data point). In the next subsection, we will describe the statistical analysis methods used to investigate within-unit and cross-unit wait time relationships.

### 3.2 Statistical Analysis

In this study, we employ the structural equation modeling (SEM) to test the proposed two-layer wait time model (Figure 3) as well as the related hypotheses. The SEM is a second generation data analysis technique [9] that is efficient in testing and estimating causal relations using a combination of statistic data and qualitative causal assumptions [17]. The SEM and traditional statistic methods (e.g., regression, ANOVA, LOGIT) differ in important ways [29]: whereas traditional statistic methods can only test pairwise relationships between observed variables, the SEM can construct latent variables (abstract concepts that cannot be measured directly) and assess complex (e.g., hierarchical, recursive) causal paths among such variables. Therefore, the SEM technique has been increasingly used in social science, behavioral science and management science, for modeling complex and multivariate relationships [31].

There are two classes of SEM: Partial Least Squares (PLS)-based SEM and covariance based SEM [29]. In this study (which is exploratory rather than confirmatory), the PLS-based SEM is employed because it is more suitable for theory building (i.e., allowing both confirmatory and exploratory modeling), whereas the covariance based SEM is more suitable for theory testing (i.e., more efficient in confirmatory modeling) [29].

In the data analysis process, the measurements for the

<sup>3</sup>LHINs: created by the government, not-for-profit corporations based on geographic regions to determine the community's health service needs and priorities (<http://www.lhins.on.ca/>).

<sup>4</sup><http://www.cpso.on.ca/>

**Table 1:** A summary of the secondary data used in this study

Characteristics	Measurements	CU	SU
Demand	Monthly average number of arrivals in a quarter	335	82
Capacity	Number of physicians, yearly	60	7
Throughput	Monthly average number of completed patients	347	83
Wait time	Median wait time of U/S/E patients	1/10/15	3/6/19
	90th percentile wait time of U/S/E patients	5/27/31	11/31/49
	90th percentile wait time of U/S/E patients	5/27/31	11/31/49
	Average number of waiting at the end of a month	101	58

CU: Catheterization unit; SU: Cardiac surgery unit; U: the urgent category; S: the semi-urgent category; E: the elective category.

*wait time* are modeled as formative indicators [29] rather than reflective ones [29]. A formative model is used when a latent construct (i.e., factor, such as *demand*, *capacity*, *throughput*, and *wait time* in this study) is viewed as an explanatory combination of its manifest variables (i.e., measurements). In contrast, in a reflective model, the manifest variables are viewed as being caused by an underlying common dimension or a construct [25]. In this study, the manifest variables for *wait time* are not interchangeable or correlated with one another because they measure the *wait time* from different perspectives. Therefore, the latent variable *wait time* is the summation of its corresponding manifest variables. In other words, the measurement items of *wait time* would be formative of the construct of *wait time*.

In addition, we utilize the data of CU and SU in the same quarter to test the cross-unit relationships. Because the longest wait time for a patient in the CU is around one month, we can assume that the great majority of patients who need cardiac surgery will be transferred from the CU to the SU within the period of a quarter. In the next section, we will present the results from the PLS analysis.

## 4 RESULTS

In this section, we discuss the findings of data analysis from two aspects: (i) how do the characteristics impact one another within a unit; (ii) how do the characteristics of CU impact the characteristics of SU, and particularly on the *wait time* of SU.

In this study, the software SmartPLS<sup>5</sup> is utilized for path modeling and PLS-based data analysis. The results are shown in Figure 4.

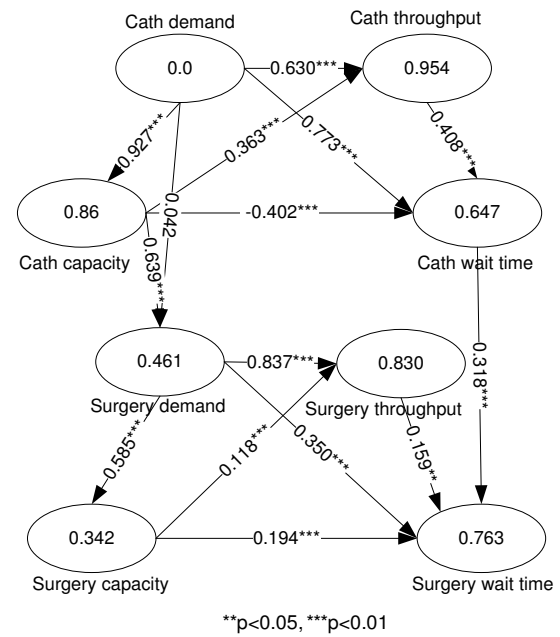


**Figure 4:** PLS test results based on a formative measurement model. (Cath: the abbreviation of catheterization; Surgery: the shorter form of cardiac surgery.)

### 4.1 Within-Unit Relationships

As illustrated in Figure 4, in support of H1-H3, *demand* has a significant positive effect on *throughput*, *capacity*, and *wait time* respectively. The path coefficients for the effect of *demand* on *throughput* for CU and SU are  $\beta = 0.630$  ( $t=23.211$ ,  $p < 0.01$ ) and  $\beta = 0.837$  ( $t=48.413$ ,  $p < 0.01$ ) respectively. The path coefficients for the effect of *demand* on *capacity* are  $\beta = 0.927$  ( $t=152.707$ ,  $p < 0.01$ ) and  $\beta = 0.585$  ( $t=24.344$ ,  $p < 0.01$ ) for CU and SU respec-

<sup>5</sup><http://www.smartpls.de/>

tively. The path coefficients for the effect of *demand* on *wait time* are  $\beta = 0.733$  ( $t=5.830, p < 0.01$ ) and  $\beta = 0.350$  ( $t=4.705, p < 0.01$ ) for CU and SU respectively. These results confirm findings from prior research, providing further evidence that *demand* is an important predictor for *capacity*, *throughput* and *wait time* within a health care unit.

In support of H4, *capacity* has a significant positive impact on *throughput*. For CU, the path coefficient for the effect of *capacity* on *throughput* is  $\beta = 0.363$  ( $t=13.404, p < 0.01$ ). For SU, the path coefficient is  $\beta = 0.118$  ( $t=4.73, p < 0.01$ ). These results also confirm findings from prior research, suggesting that improvement in capacity will lead to improved throughput within a unit.

Hypothesis H5 is only partially supported by our data. For CU, *capacity* has a significant negative impact on *wait time* ( $\beta = -0.402, t=4.186, p < 0.01$ ), thus supporting H5. However, for SU, *capacity* has a significant positive impact on *wait time* ( $\beta = 0.194, t=5.247, p < 0.01$ ). Thus H5 is not supported. This finding is different from that of prior research, which suggests that improvement in a unit's capacity can significantly shorten its patients' wait time.

The negative effect of *capacity* on *wait time* for SU could be explained by the view of Smethurst and Williams [54]. Their work figured out that the hospital waiting lists were self-regulating. That means when capacity increases for meeting the demand, the demand may change again, creating an even greater demand [54]. This is because a mass of "hidden" patients [54] (who have diseases but are not willing to go to hospitals) may be attracted to visit hospitals for believing be treated quicker. Hence, expanding the capacity in SU may help the wait time temporarily but, it will then increase, even get much longer than before because of more patients coming.

In support of H6, *throughput* has a significant positive impact on *wait time* within a unit. For CU, the path coefficient is  $\beta = 0.408$  ( $t=2.751, p < 0.01$ ). For SU, the path coefficient is  $\beta = 0.159$  ( $t=1.974, p < 0.01$ ). This finding suggests that *throughput* and *wait time* have the same changing trends, which is against the expectation that the improvement of throughput results in the improvement of wait time.

A possible explanation for this unexpected finding is the queue jumping behavior of urgent patients. Queue jumping means that urgent patients can skip the queue and jump to any position on a waiting list because of their treatment priority [27]. If more urgent patients arrive, units would like delay the treatment for the semi-urgent and elective patients in order to serve high priority patients in time, indirectly making these non-urgent patients wait longer. The overall wait time for the unit may also be increased as a result. This finding implies that *throughput* and *wait time* are inconsistency to indicate the quality of the unit's performance in some cases. Therefore, we should distinguish which char-

**Table 2:** A summary of hypotheses testing results

Hypotheses	Supported?
H1-H4, H6, H8, H9	Fully supported
H5	Partially supported
H7	Not supported

acteristics (i.e., *throughput* and *wait time*) are more suitable to evaluate the qualities of health care system in different research contexts.

## 4.2 Cross-Unit Relationships

As show in Figure 4, H7 is not supported by our data ( $\beta = 0.042, t = 0.529, p > 0.1$ ). The *demand* of CU does not have a significant impact on the *demand* of SU. While in support of H8, the *capacity* of CU has a significant positive impact on the *demand* of SU ( $\beta=0.639, t = 8.096, p < 0.01$ ).

The two findings could explain the formation of the "funnel and filter" effect [3] between the CU and the SU. Findings denote that on one hand, more arrivals in the CU usually lengthen the waiting list, but do not affect the throughput proceeding to the SU heavily. This may be because the CU always has a waiting list in reality (observed from the historical data published by CCN). On the other hand, to a large extent, the capacity of CU determines the absolute numbers and speed of throughput for patients proceeding into the SU, so that the "funnel and filter" is formed.

In support of H9, the results of our analysis reveal that the *wait time* of CU has a significant positive impact on the *wait time* of SU ( $\beta = 0.318, t = 6.672, p < 0.01$ ). It provides strong evidence that the *wait time* of CU is an important predictor for the *wait time* of SU. A possible explanation for such an effect is delay cascade [61]. Unnikrishnan et al. [61] simulated and observed that delays would cascade in an emergency department (ED) network (all the EDs in different hospitals were networked by the transfer paths of ambulances). In other words, delays in an ED will result in wait time increasing in other EDs nearby. The cardiac care has a similar unit network (Figure 1) in a hospital. Therefore, delays in one unit may spread to other related units in the unit network, forming the direct cross-unit wait time relationship as a result.

Table 2 summarizes the hypotheses testing results. Besides, an examination of our results (Figure 4) reveals both direct and indirect causal paths from characteristics of CU to the *wait time* of SU. In addition to a direct causal link from the *wait time* of CU to the *wait time* of SU, the *demand* and the *capacity* of CU also have indirect effect on the *wait time* of SU. In other words, the *wait time* of SU may be influenced by the CU via the following causal paths:

(i) the *wait time* of CU  $\rightarrow$  the *wait time* of SU; (ii) the *demand* of CU  $\rightarrow$  the *capacity* of CU  $\rightarrow$  the *demand* of SU  $\rightarrow$  the *wait time* of SU; (iii) the *demand* of CU  $\rightarrow$  the *capacity* of CU  $\rightarrow$  the *demand* of SU  $\rightarrow$  the *capacity* of SU, or the *throughput* of SU  $\rightarrow$  the *wait time* of SU. The *demand* of CU appears to be the most essential driving force for the *wait time* dynamics in the CU as well as in the SU.

## 5 DISCUSSION

In this study, we have examined whether and how characteristics of a preceding unit can affect the *wait time* of the cardiac surgery unit. Different from prior research, this study employs the structure equation modeling approach to assessing such cross-unit wait time relationships from the secondary data published in Ontario, Canada. The results of our analysis have validated the proposed two-layer wait time model, thus providing empirical support to the hypothesized relationships among four characteristics (i.e., *demand*, *capacity*, *throughput*, and *wait time*) both within a unit and across units.

The key findings in this study are as follows. First and foremost, our results show that the *wait time* of CU has a direct positive impact on the *wait time* of SU. This is a novel result, as prior research has seldom examined the influence of one unit's *wait time* on the *wait time* of a subsequent unit on the patient flow process. A possible explanation for such effect is delay cascade in the cardiac care unit network (Figure 1), proposed by Unnikrishnan et al. [61].

In addition, the results of our analysis provide empirical evidence for previous findings that: (i) within a unit, *demand* has a positive effect on *capacity*, *throughput*, and *wait time*; (ii) within a unit, *capacity* has a positive effect on *throughput*; (iii) across units, the *demand* of one unit will be positively influenced by the *capacity* of the preceding unit.

We have also obtained some surprising findings: (i) the relationship between *capacity* and *wait time* differs in units with different profiles (e.g., different patient proportion in each urgency category); (ii) *throughput* has a positive effect on *wait time* within a unit; (iii) there exist direct and indirect wait time relationships between temporally-related units; (iv) the *demand* of CU is an essential predictor for the other characteristics of CU and SU.

Besides, we have examined the quality of indicators' reflection for the latent variable *wait time* in the two-layer wait time model. Among the seven indicators, we have found that the queue length is the best reflection of *wait time*. This may be because the queue length involves the information of all the urgency categories, while other six measures only have the information of a specific urgency category. Also, we have found that the median wait time of semi-urgent/elective patient are more informative to indicate *wait time* than the rest of the indicators. Possible ex-

planations for this finding are as follows. Firstly, according to the treatment policy for cardiac patients in Ontario, the semi-urgent and elective patients should wait much longer than urgent patients. Therefore, the two kinds of patients are more significant contributors for the *wait time* of a unit in cardiac care. Secondly, in the real operation, a majority of patients in each urgency category wait close to the median wait time than the 90% percentile wait time. Therefore, the median wait time is more informative than 90% percentile wait time.

Finally, the PLS-based SEM method proves to be an appropriate tool for assessing the hypothesized within-unit and cross-unit wait time relationships illustrated in our two-layer wait time model. With its capability of multivariate modeling and latent variable construction, the SEM approach enables us to validate the relationships among characteristics both within a unit and across two temporally-related units in this study.

It should be pointed out that there are still some issues that remain to be investigated in our future study. Since the number of physicians operating catheterization is unavailable, we have substituted it with the number of physicians specialized in diagnostic radiology. This substitution might not exactly reflect the true capacity of the catheterization. Also, we have used the current physician ratio obtained from CPSO to decompose the aggregated OPHRDC data from LHIN-based to hospital-based. Data produced by this conversion process might not be very accurate because the physician ratio might change from year to year. Moreover, we have used only one indicator for *demand*, *capacity*, and *throughput*, which would make it difficult for us to assess the reliability of the constructs. Nevertheless, this study represents a valuable attempt to use the SEM method to explore factors affecting wait time from a multi-unit perspective, based on secondary data. Our findings can also provide valuable insights to researchers and practitioners in other government dominated health care systems in their efforts to reduce wait time.

## References

- [1] *The Reform of Health Care Systems: A Review of Seventeen OECD Countries*. OECD Publishing, 1994.
- [2] A. V. Ackere and P. C. Smith. Towards a macro model of national health service waiting lists. *System Dynamics Review*, 15(3):225–252, 1999.
- [3] D. A. Alter, P. Austin, and J. V. Tu. Use of coronary angiography, angioplasty and bypass surgery after acute myocardial infarction in Ontario. In D. Naylor and P. Slaughter, editors, *Cardiovascular Health and Services in Ontario*. ICES Atlas, 1999.
- [4] D. A. Alter, E. A. Cohen, G. Cernat, K. W. Glasgow, P. M. Slaughter, and J. V. Tu. Cardiac procedures. In J. V. Tu,

- S. P. Pinfold, P. McColgan, and A. Laupacis, editors, *Access to Health Services in Ontario*. ICES Atlas, 1st edition, 2005.
- [5] D. A. Alter, E. A. Cohen, X. Wang, K. W. Glasgow, P. M. Slaughter, and J. V. Tu. Cardiac procedures. In J. V. Tu, S. P. Pinfold, P. McColgan, and A. Laupacis, editors, *Access to Health Services in Ontario*. ICES Atlas, 2nd edition, 2006.
- [6] E. M. Antman, D. T. Anbe, P. W. Armstrong, E. R. Bates, L. A. Green, M. Hand, J. S. Hochman, and H. M. Krumholz. ACC/AHA guidelines for the management of patients with ST-Elevation myocardial infarction-executive summary. *Circulation*, 110:588–636, 2004.
- [7] Z. Arif and E. Roberts. Improving access to services: A practical approach to understanding demand and capacity to support service re-design. In R. Jones and F. Jenkins, editors, *Managing Money, Measurement and Marketing in the Allied Health Professions*, pages 278–290. Radcliffe Publishing Ltd, 2010.
- [8] P. V. Asaro, L. M. Lewis, and S. B. Boxerman. The impact of input and output factors on emergency department throughput. *Academic Emergency Medicine*, 14:235–242, 2007.
- [9] R. P. Bagozzi and C. Fornell. Theoretical concepts, measurements, and meaning. In C. Fornell, editor, *A Second Generation of Multivariate Analysis*, pages 24–38. Praeger, 1982.
- [10] L. C. Baker. The challenges of health system capacity growth, 2008.
- [11] D. Bamford and E. Chatziaslan. Healthcare capacity measurement. *International Journal of Productivity and Performance Management*, 58(8):748–766, 2010.
- [12] A. Basinski, D. G. Almond, R. G. G. James, and C. D. Naylor. Rating the urgency of coronary angiography: Results of an expert panel process. *The Canadian Journal of Cardiology*, 9(4):313–321, 1993.
- [13] C. M. Blanchard, R. D. Reid, L. I. Morrin, L. McDonnell, K. McGannon, R. Rhodes, J. Spence, and N. Edwards. Demographic and clinical determinants of moderate to vigorous physical activity during home-based cardiac rehabilitation: The home-based determinants of exercise (HOME) study. *Journal of Cardiopulmonary Rehabilitation & Prevention*, 30(4):240–245, 2010.
- [14] C. Brecht, D. Erik, and J. Belien. Operating room planning and scheduling: A literature review. *European Journal of Operational Research*, April 2009.
- [15] A. Brenner, Z. Zeng, Y. Liu, J. Wang, J. Li, and P. K. Howard. Modeling and analysis of the emergency department at University of Kentucky Chandler Hospital using simulations. *Journal of Emergency Nursing*, 36:303–310, 2010.
- [16] P. I. Buerhaus. Current and future state of the US nursing workforce. *The Journal of the American Medical Association*, 300(20):2422–2424, 2008.
- [17] B. M. Byrne. *Structural Equation Modeling with AMOS: Basic Concepts, Applications, and Programming (2nd)*. Routledge, 2009.
- [18] Canadian Institute for Health Information. Waiting for Health Care in Canada: What We Know and What We Don't Know, 2006.
- [19] Cardiac Care Network of Ontario. Cardiac Surgery in Ontario: Ensuring Continued Excellence and Leadership in Patient Care, 2006.
- [20] S. Creemers and M. R. Lambrecht. ISR Technical Report: Healthcare Queueing Models, 2008.
- [21] R. F. Davies. Waiting lists for health care: A necessary evil. *Canadian Medical Association*, 160(10):1469–1470, May 1999.
- [22] P. Deb and P. K. Trivedi. Demand for medical care by the elderly in the United States: A finite mixture approach. *Journal of Applied Econometrics*, 12:313–336, 1997.
- [23] N. Duan, W. G. Manning, C. N. Morris, and J. P. Newhouse. A comparison of alternative models for the demand for medical care. *Journal of Business and Economic Statistics*, 1:115–126, 1983.
- [24] M. B. Dumas. Simulation modeling for hospital bed planning. *Simulation*, 43:69–78, 1984.
- [25] C. Fornell and F. Bookstein. Two structural equation models: LISREL and PLS applied to consumer exit-voice theory. *Journal of Marketing Research*, 19:440–452, 1982.
- [26] R. P. Freckleton and W. J. Sutherland. Do power laws imply self-regulation? *Nature*, 413:382, 2001.
- [27] S. M. Friedman, L. Schofield, and S. Tirkos. Do as I say, not as I do: A survey of public impressions of queue-jumping and preferential access. *European Journal of Emergency Medicine*, 14:260–264, 2007.
- [28] D. Fusco, C. Saitto, M. Arcà, and C. A. Perucci. Cyclic fluctuations in hospital bed occupancy in Roma (Italy): Supply or demand driven? *Health Service Management Research*, 16(4):268–275, 2003.
- [29] D. Gefen, D. W. Straub, and M.-C. Boudreau. Structural equation modeling and regression: Guidelines for research practice. *Communications of the Association for Information Systems*, 4(7), 2000.
- [30] D. W. Gerbing and J. C. Anderson. An updated paradigm for scale development incorporating unidimensionality and its assessment. *Journal of Marketing Research*, 25:186–192, 1988.
- [31] J. F. Hair, R. E. Anderson, R. L. Tatham, and W. C. Black. *Multivariate Data Analysis with Readings (5th edition)*. Prentice Hall, 1995.
- [32] G. C. Harewood, H. Ryan, F. Murray, and S. Patchett. Potential impact of enhanced practice efficiency on endoscopy waiting times. *IRISH Journal of Medical Science*, 178(2):187–192, 2009.
- [33] D. J. Heaney, J. G. Howie, and A. M. Porter. Factors influencing waiting times and consultation times in general practice. *The British Journal of General Practice*, 41(349):315–319, 1991.
- [34] Hong Kong Government. Hong Kong Year Book 2006: Chapter 8, Health, 2006.
- [35] P. Hossain, B. Kavar, and M. E. I. Nahas. Obesity and diabetes in the developing world – A growing challenge. *The New England Journal of Medicine*, 356:213–215, 2007.
- [36] R. Hughes and D. Lee. Using data describing physician inpatient practice patterns: Issues and opportunities. *Health Care Management Review*, 16(1):33–40, 1991.

- [37] E. P. Jack and T. L. Powers. A review and synthesis of demand management, capacity management and performance in health-care services. *International Journal of Management Reviews*, 11(2):149–174, 2009.
- [38] J. Jun, S. H. Jacobson, and J. R. Swisher. Application of discrete-event simulation in health care clinics: A survey. *The Journal of the Operational Research Society*, 50(2):109–123, 1999.
- [39] J. B. Jun, S. H. Jacobson, and J. R. Swisher. Application of discrete-event simulation in health care clinics: A survey. *The Journal of the Operational Research Society*, 50(2):109–123, 1999.
- [40] J. E. Justman, S. Koblavi-Deme, A. Tanuri, A. Goldberg, L. F. Gonzalez, and C. R. Gwynn. HIV scale-up and global health systems. *Journal of Acquired Immune Deficiency Syndromes*, 52:s30–s33, 2009.
- [41] L. Kosnik. Breakthrough demand-capacity management strategies to improve hospital flow, safety, and satisfaction. In R. W. Hall, editor, *Patient Flow: Reducing Delay in Healthcare Delivery*, pages 101–122. Springer, 2006. International Series in Operations research & Management Science.
- [42] F. L. Lucas, A. E. Siewers, D. J. Malenka, and D. E. Wennberg. The diagnostic-therapeutic cascade revisited: Coronary angiography, CABG and PCI in the modern era. *Circulation*, 118(25):2797–2802, 2008.
- [43] W. G. Manning, J. P. Newhouse, N. Duan, E. B. Keeler, A. Leibowitz, and M. S. Marquis. Health insurance and the demand for medical care: Evidence from a randomized experiment. *American Economic Review*, 77:251–277, 1987.
- [44] National Institute for Health Research. Research Summary Report: Organizational Factors that Influence Waiting Times in Emergency Departments, 2007.
- [45] C. D. Naylor, R. S. Baigrie, B. S. Goldman, J. A. Cairns, and D. S. B. N. Berman. Assigning priority to patients requiring coronary revascularization: Consensus principles from a panel of cardiologists and cardiac surgeons. *The Canadian Journal of Cardiology*, 7(5):207–213, 1991.
- [46] E. Odubanjo, K. Bennett, and J. Feely. Influence of socioeconomic status on the quality of prescribing in the elderly – A population based study. *British Journal of Clinical Pharmacology*, 58(5):496–502, 2004.
- [47] J. J. Pandit, M. Pandit, and J. M. Reynard. Understanding waiting lists as the matching of surgical capacity to demand: Are we wasting enough surgical time? *Anaesthesia*, 65(6):625–640, 2010.
- [48] J. Patrick, M. Puterman, and M. Queyranne. Dynamic multi-priority patient scheduling for a diagnostic resource. *Operations Research*, 56(5):1507–1525, 2008.
- [49] W. Pohlmeier and V. Ulrich. An econometric model of the two-part decisionmaking process in the demand for health care. *The Journal of Human Resources*, 30:339–361, 1995.
- [50] R. M. Rosser. A health index and output measure. In S. R. Walker and R. M. Rosser, editors, *Quality of Life Assessment: Key Issues in the 1990s*, pages 151–178. Kluwer Academic Publishers, 1993.
- [51] P. Santibáñez, V. S. Chow, J. French, M. L. Puterman, and S. Tyldesley. Reducing patient wait times and improving resource utilization at British Columbia cancer agency’s ambulatory care unit through simulation. *Health Care Management Science*, 12(4):392–407, 2009.
- [52] T. Schoenmeyr, P. F. Dunn, D. Gamarnik, R. Levi, D. L. Berger, B. J. Daily, W. C. Levine, and W. S. Sandberg. A model for understanding the impacts of demand and capacity on waiting time to enter a congested recovery room. *Anesthesiology*, 110(6):1293–1304, 2009.
- [53] J. E. Seidel, C. A. Beck, G. Pocobelli, J. B. Lemaire, J. M. Bugar, and H. Quan. Location of residence associated with the likelihood of patient visit to the preoperative assessment clinic. *BMC health services research*, 6(13), 2006.
- [54] D. P. Smethurst and H. C. Williams. Are hospital waiting lists self-regulating? *Nature*, 410:652–653, 2001.
- [55] D. P. Smethurst and H. C. Williams. Self-regulation in hospital waiting lists. *Journal of the Royal Society of Medicine*, 95:287–289, 2002.
- [56] G. Spencer, J. Wang, L. Donovan, and J. V. Tu. Report on Coronary Artery Bypass Surgery in Ontario, Fiscal Years 2005/06 and 2006/07, 2008.
- [57] Texas Heart Institute at St. Luke’s Episcopal Hospital. Arrhythmia Diagnostic Tools.
- [58] A. Tramarin, S. Camprostrini, K. Tolley, and F. D. Lalla. The influence of socioeconomic status on health service utilisation by patients with AIDS in North Italy. *British Journal of Clinical Pharmacology*, 45(6):859–866, 1997.
- [59] S. Trzeciak and E. P. Rivers. A simulation model for management of operations in the pharmacy of a hospital. *Simulation*, 56:91–103, 1991.
- [60] S. Trzeciak and E. P. Rivers. Emergency department overcrowding in the united states: An emerging threat to patient safety and public health. *American Journal of Medical Quality*, 20:402–405, 2003.
- [61] K. P. Unnikrishnan, D. Patnaik, and T. J. Iwashyna. Discovering specific cascades in critical care transfer networks. In *1st ACM International Health Informatics Symposium, Arlington, Virginia, USA, 11-12 November 2010*, pages 541–544, 2010.
- [62] D. Verrilli and H. G. Welch. The impact of diagnostic testing in therapeutic interventions. *The Journal of the American Medical Association*, 275:1189–1191, 1996.
- [63] D. E. Wennberg, J. D. J. Dickens, L. Biener, F. J. Fowler, D. N. Soule, and R. B. Keller. Do physicians do what they say? the inclination to test and its association with coronary angiography rates. *Journal of General Internal Medicine*, 12:172–176, 1997.
- [64] H. C. Wijeyesundera, T. A. Stukel, A. Chong, M. K. Nataraajan, and D. A. Alter. Impact of clinical urgency, physician supply and procedural capacity on regional variations in wait times for coronary angiography. *BMC Health Services Research*, 10(5), 2010.
- [65] S. Willcox, M. Seddon, S. Dunn, R. T. Edwards, J. Pearse, and J. V. Tu. Measuring and reducing waiting times: A cross-national comparison of strategies. *Health Affairs*, 26(4):1078–1087, 2007.

# Multi-level Semantic Characterisation and Refinement for Web Image Search

Yuanxi Li

Department of Computer Science  
Hong Kong Baptist University  
Hong Kong  
yxli@comp.hkbu.edu.hk

C.H.C. Leung

Department of Computer Science  
Hong Kong Baptist University  
Hong Kong  
clement@comp.hkbu.edu.hk

**Abstract**—With the increasing number of Web images and social photograph sharing sites, effective search of real-world images becomes a formidable challenge and an important necessity. Different indexing and annotation algorithms are required for different types of Web images. To meet the challenge and provide satisfactory search results to users, we present a multi-level method with four levels differentially applied to different types of Web images. The performance of our method is evaluated by experiments on thousands of Web images and tags in different subsets, and our approach is able to yield highly promising results compared with applying a single method to all types of Web images.

**Keywords**- *image retrieval; scene analysis ; automatic annotation; CYC inference; MPEG-7*

## I. INTRODUCTION AND RELATED WORK

With the number of different types of Web images uploaded at rapid rates, effective approaches for searching diverse images are becoming critical.

Web-based images search differ from non Web-based search in several important ways. These include ( i ) The collection is potentially infinite so that some standard measures such as recall are not directly applicable; ( ii ) The lack of uniformity in metadata set, with some images containing a significant amount, while others may have none, and those providing metadata may also show significant variations in the nature of such data; (iii) The indexing and annotation algorithm must be efficient, since cumbersome or slow algorithm may not be able to adequately keep up with the rate of increase in the size of collection.

For the indexing and retrieval system, the previous research studies proposed many different approaches and framework [1, 2], which mainly fall into two categories. Concept-based method is approach that images are retrieved by high-level concept and objects [3]. While with content-based method, images are retrieved according to low-level content by extracting low level features and capturing image similarities and characteristics [4, 5, 6]. However, the existing works could only give promising result within some specific image sets, such as the images with annotation, but not all image types. For variety different types of images, such as raw images without any tags or captions, and images with full MPEG-7 annotation, in order to get high retrieval accuracy, different levels of image characterization schemes are needed.

In this paper, in order to raise and measure the semantic power of searching and discovering of web images, we propose a multi-level semantic characterization and refinement method which contains different retrieval algorithms differentially applied to different types of Web images. With this method, a higher level of semantic richness is endowed while higher accuracy of retrieval is attained.

## II. FOUR LEVEL SEMANTIC CHARACTERISATION

Web images could be mainly categorized into the following four different types, as shown in Table I .

TABLE I. WEB IMAGE CATEGORY

Image Type	Caption	Annotation, Tag, Keyword	Full MPEG-7 Annotation
1	unavailable	unavailable	unavailable
2	available	unavailable	unavailable
3	available	available	unavailable
4	available	available	available

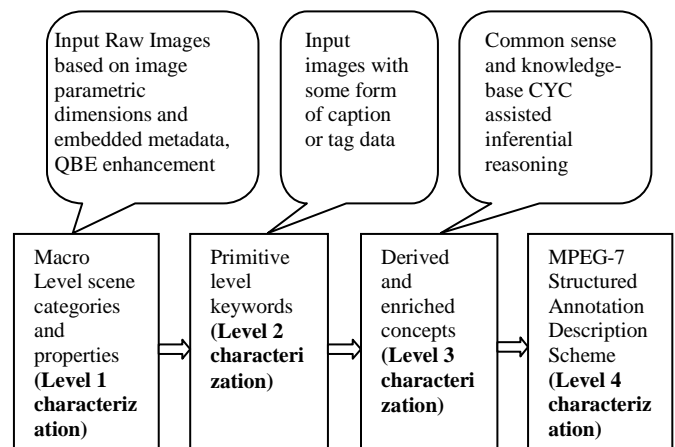


Figure 1. The four levels of semantic characterization

According to the information provided by the images, different characterization schemes are needed to deal with different types of images. Our four levels of semantic characterization model are designed as indicated in Figure 1. The corresponding tasks are: ( i ) automatic semantic class refinement by rule induction and concept validation

enhancement; (ii) object association and CYC enabled inference; (iii) structural casting to MPEG-7 representation and index building.

### III. AUTOMATIC SEMANTIC CLASSIFICATION REFINEMENT BY METADATA AND CONCEPT VALIDATION ENHANCEMENT

For images uploaded with no explicit annotation, caption nor tag, this task will carry out a classification of its semantic content. In the case of JPEG images, metadata such as aperture, exposure time, shutter speed, resolution, date and time, or in some image capture devices, the GPS coordinates, are automatically embedded. With a given image

$$I_i = (d_{i1}, \dots, d_{ik}) \quad (1)$$

characterized by a number of dimensions  $d_{ij}$  which correspond to the image acquisition parameters, each image may be represented by a point in multi-dimensional space. Figure 3 shows the image points of a set of images in which particular types of image scenes (categorized as  $S_i$ 's) tend to naturally cluster together. Our earlier paper [7] has developed a rule-based induction method to separate images into elementary semantic categories  $c_m$ . The induction rule is in the form of

$$R_{mn} : U_1 \wedge U_2 \wedge \dots \wedge U_k \rightarrow c_{mn} \quad (2)$$

where the antecedent will consist of a range of dimensional values of the form  $U_i = \{u_i \mid u_i \in D_i\}$ , with  $u_i$  representing a particular parametric dimension, and  $D_i$  representing the associated restricted domain of values. This will produce a prior probability  $P[c_{mn}]$  for the particular semantic content category. Such categorization will provide a large scale pruning of the search tree whereby highly selective procedures may be applied differentially to different refined categories. Figure 2 categorizes different scenes of images, obtained from Flickr.

Micro	Night Scenes	Indoor Activities	Day Scenes	Portraits	Outdoor Activities

Figure 2. Each column shows the different categories of "Micro", "Night Scenes", "Indoor Activities", "Day Scenes", "Portraits" and "Outdoor Activities"

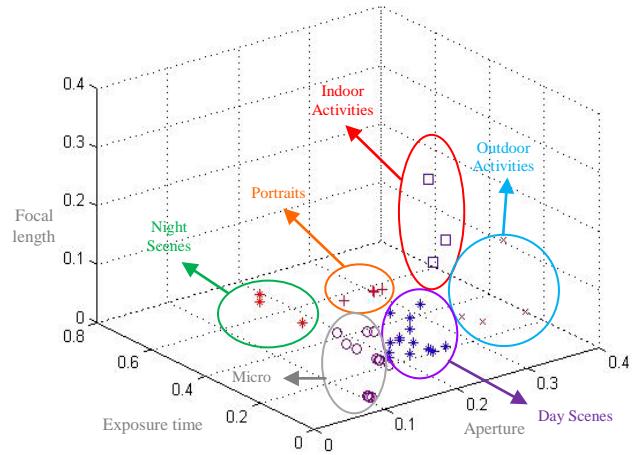


Figure 3. Image distribution in 3D space of some Flickr images

A sample rule set of Automatic Semantic Annotation is shown in Figure 4. For example, we may classify an image with the Aperture value greater than 3.5 and less than 5.6, while the Exposure time greater than 1/50 sec and less than 1/6 sec, as well as the Focal length greater than 18 and less than 33 as the category of Indoor Activities as shown in the figure 4.

- Exposure Value  $\leq 8$  AND Aperture  $< 3.0$  AND  $1/160 < \text{Exposure time} < 1/40$  AND Focal length  $< 6.0 \rightarrow$  Micro
- Timeslot  $\in$  Night AND  $3.5 < \text{Aperture} < 5.6$  AND  $1/50 < \text{Exposure time} < 1/2$  AND  $18 < \text{Focal length} < 88 \rightarrow$  Night Scenes
- $3.5 < \text{Aperture} < 5.6$  AND  $1/50 < \text{Exposure time} < 1/6$  AND  $18 < \text{Focal length} < 33 \rightarrow$  Indoor Activities
- Subject Distance  $> 30$  AND  $3.5 < \text{Aperture} < 4.5$  AND  $1/4000 < \text{Exposure time} < 1/1600$  AND  $18 < \text{Focal length} < 39 \rightarrow$  Day Scenes
- $1.4 < \text{Aperture} < 5$  AND  $1/4000 < \text{Exposure time} < 1/500$  AND  $20 < \text{Focal length} < 50 \rightarrow$  Portraits
- $4 < \text{Aperture} < 10$  AND  $1/2000 < \text{Exposure time} < 1/80$  AND  $18 < \text{Focal length} < 62 \rightarrow$  Outdoor Activities

Figure 4. Sample rules of Automatic Semantic Annotation

### IV. OBJECT ASSOCIATION AND CYC ENABLED INFERENCE

The existing image retrieval techniques seldom consider the context of the keywords present in the user's queries. When the keywords are typed into the searching engine, some information may be lost. Therefore, the refinement and expansion of keywords should be considered to assist semantic searching. The concepts in the user queries and the relationships among concepts should be understood in semantic based information retrieval techniques.

From the sub-categories derived, additional semantics will be incorporated and enriched to support higher precision retrieval. Apart from images without explicit annotation, there are those with some basic caption. Such primitive level of information may be exploited to carry out inferential reasoning based on domain content. It has been found in our study in [1, 7] that captions may sometimes harm annotation correctness, and QBE techniques will be additionally deployed to attempt to filter out the misleading captions and provided keywords. Common sense and domain knowledge from the extensive CYC knowledge base [8, 9] will be used for such enrichment; in particular, we make use of the specific CYC collections and individuals (#Sisa and #Sgens) and CYC Microtheories to carry out the expansion. Unlike the study [10], the correlation of concepts will not only be limited to hypernymy/hyponymy and holonymy/meronymy relationships, but also includes related concepts and common sense non-hierarchical associations. In addition, while [10, 11] is using WordNet, here the application of CYC commonsense knowledge is expected to be far richer, and more comprehensive than WordNet. Using CYC, certain objects in an image may be linked to related objects. Such inferences will entail examination of the conditional probabilities  $\mathbf{P}[J_i | J_j]$ , where  $J_i, J_j$  are objects and  $J_j$  is given to be present in an image. Common sense association and ontology in CYC are used to construct an inference tree, which allows the index elements  $X_i$ 's of an image to be automatically expanded according to the probability linked to the underlying ontology of the domain, see Figure 5.

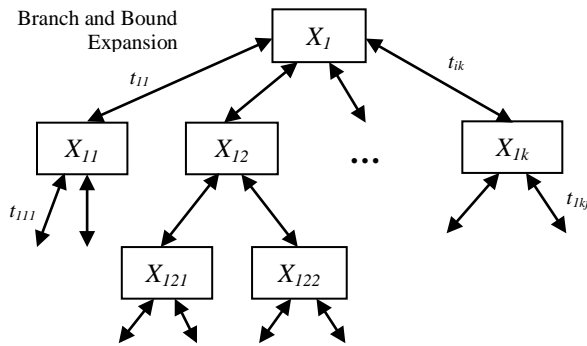


Figure 5. CYC assisted concept expansion tree

Associated with each branch is a tree expansion probability  $t_{ij}$  which signifies the probability of occurrence of the branch index element given the existence of the parent index element. Although the ontology expansion may be carried out bi-directionally, top-down traversal will yield greater expansion efficiency than bottom-up traversal, and will be the chief focus of the expansion algorithm. For high precision retrieval, branch and bound techniques will be used to maximize efficiency. An example of demonstrating concept expansion is shown as follows in Figure 6 [12]. It shows the hierarchy relationship of Orchestra family. And we may use this kind of relationship to expand or refine our queries.

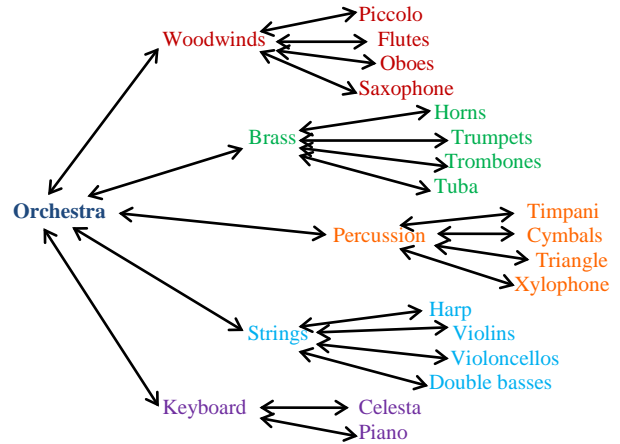


Figure 6. Example of concept expansion

Table 2 illustrates the experimental results of query expansion using the tagged Flickr images. The second column gives the precision of the query “Springfield”/“Triangle”; the third column gives the precision of the expanded query “Springfield+Missouti”/“Triangle+Percussion”; the third column gives the precision of the further expanded query “Springfield+Missouti+USA” / “Triangle+Percussion+Orchestra”. The precisions here are obtained by only observing the first two pages of the searching results.

TABLE II. EXAMPLE OF QUERY CONCEPT EXPANSION

	Plain query words	+1 holonymy	+2 holonymy	...	+k holonymy
	<b>Springfield</b>	<b>Missouri</b>	<b>USA</b>		-
Precision	5.6%	61.1%	22.2%		-
	<b>Triangle</b>	<b>Percussion</b>	<b>Orchestra</b>		-
Precision	6.3%	75.0%	29.2%		-

## V. MULTIPLE CHARACTERISATION AND STRUCTURAL CASTING INTO MPEG-7

As demonstrated in our MPEG-7 Core Experiment [13], the indiscriminate use of keyword will result in an inordinate number of returns and weaken the retrieval precision. The object, attribute, relationship in accordance with the Ternary Fact Model from the previous stages will be analyzed and the first four elements in the MPEG-7 Structured Annotation Description Scheme will be filled. In the case of images without any captions or tags, the second to fourth elements in the MPEG-7 Structured Annotation Description Scheme will be filled, which gives definite semantic properties of an image. MPEG-7 represents the final most semantically rich level of characterization from which the search index is constructed for image identification. The task of this level is responsible for casting the unstructured semantic information into MPEG-7 Structured Annotation from which an index is built. Such an MPEG-7 index relation will typically have more than one tuple associated with a given image, which will have a composite primary key ImageID,

MPEG7\_DS\_ID for mapping particular image property to the image. Figure 7 shows an example of automatic generation of semantic MPEG-7 descriptions for image from metadata.

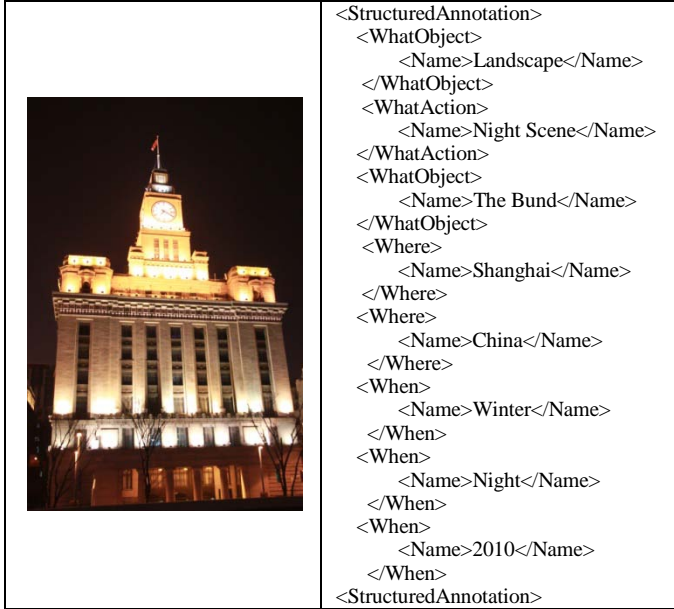


Figure 7. Automatic generation of semantic MPEG-7 descriptions for image from metadata

## VI. CONTROLLED EXPERIMENTS

To measure the effectiveness of the approach, controlled experiments are performed. 1,000+ Images are collected using an unbiased randomized mechanism from Flickr.com to form the basis of the experimentation. These represent a cross-section of the different types of Web images, and they consist of three main subsets:

- images where text information is completely absent – subset 1
- images with basic caption – subset 2
- images annotated with keywords and tags – subset 3

Measures of performance are taken between the unaided approach similar to that in search engines and the present approach for each individual subset as well as collectively for their union. A set of representative semantic queries is designed which is used for all the experiments. The following are used to measure system performance of both approaches on the same image collection:

- precision

$$Precision = \frac{|\{relevant\_images\} \cap \{retrieved\_images\}|}{|\{retrieved\_images\}|} \quad (3)$$

$$Recall = \frac{|\{relevant\_images\} \cap \{retrieved\_images\}|}{|\{relevant\_images\}|} \quad (4)$$

- average precision

- fallout

$$Fallout = \frac{|\{non-relevant\_images\} \cap \{retrieved\_images\}|}{|\{non-relevant\_images\}|} \quad (5)$$

- F $\alpha$ -score for  $\alpha \ll 1$

$$F_{\alpha} = \frac{(1 + \alpha^2)(Precision * Recall)}{(\alpha^2 * Precision + Recall)} \quad (6)$$

Recall is not included as a direct measure, since for potentially infinite collections, the total number of relevant images cannot be directly determined. However, the F $\alpha$ -score gives some indication of recall, which may be ascertained for the finite collections in these experiments. Substantially higher weight is assigned to precision ( $\alpha=0.01$ ), which is much more important for Internet search.

The experimental results are shown in Table 3. We see that the precision, F-score and average precision are all satisfactorily higher compared with the unaided approach, while the fallout or false alarm (which is the proportion of non-relevant images retrieved) is kept reasonably low. These results indicate that significant improvement in performance may be attained from using the proposed approach.

TABLE III. EXPERIMENTAL RESULT

		Unaided approach	Proposed approach
Subset 1	Precision	-	66.20%
	Fallout	-	35.00%
	F $\alpha$	-	66.20%
Subset 2	Precision	57.09%	70.26%
	Fallout	38.60%	21.13%
	F $\alpha$	58.20%	72.68%
Subset 3	Precision	82.29%	89.01%
	Fallout	16.74%	12.10%
	F $\alpha$	79.92%	90.91%
All Subsets	Average Precision	51.02%	74.76%

## VII. CONCLUSION AND FUTURE WORK

As shown from the results of our experiments, with our proposed approach of the four levels of semantic characterization, the accuracy of Web image searching has seen significant improvements. By the systematic analysis of embedded image metadata and parametric dimensions, the query refinement with object association and CYC enabled inference, as well as the image metadata enhancement with MPEG-7 Structured Annotation Description Scheme, different types of Web images could be retrieved with higher precision. The semantic meanings of Web images, including raw images, images with captions or tags, and the images with MPEG-7 full annotation, are enriched and standardized. Additional refinement is no doubt possible and desirable in

future to further increase user satisfaction. Our proposed approach is an important first step towards this.

There still exist limitations for our proposed methods. Such as for many images on the web, the metadata are not fully provided. In this case, the first level of pruning could not come into play in our model. Our future work is further optimizing each level of our model to achieve the best performance and user satisfactory.

#### REFERENCES

- [1] R. C. F. Wong and C. H. C. Leung, "Automatic Semantic Annotation of Real-World Web Images", *IEEE Trans. Pattern Analysis and Machine Intelligence*, Vol. 30, No. 11, pp. 1933-1944, 2008.
- [2] J. Li and J.Z. Wang, "Real-Time Computerized Annotation of pictures," *IEEE Trans. Pattern Analysis and Machine Intelligence*, vol.30, no. 6, pp. 985-1002, June 2008.
- [3] D. Liu and T. Chen, "Content-Free Image Retrieval Using Bayesian Product Rule," *Proc. IEEE Int'l Conf. Multimedia and Expo (ICME '06)*, pp. 89-92, 2006..
- [4] I.A. Azzam, C.H.C. Leung, and J.F. Horwood, "Implicit Concept-Based Image Indexing and Retrieval," *Proc. 10<sup>th</sup> IEEE Int'l Conf. Multimedia Modeling (MMM '04)*, pp. 354-359, 2004.
- [5] J. Vogel, A. Schwaninger, C. Wallraven, and H.H. Bu'lhoff, "Categorization of Natural Scenes: Local versus Global Information and the Role of Color," *ACM Trans. Applied Perception*, Vol. 4, No. 3, p. 19, 2007
- [6] D. Cremers, M. Rousson, and R. Deriche, "A Review of Statistical Approaches to Level Set Segmentation: Integrating Color, Texture, Motion and Shape," *Int'l J. Computer Vision*, Vol. 72, No. 2, pp. 195-215, 2007
- [7] C. H. C. Leung, W.S. Chan, A. Milani, J. Liu and Y.X. Li, "Intelligent Social Media Indexing and Sharing Using an Adaptive Indexing Search Engine", *ACM Transactions on Intelligent Systems and Technology* (To appear).
- [8] Reed, Stephen and D. Lenat. "Mapping Ontologies into Cyc," in *Proceedings of AAAI 2002 Conference Workshop on Ontologies for The Semantic Web*, Edmonton, Canada, 2002.
- [9] Matuszek, Cynthia, M. Witbrock, R. Kahlert, J. Cabral, D. Schneider, P. Shah and D. Lenat, "Searching for Common Sense: Populating Cyc from the Web," In *Proceedings of the Twentieth National Conference on Artificial Intelligence*, Pittsburgh, Pennsylvania, 2005.
- [10] Gao, Y. and Fan, J. "Incorporating Concept Ontology To Enable Probabilistic Concept Reasoning for Multi-Level Image Annotation," in *Proceedings of the 8th ACM International Workshop on Multimedia information Retrieval*, pp. 79-88, 2006.
- [11] Antonio Torralba, Rob Fergus, William T. Freeman, "80 Million Tiny Images: A Large Data Set for Nonparametric Object and Scene Recognition," *IEEE Transactions on Pattern Analysis and Machine Intelligence*, Vol. 30, No. 11, pp. 1958-1970, 2008.
- [12] Wikipedia: <http://en.wikipedia.org/wiki/Orchestra>.
- [13] A. M. Tam, C. H. C. Leung, "Semantic Content Retrieval and Structured Annotation: Beyond Keywords", *ISO/IEC JTC1/SC29/WG11 MPEG00/M5738*, Noordwijkerhout, Netherlands, March 2000.